Spectroscopy of Polaritonic Excitations in Semiconductors

Thesis presented to the Institute of Physics of the University of Dortmund, Germany
in partial fulfilment of the requirements for the degree of
Doktor rer. nat.

presented by

Gregor Dasbach

Dortmund 2003

Accepted by the faculty of the Institute of Physics of the University of Dortmund, Germany.

Day of the oral exam: 7th of November 2003

Examination board:

Prof. Dr. Klaus Wille

Prof. Dr. Manfred Bayer

Prof. Dr. Metin Tolan

Dr. Dmitri Yakovlev

Contents

Chapter 1

Motivation

It was a century ago that Max Planck's postulation of quantized radiation opened the door to the quantum world. In the following decades the theoretical framework of modern quantum mechanics was developed, giving insight into the often anti-intuitive laws of microscopic physics. This revolutionary theory gives a new meaning to fundamental physical parameters such as a particles trajectory, which was replaced by a probability amplitude. One of the most important consequences of quantum mechanics, not only for scientists, is the uncertainty principle. It gives an upper limit to the accuracy of a measurement and describes the impact of the measurement itself on the result. No matter how carefully an experiment is performed, some questions about the quantum system will remain unanswered. For example, the more precisely we know the momentum of a particle, the less information we have on its position. Determinism, which is based on the idea, that by knowing the present state of a system we can exactly derive its entire future evolution had served its time. Or, putting it figurative, Schrödingers cat expelled the Laplacian demon, which had severe consequences for science just as much as for philosophy.

At first sight, the implications of quantum mechanics might appear to be an obstacle in the classical understanding of science, as it intrinsically obscures a microscopic physical system. Indeed, the quantum theory sets severe limitations to the validity of classical physics, but it gives an alternative theory, which is by far richer in scope and applicability. In consequence, quantum systems offer a variety of non-classical phenomena, which give access to new scientific concepts. However, most applications can still be described as classical systems, as their operation involves a macroscopic number (N) of particles and variation scales as $1/\sqrt{N}$. For example, the operation of integrated circuits etc. can be described by the classical laws of physics. However, we might be facing real quantum machines in the near future.

Recent progress in fundamental science as well as nanofabrication gives us a tool at hand for developing new functional units, in which operations take advantage of peculiar quantum mechanical properties. Many proposals for such quantum machines have been made. The concept of quantum computation [1, 2] is one of the leading

ideas. While the realization of this concept for practical use is still in doubt, other quantum systems are closer to a technical application. Recent progress in the field of quantum cryptography [3] can lead to technical applications within a decade or less. However, real quantum engineering is still restricted to laboratory environments. The study presented here focuses on fundamental aspects that might help to pave a small step upon the way to future applications. Besides the perspective of potential applicability, this study is motivated by the fundamental goal of scientific research: reaching a deeper understanding of the world around us.

Actually the fraction of the world under investigation here is rather specific: exciton-photon polaritons. As we will see in chapter 2 these particles can be described as hybrids of light and matter. First, we will develop a quantum mechanical description of polaritons. Equipped with the fundamental insights, we proceed with an in-depth study of these quasi-particles. In the course of this work we will meet two types of polaritons: quadrupole polaritons in bulk semiconductors and dipole polaritons in semiconductor microcavities. We will start with quadrupole polaritons, which are investigated in cuprous oxide (chapter 3). Here a novel spectroscopic approach is chosen that provides an extreme spectral resolution (section 3.1). Using this spectroscopic technique we will search for ultra slow polaritons in section 3.3; they may be slowed down from the speed of light to the speed of sound. We also get access to a polariton fine structure never observed before (section 3.4). This fine structure will be modelled theoretically and compared to experimental data. This chapter will be concluded by studies in the high density regime (section 3.5) which will focus on the observation of absorption linewidths in the nano electron volt (neV) regime, which is exceptional for transitions in solids.

We will then proceed to the investigation of dipole polaritons in semiconductor microcavities (chapter 4). First, we will focus on the dynamics of the carriers. Therefore we apply time resolved pump-and-probe spectroscopy. Using this technique the impact of disorder in the exciton system is investigated. We will learn how exciton trapping in potential fluctuations can influence the nonlinear optical response of the cavity (section 4.2). Using these insights we tackle questions concerning the spin properties of cavity polaritons (section 4.3). After having obtained a deep understanding of polaritons, we attempt to manipulate their optical properties. In particular we want to tailor parametric polariton scattering processes by adjusting the resonator geometry (section 4.4). For this purpose polaritons in quasi-zero-dimensional and quasi-one-dimensional cavities are investigated. Finally, the results are summarized (chapter 5) and an outlook is given (chapter 6).

Chapter 2

Exciton-photon polaritons

Excitations in solids are often described by the concept of quasi-particles. The properties of such quasi-particles are determined by their environment; the solid. For example, elastic waves in solids are successfully treated in this fashion, where the energy quantum of such a lattice vibration is termed a phonon [4]. Electronic states in solids can be treated as such quasi-particles, where such a quasi-free electron is not to be mistaken with the elementary particle of negative unit charge. Such an electron feels the background of the crystal lattice. This gives rise to an effective mass, which differs form the electron mass. In a semiconductor electrons can be excited from the valence band into the conduction band. This process leaves an unoccupied state in the valence band. Again, the concept of quasi-particles can be applied, where the vacancy is described as a positive unit charge in the valence band and is termed a hole. The benefits of this concept become evident when treating the interactions between excitations.

For example, Coulomb interaction between the electron in the conduction band and the hole in the valence band gives rise to the formation of coupled electron-hole pairs. This quasi particle is referred to as an exciton [4]. We can also think of states, which consist of an excitation of the solid and a photon, which is the quantum of an electromagnetic wave. As we will see below, photons can couple, for example, to excitons via dipole interaction. The quantum of such a coupled state is termed a polariton [5]. We will now take a closer look at the physics of exciton-photon polaritons.

Typically, a photon travelling through matter is considered to be decoupled from the excitations in the solid. We can treat the electromagnetic field in the solid by simply assuming a constant dielectric background. This approximation fails when the energy of the photon is in resonance with a transition in the solid, where the photon can be absorbed. The absorption process induces a polarization in the dielectric, which in turn can again act as a source of an electromagnetic field (photon) [6]. Going back into the quasi-particle picture, this interplay is described as a cycle of photon absorption, generating an excitation (i.e. an exciton), radiative recombination of the particle and emission of a photon. The energy oscillates back and forth between an exciton population and the electro magnetic field. Under these circumstances we can no

longer treat a photon as decoupled from its environment. To describe this phenomenon we treat exciton and photon as coupled oscillators.

The effective second-quantized Hamiltonian H of the coupled eigenmodes can be written as follows [7, 8]:

$$\begin{aligned} H &= H_P + H_X + H_{int} \\ &= \sum_{\mathbf{e}} \sum_{\mathbf{k}} [E_{P,\mathbf{k}}(a^\dagger_{\mathbf{k},\mathbf{e}} a_{\mathbf{k},\mathbf{e}} + \tfrac{1}{2}) + E_{X,\mathbf{k}}(b^\dagger_{\mathbf{k},\mathbf{e}} b_{\mathbf{k},\mathbf{e}} + \tfrac{1}{2}) + \hbar\Omega_{R,\mathbf{k},\mathbf{e}}(a^\dagger_{\mathbf{k},\mathbf{e}} b_{\mathbf{k},\mathbf{e}} + a_{\mathbf{k},\mathbf{e}} b^\dagger_{\mathbf{k},\mathbf{e}})], \end{aligned} \tag{2.1}$$

where $a^\dagger_{\mathbf{k},\mathbf{e}}, b^\dagger_{\mathbf{k},\mathbf{e}}$ ($a_{\mathbf{k},\mathbf{e}}, b_{\mathbf{k},\mathbf{e}}$) are the bosonic creation (annihilation) operators of photons and excitons with momentum $\mathbf{k}$ and polarization $\mathbf{e}$, respectively. The first terms express the energy of photon E_P and exciton E_X. The coupling is given by the interaction Hamiltonian H_{int}. The coupling is characterized by the Rabi frequency Ω_R [9]. The interaction between exciton and photon depends on the oscillator strength f of the transition from the vacuum level $|0\rangle$ to the exciton state $|X\rangle$:

$$f \sim | \langle X|H'|0\rangle |^2 . \tag{2.2}$$

For dipole transitions H' is the electric dipole operator, but also higher order (i.e. quadrupole) interaction can give rise to polaritonic coupling. Dipolar coupling will be treated in chapter 4, while quadrupolar coupling is discussed in chapter 3. The Rabi frequency scales with the square root of f. Here we neglect dissipative processes [5]. That means e.g. that we assume a perfect crystal in the case of bulk polaritons. For simplicity, we do not consider interaction with phonons or between excitons. Coupling mechanisms of higher order are also neglected. This treatment allows for an exact stationary solution for the polariton modes. As no interaction between states of different $\mathbf{k}$ or $\mathbf{e}$ is included, the eigenvalue problem can be solved for each $\mathbf{k}$ and $\mathbf{e}$ independently. For the studies presented here, the $\mathbf{k}$ dependence (dispersion) of the polariton modes is of primary importance, hence we will proceed with a sample treatment at fixed $\mathbf{e}$.

The coupling between the eigenmodes is nicely seen in the matrix representation of H in the basis of exciton $|X\rangle$ and photon states $|P\rangle$.

$$H = \begin{pmatrix} E_{P,\mathbf{k}} & \frac{\hbar\Omega_R}{2} \\ \frac{\hbar\Omega_R}{2} & E_{X,\mathbf{k}} \end{pmatrix}. \tag{2.3}$$

The Hamiltonian can be diagonalized easily in the polariton basis with the upper $|\,U\rangle$ and lower polariton states $|\,L\rangle$:

$$\begin{aligned} |L\rangle &= \quad X_{\mathbf{k}}|X\rangle + P_{\mathbf{k}}|P\rangle, \\ |U\rangle &= -P_{\mathbf{k}}|X\rangle + X_{\mathbf{k}}|P\rangle. \end{aligned} \tag{2.4}$$

Here $X_{\mathbf{k}}$ and $P_{\mathbf{k}}$ are the Hopfield coefficients, which represent the exciton and photon fraction of the polariton: This yields the eigenvalues

$$E_{U/L,\mathbf{k}} = \frac{E_{P,\mathbf{k}} + E_{X,\mathbf{k}}}{2} \pm \sqrt{\left(\frac{E_{P,\mathbf{k}} - E_{X,\mathbf{k}}}{2}\right)^2 + \left(\frac{\hbar\Omega_R}{2}\right)^2}. \tag{2.5}$$

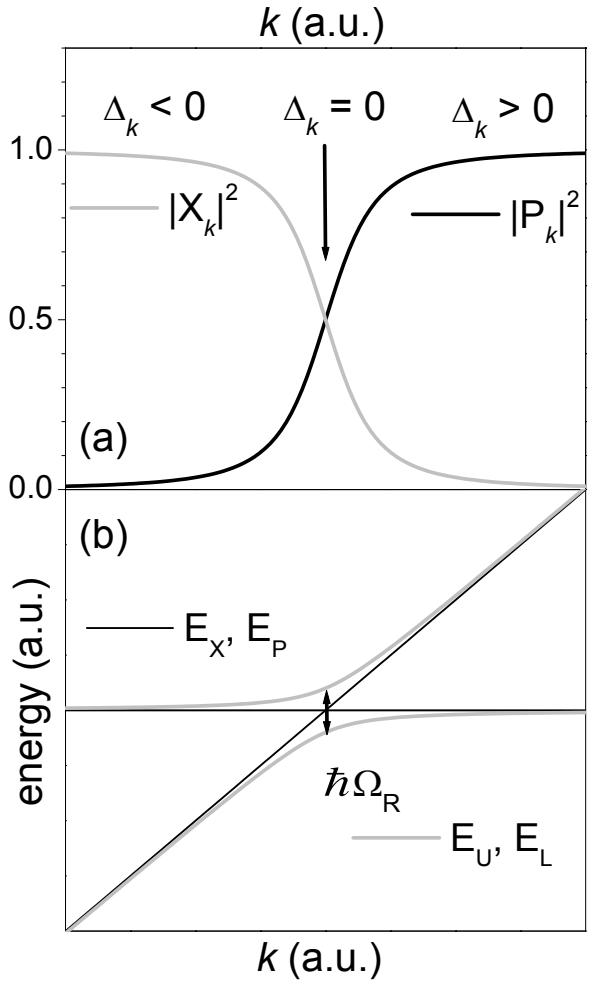

Figure 2.1: *(a) Square of the Hopfield coefficients of the lower polariton mode as a function of k. The black (grey) trace gives the photon (exciton) fraction. (b) Dispersion of exciton-photon polaritons. The polariton modes are plotted in grey. The dispersion of the uncoupled oscillators (exciton and photon) are given by the black traces.*

The corresponding Hopfield coefficients are given by:

$$|X_{\mathbf{k}}|^2 = \frac{1}{1+\left(\frac{\hbar\Omega_R}{2(E_{L,\mathbf{k}}-E_{P,\mathbf{k}})}\right)^2},$$
$$|P_{\mathbf{k}}|^2 = 1-|X_{\mathbf{k}}|^2 = \frac{1}{1+\left(\frac{2(E_{L,\mathbf{k}}-E_{P,\mathbf{k}})}{\hbar\Omega_R}\right)^2}. \tag{2.6}$$

These relations are seen in Fig. 2.1. Here the exciton is assumed to have no dispersion ($E_{X,\mathbf{k}} = \text{const.}$). The photon is described by a linear dispersion ($E_P \sim k$). The energy difference

$$\Delta_{\mathbf{k}} = E_{P,\mathbf{k}} - E_{X,\mathbf{k}} \tag{2.7}$$

is called the exciton-photon detuning. In the range of negative detunings the upper polariton branch (UPB) is strongly excitonic, while the lower branch (LPB) is photon-like. With decreasing $|\Delta_{\mathbf{k}}|$ the hybrid character of the polaritons increases. At resonance ($\Delta_{\mathbf{k}} = 0$) both modes have equal admixtures of exciton and photon $|P_{\mathbf{k}}|^2 = |X_{\mathbf{k}}|^2 = \frac{1}{2}$.

The splitting between UPB and LPB is at its minimum and equals $\hbar\Omega_R$. The reverse behavior is found when moving towards positive detunings, where the UPB approaches the light dispersion and the LPB becomes exciton-like. We see the well-known anti-crossing behavior characteristic of coupled quantum systems. The stronger the normal mode coupling, the stronger the level repulsion and the more pronounced the anti-crossing.

The treatment presented above gives a general description of exciton-photon polaritons. It is not restricted to the specific exciton and photon dispersion shown in the example of Fig. 2.1. In the introductions of chapter 3 and 4 we will specify the exciton-photon system under investigation. The simplified coupled oscillator picture gives an intuitive description of polaritons. It can easily be extended to a larger number i of modes, simply by adding these modes and their coupling terms in Eq. 2.3, which leads to an $i \times i$ matrix representation. For example, this can be useful for the description of polaritons formed by photons coupled to heavy as well as light hole excitons [10], coupling between two-particle states of photons and excitons [11] or coupling of fine structure states to light (see chapter 3.4). An example for such an extended treatment will be given in section 4.4.2.

The rigorous description of excitations coupled to light always requires the polaritonic treatment. Obviously, the detection of exciton emission in an optical experiment intrinsically requires such a coupling. Nevertheless, polaritonic effects are often neglected and both quanta are treated separately. We will now briefly discuss under which conditions this is justified and where the polaritonic treatment is required. So far we have considered a system free of dissipative processes. In the present description the energy oscillates between $|X\rangle$ and $|P\rangle$ with the frequency $\frac{\Omega_R}{2\pi}$. This phase coherent energy transfer is called Rabi flopping [9] and has been observed in many quantum systems, even for a single atom in a cavity. In real systems the oscillation will be damped, however [12]. Such damping might be due to scattering with phonons or other polaritons. Furthermore, the photon component might be affected by losses. Photons can leak out of the specimen, breaking the circle of absorption and emission. The relevance of the specific sources of damping will be discussed with the particular polariton systems. Independently of the origin of such dissipative processes, two general criteria for the relevance of the polariton description can be formulated [8]:

- temporal coherence: The pure dephasing rate $1/T_2'$ and the population decay rate T_1 are slower than the Rabi frequency. With the optical dephasing time T_2 ($\frac{1}{T_2} = \frac{1}{2T_1} + \frac{1}{T_2'}$) this can be written as: $\frac{1}{T_2} \ll \Omega_R$.
- spatial coherence: the coherence length of the exciton must be larger than the photon wavelength λ_P inside the dielectric, such that the exciton does not scatter within one spatial cycle of the electro-magnetic field. Taking the group velocity v_g we find: $T_{2,X} v_g \gg \lambda_P$.

Typically, the second criterium is the more stringent one. If these criteria are not fulfilled we speak of the weak coupling or perturbative regime. Here lossy processes

dominate and the energy transfer between photon and exciton is only a small perturbation. In this regime the dynamics of the system is described by Fermi's golden rule: The exciton population decays exponentially. However, even if in this case the mode coupling is only a small perturbation, the exact description still requires the inclusion of light-matter coupling.

If both criteria are fulfilled we speak of the strong coupling regime. It is also referred to as the non-perturbative regime, as the light-matter coupling can not be treated as a small perturbation. In the course of this work we will stick to the regime of strong coupling. As we will see, *strong* coupling does not always imply a strong interaction between light and matter. The regime of strong coupling is as well the regime of high coherence. For the polaritons investigated in chapter 3 the light matter coupling is indeed extremely weak, however the exceptional coherence of the system requires a description as coupled modes [13].

Chapter 3

Polaritons in cuprous oxide

The central topic of this chapter is the optical spectroscopy of exciton-photon polaritons in bulk semiconductors. In particular, we will investigate these excitations with extremely high spectral resolution. Besides the experimental challenges, high resolution spectroscopy also demands samples of extremely high crystallographic quality.

For this task cuprous oxide (Cu_2O) is ideally suited, which can also be considered the classic model system for exciton physics. For technical applications Cu_2O is of little interest, mostly due to is poor conductance and the difficulties in its fabrication. Many growth techniques have been reported, which typically rely on controlling temperature and partial pressure close to the melting point (see i.e. Kotsyumakha *et al.* [14]). More recently, epitaxial growth methods have been reported, where thin films of Cu_2O have been deposited on MgO. [15, 16] But still single crystal-like films, allowing for optical studies, are hard to find [17]. For some applications these thin films, which are typically highly strained, might be advantageous, however the crystal quality of such artificially grown Cu_2O remains poor. A much better quality is found in Cu_2O crystals of natural origin. Not surprisingly, most recent optical studies rely on natural crystals of cuprous oxide. Unfortunately, natural crystals with little defects, strain etc. are rare. Cu_2O is known as 'cuprite' among mineralogists or as copper-I-oxide.

A photograph of a natural Cu_2O crystal is shown in Fig. 3.1. From the first days of semiconductor spectroscopy, Cu_2O has been investigated [18] and also the first successful experimental studies of excitons were performed on Cu_2O [19, 20]. This discovery nicely confirmed theoretical predictions [21, 22] and initiated a period of successful interplay between theory and experiment [23, 24]. The early spectroscopic studies on excitons in Cu_2O are summarized in the review articles by Agekyan [25] and Nikitine [26]. After examining the linear optical properties and their dependencies on perturbations, such as electric and magnetic fields [25, 27, 28] or strain [29, 30], studies concentrated more and more on the lowest exciton series and its 1S ground state.

Nowadays this state plays a key role in proposals for Bose-Einstein condensation (BEC) of excitons [31, 32]. Even though numerous claims of such collective exciton coherence have been published [33, 34, 35, 36] no conclusive and unambiguous proof

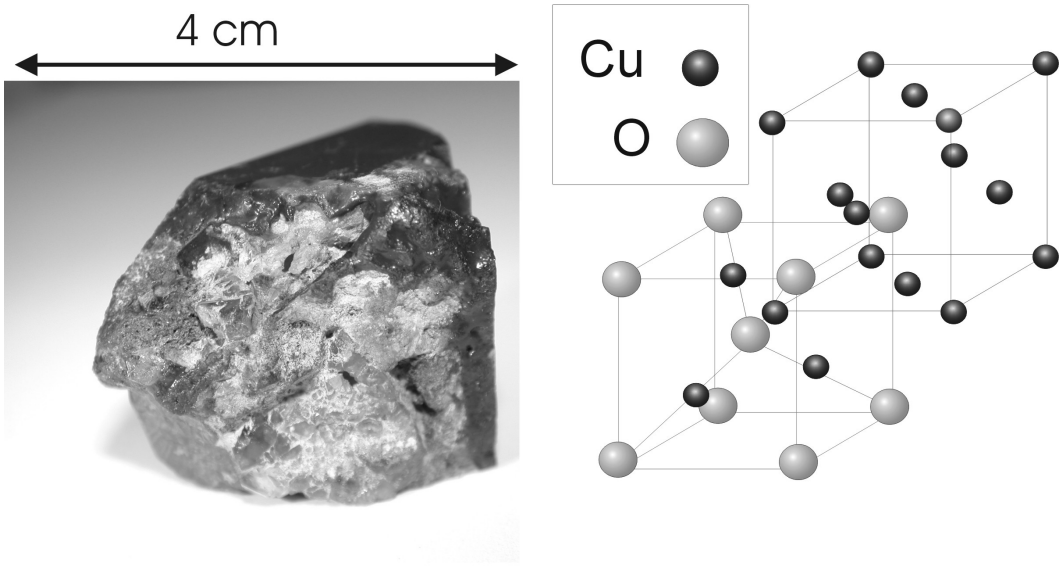

Figure 3.1: *Left: Photograph of a natural Cu_2O crystal. The size of this piece is about 30×30×30 mm^3. All samples investigated in this work were cut from this crystal. Right: Drawing of the Cu_2O lattice. Small spheres mark the positions of the copper ions, while the larger spheres mark the positions of the oxygen ions.*

of a condensation of excitons has been given, which lead to retraction [37]. However, besides studies on vertically coupled quantum wells [38] and microcavities [39, 40] (see also chapter 4) cuprous oxide keeps on playing a central role in this field. Recent projects attempt to confine excitons in harmonic strain traps [41, 42], to mimic a carrier confinement similar to ion traps used for Bose-Einstein condensation of alkali ions [43]. Here we will demonstrate that even though Cu_2O is one of the best investigated semiconductors, high resolution spectroscopy can add fundamental insight to the understanding of excitons.

Cu_2O condenses in a cubic structure, where the copper ions form a face-centered sublattice, while the oxygen ions form a body-centered sublattice. The arrangement of both sublattices is such that a copper ion is found centered between two neighboring oxygen ions (see right section Fig. 3.1). This arrangement makes Cu_2O a simple cubic crystal with inversion symmetry, described by the point group O_h. This unusual structure is only shared by Ag_2O and Pb_2O. The lattice constant of Cu_2O is 0.426 nm [44]. From the lattice structure we now turn to the band structure of this crystal [45]. We find a direct band gap, where the valence band is formed by the Cu 3d orbitals and the conduction band arises from Cu 4s orbitals[1] (see Fig. 3.2) of Γ_1^+ symmetry (we will use the notation of Koster *et al.* [46]). When considering the crystal field, the five 3d states of the valence band split further into three states of Γ_5^+ type and a twofold Γ_3^+

[1]For the excitons in Cu_2O electron and hole can be attributed to the same atom (Cu), which is very unusual.

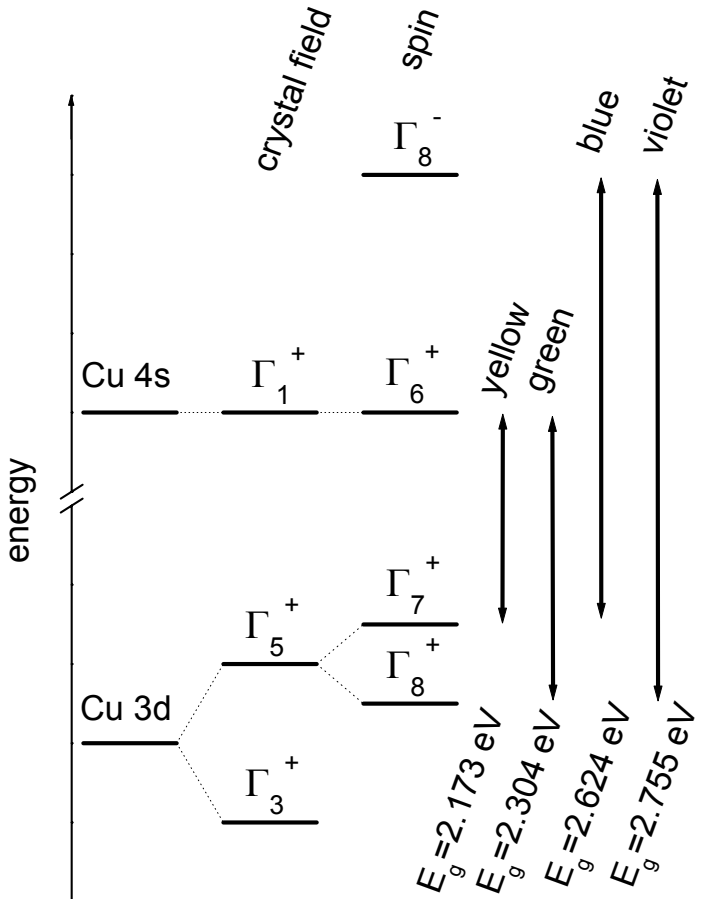

Figure 3.2: *Energy levels of Cu_2O close to the band gap. On the far left the levels as determined from the relevant atomic orbitals are shown. They are split by the crystal field (middle). Considering spin the level structure as shown on the right is obtained. The arrows mark the transitions associated with the exciton series indicated.*

level, where the Γ_5^+ state is higher in energy. Taking also spin-orbit interaction into account, the Γ_5^+ state splits further into a twofold Γ_7^+ level and a fourfold degenerate Γ_8^+ level. The Γ_7^+ states are shifted by 133 meV to higher energy with respect to the Γ_8^+ states [27]. Including spin, the lowest conduction band is described by a doubly degenerate Γ_6^+ state. The next higher state of the conduction band has Γ_8^- symmetry and is 0.476 eV higher in energy. The minimum band gap $E_g = 2.173$ eV makes Cu_2O a semiconductor.

With the hole in the Γ_7^+ or Γ_8^+ valence band and the electron in the Γ_6^+ or Γ_8^- conduction band several series of excitonic transitions can be identified. The excitonic transitions with holes in the Γ_7^+ band and electrons in the Γ_6^+ conduction band give the so-called yellow exciton series, which is lowest in energy. Exciton series of higher energy are (see Fig. 3.2):

- the green series, where the hole is in the Γ_8^+ state, with the electron in the Γ_6^+ state ($E_g = 2.304$ eV [47]);
- the blue series, where the electron is in the next higher state of the conduction band (Γ_8^-), with a Γ_7^+ hole ($E_g = 2.624$ eV [47]);
- the violet series with a Γ_8^- electron and a Γ_8^+ hole ($E_g = 2.755$ eV [47]).

The exciton representation is obtained from the direct product of electron and hole representations and the envelope function

$$\Gamma_{ex} = \Gamma_{env} \otimes \Gamma_e \otimes \Gamma_h. \tag{3.1}$$

As the yellow excitons are formed by Γ_7^+ and Γ_6^+ states they decompose into representations of Γ_5^+ and Γ_2^+ for S-excitons ($\Gamma_{env} = \Gamma_1^+$) [46]. The threefold Γ_5^+ states are termed orthoexcitons, while the single Γ_2^+ level is referred to as paraexciton. Both levels are split by electron-hole exchange interaction, where the paraexciton is found 12 meV below the orthoexciton [48, 49]. This makes the 1S paraexciton the lowest exciton level of Cu_2O. To understand the coupling of the exciton transitions to light we develop $e^{\mathtt{i}\mathbf{kr}}$ into a powers of $\mathbf{r}$:

$$e^{\mathtt{i}\mathbf{kr}} = 1 + \mathtt{i}\frac{\mathbf{kr}}{1!} + \mathtt{i}^2\frac{(\mathbf{kr})^2}{2!} + \mathcal{O}[\mathbf{r}^3]. \tag{3.2}$$

The constant term corresponds to electric dipole transitions. The next higher orders are quadrupole and octupole transitions. The transition to the paraexciton state is optically forbidden to all orders in the absence of perturbations. For the yellow excitonic P series ($\Gamma_{env} = \Gamma_4^-$) we find

$$\Gamma_{ex} = \Gamma_4^- \otimes \Gamma_6^+ \otimes \Gamma_7^+ = \Gamma_2^- \oplus \Gamma_3^- \oplus \Gamma_4^- \oplus 2\Gamma_5^-. \tag{3.3}$$

Due to their Γ_4^- components, the P-excitons of the yellow series can couple to the light field via dipole interaction. They exhibit a perfect hydrogen-like spectrum

$$E_i = E_g - \frac{E_b}{i^2}; \qquad\qquad i \geq 2, \tag{3.4}$$

with a band gap of $E_g = 2.1725$ eV at T = 4.2 K and a binding energy $E_b = 97.43$ meV [47, 50, 51]. For excitons E_b is the equivalent of the Rydberg energy E_{Ry} for the hydrogen atom. It is given by:

$$E_{Ry} = \frac{e^2 m_0}{2\hbar} \approx 13.6\ eV. \tag{3.5}$$

Here m_0 is the free electron mass and the momentum of the nucleus is neglected. In a naive approximation we rescale the Coulomb force in the dielectric $e^2 \to e^2/\epsilon_0$ ($\epsilon_0 = 7.11$ [32] is the dielectric constant in the low frequency limit) and calculate the reduced exciton mass m_r assuming $m_e \approx m_h \approx m_0$:

$$m_r = \frac{m_e m_h}{m_e + m_h} \approx \frac{m_0}{2}. \tag{3.6}$$

In this picture we find $E_b = E_{Ry}/(2\epsilon_0^2) = 136$ meV. The good agreement between the real value and the approximation indicates that the effective masses of electron m_e= 0.99 m_0 and hole $m_h = 0.69\ m_0$ [52] are close to the free electron mass m_0 [32]. The oscillator strengths of these transitions are given by $f_i = 3.0 \cdot 10^{-5}\frac{i^2-1}{i^5}$. This exciton series has been observed up to $i = 10$ [25].

The 1S exciton is found at 2.0326 eV with $E_b = 150$ meV [25]. The Bohr radius of the exciton is given by

$$a_X = \frac{2\pi\epsilon_0}{E_b}. \tag{3.7}$$

For the 1S exciton a_X is extremely small (0.5 nm) and comparable to the lattice constant [32]. In this case the description as weakly bound Mott-Wannier exciton becomes problematic and we are approaching the case of Frenkel excitons [4]. This leads to central cell corrections [53]. In this limit the effective mass of the exciton can no longer be approximated by the sum of m_e and the m_h and indeed values of $m_X = 2.7$ m_0 are measured [54, 55]. The description of this exciton series is further complicated by mixing between S and D type states [50].

The yellow 1S orthoexcitons will be studied in this chapter. The transition from the ground state (Γ_1^+) to the 1S orthoexciton (Γ_5^+) is dipole (Γ_4^-) forbidden ($\langle\Gamma_5^+|\Gamma_4^-|\Gamma_1^+\rangle = 0$). The orthoexciton couples to light via quadrupole interaction Γ_5^+ ($\langle\Gamma_5^+|\Gamma_5^+|\Gamma_1^+\rangle \neq 0$). Unlike the dipole operator, the quadrupole operator depends on the direction of the light wave vector $\mathbf{k}$ relative to the lattice and the polarization vector $\mathbf{e}$. Because of the $\mathbf{k}$ dependence the transition is anisotropic even in a cubic crystal. The amplitudes (QA_1 to QA_3) of the orthoexciton quadrupole transitions are given by the symmetric vector product of $\mathbf{k}$ and $\mathbf{e}$ [27]:

$$\begin{pmatrix} QA_1 \\ QA_2 \\ QA_3 \end{pmatrix} = \begin{pmatrix} e_y k_z + e_z k_y \\ e_z k_x + e_x k_z \\ e_x k_y + e_y k_x \end{pmatrix}. \tag{3.8}$$

The three components (QA_1 to QA_3) correspond to the cartesian representations of the Γ_5^+ group: $\Gamma_{5yz}^+, \Gamma_{5zx}^+, \Gamma_{5xy}^+$. A beam propagating along the [110] direction of the crystal would undergo maximum absorption for $\mathbf{e}$ along [001] ($|QA_1|^2 + |QA_2|^2 + |QA_3|^2 = \frac{1}{2} + \frac{1}{2} + 0 = 1$), while it will be transmitted completely for $\mathbf{e} = [1\bar{1}0]$ ($|QA_1|^2 = |QA_2|^2 = |QA_3|^2 = 0$). The oscillator strength of the quadrupole transition is low ($f = 3.7 \cdot 10^{-9}$) [13], which is about 4 orders of magnitude smaller than the value found for the dipole transitions of the P-excitons of the yellow series.

Even though the coupling to the light is extremely weak, it can not be disregarded. The observation of polariton beats in the time domain is an unambiguous indication of coherent energy transfer between photon and exciton via quadrupole interaction [13]. Hence, only polaritons describe the true eigenmodes of the exciton-photon system of the 1S orthoexciton transition in Cu_2O.

Based on the formalism derived in the previous chapter we can now describe this specific polariton. In the case of bulk polaritons the photon energy is given by

$$E_P(k) = \hbar\frac{c_0}{\sqrt{\epsilon_\infty}}k, \tag{3.9}$$

where $\epsilon_\infty = 6.46$ is the dielectric constant in the high frequency limit [47]. The parabolic exciton dispersion is given by the

$$E_X(k) = E_X(0) + \frac{\hbar^2 k^2}{2m_X}, \tag{3.10}$$

where the first term gives the potential energy and the second the kinetic energy of the exciton. This is often referred to as spatial dispersion. The Rabi energy is given by $\hbar\Omega_R = \sqrt{f}E_P = 124$ μeV for the 1S orthoexciton at resonance ($\Delta_{\mathbf{k}} = 0$) [56]. The resulting dispersions of the LPB and UPB of the yellow 1S exciton are shown in Fig. 3.3 (a). On this energy (k) scale the polariton modes are indistinguishable from the

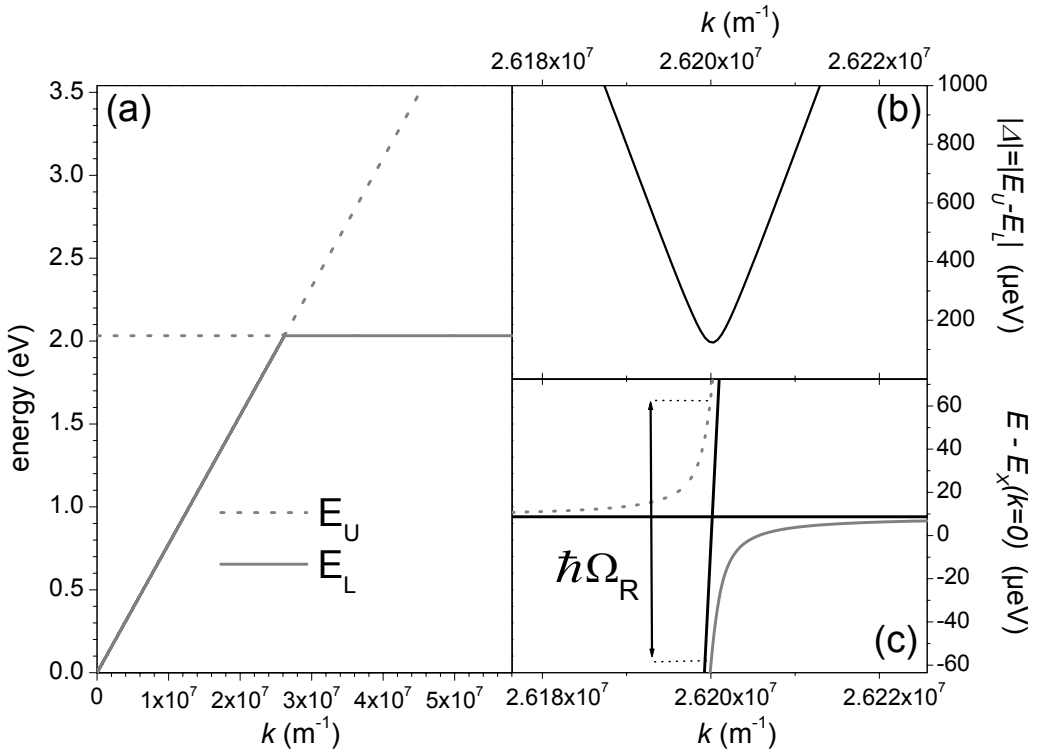

Figure 3.3: *(a) Dispersion relation of UPB (dashed trace) and LPB (solid trace) for the yellow 1S exciton in Cu_2O. (b) Energy splitting of the polariton branches in the k-range close to the exciton-photon resonance. (c) Dispersion of the polariton branches and the uncoupled modes (black solid traces) around the exciton-photon resonance.*

exciton and photon modes. Because of its high effective mass, the spatial dispersion of the exciton is weak and, compared to the steep light dispersion, the exciton dispersion appears to be flat. The splitting between UPB and LPB is shown in panel (b). Note the small energy (k) scale with respect to panel (a). When exciton and photon are in resonance ($k_R = 2.62 \cdot 10^7$ m^{-1}) the splitting reaches its minimum value $\hbar\Omega_R$. On this energy scale also the anti-crossing of both branches becomes evident (panel (c)). For clarity the energy is taken relative to the potential energy of the exciton ($E_X(0)$). As a reference the uncoupled eigenmodes are given. On this energy scale we can also identify the contribution from spatial dispersion, which is < 10 μeV.

The extremely small Rabi splitting also implies weak radiative broadening of the 1S orthoexciton. In crystals of high quality, where inhomogeneous broadening due to strain fields or crystal defects is suppressed, an extremely sharp resonance can be

expected. From measurements in the time domain, linewidths in the μeV range are expected [13]. Several problems arise when attempting to study the linewidth in the spectral domain. First of all the quadrupole character of the transition prohibits an efficient excitation of this state in a conventional photoluminescence experiment. Unlike a dipole transition, where the angular momentum transfer is ± 1 and hence equals the angular momentum of the photon, here a momentum transfer of ± 2 is required. To populate the quadrupole states efficiently, a two-photon absorption experiment would be well suited [51]. However, this would still require a spectrometer with extremely high resolution. Even using a double grating monochromator with a focal length in the 1 m range would only provide a spectral resolution of $\gtrsim 2$ μeV. This is still insufficient for the tasks tackled, here. In the following section we will introduce, how spectroscopical techniques established in the field of atom and molecule spectroscopy can be applied to problems in the field of condensed matter spectroscopy and how this permits to study such ultra narrow transitions in the spectral domain, even in a single beam experiment.

3.1 Experimental technique

Typically, a spectral resolution of few μeV is sufficient for tasks in the field of solid state spectroscopy. In most cases lines are inhomogeneously broadened due to imperfections of the solid state environment. Additionally, a rich variety of interactions gives rise to quick carrier dephasing and depopulation of the states under investigation, which causes homogeneous broadening.

However, systems which are less affected by such perturbations are of increased interest. It represents a major goal of solid state physics to find or design structures that come closer to the dephasing rates and homogeneity found in atomic systems. One prominent example are quantum dots. But self organized quantum dots show strong variation in size and alloy concentration. This gives rise to undesired variations in the transition energies. To suppress such inhomogeneous broadening, spectroscopy of single quantum dots has become fashionable. When isolating such a single quantum dot, studies with a high resolution spectrometer show a linewidth of ≈ 2 μeV [57]. Unfortunately, here the linewidths are resolution limited, which prohibits an interpretation of the line shapes or measuring a possibly even lower broadening. To deduce this information, time resolved spectroscopy offers a complementary approach. Instead of deconvoluting the dynamics of a system from its homogenous broadening, this information is often directly accessible in a time resolved experiment. Going back to the example of quantum dots recent studies show that the dephasing times of excitons in quantum dots are in ns regime at low temperatures, which again puts us in the μeV regime in the spectral domain ($\gamma = \frac{2\hbar}{T_2}$, with the homogenous linewidth γ) [58]. Other promising reports on long dephasing times of excitons are found [13]. Again, these data were obtained in the time domain. Considering the large interest in systems showing long T_2 times a simple straight forward experiment to measure the line shapes of such highly coherent long lived states is desirable.

One of the simplest optical experiments is an absorption experiment. One shines light on the specimen and monitors the transmittance. By tuning the energy of the exciting light the absorption becomes spectrally resolved. Considering a light source of continuously tunable wavelength, the spectral resolution of the experiment is only limited by the linewidth of the exciting light source. Thus the requirements for the detection unit can be extremely simple. If the transmitted signal is sufficiently intense, a simple photo detector will do. To successfully perform studies on highly coherent systems, their interaction with the phonon bath has to be suppressed, which requires cooling.

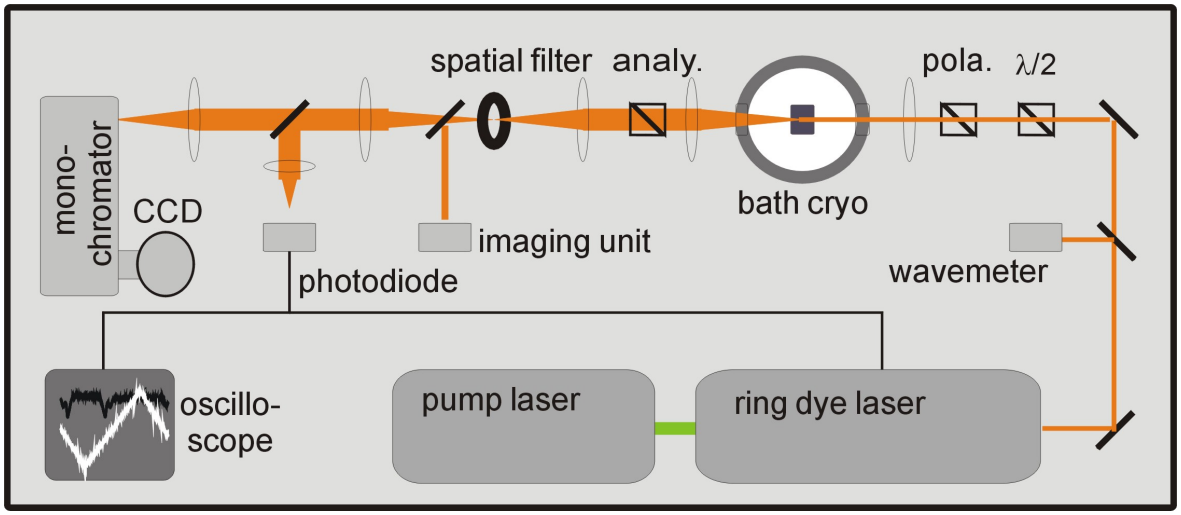

Figure 3.4: *Principle setup for semiconductor spectroscopy with high spectral resolution.*

Following these ideas the setup for a high resolution absorption experiment shown in Fig. 3.4 has been developed. It joins elements known from spectroscopy of gases with those essential for optical spectroscopy of solids. The crucial element of the assembly is a tunable, frequency-stabilized, ring dye laser (*Coherent 899-21*). A rough selection of the operation wavelength is possible by means of a three plate birefringent filter. The frequency bandwidth is further narrowed down to about 40 neV by an intra cavity etalon assembly. To stabilize the laser frequency, a fraction of the beam is coupled into a reference cavity, which is connected to an electronic servo loop. The reference cavity monitors the laser frequency and sends an electronic signal to the servo loop. The electronics readjusts the length of the laser cavity according to the reference cavity signal. The optical cavity length and hence its frequency is kept constant, by moving one of the mirrors in the cavity. For this purpose this mirror is mounted on a piezo-electric crystal. To compensate slower changes of the optical cavity length the tilt angle of an intra cavity Brewster plate is adjusted. The achievable stabilization of the laser frequency depends on the finesse of the reference cavity. In our case the active frequency control narrows the bandwidth down to 2 neV ($\approx$ 500 kHz).

In the experiment, we have to be able to tune the laser wavelength. Single mode scanning is also achieved by feedback from the reference cavity and the servo loop.

A controlled and continuous tuning of the laser energy is realized by a sophisticated interplay between tilting the intra cavity Brewster plate and quick fine tuning by the piezo mirror. A maximum scan range of ≈ 125 μeV is accessible in this fashion. Larger changes of the laser energy are done by adjusting the birefringence filter and one of the intra cavity etalons. With a laser bandwidth of 500 kHz (≈ 2 neV) we can measure linewidths well in the sub μeV range. Furthermore, it will still give access to the line shape of such extremely narrow lines. As the exciton states investigated are found at ≈ 2.03 eV, Rhodamine 6G dye was used as gain medium. The dye was excited by a frequency doubled Nd:YVO_4-laser (*Coherent Verdi 5 W*). Besides the exceptional spectral resolution, the tunable single mode source permits efficient resonant excitation of a well-defined state.

For the rough adjustment of the laser energy, a wavelength meter (*Coherent Wavemaster*) with an accuracy of ≈ 15 μeV is used. The precision of the wavelength meter gives the upper limit to the absolute energy calibration of the setup. Therefore we will typically present spectra in terms of relative energies. To calibrate the scan width of the laser a spectrum analyzer with a free spectral range of 0.617 μeV (149.2 MHz) can be implemented. After these diagnostics the laser beam is passed through polarization optics (half-wave plate and polarizer), to ensure precise control of the polarization $\mathbf{e}$ of the exciting laser light. A lens focuses the laser beam onto a spot of about 30 μm on the sample. The transmitted light again passes through two lenses, which project an image of the sample into the plane of a spatial filter. An additional polarizer (analyzer) placed between sample and detector permits selection of the detected polarization components. Using a kinematic mirror and a magnifying imaging unit the position of the excitation spot on the sample can be followed. When the kinematic mirror is moved out of the beam path, the transmitted light is no longer guided into the imaging unit, but travels further through a lens combination, which focuses the beam onto the entrance slit of an imaging monochromator (focal length 0.46 m). The dispersed light finally shines onto a liquid nitrogen cooled CCD camera. This detection unit provides a spectral resolution of ≈ 0.1 meV. As stated above, this is insufficient for the tasks tackled, here. Therefore the monochromator is only used to monitor a wider spectral window around the transitions under investigation.

For studies with high spectral resolution a second kinematic mirror is flipped into the beam path. Now the transmitted photons are detected by a photodiode, which is connected to an oscilloscope. Running the laser in the stabilized frequency scanning mode, the ramp voltage of the scan is used as trigger input for the oscilloscope. As the laser wavelength is scanned, the transmittance of the specimen is monitored on the photodiode. Synchronizing the scan and the photodiode readout on the oscilloscope, gives the spectrally resolved transmission. Typically, the scan range is set to ≈ 40 μeV with a scan time of 250 ms. Most measurements were done in a helium immersion cryostat, where the samples were kept at a temperature of ≈ 1.5 K. For temperature dependent measurements the samples were placed in a two chamber helium cryostat. The temperature could be varied from room temperature down to 4.2 K. Lower temperatures ($\lesssim 1.4$ K) were achieved by reducing the pressure above the helium. Besides these cryostats, a magnet cryostat ($B \leq 6$ T) can be implemented.

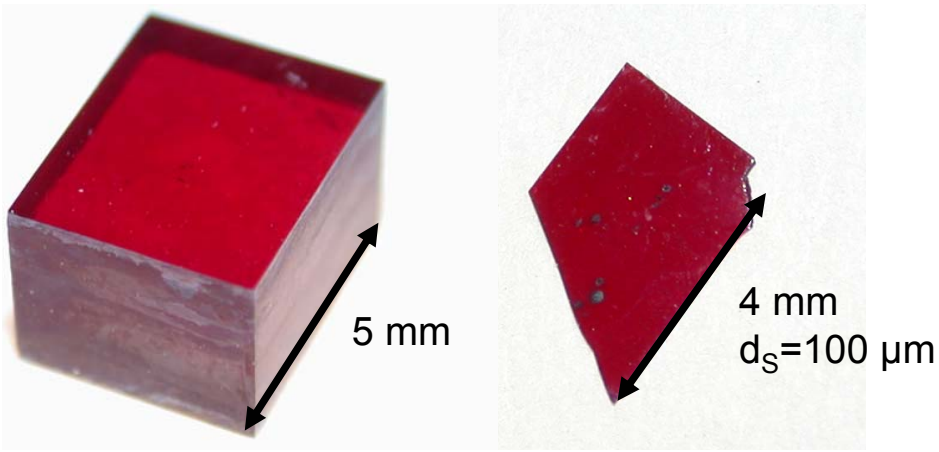

Figure 3.5: *Photographs of two typical Cu_2O samples. Left: cube shaped sample. Right: slab shaped sample.*

High resolution experiments are extremely sensitive to perturbations. One such perturbation is strain. Hence, great care was taken to mount the samples strain-free. Here two types of samples have to be distinguished. First, cube shaped samples (left in Fig. 3.5) with dimensions of ≈ 4 mm. These samples were housed in a brass cage, slightly larger than the sample itself. The second sample type is slab shaped with lateral extensions of few mm (right in Fig. 3.5), while being only $\lesssim 100$ μm thick. To ensure a strain free upright mounting, special housings have been fabricated. A sectional drawing of such a holder is shown in the left half of Fig. 3.6. The sample is sandwiched between two brass plates. These plates have openings, slightly smaller than the lateral extensions of the specimen. The sample is placed between those plates, while a spacer layer slightly thicker than the sample surrounds the specimen. The spacer layer consists of a metal foil, with a hole housing the sample. The spacer prevents the sample being squeezed between the brass plates. Two screws hold this assembly. The specimen is free to move by some tenth of a mm within the holder. The samples were cut from the same natural Cu_2O crystal (see Fig. 3.1) and were oriented by X-ray diffraction. They were cut such that the surfaces correspond to a main crystalline axis (e.g. $[001], [\bar{1}10], [111], [112]$). After cutting the surfaces were polished. Our studies show that this treatment can give rise to strain in the crystals, especially if the thickness d_S is < 100 μm. Samples showing signatures of strain were annealed. For this purpose they were slowly heated up to 450 C in an evacuated environment. The heating process took 6 hours. Then the samples were kept at this temperature for 12 hours, before they were cooled down to room temperature within 10 hours. To prevent reduction of the surfaces, the crystals were sandwiched between two quartz (SiO_2) plates, which acted as oxygen donators at high temperatures. The annealing procedure was found to be successful in some cases, however it does not guarantee a completely strain free sample.

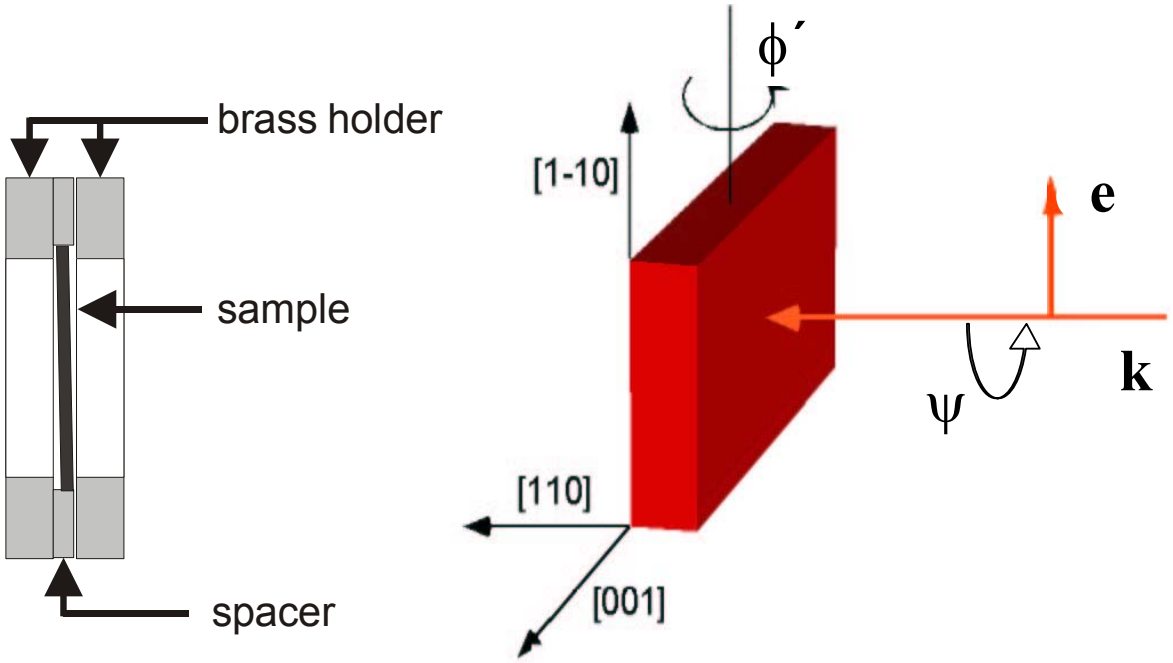

Figure 3.6: *Left: Drawing of a sample holder for thin Cu_2O slabs. Right: Geometry of the experiential configuration. See text for details.*

The mounting in the cryostat allows the rotation of the sample around the vertical axis by an angle φ', which corresponds to an angle φ ($\sin\varphi = \frac{\sin\varphi'}{\sqrt{\epsilon_\infty}}$) for the laser beam inside the crystal (Fig. 3.6). For demonstrative purposes a crystal is shown, where the rotation is around the $[1\bar{1}0]$ axis. Here for $\varphi = 0$ the light travels along [110]. For $\varphi \neq 0$ the light travels along intermediate $\mathbf{k}$ directions through the crystal. By means of the polarization optics the polarization $\mathbf{e}$ can be varied in the $[001] - [1\bar{1}0]$ plane. The direction of $\mathbf{e}$ will be characterized by the angle ψ in the following. $\psi = 0$ corresponds to horizontal $\mathbf{e}$; in our example $\mathbf{e}$ $(\psi = 0) = [001]$, while $\psi = 90°$ corresponds to vertical polarization $\mathbf{e}$=$[1\bar{1}0]$. The setup in Fig. 3.4 shows only the core elements. For the specific issues investigated in the following slight modifications have been made. These changes will be explained with the corresponding experiments. We will proceed with the experimental investigations of the yellow 1S exciton in Cu_2O. For the first time, this transition will be investigated with the appropriate spectral resolution.

3.2 High resolution spectroscopy of polaritons

Preliminary absorption experiments were performed on samples comparable to those investigated, here. For these experiments a simple halogen lamp for illumination of the sample and a double monochromator photomultiplier combination as detection unit were used. However, the spectral resolution was limited to $\gtrsim 10$ μeV [59]. While this is still sufficient for the investigation of temperature induced effects and monitoring

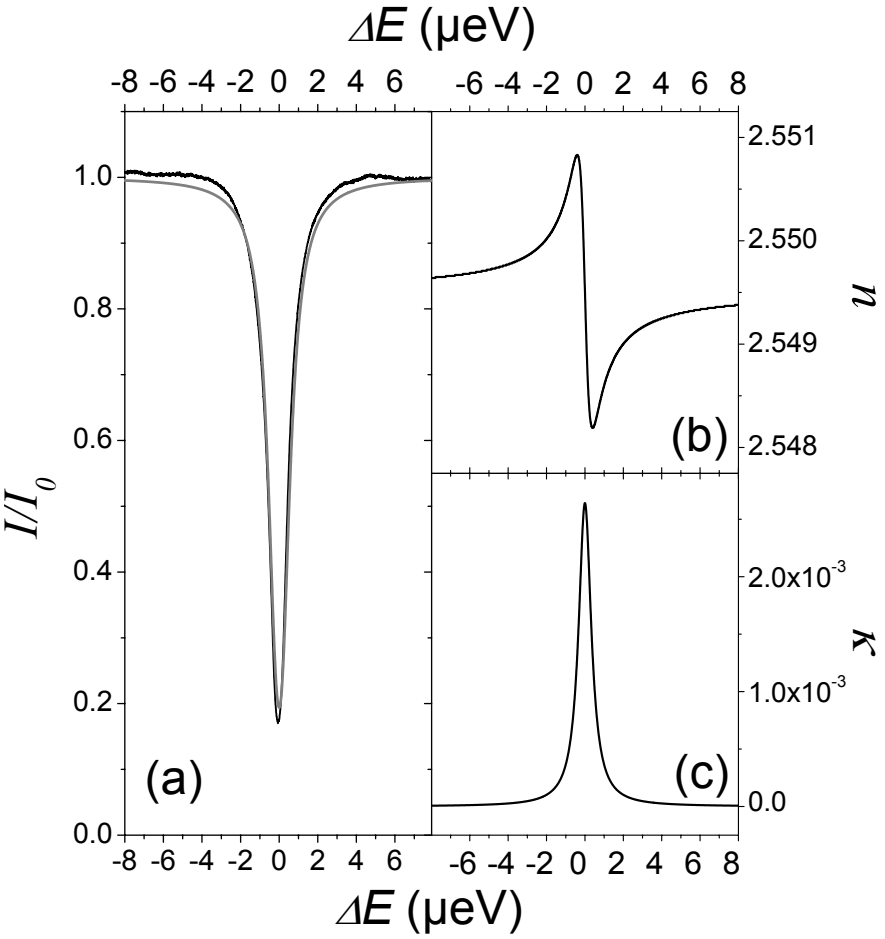

Figure 3.7: *(a) Absorption spectrum of a 30 μm thick Cu_2O sample* $\mathbf{k}$*=[111]. The black line gives the data, while the grey one gives a fit using the model introduced in the text. (b) Modulation of the real part of the refractive index n. (c) κ as function of energy. In all panels relative energies are shown, where maximum absorption defines $\Delta E = 0$.*

the total absorption, this resolution is insufficient to answer the core question arising in the low temperature regime: How narrow is the yellow 1S exciton transition?

To answer this, natural Cu_2O samples have been prepared, as described in section 3.1. To reduce inhomogenous broadening, a thin sample of thickness $d_S = 30$ μm has been chosen. The absorption of the transition is further reduced by choosing $\mathbf{k} = [111]$ for which $\sum_i |QA_i|^2 = \frac{1}{3}$ for all polarizations. The measured absorption spectrum is shown in Fig. 3.7. The line shape of the polariton transition can be modelled by the standard Sellmeier description of polaritons with i exciton transitions at $E_i(k)$ (see Eq: 3.10) which couple to light with the oscillator strength f_i [60]:

$$\epsilon(E) = \frac{\hbar c_0^2 k^2}{E^2} = \epsilon_\infty + \sum_i \frac{f_i E_i^2(k)}{E_i^2(k) - E^2 - \mathtt{i} E \Gamma_i}. \tag{3.11}$$

For the sake of simplicity the polarization dependence of the quadrupole transition has been left out. For a full treatment the oscillator strength has to be scaled by the quadrupole amplitudes of the specific transitions. Here we have included a damping parameter Γ_i, which is assumed to be independent of E. This approximation might not be correct considering, for example, the energy dependent coupling to phonons etc. [59]. In the framework of this zero order approach to the polariton lineshape Γ_i can

only be understood as a phenomenological parameter. It cannot be interpreted as a damping in the classical sense of absorption and the linewidth cannot be associated with the lifetime of the exciton [59]. It was argued that scattering processes that change **k** give rise to absorption-like signatures. To account for this we would have to take propagation effects into account. As the group velocity v_g of the polaritons is strongly reduced close to the exciton-photon resonance (see chapter 3.3), such slow polaritons are more likely to undergo scattering on their way through the crystal. A v_g dependent Γ proportional to the time of flight in the sample $\Gamma \sim \frac{d_S}{v_g}$ would yield a much better description of the damping mechanisms [61]. However, this complicates the calculations significantly. A full treatment is beyond the scope of this work and does not change the central points of our analysis.

In the general form (Eq. 3.11) sums over all resonances i. Even though the yellow 1S quadrupole transition is far from all other exciton states on the energy scales of interest, we cannot completely disregard the other resonances, here. In the case of well separated resonances, a simplified treatment is appropriate. We assume a background oscillator (E_B, f_B, Γ_B), which substitutes for the entire set of exciton transitions. This hypothetic background oscillator is then superimposed by the 1S transition of interest:

$$\epsilon(E) = \frac{\hbar c_0^2 k^2}{E^2} = \epsilon_\infty + \frac{f_{1S} E_{1S}^2(k)}{E_{1S}^2(k) - E^2 - \mathtt{i} E \Gamma_{1S}} + \frac{f_B E_B^2(k)}{E_B^2(k) - E^2 - \mathtt{i} E \Gamma_B}. \tag{3.12}$$

From $\epsilon(E)$ we deduce the complex refractive index $\widetilde{n}(E) = n(E) + \mathtt{i}\kappa(E) = \sqrt{\epsilon(E)}$. The absorption coefficient α is given by $\alpha(E) = \frac{2E}{c_0 \hbar}\kappa(E)$. The transmitted intensity $I(\omega)$ (which is monitored in our experiment) is then given by

$$I(E) = I_0 e^{-\alpha(E) d_S}, \tag{3.13}$$

where I_0 is the transmitted intensity outside the absorption resonance (not the intensity shining on the sample front surface). The problematic evaluation of Γ_{1S} typically leads to an overestimation of the oscillator strength. Determining f_{1S} from the polariton dispersion and v_g is a more suited approach, which will be described in chapter 3.3. For simplicity the kinetic energy of the exciton is assumed to be constant in the following. This is a very good approximation, as the dispersion of the exciton is extremely flat in the spectral window under investigation.

From the fit of Fig. 3.7 (a) we determine $\Gamma_{1S} = 0.8$ μeV. Using quantum beat spectroscopy exciton coherence times of up to 2 ns were reported [13, 62]. Despite the crude modelling, this is in good agreement with our results. Previous studies show that Γ_{1S} is dominated by phonon scattering [61], while contributions from pure dephasing can be neglected. The radiative exciton lifetime is about 30 ns [63] and gives no significant contribution to Γ_{1S}. From the absorption spectrum we find $T_2 =$ 1.6 ns. From the fit we can directly calculate $\widetilde{n}$. The modulation of the real n (Fig. 3.7 (b)) and imaginary (Fig. 3.7 (c)) part κ of the refractive index are also shown. While κ basically has a dispersion-like form we also find notable modulations in n in the spectral vicinity of the resonance.

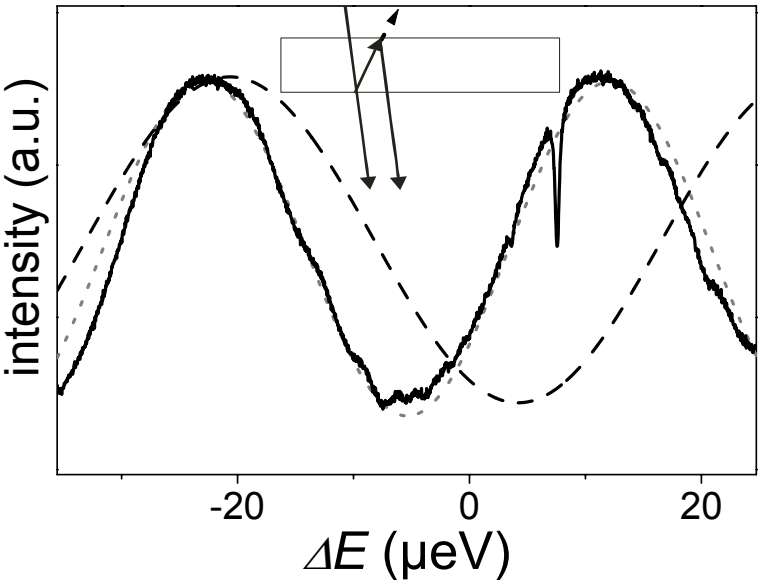

Figure 3.8: *Transmission spectrum of a 4.9 mm thick crystal (***k***=[110]). The dark line gives the experimental data. The dashed trace gives the calculated interference fringes assuming a constant refractive index. The dotted trace was calculated using a background oscillator at the spectral position of the 2P exciton (2.1473 eV) with* $f_B = 4.9 \cdot 10^{-2}$.

3.2.1 Interference phenomena in Cu_2O

These modulations in n should become evident in interference experiments, where two principle cases can be investigated.

- Interferences between the directly transmitted beam and the fraction of the beam which is reflected at the front and back sample surface (see sketch in Fig. 3.8).
- Interferences between two beams with different polarizations. Depending on **k** they can have different QA's (Eq. 3.8) and hence feel different modulations in n.

Let us begin with interferences between the transmitted beam and the doubly reflected fraction. The resulting transmitted signal is then described by

$$I(E) = I_0 e^{-\frac{2\kappa E d_S}{\hbar c_0}} \left[1 + r^4 e^{-\frac{4\kappa E d_S}{\hbar c_0}} + 2r^2 e^{-\frac{2\kappa E d_S}{\hbar c_0}} \cos\left(\frac{2nEd_S}{\hbar c_0} \right) \right], \qquad (3.14)$$

where $r = \frac{\sqrt{\epsilon_\infty - 1}}{\sqrt{\epsilon_\infty + 1}}$ gives the reflectivity for the field (not the intensity) at the sample surface. The first term in the sum describes the transmitted beam, while the second term gives the doubly reflected fraction. The third term finally describes the interference between both. As I_0 is defined as the intensity transmitted outside the absorption resonance, the transmission coefficients at the front $t_F = \frac{2}{\tilde{n}+1}$ and back $t_F = \frac{2\tilde{n}}{\tilde{n}+1}$ surface do not enter Eq. 3.14. Their slight energy dependence does not affect our calculations.

Interference phenomena were studied on a 4.9 mm thick sample, where the beam propagates along the [110] direction. When the polarization is along $[1\bar{1}0]$ the 1S quadrupole transition is forbidden ($\sum_i |QA_i|^2 = 0 = f_{1S}$), which allows study of the relevance of the assumed background oscillator (see Eq. 3.12). The experiment shows a characteristic spectral interference with a period of 33 μeV. When calculating the

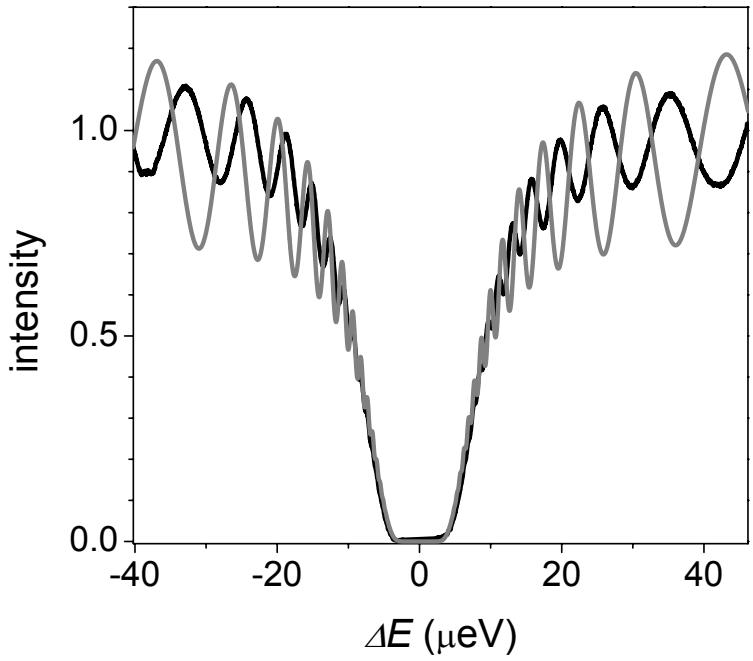

Figure 3.9: *Transmission spectrum of a 4.9 mm thick crystal (*$\mathbf{k}$ *= [110]). The dark line gives the experimental data. The grey trace gives the calculated interference fringes with* $f_{1S}= 2.1 \cdot 10^{-8}$, $\Gamma_{1S}=$ 0.29 μeV.

interference fringes assuming $f_B = 0$ an intensity oscillation with a frequency of 59 μeV is obtained. Therefore, the data indicate that we cannot disregard the modulation of the refractive index induced by the other exciton transition. The dotted trace was calculated using the 2P exciton transition as background oscillator ($E_B = 2.1473$ eV), where the oscillator strength was taken as adjustable parameter. A good description of the experiment is achieved for $f_B = 4.9 \cdot 10^{-2}$. The broadening parameter Γ_B is not evaluated quantitatively, as it is only relevant for the damping of the oscillation and hence the amplitude of the oscillation. A good description is obtained for $\Gamma_B \approx$ 17 μeV. As we are dealing with systems of macroscopic thickness, several thousand times larger than λ, even the slightest modulation of the refractive index leads to deviations from the naively expected interference pattern. In the special case of this quadrupole transition, we can nicely study this effect, as the quadrupole transition is orders of magnitude weaker than the dipole transitions of the odd parity P excitons. Selecting a forbidden polarization provides a sufficient suppression of the quadrupole signal to study the impact of the background oscillators separately. For the following evaluations, the parameters of the background oscillator are kept fixed.[2]

We now rotate the polarization of the laser beam to the [001] direction, which makes the 1S transition allowed. The resulting transmission spectrum is shown in Fig. 3.9 (dark curve). We find the absorption resonance, where in a spectral range of 7 μeV, the light is completely absorbed. More strikingly, pronounced interference signatures are found, where the amplitude of the oscillation increases with detuning ΔE from the resonance. Furthermore, the oscillation period is a function of ΔE. Note, that even oscillations with a period of 0.5 μeV are clearly resolved. To describe this complex

[2]The sharp line appearing in the spectrum at about $\Delta E \approx 7$ μeV arises from a slight misorientation of the crystal. The exact origin will be discussed in section 3.4.

behavior we apply Eq. 3.14. The grey trace in Fig. 3.9 gives the calculated spectrum using the parameters $f_{1S}= 2.1 \cdot 10^{-8}$, $\Gamma_{1S}= 0.29$ μeV. The simulation shows qualitative agreement with the experiment. The calculated interference fringes strongly depend on ΔE. This is directly understood, when looking at Fig. 3.7 (b) and (c). The amplitude of the interference is determined by the fraction of the beam travelling through the sample back and forth. Close to the resonance κ increases drastically, which means that the beam is strongly absorbed. Consequently, only a very small fraction remains to interfere with the directly transmitted beam, quenching the interference amplitude.

The period of the interference fringes depends on $\frac{\partial n}{\partial E}$. In the spectral vicinity of the resonance, the modulation of n is most pronounced, which gives rise to a fast sequence of interference maxima and minima. The further we move from $\Delta E \approx 0$ the more n flattens and the larger the interference period. Looking closely at Fig. 3.9, we find that the chosen set of parameters well describes the oscillation in the spectral range close to the resonance, while the oscillations get out of phase for larger ΔE. In addition, the amplitude of the oscillation is not well approximated by the set of parameters. The amplitude could easily be adjusted when assuming a reduced reflectivity of the sample. However, the fit shown is based on a set of parameters where at least the oscillator strength is far from the values found above and in literature [13]. The modelling is to be understood as a first approach. Obviously, the assumption of a Lorentzian with a constant Γ does not provide a sufficiently good description of the dielectric properties, such that the modelling of the interference fringes also runs into difficulties. In the course of the chapter we will take a closer look at the shortcomings of this description.

Besides interferences induced by the superposition of transmitted and a doubly reflected beam, we can take advantage of the polarization dependence of the quadrupole amplitudes to generate interferences between waves of different polarization. In all following experiments the front and back surfaces of the samples are not perfectly coplanar. Hence, we no longer observe interferences between the transmitted and the doubly reflected beam. Taking the same geometry as above ($\mathbf{k} = [011]$) and simply rotating the polarization by means of a $\lambda/2$ retarder we find the spectra of Fig. 3.10. Looking at panel (a) we see the well-known absorption line ($\mathbf{e} = [001]$). The polarization is along a good eigenpolarization of the quadrupole and no interference is expected. As we tilt the polarization plane, we superimpose the remaining fraction of the beam polarized along [001] ($|QA|^2 = 1$) with a fraction polarized along $\mathbf{e} = [0\bar{1}1]$ ($|QA|^2 = 0$). Since the quadrupole transition is forbidden, this polarization component is not subject to absorption induced modulations of n. As the wavelengths of the two polarization components differ inside the crystal, they show destructive or constructive interference on the detector. To be precise, as the polarization components are orthogonal they cannot show an interference. This is overcome by placing a polarizer (analyzer) between sample and detector. For simplicity the orientation of the analyzer was fixed at $\frac{1}{\sqrt{2}}([001] + [0\bar{1}1])$. The origin of the interferences can be tested experimentally by rotating the orientation of the analyzer. When orienting this polarizer along [001] or $[0\bar{1}1]$ no interferences can be observed independently of the incoming $\mathbf{e}$. As long as the analyzer is along one of the polarization eigenstates, no coherent superposition of the polarization states can be generated and hence no interference pattern can be observed.

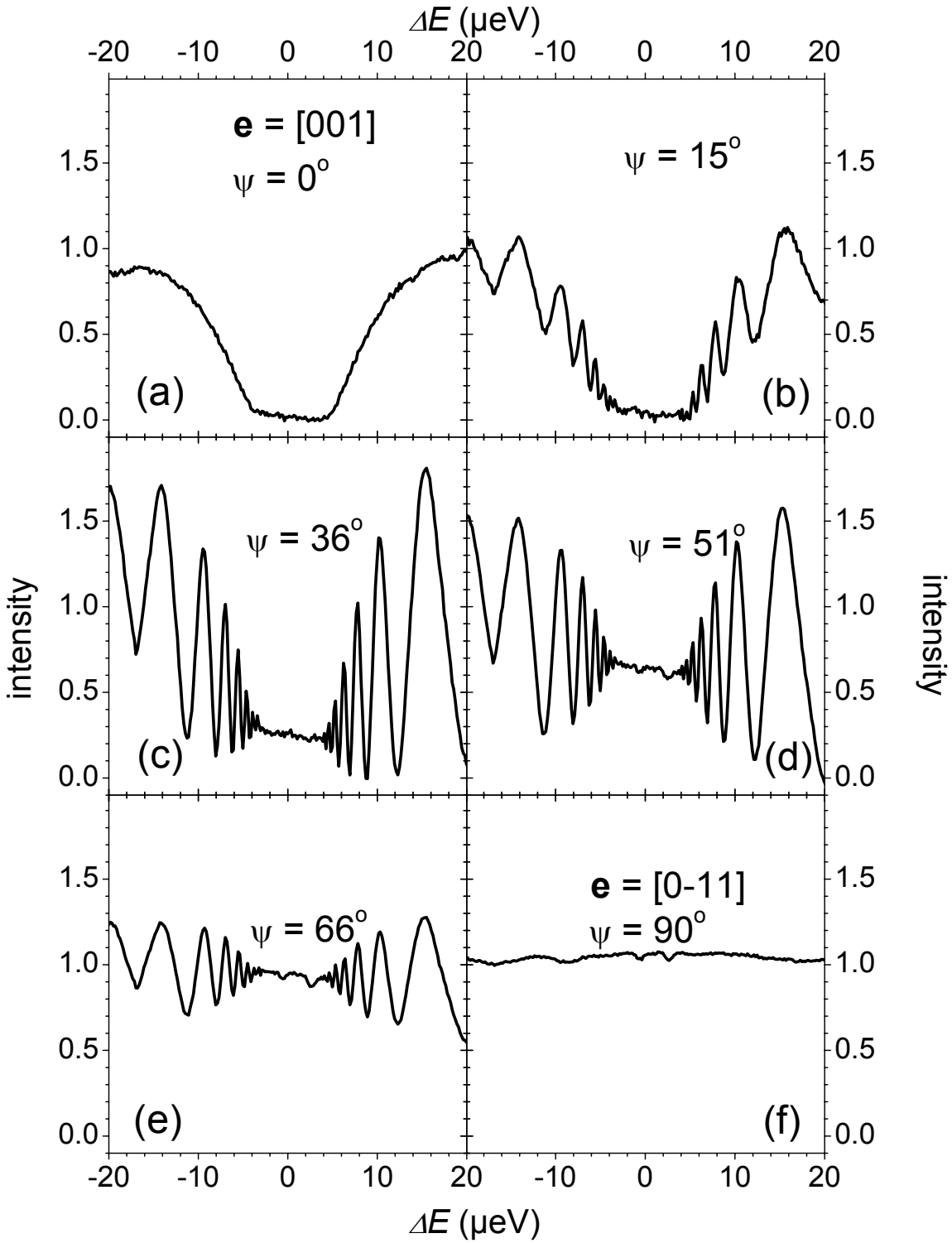

Figure 3.10: *Transmission spectrum of a 4.0 mm thick crystal (*$\mathbf{k}$ *= [110]) for various orientations of* $\mathbf{e}(\psi)$*. In panel (a)* $\mathbf{e}$ *is along* [001]*. Step by step the polarization is rotated towards* $\mathbf{e} = [0\bar{1}1]$ *(panel (f)).*

This gives further evidence for the above findings. By changing the orientation of the analyzer, the amplitude of the interferences can be maximized for each **e**. We see that the flattening of the absorption close to the resonance is not an artefact arising from limited sensitivity of the detector. The interferences can be described as

$$I(E) = I_0 \left[\cos^2(\psi) e^{-\frac{2\kappa E d_S}{\hbar c_0}} + \sin^2(\psi) e^{-\frac{2\kappa_0 E d_S}{\hbar c_0}} + \sin(\psi)\cos(\psi) e^{-\frac{(\kappa+\kappa_0) E d_S}{\hbar c_0}} \cos\left(\frac{(n_0-n) E d_S}{\hbar c_0}\right) \right], \tag{3.15}$$

where ψ gives the tilt angle of **e** from the [001] direction. n_0 (κ_0) gives the refractive index (extinction coefficient) for the beam polarized along $[1\bar{1}0]$. Using Eq. 3.15 we have modelled the experimental findings (Fig. 3.11).

Comparing Figs. 3.10 and 3.11 we find a good description of the data, by using the set of parameters found for the interference phenomenon. Naturally, the interferences vanish for **e** along [001] and $[0\bar{1}1]$. For intermediate polarizations we find a gradual transition between those limiting cases where the oscillations are most pronounced if the intensities of both polarization components are equal. The curves remain flat in this spectral range even if the intensity is nonzero. In general, the amplitude of the oscillation is a little larger in theory than in the experiment, which might be explained by additional damping mechanisms not covered in this model. Experimentally, we resolve oscillation periods down to 0.36 μeV, which become larger as we move out of resonance. This behavior has been discussed above. In the modelling, we can again describe this qualitatively. However, theory and experiment do not agree quantitatively over the entire spectral range.

Comparing the two interference phenomena, we find characteristic differences. In the case of polarization interferences the amplitude of the oscillation can become much larger, as both waves travel through the crystal only once and the intensity of both beams does not differ that much. Coming closer to the resonance, however, the [001] component is strongly absorbed, damping the interference amplitude. These simplified and intuitive models identify the origins of the interference patterns and agrees reasonably well with the experiments on a semi quantitative level.

3.2.2 Polariton damping

Our modelling suffers from an insufficient treatment of the damping. Now we will take a closer look at potential damping mechanisms. One decay channel for the polariton would be radiative recombination at the sample surface. The polariton excited in the sample propagates with its group velocity v_g through the crystal. At the sample surface the translation invariance is broken and the photon is only reabsorbed when reflected at the surface. For a polished surface, as in the present experiment, the likelihood of reflection is given by the reflectivity ($|r|^2$) of the sample, which is about 0.2 for the

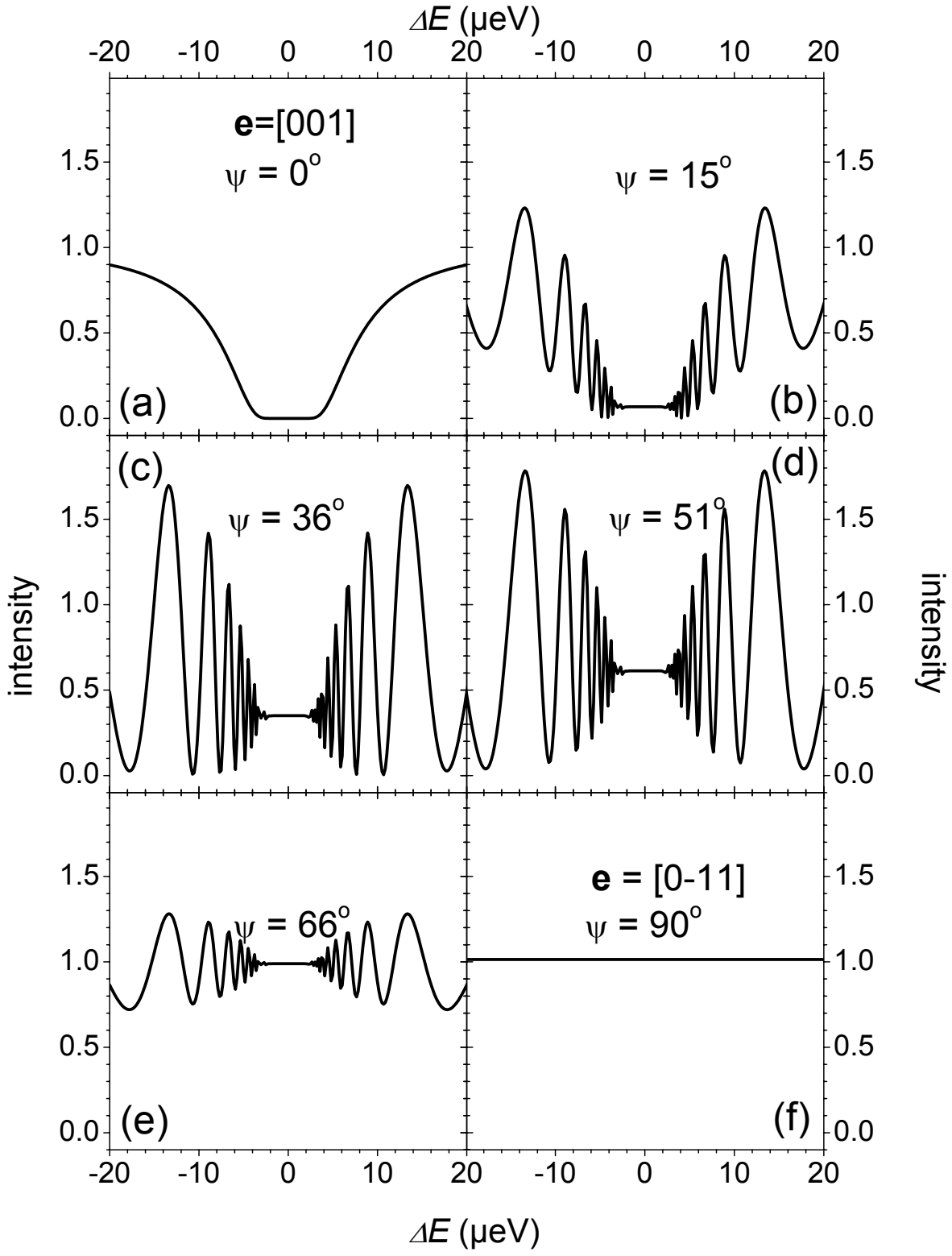

Figure 3.11: *Calculated transmission spectrum of a 4.0 mm thick crystal (*$\mathbf{k}$ *along* [110]*) for various orientations of* $\mathbf{e}$*. In panel (a)* $\mathbf{e}$ *is along* [001]*. Step by step the polarization is rotated towards* $\mathbf{e} = [0\bar{1}1]$ *(panel (f)). For the calculation the parameters* $f_{1S}= 2.1 \cdot 10^{-8}$ *and* $\Gamma_{1S}= 0.29\ \mu eV$ *have been applied.*

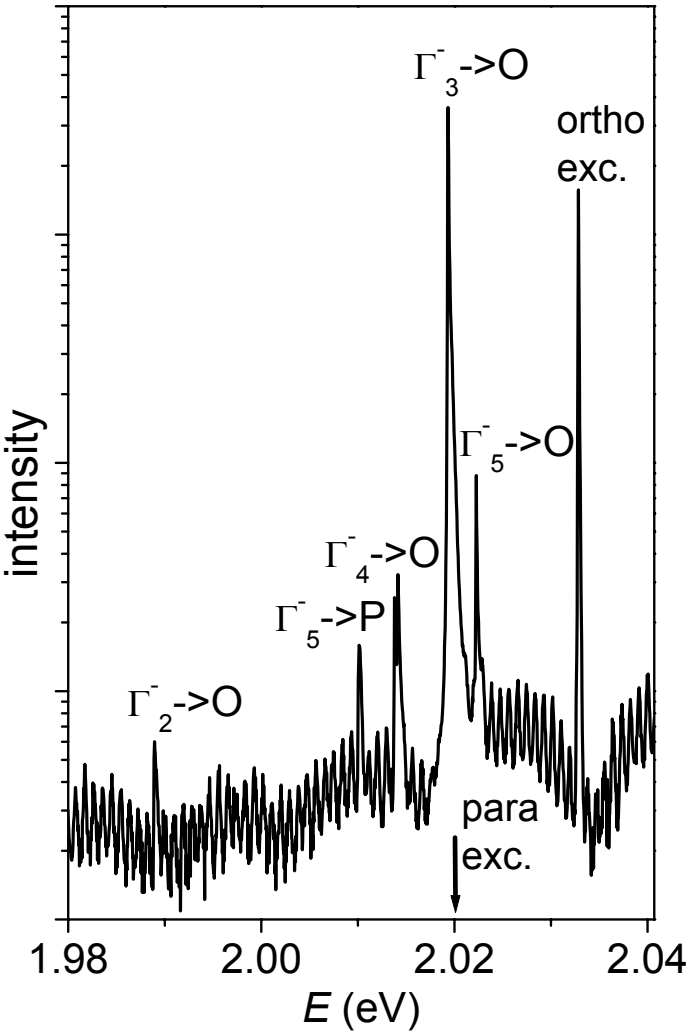

Figure 3.12: *Spectrally resolved phonon spectrum under resonant excitation of the yellow 1S orthoexciton. For these measurements a thick crystal (d_S= 4 mm) was used. The laser is strongly absorbed in the specimen, which allows resolution of the weak phonon luminescence relative to the otherwise intense laser. The signal is dispersed by a monochromator and detected by a LN_2 cooled CCD camera. The laser beam propagates along* [001]*. The spectral positions of ortho- and paraexciton are indicated.*

Cu_2O-helium interface at normal incidence. This decay channel would again give an energy or, more precisely, v_g dependent Γ. We expect $\Gamma \sim \frac{v_g}{d_S}$, which is inverse to the scattering induced damping discussed above. Such radiative damping would lead to line broadening in thinner samples. Even for $d_S = 15$ μm no such effect is found. This already indicates that the line broadening is not due to losses at the sample surfaces.

In addition to this loss channel polaritons interact with phonons. The final states of such polariton-phonon scattering processes are found in the excitonic section of the polariton dispersion and hence outside the radiative region. As the unit cell of Cu_2O has six atoms with three degrees of freedom (x, y, z), there are $3 \cdot 6$ zone center phonons. There are two transverse acoustic and one longitudinal acoustic phonons and 15 optical phonons remain. Cu_2O is of O_h symmetry and the optical zone-center phonons can be classified as $\Gamma_2^- \oplus \Gamma_3^- \oplus 2\Gamma_4^- \oplus \Gamma_5^- \oplus \Gamma_5^+$ [64]. The phonon spectrum of Cu_2O is shown in Fig. 3.12. We see a series of phonons of Stokes type. In the spectral range under investigation we find all expected phonon related emission lines. The Γ_5^- phonon line 10.6 meV below the orthoexciton, the Γ_3^- phonon (13.5 meV), the

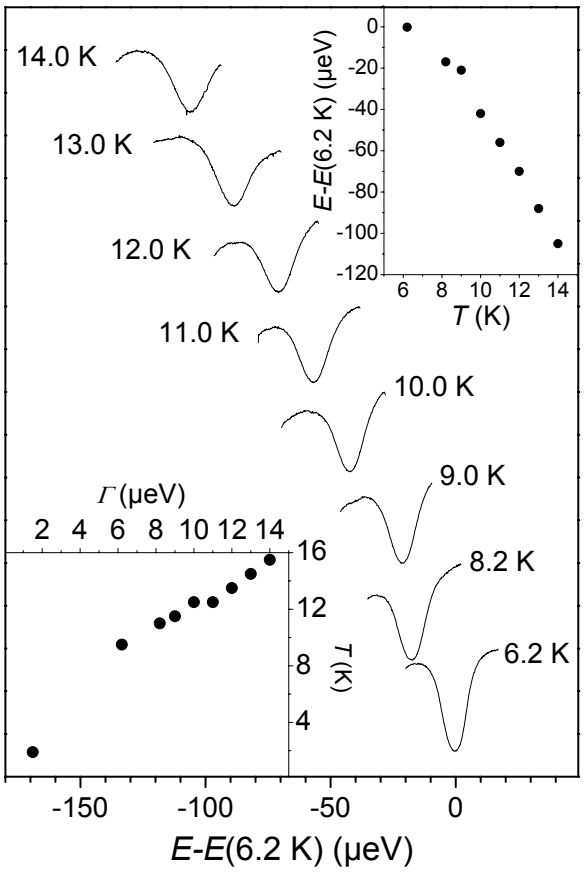

Figure 3.13: *Absorption spectra of a 54 μm thick sample ($\mathbf{k} = [\bar{1}10]$, $\mathbf{e} = [00\bar{1}]$) for the temperatures indicated. Upper inset: Spectral shift of the line as a function of T, relative to the line position at T= 6.2 K. Lower inset: Linewidth as a function of T. Γ was evaluated using Eq. 3.11.*

Γ_4^- phonon (18.8 meV), and the Γ_2^- phonon (44 meV). The relative intensities strongly depend on the polarization component detected. While the Γ_3^- is polarized orthogonal to the polarization of the orthoexciton, the other phonons are polarized parallel to the exciton. Here the analyzer polarization is parallel to $\mathbf{e}$. Still the Γ_3^- phonon is most intense. The Γ_4^- line shows a doublet structure. As the Γ_4^- phonon is polar, it splits into a longitudinal and transversal optical mode. Here a splitting of 0.4 meV is found, which is in good agreement with the Lyddane-Sachs-Teller relation ($\frac{\omega_L^2}{\omega_T^2} = \frac{\epsilon_0}{\epsilon_\infty}$) [65].

The relevance of phonon scattering is tested in temperature dependent measurements (Fig. 3.13). The line shows the expected red shift with increasing temperature. The line shifts by 0.1 meV for a temperature increase of 8 K (upper inset). More importantly, the line broadens with T, which is the fingerprint of phonon interaction. The lower inset gives the linewidth as a function of T. While Γ is in the 1 μeV range for $T \approx 2$ K it is already significantly broadened at moderate T. At 14 K Γ has increased by one order of magnitude. While this high resolution spectroscopy is well suited to follow slight changes in the linewidth at low T, a systematic study of the transition energy as a function of T is complicated, as the line shifts and the linewidth quickly exceed the available spectral window of the laser scan. Therefore, Fig. 3.13 covers only a relatively small temperature range. However, we see that phonon interaction has a severe impact on the linewidth and is probably the most important source of dephasing, even in the low T regime. In power dependent measurements no significant

broadening is found with increasing excitation power, hence exciton-exciton scattering is of little relevance. The effects in the high power regime will be discussed in section 3.5.

One further source of broadening can be deduced from Fig. 3.12. In addition to phonons coupling to the orthoexciton, we also find a phonon resonance connected to the paraexciton. This is direct evidence of a paraexciton population and the presence of relaxation channels from the orthoexciton into the paraexciton. As the paraexciton is the lowest exciton state in Cu_2O and the orthoexciton is the second lowest state, no further relaxation channels have to be taken into account. Since the paraexciton state is optically forbidden we cannot resolve it directly in the present experiment. It would be located slightly above the the Γ_3^- phonon. By applying a magnetic field or uniaxial stress [66], the paraexciton becomes visible in an optical experiment.

Even though the lineshape found in Fig. 3.7 is well approximated by a Lorentzian, deviations are found. Furthermore, for the paraexciton a linewidth of ≈ 1 μeV is found at low magnetic fields in a 4 mm thick crystal. We would expect a much narrower line from the extremely small f and the increased lifetime. This indicates inhomogenous broadening in addition to the homogenous broadening discussed above. Comparison of spectra obtained on thick samples compared to those for thin samples (Fig. 3.7) show that the lines broaden with increasing sample thickness. Considering the extremely narrow lines, even the slightest residual strain gives rise to a notable line shift. Variations of the strain along the sample cross section give rise to inhomogenous broadening.[3] These studies show that a better understanding modelling of the polariton line shape has to include phonon interaction and inhomogenous broadening.

3.3 Propagation of polaritons in Cu_2O

Wavepackets propagating with ultra slow group velocity have attracted great interest in solid state as well as atom physics. Ultra slow photons might be of interest, for example, in quantum computation schemes [67], for highly efficient photon counting [68] or even for new acousto-optical devices [69]. When talking about the velocity of a wavepacket, we have to distinguish between group and phase velocity. The phase velocity is the speed at which the modes of the wavepacket propagate. It is simply given by $v_P = c_0/n$. The phase velocity can be obtained directly from the interference measurements presented in the previous chapter. In this section we focus on the group velocity v_g, which gives the speed of the envelope of the electromagnetic field. The group velocity can be deduced from the dispersion of the polariton modes

$$v_{gU,L} = \frac{1}{\hbar}\frac{\partial E_{U,L}}{\partial k}. \tag{3.16}$$

Close to an absorption resonance v_g can change by several orders of magnitude. However, also the absorption of the sample increases drastically, which typically prohibits

[3] The impact of strain will be discussed in detail in section 3.4.

measuring such ultra slow v_g in a transmission experiment. To overcome this problem recent experiments use the effect of electromagnetically induced transparency [70], where quantum interference leads to a cancellation of absorption. In this technique a first coupling laser field is absorbed in the medium and generates so-called laser dressed coherent atoms. The second beam travels through the medium and, while it feels its dispersive properties, it is no longer absorbed. Using this approach $v_g = \frac{c_0}{165}$ has been measured in lead vapor [71] and even $v_g < 90$ m s^{-1} has been measured in a hot rubidium gas [72]. To reduce v_g even further Doppler induced line broadening was suppressed by cooling sodium atoms. At temperatures around the critical temperature for BEC v_g dropped to 17 m s^{-1} [73]. Switching the coupling laser off the probe pulse is effectively stopped. When switching the coupling laser back on after 1 ms, the probe pulse is regenerated [74]. This trapping of light [75, 76] can be looked at as a coherent information storage. Such ultra cold atoms are not suited to many of the potential applications of slow light. It is preferable to use solid state media. In the search for a solid state realization similar effects have been demonstrated for rare earth doped insulators [77].

The system we are investigating clearly differs from such ultra-cold atomic systems and also from doped solid state media. We are not dealing with an isolated optical transition, free of dispersion. The exciton is a quasi-free particle and its spatial dispersion describes the lower limit to v_g. The situation for polaritons is still more complex. They show mixed properties of light and matter. Around the exciton-photon resonance v_g changes over from photon to exciton-like or vice versa (see Fig. 4.2). As photons do not carry mass, while the excitons have a high effective mass (see chapter 3), the propagation of the polaritons is significantly slowed down, when compared to bare photons, by their exciton admixture.

The problem of polariton wave packet propagation in a dispersive dielectric has been tackled earlier in theory [78, 79] and experiment [80]. In bulk GaAs group velocities as low as $1.5 \cdot 10^5$ ms^{-1} have been measured in an up-conversion experiment. The studies have been complicated by the strong absorption of this dipole allowed transition. Therefore only relatively thin samples could be investigated. This requires a good time resolution and the usage of short laser pulses. Here we are facing a quadrupole transition, which permits transmission experiments with rather thick samples. Arising from the weak exciton-photon coupling, the transition from exciton-like to photon-like is restricted to an extremely narrow k-range $\Delta k \approx \frac{1}{1000} k_R$, here. Consequently the dispersion shows a pronounced curvature in the optically active region (Fig. 3.3) and we expect steep changes in v_g as shown in Fig. 3.14. For the calculation using Eq. 3.16 and 3.11 the parameters $f_{1S} = 3.9 \cdot 10^{-9}$, $m_X = 2.7\, m_0$, and $\epsilon_\infty = 6.46$ have been used. Coming from the low energy (low k) side the upper branch (dashed trace) is exciton-like and v_g is determined by the exciton's spatial dispersion. At resonance ($\Delta E_{exc} = 0$) the calculated group velocity is as low as $v_g = 2.2 \cdot 10^3$ m s^{-1}. For positive ΔE_{exc} the upper branch converges to the velocity of the uncoupled photon in the dielectric. For the lower branch a vice versa behavior is expected. Following these considerations the polaritons at resonance are predicted to move at a speed about 5 orders of magnitude slower than c_0.

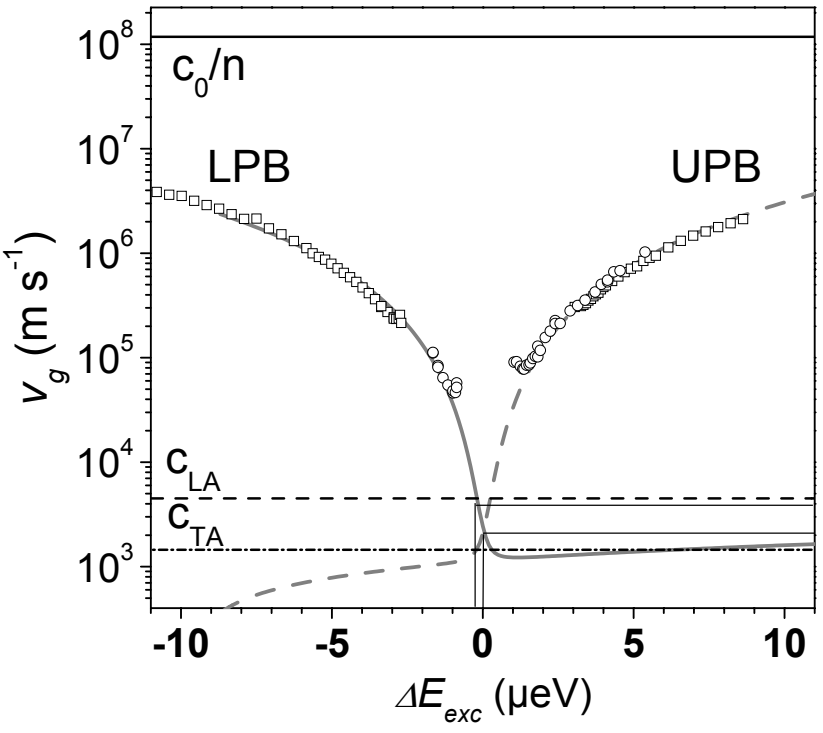

Figure 3.14: *Group velocity as a function of energy. Calculations for the UPB (LPB) are given by the dashed (solid) grey line. For reference the velocity of the longitudinal acoustic phonons (dashed trace) and the transversal acoustic (dash-dotted trace) as well as the speed of light in the dielectric medium outside a resonance (dark solid trace) are shown. The open squares (dots) give data for a 1.96 mm (1.03 mm) thick sample.*

This demands experimental studies of such ultra slow polaritons. To obtain a suitable time resolution, the setup as shown in Fig. 3.4 has been extended. An electro-optical modulator has been placed in the beam path to chop the exciting beam. The pulses transmitted through the modulator had a Gaussian shape at a temporal width of ≈ 10 ns. To obtain time resolution on the detection side a fast photodetector connected to a 1.5 GHz oscilloscope was used. To measure the energy dependent slowing down of the pulse inside the sample, we take advantage of the polarization dependence of the absorption. If the light propagates along the [110] direction (see Fig. 3.6), the absorption is maximum for **e** along [001]. If the polarization points along $[1\bar{1}0]$ the quadrupole transition is forbidden and the light is simply transmitted. To be precise, the [110] beam is also slowed down in the medium by a factor of $\sqrt{\epsilon_\infty}$, but this effect is insignificant compared to the massive reduction of v_g expected for the [001]-beam. The arrival time of the $\mathbf{e} = [1\bar{1}0]$ polarized pulse marks the zero delay. Then the polarization is shifted back to $\mathbf{e} =$[001] and the arrival time of this pulse is subtracted from that of the [001]-pulse. In this time of flight measurement v_g is given by $v_g = \frac{d_S}{\tau}$, where τ is the delay between the pulses. Obviously, this delay crucially depends on the excitation energy. To map $v_g(E)$ the spectral shape of the transition was first recorded with the laser running in the energy scan modus (see chapter 3.1). Then the laser was switched to stabilized single mode operation, where the photon energy was set to the low energy tail of the transition. At fixed laser energy τ was measured. Then e_{exc} was increased by a well defined amount and τ was determined. With this procedure of consecutively measuring the delay while step by step scanning the spectral domain, $v_g(E)$ was determined.

For these studies two samples have been prepared, with d_S = 1.96 mm and d_S =1.03 mm. For the range of high v_g the thicker sample provides a sufficient delay of the pulses, while at resonance the transmission through thick samples drops below the detection threshold. To explore this range the thinner sample was investigated. The results of such time resolved studies are given by the symbols in Fig. 3.14. In the range of comparably high velocities, the data nicely follow the calculations.[4] The closer we get to the resonance the slower the polaritons propagate. When we finally are only 1 μeV from the resonance a group velocity of $4.5 \cdot 10^4$ m s^{-1} is measured. This means that v_g has been decreased by almost four orders of magnitude compared to c_0. This value is by more than a factor of three lower than the lowest value reported so far for the group velocity of polaritons [80]. When getting even closer to the exciton-photon resonance, significant deviations from the expected behavior arise. v_g seems to saturate at values well above the calculated ones.

Let us now evaluate the origin of this systematic deviation. Around $\Delta E_{exc} = 0$ delays of few ns are obtained, which are smaller than the length of the exiting laser pulses. However, the delay should increase the closer we get to the resonance, which again should allow resolving of τ. Hence, the limited time resolution cannot cause the saturation effect. Another issue is the spectral width of the laser pulses. With a temporal width of 10 ns the pulses have a spectral width of at least 0.15 μeV for a Fourier transform limited Gaussian pulse. In the range of interest v_g drops by a factor of 2 (see Fig. 3.14) in this spectral window. It means that the measured τ is averaging over the range of group velocities covered by the pulse. In addition, the absorption increases as we move closer to the resonance. The slower the polaritons propagate, the less signal reaches the detector. Consequently, the weight of slower polaritons is lowered and we measure a seemingly higher v_g. Following these considerations the saturation of v_g is explained by the width of the exciting pulse and the extreme chirp around the resonance.

At resonance polaritons from both branches propagate with the velocity of the longitudinal acoustic phonon and our experimental values are only about one order of magnitude from this sonic limit. It can be expected that the interaction of phonons and polaritons is strongly enhanced if both propagate at the same speed. Acousto-optic phenomena have always been studied with photons propagating much faster than sound. Let us, for example, look at stimulated Brillouin scattering: If the photon is faster than the phonon phase matching between the fields constrains scattering to the backward direction. When the group velocity of the wavepacket equals the velocity of sound in the medium an anomalous stimulated Brillouin scattering is expected, where the generated sound is strongest in the forward direction and vanishes in the backward direction. Furthermore, it has not been possible to measure v_g of the exciton dominated polaritons. These polaritons couple only weakly to light, which hinders their observation. Previous studies show that the damping increases as v_g decreases [61]. Hence, these ultra slow polaritons are strongly damped, which makes their observation even

[4] $f_{1S} = 3.9 \cdot 10^{-9}$ gives a good agreement with the data. This value is slightly higher than the value reported in literature [13].

more difficult. However, the extremely weak light-matter coupling of the quadrupole transition and the high crystal quality should in principle allow observation of such extremely slow polaritons. Therefore it might be rewarding to improve the experiment in order to be able to measure even lower v_g's.

From above considerations we conclude that the current limitations can be overcome by using spectrally sharper pulses, which in turn means losing on the time resolution side. This should, however, be more than compensated, as the expected delays are supposed to increase strongly in the direct vicinity of the resonance. In this case τ will reach values of ≈ 1 μs in a 1 mm thick specimen, which permits the use of spectrally sharp pulses. A second improvement can be done on the detection unit. In the present experiment a simple photodiode is used. The sensitivity can be improved by several orders of magnitude when using a fast photomultiplier. The signal to noise ratio could also be improved by using a lock-in or differential detection scheme. Considering the potential of such simple modifications, it seems realistic to measure group velocities below the velocity of sound.

3.4 Wavevector dependent exchange interaction

The spin properties of excitations in semiconductors are one of the main foci of research in the field of solid state physics. While nowadays most efforts concentrate on spin phenomena in micro- and nanostructures, bulk semiconductors offer a challenging variety of unanswered questions [81]. In this section we will study spin-spin interactions and, in particular, exciton exchange interaction. It couples the spins of electron and hole and splits excitonic levels of different total angular momenta. Taking advantage of the exceptional spectral resolution, we can put the conventional description of electron-hole exchange in solids to a test [82].

While electron-electron exchange is well understood in atomic systems, the picture is of increased complexity for the electron-hole exchange interaction in semiconductors. Investigations of electron-hole exchange, beginning with bulk semiconductors [83, 84], have been extended to quantum wells [85] and, recently, also to quantum dots [86]. Coulomb interaction couples an excited electron in the conduction band to the vacant state (hole) in the valence band. Consequently, the exciton properties are determined by both bands, which arise from the atomic orbitals of the lattice constituents. Due to the complexity of the semiconductor band structure difficulties in calculating the exciton exchange microscopically arise. Attempts to describe it on a quantitative level can hardly be found [87]. For simplicity, in higher dimensional structures exchange is normally treated as a wavevector independent spin-spin interaction. This is in agreement with the experiments reported so far. These studies, however, were performed with modest spectral resolution of typically $\gtrsim 20$ μeV. Spectroscopic studies of the exchange fine structure are often hindered as the exchange splittings are rather small. In addition, difficulties arise from inhomogenous line broadening. Both complications can be overcome, here. As we have seen above, the yellow 1S orthoexciton resonance is ex-

tremely sharp and the absorption experiment introduced above allows for the spectral resolution of lineshifts well below the μeV regime.

3.4.1 Theory

From the theory of exchange a wavevector ($\mathbf{k}$) dependence of the interaction is expected. However, typically the theoretical treatment does not go beyond the k-independent terms, as this already provides a reasonable agreement with the data reported so far. For our purposes such a treatment is insufficient and terms of higher order in $\mathbf{k}$ need to be taken into consideration. In the following we will develop the electron-hole exchange up to order k^2.

In the most general case the exchange interaction J_{ex} is given by the Coulomb interaction of the two charge distributions ρ and ρ' [83]

$$J_{ex} = \delta_{\mathbf{k},\mathbf{k}'} \sum_{\mathbf{R}} e^{\mathtt{i}\mathbf{k}\cdot\mathbf{R}} \int\int \frac{\rho^*(\mathbf{r}_1)\rho'(\mathbf{r}_2) d\mathbf{r}_1 d\mathbf{r}_2}{|\mathbf{r}_1 + \mathbf{r}_2 - \mathbf{R}|}, \tag{3.17}$$

with the lattice vectors $\mathbf{R}$ and the spatial vector $\mathbf{r}$. The orthoexciton exchange is determined by the interaction of the spin-singlet exciton charge distributions, which are given by $\rho(\mathbf{r}) = e\sum_{\mathbf{R}} \Psi(\mathbf{R}) \sum_\sigma a(\mathbf{r}) b(\mathbf{r}+\mathbf{R})^*$, whereby $a(\mathbf{r})$ and $b(\mathbf{r}+\mathbf{R})$ denote the conduction and valence band Wannier functions and $\sum_\sigma$ denotes a summation over all spin states [83]. The exchange is diagonal in $\mathbf{k}$ as expressed by $\delta_{\mathbf{k},\mathbf{k}'}$, or in other words, only charges with identical $\mathbf{k}$'s interact with each other.

Introducing the Fourier transform of the charge distributions

$$\mathcal{M}(\mathbf{k}) = \int d\mathbf{r} \rho(\mathbf{r}) \exp(-\mathtt{i}\mathbf{k}\cdot\mathbf{r}), \tag{3.18}$$

the exchange integral is transformed into a sum over all reciprocal lattice vectors $\mathbf{K_i}$ [83]

$$J_{ex} = \delta_{\mathbf{k},\mathbf{k}'} \frac{4\pi}{\Omega} \sum_i \frac{\mathcal{M}^*(\mathbf{k}+\mathbf{K}_i)\mathcal{M}'(\mathbf{k}+\mathbf{K}_i)}{(\mathbf{k}+\mathbf{K}_i)^2}. \tag{3.19}$$

The exchange can be split into a long range (LR) and a short range (SR) fraction. The LR exchange splitting of excitons originates from the interaction of an electron and a hole located in different unit cells. The SR gives the interaction between an electron and a hole in the same unit cell. First, we concentrate on the LR exchange ($\mathbf{K}_i = 0$ in Eq. 3.19) of quadrupolar excitons

$$J_{ex}^Q = \delta_{\mathbf{k},\mathbf{k}'} \frac{4\pi}{\Omega} \frac{\mathcal{M}^*(\mathbf{k})\mathcal{M}'(\mathbf{k})}{k^2}. \tag{3.20}$$

We expand $\exp(-\mathtt{i}\mathbf{k}\cdot\mathbf{r})$ in Eq. 3.18 into spherical harmonics $Y_{l,m}$

$$\exp^{-\mathtt{i}\mathbf{k}\cdot\mathbf{r}} = \sum_{l=0}^{\infty} \sum_{m=-l}^{m=+l} 4\pi(-\mathtt{i})^l j_l(kr) Y_{l,m}^*(\alpha,\beta) Y_{l,m}(\theta,\phi), \tag{3.21}$$

where θ, ϕ are the polar angles of $\mathbf{k}$ and α, β those of $\mathbf{r}$ with respect to the x, y, z coordinate system (cubic axes). $j_l(kr)$ is the modified Bessel functions of order l [88]. The Bessel function of order $l = 2$ is given by $j_2(kr) = \frac{(kr)^2}{15} + \ldots$, where we neglect higher order terms. Decomposing ρ into multipoles [89]

$$\rho_{l,m} = \int d\mathbf{r} r^l \sqrt{\frac{4\pi}{2l+1}} Y^*_{l,m} \rho(\mathbf{r}), \tag{3.22}$$

we find the quadrupole moments ($l = 2$)

$$q_m = \sqrt{\frac{4\pi}{5}} \int d\mathbf{r} r^2 Y^*_{2,m} \rho(\mathbf{r}). \tag{3.23}$$

Using the relations Eqs. 3.21 and 3.23 we find for the Fourier transform of the charge distribution:

$$\begin{aligned}
\mathcal{M}(\mathbf{k}) &= \int d\mathbf{r} \rho(\mathbf{r}) \sum_{m=-2}^{m=+2} 4\pi(-\mathtt{i})^2 j_2(kr) Y^*_{2,m}(\alpha,\beta) Y_{2,m}(\theta,\phi) \\
&= -\frac{4\pi}{15}\sqrt{\frac{5}{4\pi}} k^2 \sum_{m=-2}^{m=+2} \sqrt{\frac{4\pi}{5}} \int d\mathbf{r} r^2 Y^*_{2,m}(\alpha,\beta) \rho(\mathbf{r}) Y_{2,m}(\theta,\phi) \\
&= -\sqrt{\frac{4\pi}{45}} k^2 \sum_{m=-2}^{m=+2} q_m Y_{2,m}(\theta,\phi).
\end{aligned} \tag{3.24}$$

Substituting Eq. 3.24 into Eq. 3.19 the LR quadrupole-quadrupole exchange is given by

$$J^Q_{ex} = \delta_{\mathbf{k},\mathbf{k}'} \frac{16\pi^2}{45\Omega} k^2 \sum_{m_{1,2}=-2}^{2} q^*_{m_1} q'_{m_2} Y^*_{2,m_1}(\theta,\phi) Y_{2,m_2}(\theta,\phi). \tag{3.25}$$

To explicitly calculate the exchange, we take a look at the specific charge distribution. For the 1S orthoexciton the spin singlet part of the Wannier functions can be written as $\phi_{c,s}$ for the conduction and $\phi_{v,yz}, \phi_{v,xz}, \phi_{v,xy}$ for the valence band, with S- and D-like character, respectively. Ortho- and paraexciton are not pure spin states, as the Γ_7^+ hole states ($|\uparrow_H\rangle$, $|\downarrow_H\rangle$) are not pure hole spin states $|\uparrow_h\rangle$, $|\downarrow_h\rangle$. $|\uparrow_H\rangle$, $|\downarrow_H\rangle$ have to be expressed as total angular momentum states:

$$\begin{aligned}
|\uparrow_H\rangle &= -\tfrac{1}{\sqrt{3}}[\phi_{v,xy} |\uparrow_h\rangle + (\phi_{v,yz} + \mathtt{i}\phi_{v,zx}) |\downarrow_h\rangle], \\
|\downarrow_H\rangle &= -\tfrac{1}{\sqrt{3}}[-\phi_{v,xy} |\downarrow_h\rangle + (\phi_{v,yz} - \mathtt{i}\phi_{v,zx}) |\uparrow_h\rangle].
\end{aligned} \tag{3.26}$$

Together with the electron states ($|\uparrow_e\rangle$, $|\downarrow_e\rangle$) we can construct four exciton basis states

$$\begin{aligned}
|\uparrow_e,\uparrow_H\rangle &= \tfrac{-1}{\sqrt{3}}\phi_{c,s}[\phi_{v,xy} |\uparrow_e,\uparrow_h\rangle + \phi_{v,yz} |\uparrow_e,\downarrow_h\rangle + \mathtt{i}\phi_{v,zx} |\uparrow_e,\downarrow_h\rangle], \\
|\uparrow_e,\downarrow_H\rangle &= \tfrac{1}{\sqrt{3}}\phi_{c,s}[\phi_{v,xy} |\uparrow_e,\downarrow_h\rangle - \phi_{v,yz} |\uparrow_e,\uparrow_h\rangle + \mathtt{i}\phi_{v,zx} |\uparrow_e,\uparrow_h\rangle], \\
|\downarrow_e,\uparrow_H\rangle &= \tfrac{-1}{\sqrt{3}}\phi_{c,s}[\phi_{v,xy} |\downarrow_e,\uparrow_h\rangle + \phi_{v,yz} |\downarrow_e,\downarrow_h\rangle + \mathtt{i}\phi_{v,zx} |\downarrow_e,\downarrow_h\rangle], \\
|\downarrow_e,\downarrow_H\rangle &= \tfrac{1}{\sqrt{3}}\phi_{c,s}[\phi_{v,xy} |\downarrow_e,\downarrow_h\rangle - \phi_{v,yz} |\downarrow_e,\uparrow_h\rangle + \mathtt{i}\phi_{v,zx} |\downarrow_e,\uparrow_h\rangle].
\end{aligned}$$

By coupling the spins of electron and hole we get a singlet $\mid S\rangle$ and three triplets $\mid T_{+1}\rangle$, $\mid T_{-1}\rangle$, and $\mid T_0\rangle$ states:

$$\begin{aligned} \mid S\rangle &= \tfrac{1}{\sqrt{2}}(|\uparrow_e,\downarrow_h\rangle - |\downarrow_e,\uparrow_h\rangle), \\ \mid T_0\rangle &= \tfrac{1}{\sqrt{2}}(|\uparrow_e,\downarrow_h\rangle + |\downarrow_e,\uparrow_h\rangle), \\ \mid T_{-1}\rangle &= |\downarrow_e,\downarrow_h\rangle, \\ \mid T_{+1}\rangle &= |\uparrow_e,\uparrow_h\rangle. \end{aligned} \tag{3.27}$$

The four 1S exciton states in the momentum basis are given by

$$\begin{aligned} \mid J=0, J_z=0\rangle &= \tfrac{1}{\sqrt{2}}(|\uparrow_e,\downarrow_H\rangle - |\downarrow_e,\uparrow_H\rangle), \\ \mid J=1, J_z=0\rangle &= \tfrac{1}{\sqrt{2}}(|\uparrow_e,\downarrow_H\rangle + |\downarrow_e,\uparrow_H\rangle), \\ \mid J=1, J_z=-1\rangle &= |\downarrow_e,\downarrow_H\rangle, \\ \mid J=1, J_z=1\rangle &= |\uparrow_e,\uparrow_H\rangle, \end{aligned} \tag{3.28}$$

where the $J=0$ state is the paraexciton and the $J=1$ states describe the orthoexcitons. For convenience we will treat the exchange interaction not in the momentum basis, but in the cartesian basis $\Gamma^+_{5,xy}, \Gamma^+_{5,yz}, \Gamma^+_{5,zx}$ with the orthoexciton states $\mid O_{yz}\rangle, \mid O_{zx}\rangle, \mid O_{xy}\rangle$ plus the Γ_2^+ paraexciton state $\mid P\rangle$ where the exciton states are written as

$$\begin{aligned} \mid P\rangle &= \mid J=0, J_z=0\rangle \\ &= \tfrac{1}{\sqrt{2}}(|\uparrow_e,\downarrow_H\rangle - |\downarrow_e,\uparrow_H\rangle), \\ \mid O_{xy}\rangle &= \mid J=1, J_z=0\rangle \\ &= \tfrac{1}{\sqrt{2}}(|\uparrow_e,\downarrow_H\rangle + |\downarrow_e,\uparrow_H\rangle), \\ \mid O_{yz}\rangle &= \tfrac{-1}{\sqrt{2}}(\mid J=1, J_z=1\rangle - \mid J=1, J_z=-1\rangle) \\ &= \tfrac{-1}{\sqrt{2}}(|\uparrow_e,\uparrow_H\rangle - |\downarrow_e,\downarrow_H\rangle), \\ \mid O_{zx}\rangle &= \tfrac{\mathtt{i}}{\sqrt{2}}(\mid J=1, J_z=1\rangle + \mid J=1, J_z=-1\rangle) \\ &= \tfrac{\mathtt{i}}{\sqrt{2}}(|\uparrow_e,\uparrow_H\rangle + |\downarrow_e,\downarrow_H\rangle), \end{aligned} \tag{3.29}$$

or using the singlet-triplet notation the exciton states can be written as

$$\begin{aligned} \mid P\rangle &= \tfrac{1}{\sqrt{6}}\phi_{c,s}[\phi_{v,xy}\sqrt{2}\mid T_0\rangle + \phi_{v,yz}(\mid T_{-1}\rangle - \mid T_{+1}\rangle) + \mathtt{i}\phi_{v,zx}(\mid T_{-1}\rangle + \mid T_{+1}\rangle)], \\ \mid O_{xy}\rangle &= \tfrac{-1}{\sqrt{6}}\phi_{c,s}[\phi_{v,xy}(-\sqrt{2}\mid S\rangle) + \phi_{v,yz}(\mid T_{+1}\rangle + \mid T_{-1}\rangle) - \mathtt{i}\phi_{v,zx}(\mid T_{+1}\rangle - \mid T_{-1}\rangle)], \\ \mid O_{yz}\rangle &= \tfrac{1}{\sqrt{6}}\phi_{c,s}[\phi_{v,xy}(\mid T_{+1}\rangle + \mid T_{-1}\rangle) + \mathtt{i}\phi_{v,yz}\sqrt{2}\mid S\rangle + \phi_{v,zx}\sqrt{2}\mid T_0\rangle], \\ \mid O_{zx}\rangle &= \tfrac{-\mathtt{i}}{\sqrt{6}}\phi_{c,s}[\phi_{v,xy}(\mid T_{+1}\rangle - \mid T_{-1}\rangle) + \phi_{v,yz}\sqrt{2}\mid T_0\rangle + \mathtt{i}\phi_{v,zx}\sqrt{2}\mid S\rangle]. \end{aligned} \tag{3.30}$$

After having put up a basis, we can now use the wavefunctions to calculate the exchange. As electron-hole exchange interaction affects states with opposite spin, only the singlet $\mid S\rangle$ terms contribute to the exchange interaction. Or, more mathematically, the sum over the spin configurations leads to vanishing ρ and hence the exchange for

the spin triplet terms vanishes [83]. Looking at Eq. 3.30 we find that the paraexciton $\mid P\rangle$ is a pure triplet state and therefore does not contribute to the exchange. The quadrupole moments in the cartesian Γ_5^+ basis can now be calculated from the singlet fractions of the wavefunctions with the singlet charge densities

$$\begin{aligned}
\rho_P(\mathbf{r}) &= 0, \\
\rho_{xy}(\mathbf{r}) &= e\sqrt{\frac{2}{6}}\phi_{c,s}\phi_{v,xy}, \\
\rho_{yz}(\mathbf{r}) &= e\sqrt{\frac{2}{6}}\phi_{c,s}\phi_{v,yz}, \\
\rho_{zx}(\mathbf{r}) &= e\sqrt{\frac{2}{6}}\phi_{c,s}\phi_{v,zx}.
\end{aligned} \tag{3.31}$$

The valence band Wannier functions can be written as

$$\begin{aligned}
\phi_{v,xy} &= d(r)\sin^2\theta\cos\phi\sin\phi &&= d(r)(Y_{2,2} - Y_{2,-2})/2\mathtt{i}, \\
\phi_{v,yz} &= d(r)\sin\theta\cos\theta\sin\phi &&= d(r)(Y_{2,1} - Y_{2,-1})/2\mathtt{i}, \\
\phi_{v,zx} &= d(r)\sin\theta\cos\theta\cos\phi &&= d(r)(Y_{2,1} + Y_{2,-1})/2.
\end{aligned} \tag{3.32}$$

Plugging Eqs. 3.31 and 3.32 into Eq. 3.23 and using the orthogonality relation of the spherical harmonics, one sees that $\phi_{v,zx}, \phi_{v,yz}$ contribute only to q_1 and q_{-1}, while $\phi_{v,xy}$ contributes to q_2 and q_{-2}. q_0 is always equal to zero. Calculating the quadrupole moments and decomposing it into the contributions from the basis states $\mid O_{yz}\rangle, \mid O_{zx}\rangle, \mid O_{xy}\rangle$ we find

$$\begin{pmatrix} q_{-2} \\ q_{-1} \\ q_0 \\ q_{+1} \\ q_{+2} \end{pmatrix} = C_0 \left[\underbrace{\begin{pmatrix} -\mathtt{i} \\ 0 \\ 0 \\ 0 \\ \mathtt{i} \end{pmatrix}}_{|O_{xy}\rangle} + \underbrace{\begin{pmatrix} 0 \\ -\mathtt{i} \\ 0 \\ \mathtt{i} \\ 0 \end{pmatrix}}_{|O_{yz}\rangle} + \underbrace{\begin{pmatrix} 0 \\ 1 \\ 0 \\ 1 \\ 0 \end{pmatrix}}_{|O_{zx}\rangle} \right]. \tag{3.33}$$

The amplitude of the transition quadrupole is given by

$$e\int_0^\infty r^4 \phi_{c,s}(r) d(r) dr. \tag{3.34}$$

Together with all other constant prefactors it has been included in C_0. We now express the LR exchange in matrix form in the basis of $\mid O_{yz}\rangle, \mid O_{zx}\rangle$ and $\mid O_{xy}\rangle$. Each element (J_{ex}^Q (ij,i'j'); (ij=xy,yz,zx)) of the matrix representation of J_{ex}^Q can be calculated as

$$J_{ex}^Q((ij, i'j')) = \delta_{\mathbf{k},\mathbf{k}'} \frac{16\pi^2}{45\Omega} k^2 \sum_{m_{1,2}=-2}^{2} (q_{m_1}^*)_{ij} (q'_{m_2})_{i'j'} Y_{2,m_1}^*(\theta,\phi) Y_{2,m_2}(\theta,\phi), \tag{3.35}$$

which gives the matrix representation of the exchange

$$J_{ex}^Q \sim \sin(\theta)^2 \cdot \begin{pmatrix} (\cos\theta\sin\phi)^2 & \cos\theta^2\cos\phi\sin\phi & \sin\theta\cos\theta\cos\phi\sin\phi^2 \\ \cos\theta^2\cos\phi\sin\phi & (\cos\theta\cos\phi)^2 & \sin\theta\cos\theta\cos\phi^2\sin\phi \\ \sin\theta\cos\theta\cos\phi\sin\phi^2 & \sin\theta\cos\theta\cos\phi^2\sin\phi & (\sin\theta\cos\phi\sin\phi)^2 \end{pmatrix},$$

or in terms of $\mathbf{k}$ and introducing the constant LR quadrupole-quadrupole exchange parameter Δ_Q

$$J_{ex}^{Q} = \Delta_Q \cdot \frac{1}{k^2} \begin{pmatrix} k_z^2 k_y^2 & k_z^2 k_x k_y & k_y^2 k_z k_x \\ k_z^2 k_x k_y & k_z^2 k_x^2 & k_x^2 k_y k_z \\ k_y^2 k_z k_x & k_x^2 k_y k_z & k_x^2 k_y^2 \end{pmatrix}. \tag{3.36}$$

In contrast to dipole excitons, the LR part of the quadrupole-quadrupole exchange scales as k^2 and is analytic at $k = 0$. The first attempt to calculate the quadrupolar exchange interaction was recently done by Moskalenko *et al.* [90]. In their treatment the quadrupolar interaction between the exciton states was given as an effective dipole-dipole interaction, but did not take the off-diagonal interaction matrix elements into account. As these are of the same magnitude as the diagonal terms, their treatment is an unjustified oversimplification.

We now turn to the derivation of the SR exchange. The $\mathbf{k}_i \neq 0$ terms of Eq. 3.19 give the SR exchange, which we expand into orders of $\mathbf{k}$ and treat each order by the method of invariants [83, 91]. The Hamiltonian has to be invariant under the operations of the cubic group and has to retain its scalar form. The well-known $\mathbf{k}$-independent SR contribution splits the orthoexcitons from the paraexciton by Δ_0=12 meV [48], but leaves the orthoexcitons degenerate. The next higher-order term would scale linearly with $\mathbf{k}$, but vanishes due to the inversion symmetry of the lattice. The SR exchange of order k^2 gives non-vanishing contributions: The electron and hole spin operators ($\mathbf{J_e}$, $\mathbf{J_h}$) transform as Γ_4^+, while $\mathbf{k}$ is a polar vector and transforms as Γ_4^-. The direct product of the spin operators and $\mathbf{k} \cdot \mathbf{k}$ terms is decomposed into invariant representations as follows:

$$\begin{aligned} \Gamma_4^+ \otimes \Gamma_4^+ &= \Gamma_1^+ \oplus \Gamma_3^+ \oplus \Gamma_4^+ \oplus \Gamma_5^+, \\ \Gamma_4^- \otimes \Gamma_4^- &= \Gamma_1^+ \oplus \Gamma_3^+ \oplus \Gamma_4^+ \oplus \Gamma_5^+. \end{aligned} \tag{3.37}$$

Consequently, the SR exchange is given by representations of Γ_1^+, Γ_3^+, Γ_4^+, and Γ_5^+ [46]. Now the total exchange Hamiltonian can be split into invariant representations (H_i) of symmetry Γ_i^+. As the representations are linearly independent, each component scales with the constant exchange parameter Δ_i. Each exchange representation is formed by the electron and hole spin operators and contributions of $\mathbf{k} \cdot \mathbf{k}$ type.

The exchange Hamiltonian of Γ_1^+ symmetry is given by

$$H_1 \sim (\mathbf{J_e} \cdot \mathbf{J_h})(\mathbf{k} \cdot \mathbf{k}). \tag{3.38}$$

Using the wavefunctions of Eq. 3.30 we can calculate the matrix elements of the SR exchange contribution in the orthoexciton basis ($\langle O_{ij}|H_1|O_{i'j'}\rangle$). After lengthy algebra (see appendix) we find the matrix representation of the Γ_1^+ electron-hole exchange energy

$$J_1 = \Delta_1 \cdot \begin{pmatrix} k_x^2 + k_y^2 + k_z^2 & 0 & 0 \\ 0 & k_x^2 + k_y^2 + k_z^2 & 0 \\ 0 & 0 & k_x^2 + k_y^2 + k_z^2 \end{pmatrix} = \Delta_1 k^2 \cdot \mathbf{1}. \tag{3.39}$$

J_1 is proportional to the identity matrix and causes identical spectral shifts for all three orthoexciton states. Since J_1 scales as k^2 it contributes to the spatial dispersion where it can be interpreted as a correction to the effective mass. As Δ_1 cannot be determined independently in the current experiment. It will be included in the energy E_0 of the degenerate orthoexciton states.

The Hamiltonian of Γ_3^+ symmetry is given by

$$H_3 \sim \tfrac{1}{6}(\mathbf{J_e}\cdot\mathbf{J_h} - 3J_{e,z}J_{h,z})(\mathbf{k}\cdot\mathbf{k} - 3k_z^2) + \tfrac{1}{2}(J_{e,x}J_{h,x} - J_{e,y}J_{h,y})(k_x^2 - k_y^2), \tag{3.40}$$

with the matrix representation

$$J_3 = \Delta_3 \cdot \begin{pmatrix} 2k_x^2 - k_y^2 - k_z^2 & 0 & 0 \\ 0 & 2k_y^2 - k_x^2 - k_z^2 & 0 \\ 0 & 0 & 2k_z^2 - k_x^2 - k_y^2 \end{pmatrix}. \tag{3.41}$$

Again, all off-diagonal elements vanish and no mixing of the basis states occurres. However, the discriminative **k**-dependence of the diagonal elements should give rise to a fine structure. This will allow to determine the magnitude of the J_3 contribution (Δ_3).

The Γ_4^+ electron-hole exchange is given by

$$\begin{aligned} H_4 \sim [\quad & (J_{e,y}J_{h,z} - J_{e,z}J_{h,y}) && (k_yk_z - k_zk_y) \\ & +(J_{e,z}J_{h,x} - J_{e,x}J_{h,z}) && (k_zk_x - k_xk_z) \\ & +(J_{e,x}J_{h,y} - J_{e,y}J_{h,x}) && (k_xk_y - k_yk_x)] = 0. \end{aligned} \tag{3.42}$$

Obviously, this term vanishes, which finally leaves the contribution of Γ_5^+ symmetry

$$\begin{aligned} H_5 \sim \quad & (J_{e,y}J_{h,z} + J_{e,z}J_{h,y}) && (k_yk_z) \\ & +(J_{e,z}J_{h,x} + J_{e,x}J_{h,z}) && (k_zk_x) \\ & +(J_{e,x}J_{h,y} + J_{e,y}J_{h,x}) && (k_xk_y), \end{aligned} \tag{3.43}$$

with the matrix form

$$J_5 = \Delta_5 \cdot \begin{pmatrix} 0 & k_xk_y & k_xk_z \\ k_xk_y & 0 & k_yk_z \\ k_xk_z & k_yk_z & 0 \end{pmatrix}. \tag{3.44}$$

J_5 has only off-diagonal terms. As for the long-range term (Eq. 3.36), a **k**-dependent mixing of the orthoexciton states is also expected. Summarizing: we have derived three terms of order k^2, that can give rise to an orthoexciton fine structure: the LR quadrupole interaction J_Q^{ex}, and the SR contributions J_3, J_5, where the absolute splittings are determined by the exchange parameters Δ_Q, Δ_3, and Δ_5, which remain to be determined.

For high symmetry **k**'s (see Fig. 3.15) the matrices 3.36, 3.41, and 3.44 can be diagonalized analytically. The new eigenstates are linear combinations of $|O_{xy}\rangle$, $|O_{yz}\rangle$,

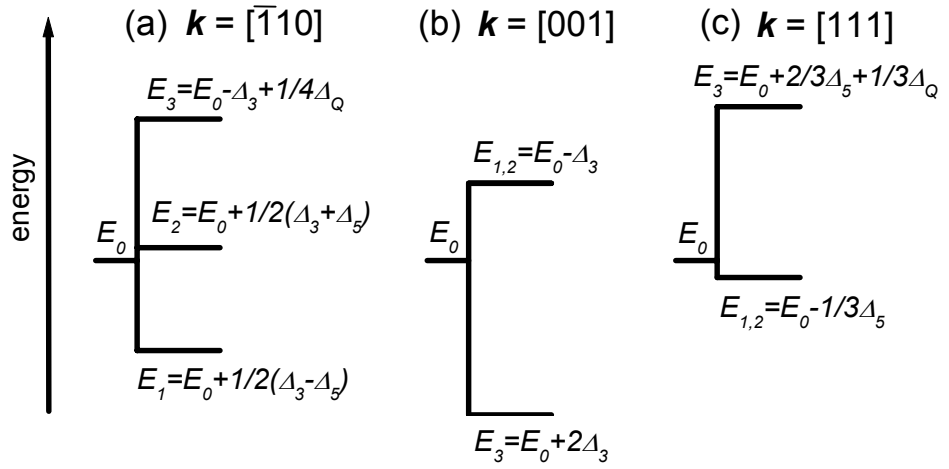

Figure 3.15: *Energy level diagram of the exciton fine structure.* E_0 *gives the orthoexciton energy including the exchange shifts* Δ_0 *and* Δ_1*. Panels (a), (b), and (c) give the energy schemes for* $\mathbf{k} = [\bar{1}10]$, [001], *and* [111], *respectively (*$\Delta_Q = 5\ \mu eV$, $\Delta_3 =$ *- 1.3* μeV, $\Delta_5 = 2\ \mu eV$ *).*

and $|O_{zx}\rangle$. For $\mathbf{k}$ along $[\bar{1}10]$ exchange should lift the degeneracy of the orthoexcitons and three separate lines are expected (Fig. 3.15 (a)), where the $E_2 - E_1$ splitting directly gives Δ_5. For $\mathbf{k}$ along [001] there is no contribution from J_{ex} and J_5. One thus expects a doubly degenerate level $E_{1,2}$ and a single level E_3 with a total splitting of $3\Delta_3$. In the [111] direction we expect to find a degenerate low energy state besides a single high energy level.

3.4.2 Experiment

The $\mathbf{k}$-dependence of the exchange can be investigated experimentally in an absorption experiment, where the laser beam propagating along $\mathbf{k}$ directly probes the corresponding fine structure. Rotating the samples around the vertical axis by an angle φ' gives access to intermediate k-directions (see Fig. 3.6). The dependence of the orthoexciton energies E_1, E_2, and E_3 on φ (angle inside the sample) could thus be measured. The $\mathbf{k}$-dependence of the exchange has not been resolved in experiments with limited spectral resolution ($\gtrsim 20\ \mu$eV). Thus the splittings are expected to be not larger than few μeV. Again, special care was taken to insure a strain free mounting in the helium bath cryostat ($T = 1.4$ K).

The exchange at $\mathbf{k}$ along $[\bar{1}10]$ is investigated in the experiments presented in Fig. 3.16, where the left panels show the expected transition amplitudes for $\varphi = 0$ (a) and $\varphi = 4°$ (b) (rotation around the [111]-axis). Calculating $|QA_2|^2$ at $\mathbf{k}$ along $[\bar{1}10]$ ($\varphi = 0$) shows that for $\psi = -36°$ ($\mathbf{e}(-36°) = [00\bar{1}]$) the transition E_2 is maximally allowed (Fig. 3.16 (a)). In the corresponding experiment, given by the full line in Fig. 3.16 (c) one indeed finds a strong absorption. For $\psi = +54°$ ($\mathbf{e}(54°) = [110]$)

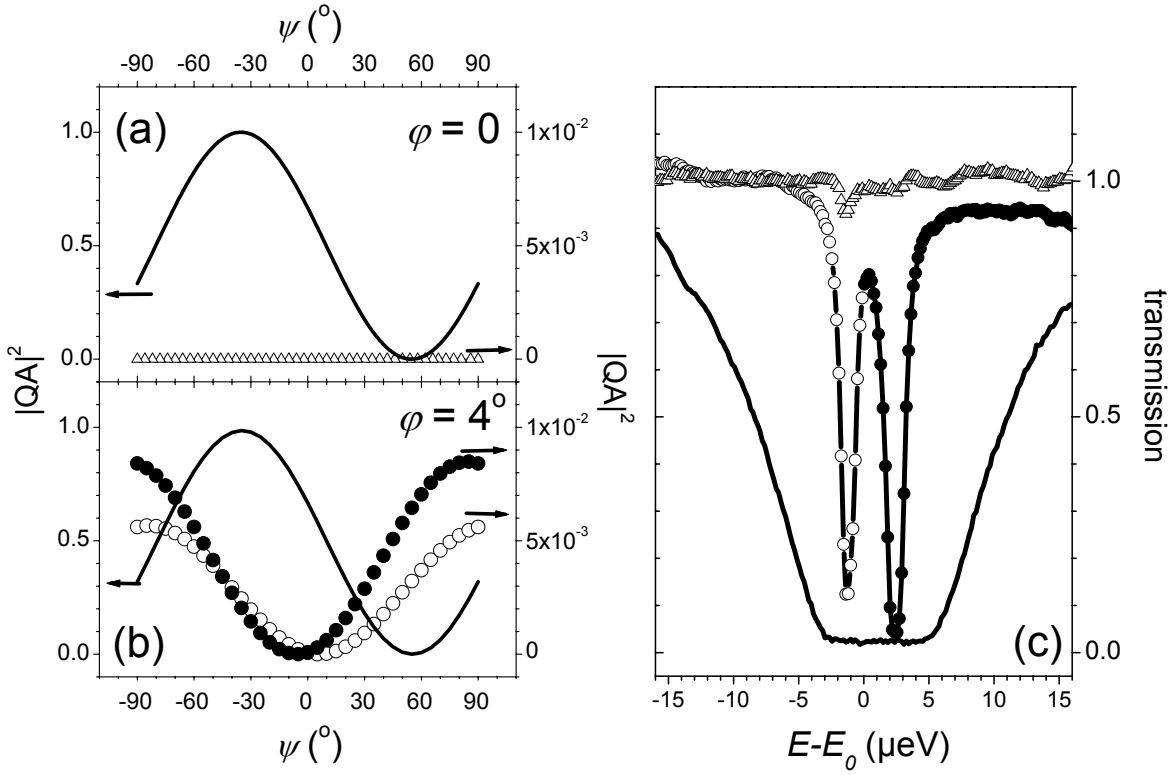

Figure 3.16: *(a) Calculated intensities* $|QA_1|^2, |QA_3|^2$ *(triangles), and* $|QA_2|^2$ *(full line) as a function of* ψ *for* $\varphi = 0$*.* $\mathbf{k}$ *is along* $[\bar{1}10]$ *and for* $\psi = 0$ *the polarization vector* $\mathbf{e}(\psi)$ *points along* $[11\bar{2}]$*. (b) Calculated intensities* $|QA_2|^2$ *(full line),* $|QA_1|^2$ *(open dots) and* $|QA_3|^2$ *(full dots) as a function of* ψ *for* $\varphi = 4°$*. Note the different scales for* $|QA_1|^2$*,* $|QA_3|^2$ *(right axis) and* $|QA_2|^2$ *(left axis). (c) Transmission spectra of a 4 mm thick crystal. The full line and the triangles show the transmission spectra for* ψ *= -36°* ($\mathbf{e} = [00\bar{1}]$) *and* $\psi = 54°$ ($\mathbf{e} = [110]$)*, respectively. The spectrum for* $\psi = 54°$ *and* $\varphi = 4°$ *(rotation around* [111]*-axis) is shown by open dots (*E_1 *resonance in Fig. 3.15 (a)) and full dots (*E_3 *resonance in Fig. 3.15 (a)).*

the E_2 transition is forbidden, as confirmed by the experiment (triangles in Fig. 3.16 (c)). The transitions E_1 and E_3 are forbidden for all ψ (triangles in Fig. 3.16 (a)). No absorption is found in the entire spectral range investigated for $\psi = +54°$ ($\mathbf{e} = [110]$). This confirms the calculations of panel (a) and demonstrates the high crystallographic quality of the sample and the absence of symmetry breaking perturbations. The picture changes drastically if the sample is tilted slightly from $\varphi = 0°$ to $\varphi = 4°$, where $\mathbf{k}$ no longer points exactly along $[\bar{1}10]$. In this case the strong quadrupole absorption is again found for ψ = -36°. For $\varphi \neq 0$ and $\psi = +54°$, however, E_1 and E_3 should become weakly allowed ($|QA|^2 \neq 0$), while E_2 remains forbidden (Fig. 3.16 (b)). This might allow for the observation of the predicted fine structure. The dots in Fig. 3.16 (c) show the results of the corresponding experiment and we indeed observe the $E_1 - E_3$ doublet with a splitting of 4.0 μeV. Both lines are extremely narrow with a width $\lesssim 1$ μeV. Apparently the degeneracy of the orthoexciton has been lifted. Besides the spectral

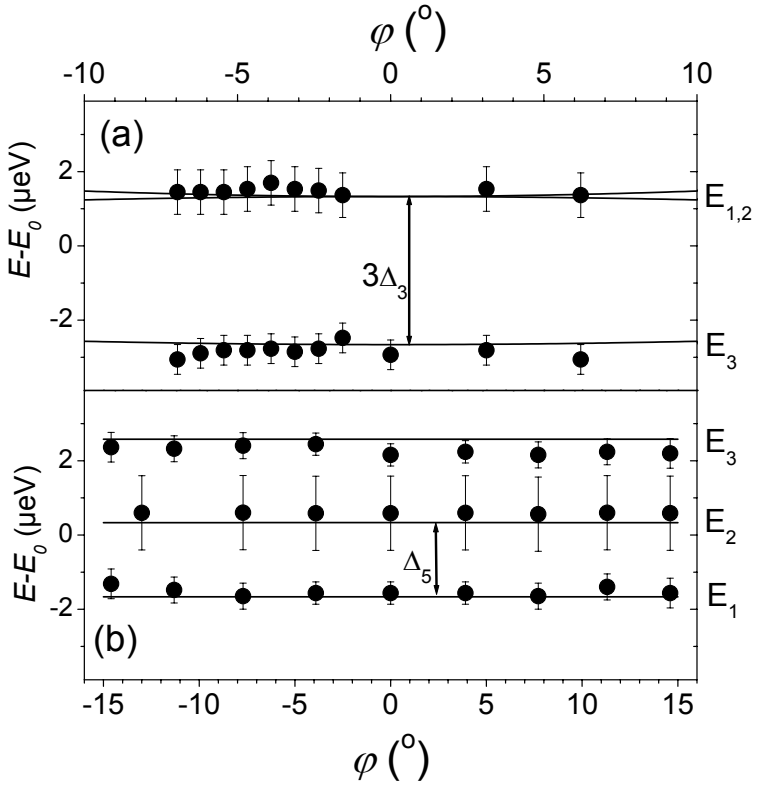

Figure 3.17: *E_1, E_2, E_3 as a function of φ for 4 mm thick samples. Dots mark the experimental data. Full lines give the calculated values. (a) For $\varphi = 0$,* **k** *is along* [001]*. φ describes a rotation around the* $[1\bar{1}0]$*-axis. (b) For $\varphi = 0$,* **k** *is along* $[\bar{1}10]$*. φ describes a rotation around the [111] axis.*

signatures, we observe that the E_1 absorption is smaller than the E_2 absorption, as predicted by calculations (Fig. 3.16 (b)).

Having demonstrated qualitative agreement between theory and experiment, we proceed with the quantitative analysis of the three exchange parameters Δ_Q, Δ_3, and Δ_5. For **k** along [001] the fine structure is only determined by J_3, which gives us the chance to measure Δ_3 independently. We expect two lines ($E_{1,2}$ and E_2) (Fig. 3.15 (b)) split by $3\Delta_3$. Indeed, this fine structure is observed in the experiment (Fig. 3.17 (a)). The levels $E_{1,2}$ and E_3 are distinguished by analyzing $|QA_{1,2}|^2$ and $|QA_3|^2$ as a function of ψ, which allows us to determine the sign of Δ_3= -1.3 μeV. In the angular range investigated no significant line shifts are expected and the degeneracy of E_1 and E_2 is only slightly lifted, which is masked by their spectral widths. For the sample orientation of Fig. 3.16 E_1, E_2 and E_3 are shown as a function of φ in Fig. 3.17 (b). $E_2 - E_1$ gives directly $\Delta_5 = 2$ μeV. Finally, $\Delta_Q = 5$ μeV is determined from E_3. These parameters also give the correct relative line positions, when comparing the absolute energies obtained for **k** along [001] to those for **k** along $[\bar{1}10]$. The direct comparison of two measurements is non trivial, as the absolute laser energy is not known with sufficient accuracy. Therefore, the experiments were performed with two samples mounted in the cryostat. While keeping the laser locked on one mode, two consecutive measurements were performed on both samples which allows comparison of the relative energies of the absorption lines. Typically, the sample shown in Fig. 3.16 with the characteristic E_1-E_3 doublet was taken as spectral reference.

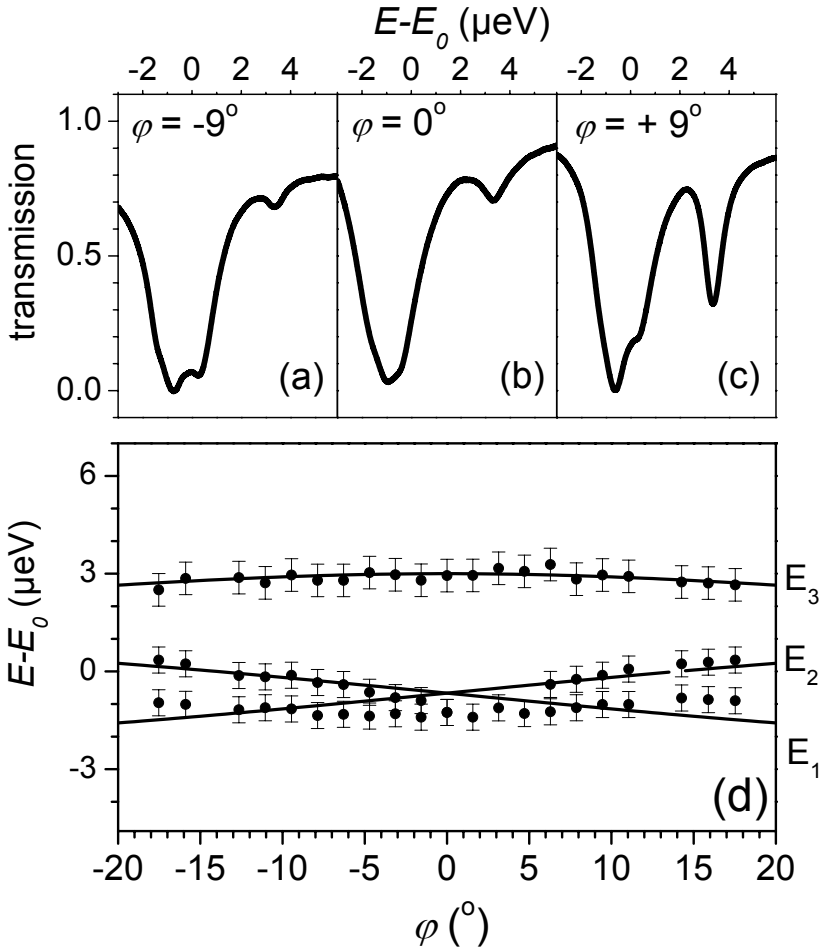

Figure 3.18: *Transmission spectra for $\varphi = -9°$ (a), 0 (b), and $+9°$ (c), where the sample ($d_S = 85$ μm) was rotated around the $[11\bar{2}]$ axis and* **k** *is along* [111] *at $\varphi = 0$. (d) E_1, E_2, and E_3 versus φ. Full dots give the data, while full lines mark the theory.*

Now all exchange parameters haven been evaluated at **k**'s of high symmetry. According to theory, these exchange parameters should apply for any arbitrary **k**. Hence, the crucial test for our description is done by measuring the exchange fine structure for lower symmetry **k**'s. As a test of consistency we present data for **k** along [111] (Fig. 3.18). According to Fig. 3.15 (c) we expect for $\varphi \to 0$ a degenerate level $E_{1,2}$ plus a high energy state E_3, where $|QA_3|^2$ should be much weaker than $|QA_{1,2}|^2$. Looking at the experimental data in Fig. 3.18 (b), we find the pronounced $E_{1,2}$ absorption plus a weak line (E_3) at higher energy. The degeneracy of E_1 and E_2 should be lifted for $\varphi \neq 0$. In agreement with theory $E_{1,2}$ splits into a doublet at $\varphi \pm 9°$ (Fig. 3.18 (a) and (c)). Also the asymmetric changes in $|QA_3|^2$ coincide with the theoretical treatment. In panel (d) E_1, E_2, and E_3 are shown versus φ. The $E_1 - E_2$ splitting increases with $|\varphi|$, while E_3 shows only slight shifts. The fine structure is modelled (full lines) using the parameters obtained above. Obviously, Δ_Q, Δ_3, and Δ_5 allow a consistent description for these **k**-directions. In samples of $d_S > 1$ mm lines of large $|QA|^2$ become rather broad. This hinders the precise quantitative evaluation of the fine structure (see e.g. error bar for E_2 in Fig. 3.17 (b)). To overcome this broadening a thin sample ($d_s = 30$ μm) had to be employed, which permits resolving the $E_1 - E_2$ splitting (Fig. 3.18 (a) and (c)).

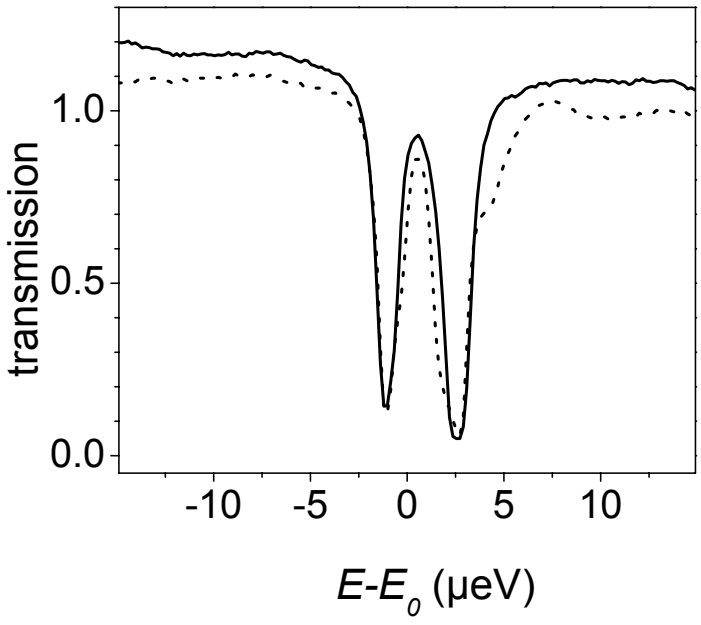

Figure 3.19: *Transmission spectra for $\varphi = 4°$ (rotation around the [111] axis) and $\psi = 54°$ (close to $\mathbf{e} = [110]$). The spectra are recorded for excitation in the sample center (solid line) and excitation close to the edge of the sample (dotted line).*

3.4.3 Impact of strain

The degeneracy of the orthoexcitons could also be lifted by perturbations, such as strain[30, 29]. Considering the energy scales we are dealing with, even slightest strain of the order of $1 \cdot 10^3$ N m^{-2} can cause a notable effect. Two sources of strain have to be taken into account. First, external strain originating from the sample mounting. Our sample holders (see section 3.1) exclude this source. Second, the crystal itself can also be intrinsically strained. Such stress can originate from imperfections in the lattice structure, cutting and polishing during the sample preparation, or thermal stress. These issues were examined with great care. For example, to avoid thermal stress the samples were slowly cooled down to 2 K, were the temperature was lowered from room temperature to ≈ 100 K within ≈ 10 h. In addition, the annealing procedure as described in section 3.1 was applied to samples which showed signatures of strain. Despite these efforts we cannot completely exclude strain. In the following we will evaluate to which extent this can explain our experimental findings [92].

Let us first focus on cube shaped samples with extensions of ≈ 4 mm. Because of the relatively large size of the specimen, an inhomogeneous strain distribution across the sample is expected. The central parts should be less affected by strain than the outer sections of the cube, where cutting and polishing can give rise to an increased stress. Hence, a strain induced fine structure should depend on the sample section being probed.

To clarify this issue the experiment of Fig. 3.16 was repeated for illumination of the specimen in the sample center (solid line) and close to the sample edge (dotted line) in Fig. 3.19. Otherwise the experimental conditions are identical to those for the data given by the dots in Fig. 3.16. In both spectra two lines with a splitting of ≈ 4 μeV are found. The comparison of the spectra shows that the spectral shifts of

E_1 and E_3 are insignificant when compared to the splitting. Additional spectra were recorded covering the entire surface area of the sample and the fine structure remained more or less the same. This indicates that the fine structure cannot be interpreted as being stress induced. A second argument along these lines is the following: In a thick sample a rather large volume of the specimen is probed, even with a focused beam. Thus, inhomogeneous strain would give rise to an inhomogeneous broadening of the lines. However, for the laser beam passing through the sample center the lines remain extremely narrow (FWHM ≤ 1 μeV) and Lorentzian in shape. For the beam travelling along the edge of the sample, the line shape of E_3 deviates from a Lorentzian. The shoulder on the high energy side might arise from a strained section of the sample. The data show that slight stress can be found in the surface regions of the sample. However, this does not have a significant impact on the fine structure and can be disregarded when the laser strikes the center of a thick sample. The situation is more complex

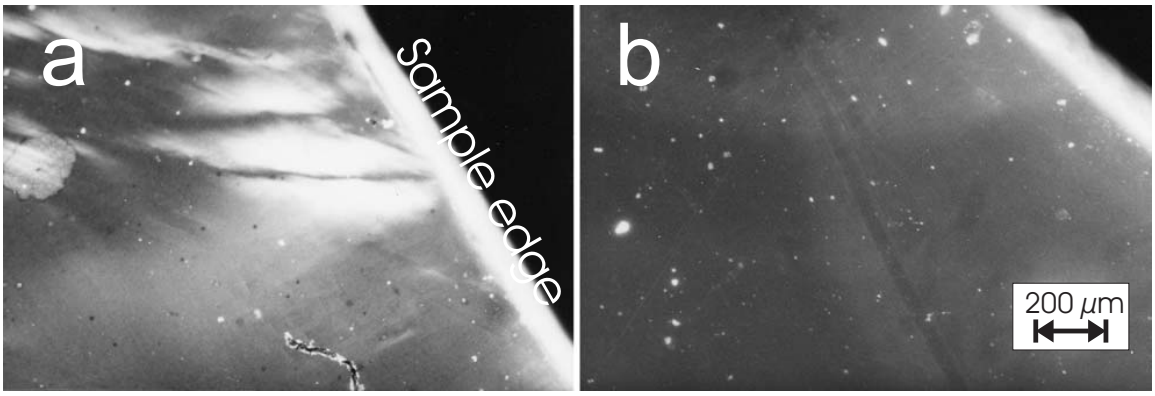

Figure 3.20: *Microscopic pictures of two slab shaped samples. The specimens were positioned between two crossed polarizers. Hence, bright areas indicate where the sample is stressed. The bright white line is the sample edge. The dark areas in the upper right corners give a reference without sample. Both samples are about 100 µm thick.*

for thin samples of $d_s < 1$ mm. For such slab shaped samples surface effects gain importance and stress induced perturbations can no longer be disregarded a priori. Each sample has to be examined carefully. A first impression can be obtained via polarization microscopy: The crystal is placed between two crossed polarizers. In a strain free sample, the polarization of the transmitted light is unchanged and the light is blocked by the second polarizer. If the crystal is strained, it acts as a birefringent material. The transmitted light becomes elliptically polarized and thus some light passes through the second polarizer. In Fig. 3.20 sections of two samples are shown. For the sample on the left we find clear signatures of strain, which is inhomogeneous across the specimen. The picture on the right shows a weakly strained sample (the bright spots arise from dirt particles). Although it is rather homogenous, weak traces of strain can still be found. Such tests are only preliminary. Even if a crystal appears to be perfectly strain free in the polarization microscope, it does not mean that it

is free of strain. High resolution spectroscopy provides a much more sensitive tool. Therefore each sample is tested for homogeneity by probing various sections of the specimen. Only if the spectral positions of the exciton resonances do not depend on the sample section being probed and agree with those measured on thick crystals, is the sample is suited for our purposes, even though this still does not prove that the it is absolutely unstrained. It only shows that the strain induced perturbation is of the same magnitude as the k^2 exchange and homogenous across the crystal.

As we still cannot exclude this perturbation we have to clarify how such residual strain affects the orthoexciton fine structure. The impact of strain can be approached by symmetry considerations: The strain tensors possess the same symmetry as the SR k^2-exchange terms. Therefore the effect of strain on $\mid O_{xy}\rangle$, $\mid O_{yz}\rangle$, and $\mid O_{zx}\rangle$ is described by the same types of symmetry operators as given in equations 3.39 to 3.44. Replacing $k_{x,y,z}$ by the corresponding elements of the strain tensor $\overleftrightarrow{\varepsilon}$ we find:

$$S_1 = \delta_1 \cdot \begin{pmatrix} \epsilon_{xx}+\epsilon_{yy}+\epsilon_{zz} & 0 & 0 \\ 0 & \epsilon_{xx}+\epsilon_{yy}+\epsilon_{zz} & 0 \\ 0 & 0 & \epsilon_{xx}+\epsilon_{yy}+\epsilon_{zz} \end{pmatrix}, \tag{3.45}$$

$$S_3 = \delta_3 \cdot \begin{pmatrix} 2\epsilon_{xx}^2-\epsilon_{yy}^2-\epsilon_{zz}^2 & 0 & 0 \\ 0 & 2\epsilon_{yy}^2-\epsilon_{xx}^2-\epsilon_{zz}^2 & 0 \\ 0 & 0 & 2\epsilon_{zz}^2-\epsilon_{xx}^2-\epsilon_{yy}^2 \end{pmatrix}, \tag{3.46}$$

$$S_4 = 0; \qquad S_5 = \delta_5 \cdot \begin{pmatrix} 0 & \epsilon_{xy} & \epsilon_{zx} \\ \epsilon_{yx} & 0 & \epsilon_{yz} \\ \epsilon_{xz} & \epsilon_{yz} & 0 \end{pmatrix}, \tag{3.47}$$

where ϵ_{ij} is an element of the strain tensor. Hence, the stress can be quantified by three parameters δ_1, δ_3, and δ_5, where S_1 simply shifts all three states and S_3 and S_5 give rise to a splitting. With the tensor

$$\overleftrightarrow{\varepsilon} = \begin{pmatrix} \frac{1}{2} & \frac{1}{2} & \frac{1}{2} \\ \frac{1}{2} & \frac{1}{2} & 0 \\ \frac{1}{2} & 0 & 1 \end{pmatrix} \tag{3.48}$$

we can now model the strain induced effects quantitatively. Strain induced shifts can be discriminated from exchange as they are fixed to the lattice and hence depend only on the orientation of the crystalline axes, but not on $\mathbf{k}$. Therefore, when turning the crystal one would not expect any dependence of the energy levels on φ for stain induced effects.

In Fig. 3.21 the spectral positions of the orthoexciton resonances are studied vs. φ with $\mathbf{k} = [111](\varphi = 0)$ and rotation around $[11\bar{2}]$. The experimental data are given by the dots in both panels. In panel (a) the exchange splittings according to the parameter set obtained on unstrained ($d_S = 4$ mm) samples are shown (solid traces). Apparently

the calculations do not match the data, as the $E_{1,2}$-E_3 splitting is by a factor of two too large in the experiment. The experiments also show an asymmetry with respect to $\varphi = 0$. The data seem to be shifted towards lower angles by about 2°. Nevertheless, we find the qualitative structure as known from Fig. 3.18. In panel (b) the calculations include strain of Γ_3^+ and Γ_5^+ type, while the exchange parameters remain unaltered. When subtracting the exchange induced shifts, we end up with constant energy levels (dashed lines in Fig. 3.21 (b)), while the sum of strain and k^2 exchange gives a good description of the data (solid lines in Fig. 3.21 (b)). As evident from this modelling, the φ (**k**) dependence solely arises from exchange, while the increased splittings arise from residual strain. Most convincingly, the **k** dependence is very well described by the set of exchange parameters established above. The inclusion of strain also gives the explanation for the shift towards lower φ observed in the data. It simply originates from the strain offsets on E_1 and E_2. In total the strain induced shifts are about as large as the exchange induced ones.

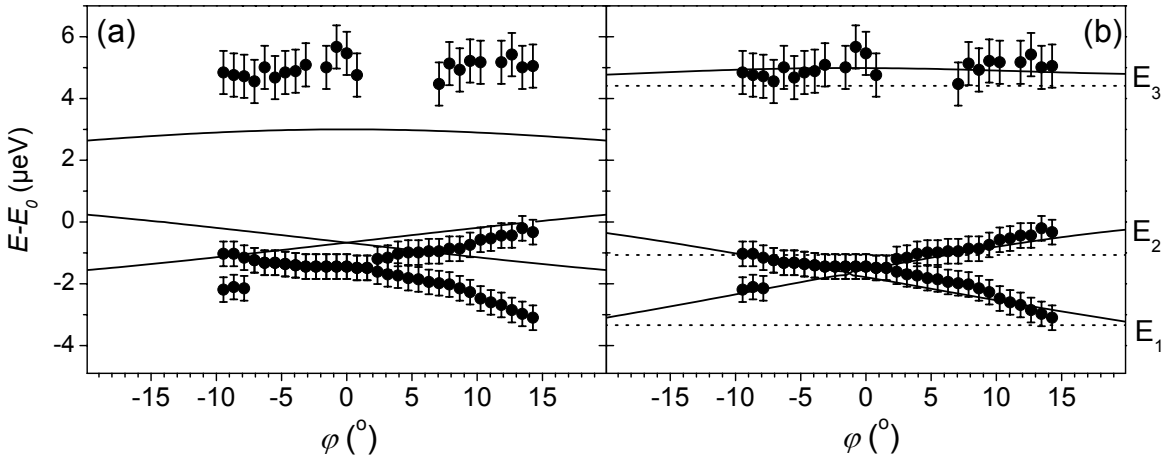

Figure 3.21: *Dispersion of the orthoexciton resonances vs. φ (rotation around the* $[11\bar{2}]$ *axis) measured on a 30 μm thick Cu_2O slab (*$\mathbf{k} \approx [\mathbf{111}]$*). The experimental data are given by open squares. In panel (a) calculations based on the parameters Δ_Q= 5 μeV, Δ_5= 2 μeV and Δ_3= - 1.3 μeV are plotted. In panel (b) the calculations also include strain of Γ_3^+ (δ_3 = - 1.4 μeV) and Γ_5^+ (δ_5 = - 2.1 μeV) type, keeping the exchange parameters fixed. The dashed lines give the strain offsets.*

As a final test for the analysis of k^2 exchange, we proceed with a **k** direction of even lower symmetry. For this crucial experiment we have chosen a crystal with **k** along $[11\bar{2}]$ at $\varphi = 0$. The experimental findings are shown in Fig. 3.22, where the left panel shows E_1, E_2, and E_3 versus φ and the right panel gives the corresponding $|QA|^2$ for each level. Including slight strain offsets again gives a good agreement between theory and experiment. Especially the characteristic **k** dependence is well described by the same exchange parameters. As the exchange parameters determine the mixing between $|O_{xy}\rangle$, $|O_{yz}\rangle$, and $|O_{zx}\rangle$, they also have impact on the quadrupole amplitudes of the transitions. The calculated values deviate slightly from the measured ones. Despite these discrepancies, qualitative agreement is found.

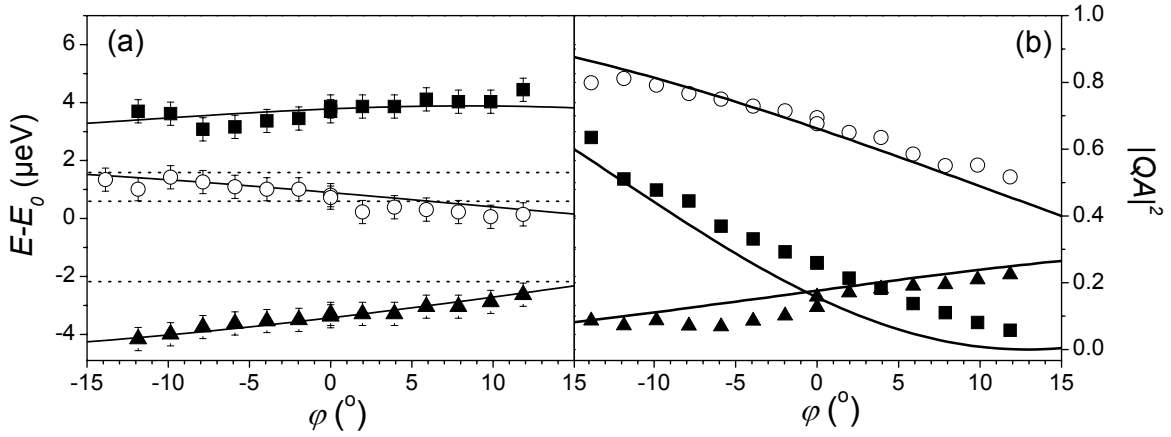

Figure 3.22: *(a) Dispersion of the orthoexciton resonances as a function of φ for a slightly strained sample (d_S = 95 μm,* **k** *along* $[11\bar{2}]$ *at $\varphi = 0$, axis of rotation* $[\bar{1}10]$*). The experimental data are given by the symbols. Calculations based on the parameters Δ_Q= 5 μeV, Δ_5= 2 μeV and Δ_3= -1.3 μeV are plotted (solid traces). The calculations also include strain of Γ_3^+ (δ_3 = 0.7 μeV) and Γ_5^+ (δ_5 = 1.0 μeV) type. The strain offsets are given by the dotted lines. (b) $|QA_i|^2$'s of the quadrupole transitions, where symbols give experimental data (the symbols in panel (b) correspond to the one in panel (a)), while the solid traces give the calculated $|QA|$'s.* **e** *is along* [111] *(*$[\bar{1}10]$*) for the solid (open) symbols.*

Concluding this section, we have derived and demonstrated k^2-dependent exchange interaction of excitons. For the yellow 1S orthoexcitons in Cu_2O the exchange parameters $\Delta_Q = 5 \pm 1.5$ μeV, Δ_3 = -1.3 $\pm$ 0.2 μeV and $\Delta_5 = 2 \pm 0.3$ μeV are obtained, where the errors are estimated by evaluating a series of experiments performed on crystals of various thicknesses and orientations. The k^2 dependent exchange can also be interpreted as an anisotropic effective mass. The magnitude of this mass is of the same order as the effective mass derived from the spatial dispersion. In addition to the corrections due to Δ_Q, Δ_3, and Δ_5, which are direction dependent, we predict an isotropic correction due to Δ_1, which is expected to be of the same magnitude as the other exchange parameters. Naturally these contributions have been disregarded so far. Possibly these findings might help to explain the discrepancies found in measurements of the effective mass of the 1S orthoexciton. The exchange parameters apply only for this specific exciton transition, however the k^2 exchange is a fundamental property of spins in solids. Even though this effect has not been observed before, it should be present for every exciton transition in bulk solids. The theoretical approach presented here is a semi empirical analysis and the exchange parameters are only accessible experimentally. A microscopic calculation of the higher order exchange terms can be rewarding, as it also determines the magnitude of these exchange parameters. However, considering the complexity of such calculations and experiences with earlier microscopic descriptions of exchange, a quantitative agreement between theory and experiment is not expected.

3.5 High density effects

The studies presented above were performed in the low density regime. In this chapter we will investigate phenomena appearing at high excitation densities. Ground state excitons represent the lowest electronic transition in a nonmetallic crystal. This motivates studies at high carrier densities, as further relaxation is suppressed. When increasing the exciton density inter-particle interactions gain importance. A well-known example is the formation of an exciton molecule (biexciton). A second example is the formation of an electron-hole liquid [4], where the excitons form a new collective phase. In Cu_2O the situation is different. The formation of a biexciton [93], as well as the formation of an electron-hole liquid are inhibited as electron-hole exchange compensates the attractive exciton-exciton interaction. This makes Cu_2O an interesting candidate for the study of excitons at high densities. This interest is increased further by the facts that these excitons have a small Bohr radius (see chapter 3). Hence, the Mott density, where excitons transform into an electron-hole plasma, is extremely high. Furthermore, the lowest exciton states show long lifetimes, as they are dipole forbidden. The initial question was whether the ortho- and paraexciton at high densities can be described by Bose-Einstein statistics. After this was successfully demonstrated [94], studies focused on the demonstration of BEC of excitons [32, 95]. Here studies concentrated on the paraexciton [36, 34]. Despite tremendous effort no conclusive demonstration of BEC of para- nor orthoexcitons has been reported.

The appeal of BEC of excitons lies in the high critical temperatures, which can reach 10 K and above for realistic carrier densities, as compared to 50 nK required for alkali atoms. This advantage is due to the small mass of excitons. In contrast to ions, excitons do not carry a nucleus, which reduces the mass by 5 orders of magnitude. The major obstacle to the creation of high 1S exciton densities in Cu_2O is the weak oscillator strength of these transitions, orders of magnitude lower than that of dipole excitons. Therefore a direct optical excitation is inefficient for resonant excitation. Typically, the excitation was done by resonantly pumping a phonon side band or using non resonant ns pulses from Ar^+ lasers at $E = 2.41$ eV. An alterative is a two-photon absorption experiment [51, 96, 97, 98, 41].

In the previous sections, we have seen that our high resolution absorption experiment gives access to the yellow 1S orthoexciton state. As we can tune the laser energy precisely to the orthoexciton resonance, a significant fraction of the laser power can be absorbed even in crystals of $d_S = 100$ μm. In Fig. 3.23 (left panel) the absorption spectrum is shown for increasing excitation powers (top to bottom). At low P_{exc} we find the well-known sharp symmetric line. With increasing P_{exc} the absorption shifts towards lower energies and becomes asymmetric. While the low energy side becomes more and more steep, the high energy side transforms into a rather flat tail. Increasing the power further we find a step-like onset of the absorption followed by a more and more flat tail. Even though the absolute peak of the absorption decreases as P_{exc} increases, the spectrally integrated absorption remains constant within the experimental accuracy. We note that these experiments were performed in helium gas at $T \approx 2$ K.

When repeating the same experiment with the sample immersed in liquid helium these features can not be observed. At high P_{exc} density fluctuations in the liquid helium at the helium-sample interface give rise to diffuse diffraction of the beam. This obscures the line shape of the absorption resonance.

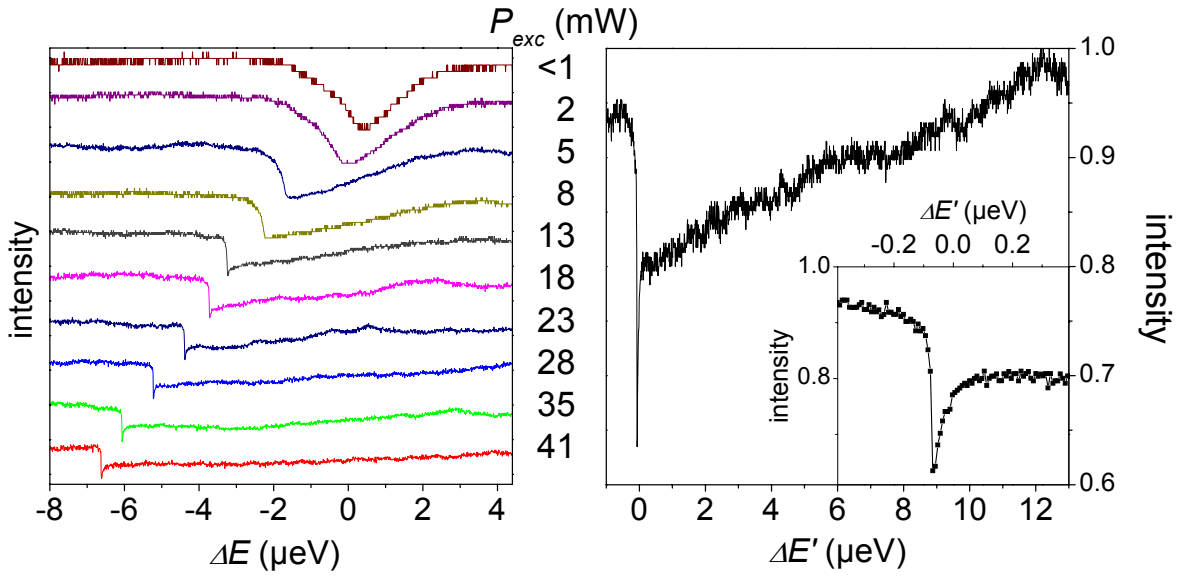

Figure 3.23: *Left: Absorption spectrum for various P_{exc} (**k** along [111], $d_s = 30\ \mu m$). From top to bottom P_{exc} has been increased. For clarity the spectra have been shifted vertically. Right: Absorption spectrum for $P_{exc} = 35\ mW$. Inset: closeup of the spike. Symbols mark the data points. All spectra were recorded at $T \approx 2\ K$ in helium gas.*

Looking closely at the high density spectra a sharp spike at the low energy edge of the absorption resonance is seen. In the right panel of Fig. 3.23 we take a closer look at the peculiar absorption line shape at higher P_{exc}. We find an abrupt absorption onset and the extremely sharp line that changes over into a tail of constantly decreasing absorption. This tail extends over a range of $\approx 10\ \mu$eV. In the inset of Fig. 3.23 a close up of the absorption onset is shown. On this energy scale we see that the absorption onset coming from the low energy side is smooth at first and becomes extremely steep close to the absorption maximum. On the high energy side a reverse behavior is found. While the absorption drops quickly at first, it changes over into the decay tail described above. Deriving a linewidth from the low energy flank of the spike a FWHM of 15 neV is found! This is about two orders of magnitude lower than any exciton linewidth reported so far. This exciting observation raises several questions: Is it at all feasible to interpret the absorption spectrum in this fashion? Can experimental artefacts be excluded? What is the physical origin of the red shift, the high energy tail and, especially, what gives rise to such a spectrally narrow absorption feature?

This experiment has been repeated for various samples with different orientations. Different states of the exchange fine structure have also been investigated (see chapter 3.4) and in all thin samples similar features are found. The reproducibility of the effect

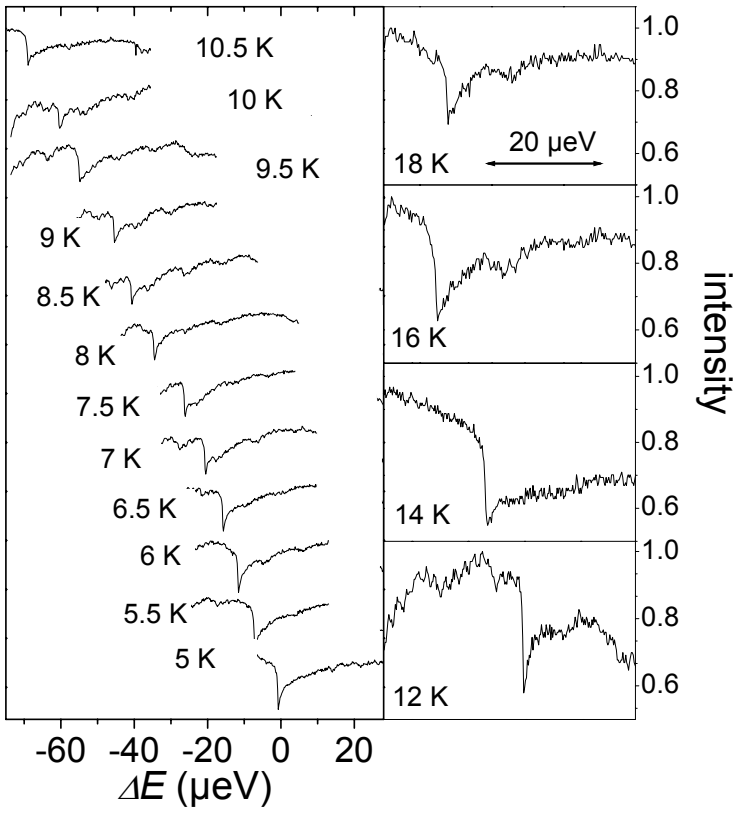

Figure 3.24: *Absorption spectra for various temperatures under high power excitation (***k** *along* $[1\bar{1}0]$, $d_s = 54$ μm, $P_{exc} = 73$ mW*). In the left panel the spectra have been shifted vertically for clarity. In the right panels the spectra have been shifted spectrally.*

shows that this is not an experimental artefact. Furthermore, repeating the experiment with a slower energy scan or with a wider scan range not influence the outcome. Hence, we conclude that the experiments indeed give the absorption spectrum of the sample at high exciton densities. It should be noted that the laser energy was scanned from low to high energy. Coming from the high energy side a similar effect is observed, however the spike is not found.

To obtain further insight we have investigated the temperature dependence of the effect (Fig. 3.24. Under intense excitation the temperature has been increased from $T = 5$ K to $T = 18$ K. In the left panel the relative spectral positions are to scale. The right panels cover the same relative spectral range, but the absolute line positions are not to scale.[5] Comparing Fig. 3.24 to Fig. 3.13 we find the same thermal line shift under high and low power excitation. In Fig. 3.23 we found a total line shift of -6.5 μeV from the lowest to the highest excitation powers. This would correspond to a temperature increase of ≈ 1.5 K. Hence, the red shift with increasing P_{exc} could be explained by a slight heating of the sample, but we cannot exclude additional mechanisms which will be discussed below. More strikingly, the characteristic absorption edge is not only found at the lowest temperatures, but can also be observed even for $T = 20$ K. Though the absorption edge becomes less pronounced at high T and no spike is found the line shape is still observed.

[5]As a temperature change of 2 K already shifts the line out of the spectral range covered by one energy scan, keeping track of the relative spectral positions of the spectra is difficult.

The sharp cutoff at the low energy flank of the absorption with increasing power density might indicate the transition from a Maxwell-Boltzmann type of thermal carrier distribution to a Bose-Einstein-like energy distribution. So far only indirect evidence of this changeover was found by analyzing the line shape of the ortho- and paraexciton phonon lines [35, 33, 36]. The line shape of the phonon directly reflects the energy distribution of the corresponding exciton state. Here we can take the direct way. Let us assume that the carriers are weakly interacting which is justified, as we are still well below the Mott density. As excitons have integer spin we can describe their kinetic energy distribution ζ by Bose-Einstein statistics:

$$\zeta(E_{kin}, \mu) = \frac{1}{e^{\frac{E_{kin}-\mu}{k_B T}} - 1}, \tag{3.49}$$

where μ is the chemical potential and k_B is the Boltzmann constant. The number of particles $N(E)$ with energy E_{kin} is then given by

$$N(E_{kin}) \sim \zeta(E_{kin}, \mu) \cdot D(E_{kin}), \tag{3.50}$$

where $D(E_{kin})$ gives the density of states, which is $\sim \sqrt{E_{kin}}$ for the free exciton. Fig. 3.25 shows N for various values of $-\frac{\mu}{k_B T}$. At the transition from Maxwell-Boltzmann ($-\frac{\mu}{k_B T} > 0.5$) to Bose-Einstein distribution the carriers shift towards lower energy. As also observed in the experiment the energy distribution shows a sharp cutoff and a high energy tail. For $\mu/k_B T \to 0$ N transforms into a spike shaped spectral feature, followed by a pronounced tail. The comparison between the particularities of the experiments at increased carrier densities and the calculated carrier distributions indicate that the formation of a cutoff energy, the red shift and the absorption tail on the high energy side might indicate a changeover from a Maxwell-Boltzmann to a Bose-Einstein statistics. A quantitative comparison with the experiment is not feasible, as we assume a constant carrier density in the entire spectral range, disregarding polaritonic effects. This leaves the most interesting question open: How large is μ and can we possibly observe the phase transition towards an exciton condensate for $\mu \to 0$? For a condensation we would expect a sharp peak near zero kinetic energy. This puts the focus on the few neV sharp spike shown in Fig. 3.23. Does this indicate that a fraction of the exciton gas already forms a macroscopic coherent phase?

Let us estimate the carrier density generated inside the sample: We excite the sample with $P_{exc} = 40$ mW. After losses at the focusing optics and the cryostat windows about $\frac{3}{4}P_{exc}$ reaches the sample. The focus diameter is $d_f \approx 10$ μm. With a photon energy of $E = 2.033$ eV this leads to photon flux $N = \frac{4P_{exc}}{\pi d_f^2 E} = 1.2 \cdot 10^{27} \mathrm{m}^{-2}\mathrm{s}^{-1}$ photons per second per m^2 at the sample surface. To calculate the actual carrier density we have to take into account the group velocity of the carriers which crucially depends on the carrier energy. At resonance the polaritons are slowed down to $v_g = c_0 \cdot 10^{-5}$ (see chapter 3.3). This leads to a massive 'polariton traffic jam' inside the sample and the carrier density $\bar{n}$ is increased by a factor of $\frac{c_0}{v_g}$. Now we calculate the critical density for the condensation of the exciton gas $\bar{n}_{crit}$. The kinetic energy of the exciton is given by $E_{kin} = \frac{\hbar k^2}{2m_X}$ (compare Eq. 3.10). In a thermal distribution the number of particles

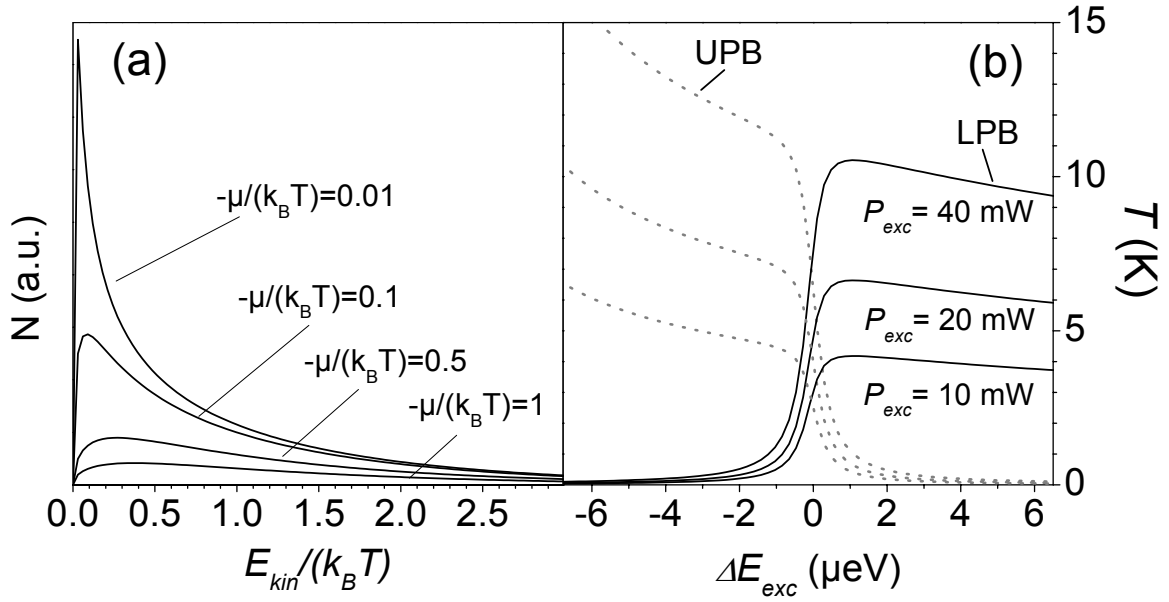

Figure 3.25: *(a) Thermal energy distribution of bosons for various $\mu/(k_bT)$. (b) Critical temperature for BEC of the 1S orthoexciton as a function of the excitation energy and P_{exc}. ΔE_{exc} is measured from the exciton-photon resonance. The dotted (solid) trace gives the values for the UPB (LPB).*

in the volume V is given by the integral of N over all $\mathbf{k}$ [32]

$$\bar{n} = \lim_{V\to\infty} \frac{N}{V} = \frac{g}{2\pi^3} \int_{-\infty}^{+\infty} \frac{d\mathbf{k}}{e^{\frac{1}{k_B T}(\frac{\hbar^2 k^2}{2m_X} - \mu)} - 1}, \tag{3.51}$$

with g the spin degeneracy of the state. Due to the wavevector dependent exchange (see previous section) g equals one. For $\mu = 0$ the thermal distribution changes over into the BEC. Solving the integral for $\mu = 0$ we obtain:

$$\bar{n}_{crit} = 2.612 \cdot g \cdot \left(\frac{m_X k_B T}{2\pi\hbar^2}\right)^{\frac{3}{2}}, \tag{3.52}$$

or for T_{crit}

$$T_{crit} = \left(\frac{2\pi\hbar^2}{m_X k_B}\right) \cdot \left(\frac{\bar{n}}{2.612 g}\right)^{\frac{2}{3}}. \tag{3.53}$$

In Fig. 3.25 T_{crit} is shown as a function of the excitation energy relative to the exciton-photon resonance ΔE_{exc} of various P_{exc}. The energy dependence arises from the changes in v_g and hence $\bar{n}$. Looking at $T_{crit}(\Delta E =_{exc} 0)$ we find for the highest $P_{exc} = 40$ mW a T_{crit} of 7 K. Even for $P_{exc} = 10$ mW a critical temperature above helium temperature is found.

From these considerations we can conclude that condensation phenomena can not be excluded a priori. The relatively small red shift (see Fig. 3.23) shows that the

sample temperature is well below 5 K, even for the highest P_{exc}. Still it would be desirable to identify the origin of the red shift. The magnitude of the shift ≈ 7 μeV is comparable to the kinetic energy of the excitons at $k = 2.62 \cdot 10^7$ m^{-1} (compare Fig. 3.3 (c)). The red shift could also be attributed to attractive exciton-exciton interaction. Further insight into the origin of the red shift could be gained by chopping the laser beam. Adjusting the chopper such that the laser light shines onto the sample only in spectral vicinity of the resonance does not change the spectrum. Hence, slow sample heating can be excluded. It might be argued, however, that the red shift is caused by quick temperature changes on a μs timescale. Temperature changes on the time scale of the energy scan can give an alternative explanation for the line shape. In this framework the spike can be interpreted as an increased absorption, present in a time window ≈ 200 μs (derived from the scan speed). By chopping the beam on ns timescale and adjusting the chopping rate the time averaged laser power can remain constant while increasing peak powers. In this fashion the impact of temperature changes can be identified.

To date a clear identification of the origin of this absorption feature is not possible. We have seen that the asymmetry in the line shape suggests an explanation by considering a bosonic thermal distribution. For a better estimate of the critical density etc. it is necessary to include the full polaritonic picture. The photon admixture reduces the effective mass further and lowers the density of states in the resonance region. At present it is unclear which state could show a macro occupation. In principle, one would expect condensation in the ground state at $\mathbf{k} = 0$, which is about 8 μeV below the exciton at $\mathbf{k} = 2.62 \cdot 10^7$ m^{-1}. The spike is already observed well above the ground state energy. This would imply a propagation of the macro population, which will lead to decoherence at the sample surface. From the linewidth (15 neV) a T_2 of 120 ns is derived. For a 30 μm thick sample this gives an upper limit to $v_g = 250$ ms^{-1}. This would imply that we are dealing with excitons at $\mathbf{k} \approx 0$ (compare Fig. 3.14), which does not agree with the spectral position of the spike. The data available at present are insufficient to judge whether the spike is a fingerprint of a macroscopic collective exciton coherence. For its demonstration several aspects have to be clarified:

- the $T^{3/2}$ dependence for the critical density,
- the collective coherence of the carriers,
- the actual occupation numbers of the states.

Chapter 4

Polaritons in microcavities

In section 3 we have discussed exciton-photon polaritons in bulk crystals. Due to the translational invariance of the crystal, exciton and photon describe Rabi oscillations. Both modes cannot be described independently, but form coupled eigenmodes. If we now turn to a heterostructure, where the dielectric properties change on a wavelength scale, no cycle of radiative recombination and reabsorption is expected. The emitted photon leaves the sample without further interaction with the exciton system. Hence, the uncoupled exciton typically gives a good description of the processes in quantum dots or quantum wells. In the course of this chapter we will see how careful design of a semiconductor heterostructure permits the observation of exciton-photon polaritons in so-called semiconductor microcavities. Unlike in bulk, where the lattice determines the polariton properties, we can here tailor the polariton properties by designing the chemical composition and geometry of the heterostructure. The potential of such custom-made polariton systems will be explored.

4.1 Basic microcavity physics

How can polaritons form in systems of broken translational invariance? This obstacle can be overcome by a simple idea: When placing the exciton system (here we consider excitons in a quantum well (QW)) between high reflectivity mirrors we mimic translational invariance. The exciton decays radiatively and emits a photon. The mirror reflects the photon back into the optically active layer where it can be reabsorbed. This allows the energy transfer between exciton and electro-magnetic field, just as in bulk material. This is the key principle of a semiconductor microcavity (MC). The structure of the cavity used in the following experiments is shown in Fig. 4.1. The hybrid nature of cavity polaritons reflects in the design of the MC-structure, which is a hybrid of two types of heterostructures: a photon confining resonator plus an exciton confining QW. Having in mind the general discussion of chapter 2, we now introduce the particularities of exciton-photon coupling in a semiconductor MC [7, 99, 100, 101].

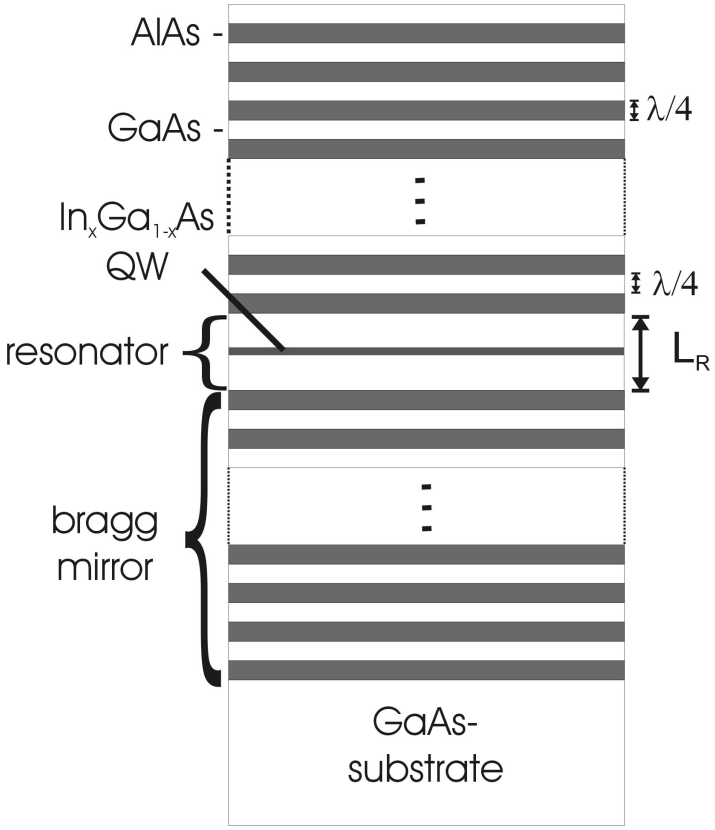

Figure 4.1: *Schematic drawing of the cross section of a semiconductor microcavity.*

The core of the MC is the resonator layer with thickness L_R (here GaAs). To keep the photons inside the resonator, it is sandwiched between two stacks of Bragg mirrors. In our case the mirrors consist of layers of GaAs with refractive index $n_{GaAs} = 2.95$ and AlAs ($n_{AlAs} = 3.65$). These materials have almost identical lattice constants, which allows the growth of the heterostructure by molecular beam epitaxy. The reflectivity of the mirrors is close to unity in a wide spectral region, which is referred to as the stop-band. The resonator design is such that the mode with wavelength $\lambda/n_{GaAs} = L_R$ lies in the stop-band of the Bragg mirrors. Hence, we speak of a λ-cavity and the electromagnetic field is described by a standing wave with the field maximum at the resonator center. The field amplitude also has maxima at the resonator edge. Hence, it penetrates into the Bragg structure [99]. The reflectivity of each double layer is given by the ratio of the refractive indices $\frac{n_{GaAs}}{n_{AlAs}} \approx 0.8$. Including the penetration depth of the field in the Bragg mirrors we can define an effective cavity length L_{eff}. It is given by

$$L_{eff} = L_R + \frac{\lambda}{2n_{GaAs}} \frac{n_{GaAs} n_{AlAs}}{n_{AlAs} - n_{GaAs}}. \tag{4.1}$$

The total reflectivity of a Bragg mirror scales with the power of the number of double layers N [7]:

$$R = 1 - 4\frac{1}{n_{GaAs}} \left(\frac{n_{GaAs}}{n_{AlAs}} \right)^N, \tag{4.2}$$

The evanescent field penetrating through all layers determines the total reflectivity of the structure. In the structures under study, 23 mirror pairs are found on the substrate

side, while 20 mirror pairs form the sample top mirror. This assures a reflectivity > 99.9 % in the stop-band. In analogy to a Fabry-Pérot-interferometer the energies of the cavity modes ($E_P(i)$) are determined by the thickness of the resonator (see Fig. 4.1):

$$E_P(i) = i\frac{hc_0}{2L_R n} \qquad i = 1, 2, \ldots \tag{4.3}$$

In our case the $i = 2$ mode is the relevant one. In this simplified picture the momentum of the photon in the resonator plane $k_{||}$ is neglected. The dispersion, including the in-plane momentum of the photon, is given by

$$E_P(k_{||}) = \frac{\hbar c_0}{n}\sqrt{\left(\frac{2\pi i}{2L_R}\right)^2 + k_{||}^2}. \tag{4.4}$$

For $k_{||} \ll \frac{2\pi i}{2L_R}$ the dispersion is well approximated by a parabola and an effective mass can be attributed to the photon $m_P = hn/c_0 L_R$, which is about 5 orders of magnitude lower than the effective exciton mass.

The quality of a MC is determined by the finesse of the resonator, which is given by the ratio of the linewidth to E_P. For the investigated high quality samples the cavity mode is at $E_P \approx 1.4$ eV with a radiative broadening of $\Gamma \approx 0.2$ meV. Hence, on average a photon is confined in the cavity for ≈ 10 picoseconds (ps) and an excellent finesse of ≈8000 is achieved. The energy of the cavity mode can be tuned by changing the resonator thickness. During the growth process the sample rotation was stopped. This leads an inhomogeneous growth velocity across the waver and gives rise to a slight wedge shape of the resonator. This means that E_P varies systematically across the sample. By moving the spot of excitation along this wedge we find that E_P shifts by ≈ 5 eV m^{-1} (see Fig. 4.2).

This concludes the description of the photon component of MC polaritons and brings us to the exciton component. In a MC the exciton is defined by the properties of the so-called active layer. This active layer typically consists of quantum dots or a quantum well. Even configurations with several active layers can be found. In our case a single 7 nm thick $In_{0.14}Ga_{0.86}As$ QW was chosen. The exciton dispersion is then given by

$$E_X(k_{||}) = E_X(0) + \frac{\hbar^2 k_{||}^2}{2m_X}, \tag{4.5}$$

where m_X is the effective exciton mass in the resonator plane. In the studied cavity the QW is centered in the resonator, where the confined photon field has maximum amplitude. Because of the unidirectional confinement in the QW, E_X is discretized in this direction (z-direction). We will solely concentrate on the lowest exciton level. The highest valence band has angular momentum $L = 1$. Together with the spin we find a hole quadruplet (Γ_8 symmetry) $[J_h = \frac{3}{2}, J_{z,h} = (\pm\frac{3}{2}, \pm\frac{1}{2})]$ and a doublet (Γ_7 symmetry) $[J_h = \frac{1}{2}, J_{z,h} = (\pm\frac{1}{2})]$, where the doublet is lower in energy. For the bulk case the quadruplet states are degenerate at $\mathbf{k} = 0$ (Γ-point), but have different effective masses, which gives rise to a splitting for $\mathbf{k} \neq 0$. The components with higher m_X are termed heavy hole $[J_h = \frac{3}{2}, J_{h,z} = (\pm\frac{3}{2})]$, while the others are termed light hole

$[J_h = \frac{3}{2}, J_{h,z} = (\pm\frac{1}{2})]$. Because of the quantization of the QW potential in z-direction the heavy hole states are at higher energy, lifting the quadruplet degeneracy at $\mathbf{k} = 0$. While the heavy hole has higher effective mass in the growth direction, it has a lighter in-plane mass. Therefore, a crossing between heavy and light hole band would be expected. Because of band mixing effects both bands anti-cross. In the following we will disregard this band mixing and treat the highest valence band state as pure heavy hole. The exciton of interest here is formed with the lowest conduction band electron ($J_{e,z} = \pm\frac{1}{2}$). This gives the exciton momenta $M = \pm 1$ and $M = \pm 2$. The excitons with $M = \pm 2$ are optically inactive (dark excitons). Therefore only the optically active excitons with $M = \pm 1$ (bright excitons) are of interest, here. The confinement in the QW increases the overlap of the electron and hole wave functions, which in turn increases the oscillator strength of the transition. The exciton resonance broadens due to imperfections of the QW, such as alloy fluctuations. In our case the indium content (14%) of the QW is rather high, which gives rise to interface roughness and thickness fluctuations. Therefore the exciton mode shows a linewidth of about 1 meV.

To describe the coupled exciton-photon eigenmodes the same formalism as introduced in chapter 2 is applied. To achieve maximum exciton-photon coupling the geometries of QW and cavity are adjusted such that $E_X \approx E_P$ for $k_{||} = 0$. If a photon is emitted from the QW and the likelihood of reabsorption after reflection at the Bragg mirror is greater than the likelihood of leaking out of the cavity, the cavity moves from the weak coupling regime into the regime of strong coupling, where we are dealing with cavity polaritons [102]. The Rabi splitting in a MC is given by [100]

$$\hbar\Omega_R \approx 2\hbar\sqrt{\frac{2c_0\Gamma_X}{n_{GaAs}L_{eff}}}, \tag{4.6}$$

where $\hbar\Gamma_X$ is the radiative width of the free exciton, which is again proportional to f. As with in the case of polaritons in bulk semiconductors Ω_R scales with $\sqrt{f}$ [7], but in contrast to chapter 3 we are here dealing with a dipole transition. To increase Ω_R a large contrast in the refractive indices of the mirror materials is desirable. The splitting can be enhanced further by growing several QW's with a spacing of $\lambda/2$. The figure of merit for a MC is not the Rabi splitting itself, but the ratio between splitting and linewidth. As increasing the number of QW's necessarily gives rise to inhomogeneous broadening, this might compensate partly the increase in Ω_R. To increase f various material systems can be thought of. Besides the common InGaAs ($\hbar\Omega_R \approx 4$ meV), AlGaAs or CdMgTe cavities are also investigated. As II-VI materials have a larger exciton binding energy and hence a larger f, splittings of $\hbar\Omega_R \approx 22$ meV are reported [103]. The splitting can be increased by one order of magnitude by using organic materials [104, 105], however the splitting to linewidth ratio does not improve.

Unlike bulk polaritons we can now adjust Δ in two ways: As the resonator is wedge shaped E_P relative to E_X can be manipulated by exciting specific regions of the specimen. This is shown in Fig. 4.2. The measured energies of the two polariton modes are given by open symbols. The solid lines were calculated using the coupled oscillator model. The resulting dispersion relations of the uncoupled modes are given

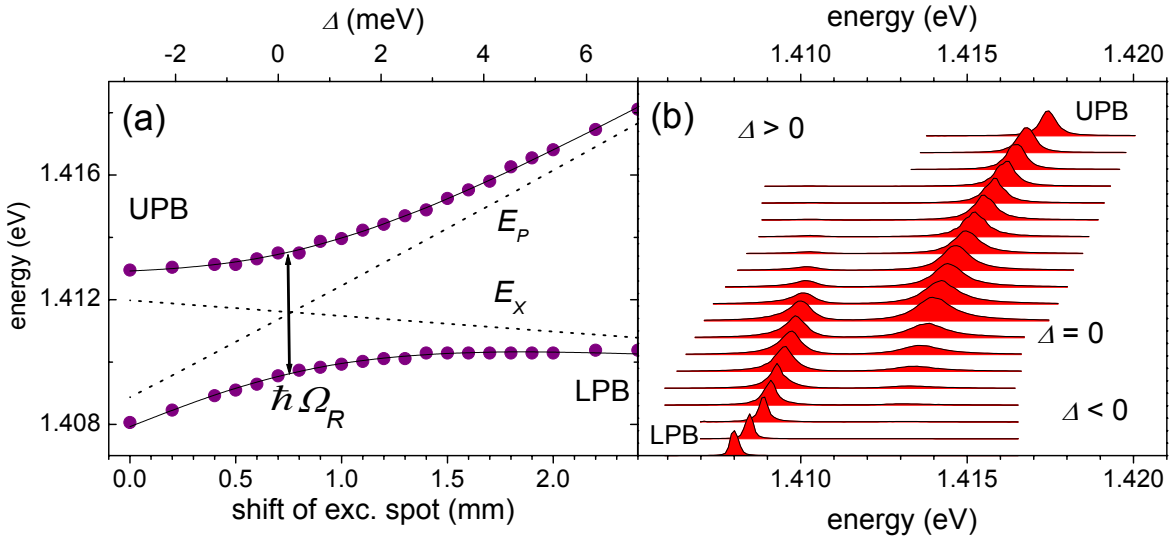

Figure 4.2: *(a) E_L and E_U as the excitation spot is moved across the sample. Symbols give the data. The solid lines give a fit to the data using the coupled oscillator model. The dashed lines give the uncoupled eigenmodes obtained from the fit. (b) Cavity transmission spectra for various detunings.*

by the dashed lines. E_P shows strong dispersion to higher energies as the excitation spot is moved towards the sample edge (smaller L_R), while E_X shifts only slightly. The latter can be due to alloy fluctuations or variations of the QW thickness. In the right panel of Fig. 4.2 the corresponding transmission spectra are shown. For negative Δ (lower traces) the LPB is strongly photonic. Therefore it has high intensity and is spectrally sharp. As the UPB is exciton-like its intensity is rather low. As we move towards positive detuning both branches gradually exchange their character. We see nicely how the LPB loses intensity, broadens and its dispersion becomes flat. The UPB exhibits the vice versa behavior. The normal mode coupling causes the anti-crossing of the polaritonic modes. The normal mode splitting at resonance gives the Rabi energy $\hbar\Omega_R = 3.8$meV. The spectra shown above were obtained for $k_{||} = 0$. A second way to shift E_P is by taking advantage of the strong dispersion of the photon mode relative to the exciton [106]. The in-plane momentum $k_{||}$ is directly related to the external angle of emission θ:

$$\sin\theta = \frac{k_{||}\hbar c_0}{E}. \tag{4.7}$$

Hence, angle resolved spectroscopy gives access to the dispersion $E_{U/L}(k_{||})$. The calculated angular dispersions are shown in Fig. 4.3. Here and in the following Δ denotes the $E_P - E_X$ at $k_{||} = 0$. Due to their photon fraction both polariton modes show strong dispersion in an angular range easily accessible in an optical experiment. Note also the characteristic curvature of the polariton branches, as compared to the uncoupled modes. The dispersion shown here gives only a cut through the momentum space, where the one of the components ($k_{||}^2 = k_x^2 + k_y^2$) of the in-plane momentum (e.g. k_y)

is fixed. The full two-dimensional picture in momentum space is obtained by rotating the dispersion around the energy axis ($k_{||} = 0$).

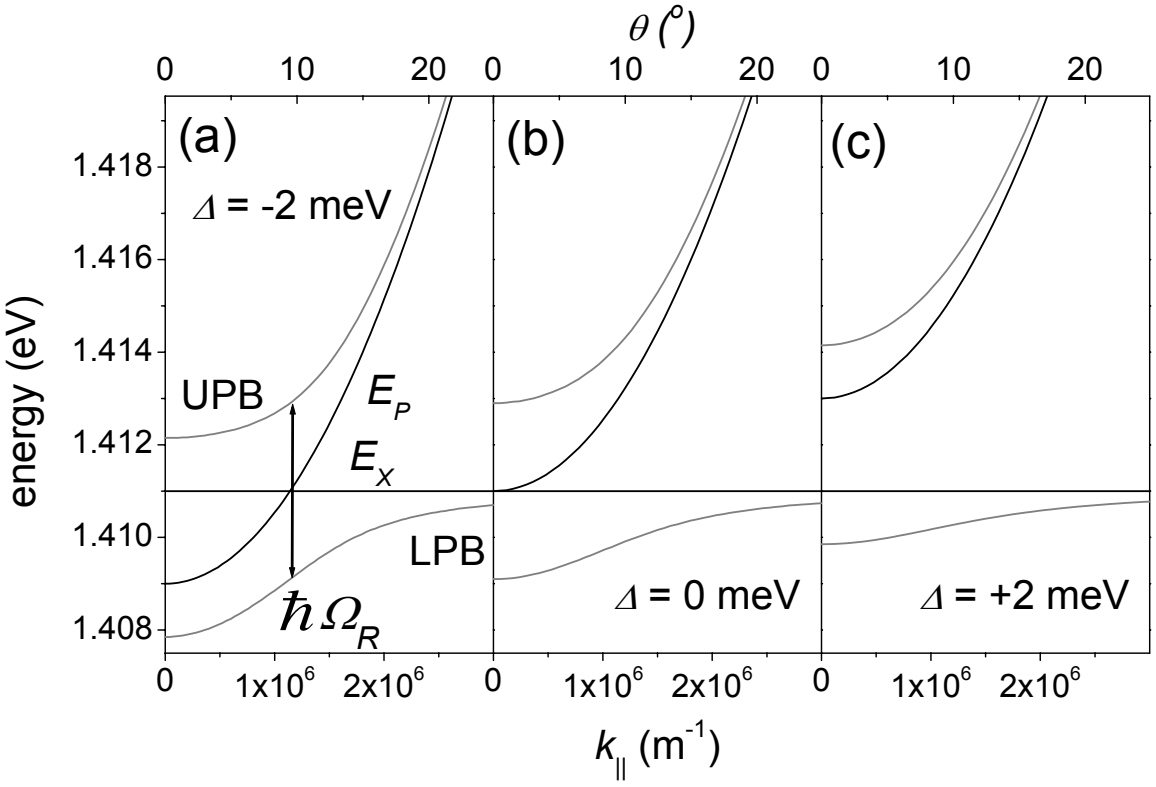

Figure 4.3: *E_L and E_U (grey traces) and E_X and E_P (black traces) as a function of $k_{||}$ (lower scale) and θ (upper scale) for three different detunings ((a) Δ = -2 meV, (b) Δ = 0, and (c) Δ = +2 meV.)*

Comparing bulk polaritons to cavity polaritons, one important advantage of cavity polaritons has been pointed out already: we can tailor the mode energies at will by adjusting e.g. the QW thickness and composition or by choosing L_R. Furthermore, the light matter coupling can be adjusted to some extent (see above). A third important difference is the accessibility of the dispersion in an optical experiment. For bulk polaritons directly measuring the dispersion of the polariton modes is a difficult task. Different nonlinear optical methods can be applied to measure resonances on the two polariton branches [107]. The lower polariton branch is always outside the light cone. To map its dispersion resonant two-photon Raman scattering was used, where the recombination process includes a lower polariton state [108]. Mapping the upper polariton is also non trivial; The first study was done on CuCl in a two-photon experiment [109]. In a linear experiment the momentum conservation constraint limits the k-space to be probed to the intersection between exciton and photon dispersion. In a two-photon absorption experiment this limitation can be overcome, as the relative angle between the two exciting beams offers an additional degree of freedom. The po-

lariton become most evident when studying propagation effects [13] such as the group velocity of a polaritonic wave packet (see chapter 3.3).

In a MC the spectral signature of the normal mode splitting is the most evident sign of strong light-matter interaction. The reason for the accessibility of this spectral feature lies in the dispersion of the photon. In cavities the linear dispersion of the free photon is replaced by a parabolic one with $E_P \neq 0$ at $k_{||} = 0$ and the $k_{||}$ range of interest lies entirely inside the light cone. Typically, the cavity photon intersects with the exciton at wavevectors one order of magnitude smaller than the intersection of exciton and free photon. We can therefore map the dispersion simply by sending light at different angles through the cavity. Another aspect is the process of emission; a bulk polariton is typically 'invisible'. It can only be detected if it propagates to the sample surface, where it is converted into a photon. The exact mechanisms for the polariton-photon conversion are non trivial and still under discussion [107]. In a MC, this process is different, as the polariton does not propagate in this sense. The exciton is locked in the QW and the photon travels back and forth between the cavity mirrors. The detected photons are simply those which penetrate through the Bragg mirror [110, 111].

Being equipped with a basic understanding of cavity polaritons we proceed with a brief glance back at the history of nonlinear processes in microcavities. Ever since the discovery of the strong coupling regime optical nonlinearities in semiconductor microcavities have attracted considerable interest. The hybrid nature of cavity polaritons inspired several proposals of low threshold lasing, based on bosonic stimulation [112, 113]. The corresponding experiments [114] showed a super-linear behavior, which goes in line with a reduced Rabi splitting. Hence, the strong coupling is broken and the validity of the bosonic description can be questioned. This is supported by detailed calculations [115], which showed that the super-linear phenomena are not related to bosonic effects, but can be interpreted as conventional laser action [116]. However, in the low density regime, where the strong coupling remains unbroken, polaritonic nonlinearities are also observed [103, 117]. The basic ideas behind these efforts can be understood from the unique properties of cavity polaritons.

Looking at the dispersion of the LPB ($\Delta = 0$), we find that it deviates from the flat exciton dispersion in the radiative region around $|k_{||}| < 3 \cdot 10^6$ m^{-1}. The light-matter coupling pushes these polaritons away from the exciton dispersion. Let us discuss in which way polaritons can be scattered from excitonic states into the radiative region. One candidate would be scattering with phonons, however an acoustic phonon would take away a large momentum but little energy. This prohibits a phonon cascade towards $k_{||} \approx 0$ [118, 119]. Also, exciton-exciton scattering is only efficient in the excitonic section of the dispersion, where energy and momentum conservation can be satisfied simultaneously. For population of the radiative states exciton-exciton scattering is inefficient [120, 121]. Changing the perspective and looking from the point of view of a polariton at $k_{||} \approx 0$ this means that it cannot be scattered out of this k-space region easily [122, 123, 124]. The strong coupling isolates the carriers at $k_{||} \approx 0$ from the exciton reservoir. This can be interpreted as a kind of polariton trap in momentum

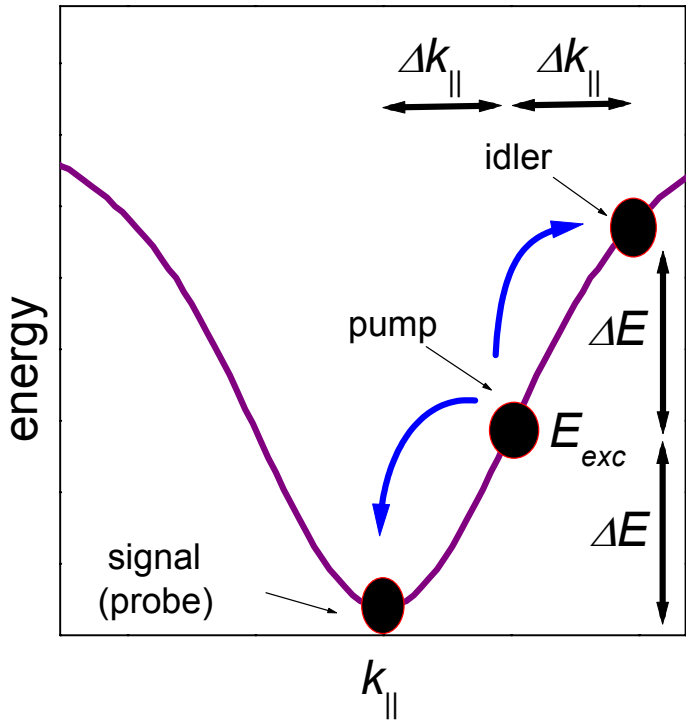

Figure 4.4: *Parametric polariton scattering: The solid line gives the LPB dispersion $\Delta = 0$. The dots mark the signal, idler and pump states. See text for details.*

space. As a side effect the density of states is strongly reduced. These aspects triggered the initial studies on low threshold lasing and bosonic stimulation. Having a low density of states and little interaction with the environment, cavity polaritons inspired proposals to achieve quantum degeneracy at low absolute excitation densities. In the photon picture this would lead to low threshold lasing. For the exciton component this brings us back to BEC scenarios discussed in chapter 3.5. The photon admixture again decreases the mass by four orders of magnitude with respect to the exciton (nine orders with respect to alkali ions). For this purpose an efficient population of the 'trap' is desired.

The key to a systematic study of polaritonic nonlinearities was the demonstration of so-called parametric polariton scattering [125, 126]. To overcome the relaxation bottleneck the peculiar polariton dispersion is utilized. Due to the changeover from the steep photon dispersion to the flat exciton dispersion, a point of inflection is found in the dispersion of the lower polariton branch (see Fig. 4.4). If polaritons are now resonantly excited in the vicinity of the point of inflection, a parametric polariton conversion is observed[1]; One polariton is transferred into the signal state at the bottom of the LPB ($k_{||} = 0$, $E = E_{exc} - \Delta E$), while a second polariton compensates the excess energy and momentum by being lifted into the so-called idler state ($k_{||} = 2k_{exc}$, $E = E_{exc} + \Delta E$). The efficiency of this parametric conversion process relies on the proper adjustment of the excitation parameters. The pump state has to be chosen such that the parametric process conserves energy as well as momentum for final states on the LPB dispersion. In angle resolved pump-and-probe experiments this efficiency can be demonstrated

[1]Due to similarities to optical parametric oscillation the vocabulary established for such systems will be used.

[125]. The pump pulse excites the initial while the probe pulse tests the signal state $k_{||}= 0$.

These experiments triggered a variety of studies on parametric processes in cavities [127, 128]. The scattering can be understood as a coherent wave mixing process between the pump and probe states giving rise to the up-converted idler emission [129, 130]. Under continuous wave excitation these polariton conversion processes can be demonstrated, as well [131, 132]. They are explained by so-called parametric luminescence driven by the correlations between the polariton populations [133]. In particular, the aspect of a macroscopic filling of the polariton states [134, 135] attracted considerable interest. The findings were interpreted in terms of a polariton condensate [39, 136] and lead to a revival of proposals on Bose-Einstein condensation in microcavities [137, 40] and several forms of polariton lasers [138, 139, 140]. In the following various aspects of nonlinear processes in microcavities will be discussed.

4.2 Exciton localization in microcavities

So far we have treated QW excitons exclusively as quasi-free particles, which demands a perfectly homogenous QW. Considering the large indium content (14%) and the linewidth of 1 meV this approximation becomes questionable, here. It can be expected that surface roughness gives rise to localization of excitons at the resulting steps in the QW potential. We will have to investigate to which extent the excitons can still be treated as quasi-free particles and where this description fails. In many cases the free exciton assumption is justified, even in disordered systems, because relatively weak fluctuations of the confinement potential do not change the exciton dispersion. Nor do they cause strong scattering of polaritons because of their large coherence size of a few μm.

However, the ultra fast nonlinearities in the emission from the LPB observed in time resolved experiments with ps pulses occur [125, 129, 141, 142] at about one order of magnitude higher excitation densities than those observed for cw-excitation [103, 117, 121]. It can be argued that the parametric scattering as described in the previous section cannot account for a variety of nonlinear effects observed in microcavities. Indications of additional nonlinear processes are, for example, found in initial studies on parametric scattering, where the fast gain was followed by a slowly decaying tail (Fig. 4.5) [141, 143]. While the initial fast contribution can be identified as parametric polariton scattering, the origin of the incoherent (slow) contribution could not be resolved. A scattering process between two excitons with large $k_{||}$ involving the UPB was suggested (see arrows in Fig. 4.5 (b)) giving an intuitive explanation, but this demanded further investigation. As nonlinear processes are also observed in cw-experiments at much lower excitation densities this suggests that excitons trapped in potential fluctuations close to the free exciton energy might be responsible for the slowly decaying nonlinearities.

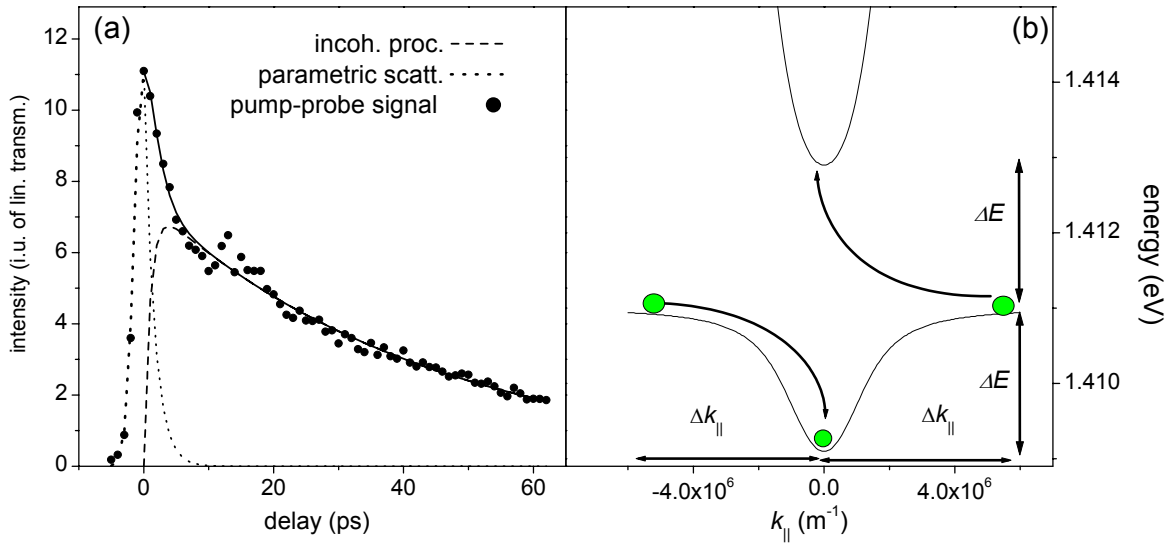

Figure 4.5: *Spectrally integrated nonlinear transmission as a function of delay ($\Delta = 0$), when the LPB is pumped in the parametric polariton scattering resonance. The solid dots represent data for co-circular pump-and-probe excitation. The solid line shows the fitted intensity and is calculated from the sum of parametric scattering (dotted line) and incoherent processes (dashed line). The postulated process for the incoherent gain is shown in the right panel, where the black arrows mark the proposed scattering channel (see Dasbach et al. [141, 143] for details).*

This problem will be tackled in the following by pump-and-probe spectroscopy. This technique allows for a time resolved study of dynamic processes. The idea of a pump-and-probe [144] experiment is straight forward. The setup used for this type of experiment is shown in Fig. 4.6. The specimen is excited by an intense pump pulse, which is typically resonant with the transitions under investigation. The state of the system is tested by a weak probe pulse. By stepwise adjusting the delay between pump and probe pulse the carrier dynamics can be monitored.

In our case ultra short laser pulses (pulse width $\approx$ 80 fs) are generated by a titanium-sapphire oscillator, which is inverted by an Ar^+-laser. The pulse is diffracted by an optical grating (1200 groves mm^{-1}). The zero order reflection remains spectrally broad ($\approx$ 30 meV) and is used as probe pulse. The first order diffraction pattern passes through a slit, where slit width and position determine the spectral components passing through. In this fashion grating and slit function as a pulse shaper, adjusting the spectral components and the temporal width of the pump pulse. The pump pulse was spectrally tailored for selective excitation of the LPB ($E_{exc} = E_L(k_{exc})$). It had a duration $\approx$ 1.6 ps and a spectral width $\approx$ 1.5 meV. The pump pulse is then directed onto a delay stage, which allows for precise adjustment of the temporal delay between the two pulses ($\tau = t_{probe} - t_{pulse}$). After passing through polarization optics both pulses are focused onto the same spot of the sample. The angle of incidence of both beams (θ_{exc}, θ_{probe}) could be adjusted independently, which means that we were able to select which states in momentum space were pumped and which states were probed.

The transmitted pump beam was blocked by a spatial filter, while the transmitted probe was focused onto the entrance slit of monochromator (focal length 30 cm). The spectral diffraction pattern is finally detected by a liquid nitrogen cooled charged coupled devices camera (CCD). This detection unit provides a spectral resolution of $\approx$ 100 μeV, while the time resolution is limited by the duration of the spectrally sharper pump pulse. The sample is placed in a helium cryostat, which allows for studies in the temperature range 2-300 K. If not explicitly stated, all experiments were performed at $T = 2$ K. When investigating optical nonlinearities by pump-and-probe experiments the following principle difficulty arises: An amplification of the transmission signal can either be due optical gain, or due to an increase of the sample transmission (decrease of absorption). For a clear separation of these phenomena, besides measurements in transmission geometry, the reflected nonlinear signal has been recorded. To minimize absorption in the GaAs substrate, the thickness of the substrate has been reduced in a polishing procedure.

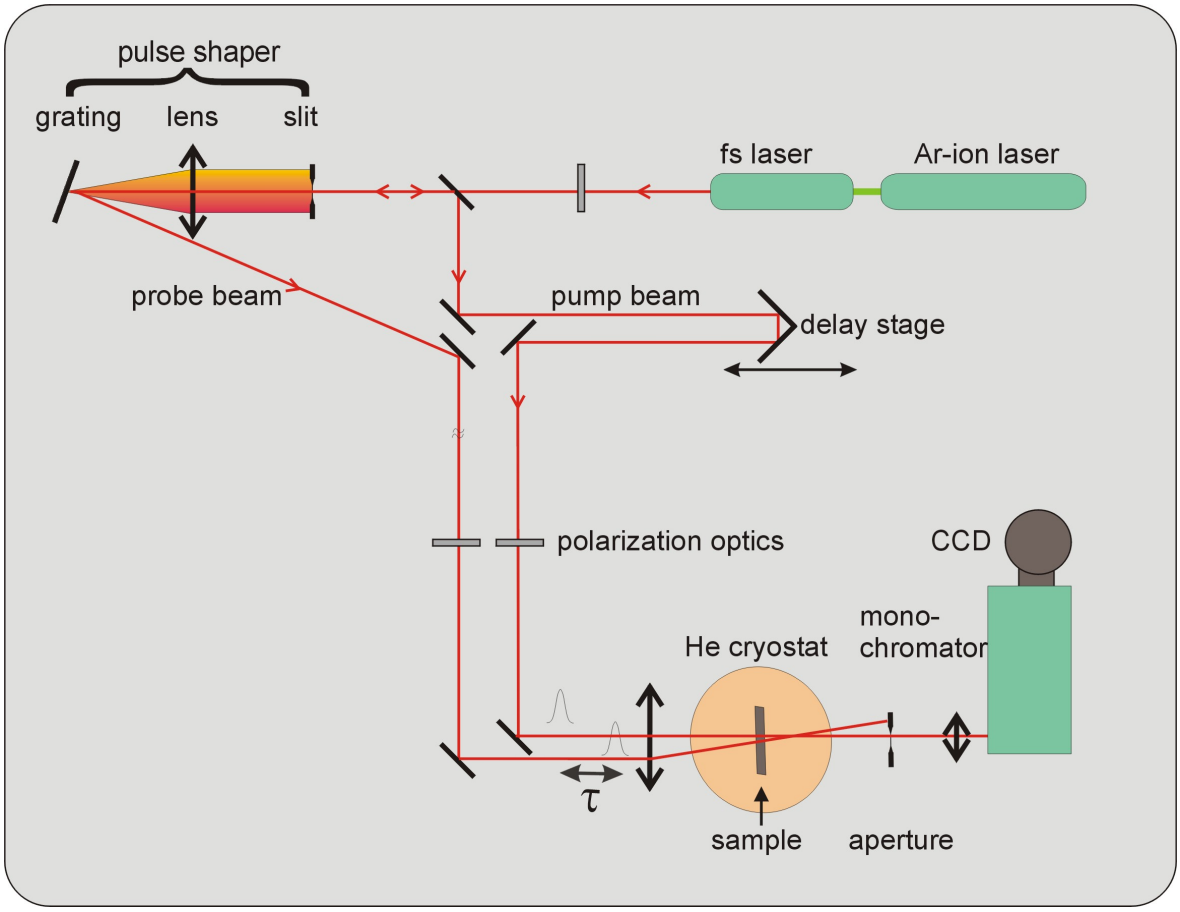

Figure 4.6: *Setup of the pump-and-probe experiment.*

From previous studies we know that, because of momentum conservation, the parametric polariton scattering shows a sharp angular resonance [125, 141]. To distinguish other nonlinearity from this process it is essential to study their angular dependence. While θ_{exc} was kept fixed, θ_{probe} was varied to scan $k_{||}$. The experimental conditions

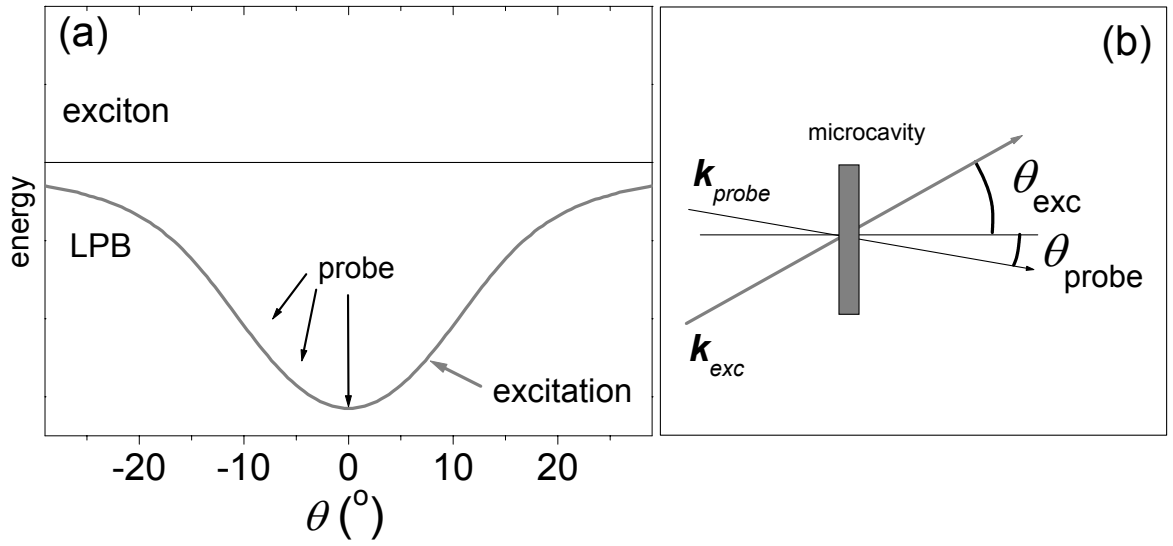

Figure 4.7: *Angular configuration of the pump and the probe beam. (a) The grey line gives the LPB dispersion at $\Delta = -3$ meV. Arrows mark the polariton states being pumped and probed. The black line marks the uncoupled exciton level. (b) Schematic of the pump-and-probe geometry.*

are depicted in Fig. 4.7, where the dispersion relations of the LPB and E_X are shown vs. θ. The probe angles ($\theta_{probe} = 0, -4°, -8°$) and the pump angle θ_{exc} are indicated by arrows. Fig. 4.7 (b) shows this configuration.

Fig. 4.8 (a) displays MC transmission spectra recorded for θ_{probe} under resonant excitation ($E_{exc} \sim 1.408$ eV) of the LPB under $\theta_{exc} = 8°$ for a series of τ and a cavity detuning of $\Delta = -3$ meV. Hence, the probe beam tests the $k_{||} = 0$ ground state of the polariton system. For this detuning a strong stimulated polariton pair scattering would be observed at $\theta_{exc} = 11°$. To suppress this scattering channel $\theta_{exc} = 8°$ was chosen (see Fig. 4.7). The probe signal is detected either for co-circular (both pulses have the same circular polarization) or anti-circular ($\sigma^{\pm}$ probe and $\sigma^{\mp}$ pump polarization) excitation conditions. Looking at the case of co-circular excitation we find pronounced nonlinear behavior, i.e. the transmission increases by a factor of 8 under the influence of the pump pulse. The nonlinearity is observed in the entire delay range recorded, here. The rise of the signal goes in line with a blue shift of the transmission line, where the shift ΔE_L is maximum for maximum transmission. It decreases as the transmission signal decays. In addition, the linewidth γ of the transmission resonance decreases as the signal increases. Looking at the same experiment for anti-circular polarization we find no superlinear behavior. Obviously, the underlying nonlinear process satisfies strict polarization selection rules.

The findings of Fig. 4.8 are summarized in Fig. 4.9. Panel (a) shows the changes in the spectrally integrated differential intensity of the LPB line $\delta T = \frac{\Delta T + T_0}{T_0}$, where T_0 is the probe transmission signal in the absence of the pump beam and ΔT denotes the nonlinear transmission signal. In Fig 4.9 δT, ΔE_L, and γ are shown for two intensities

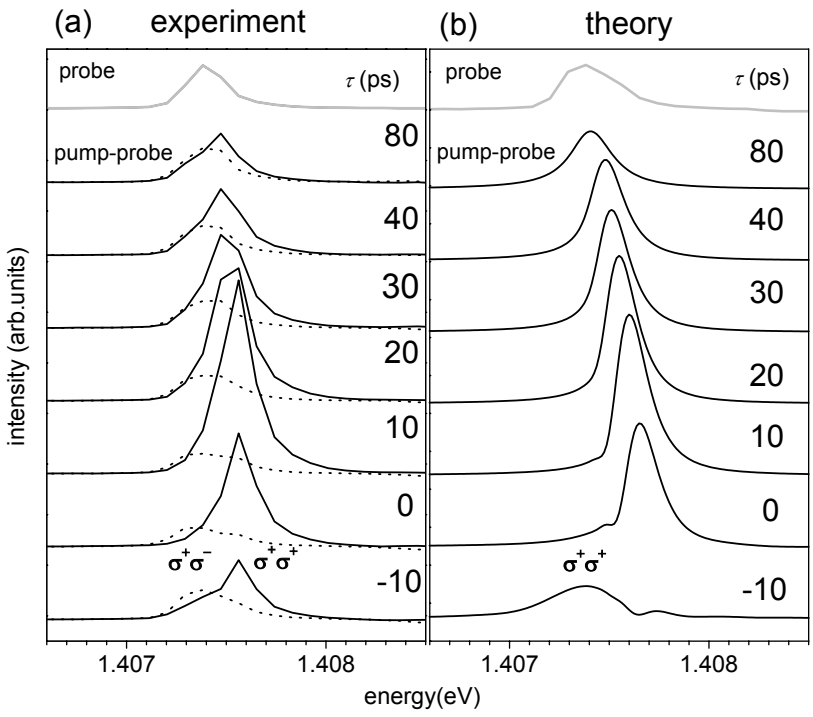

Figure 4.8: *(a) MC transmission spectra recorded at $\theta_{probe} = 0$ under resonant excitation at $\theta_{exc} = 8°$ for various τ. Solid (dotted) traces indicate co-circular (anti-circular) excitation. (b) Corresponding calculations for co-circular excitation. For reference the linear transmission (T_0) of the probe in the absence of the pump pulse is shown on top of each panel (grey trace).*

I_{exc}. In the low intensity regime δT rises quickly and decays nearly exponentially with a time constant $\tau_1^D \approx 60$ ps. Strong deviations from this behavior are observed at high I_{exc}: We find an enhancement of δT at $\tau \approx 10 - 30$ ps. ΔE_L and its time evolution are shown in panel (c). While the line does not shift for anti-circular excitation, we find blue-shifts of up to 0.15 meV for co-circular excitation, which is about the linewidth of the linear transmission (compare Fig. 4.8). Again, the shift increases with I_{exc} and decays on timescales comparable to the intensity decay. Finally, the changes in the linewidth are shown in panel (e). As already expected from Fig. 4.8 the nonlinear signal narrows significantly as compared to the linear probe transmission.

Besides the density dependence, the dependence on $k_{||}$ is of crucial importance. This is tested by scanning of $\theta_{probe} = 0, -4°, -8°$. In panel (a) of Fig. 4.10 we see that δT becomes larger, when we move along the dispersion of the LPB from the energy minimum ($\theta = 0$) towards higher energies ($\theta_{probe} = -4°$). Further up ($\theta_{probe} = -\theta_{exc} = -8°$) the signal decreases again. The line shift increases with θ_{probe} even at the highest angles recorded (see panel (c)), however we should keep in mind that the line also becomes broader for higher θ_{probe}, as the exciton fraction increases. The qualitatively similar behavior for all probe angles confirms that the effect observed here differs from parametric scattering, which would be restricted to an angular range of $< \pm 2°$ [125, 141]. Independently of the probe configuration and the pump intensity, the changes in δT, E_L and γ with τ are correlated, however, the maximum in δT is delayed as compared to the maximum in ΔE_L that occurs at $\tau = 0$.

Let us compare the changes of the LPB transmission under resonant excitation to those under above band gap excitation investigated by Jahnke *et al.* [145]. The latter also causes a blue-shift of the LPB but there are two decisive differences [145]:

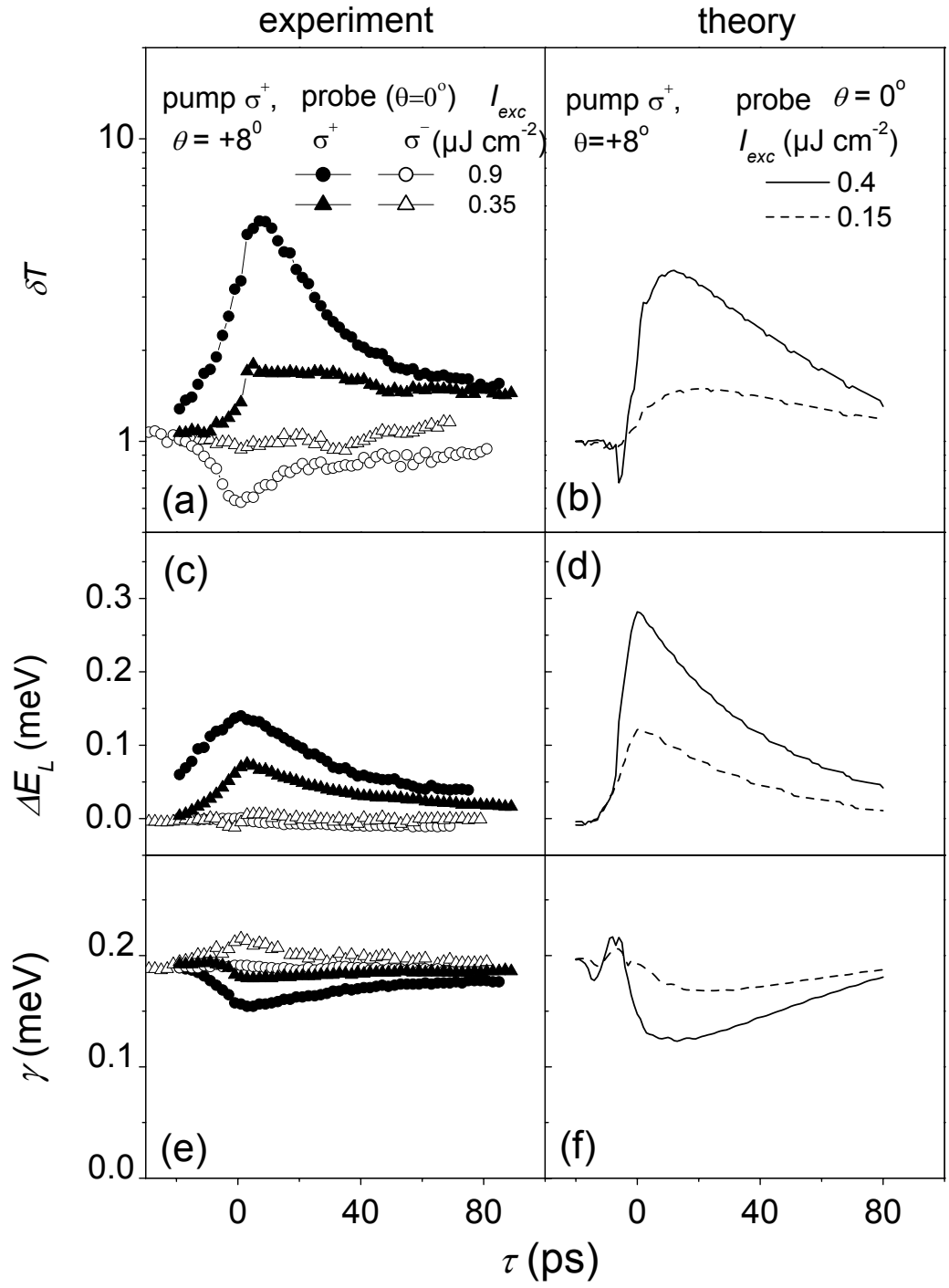

Figure 4.9: *Experimental (left panels) and calculated (right panels) dependencies of the δT (a) and (b), ΔE_L (c) and (d), and the linewidth γ (e) and (f) on τ for intensities $I_{exc} = 0.9 \mu J cm^{-2}$ (circles) and $I_{exc} = 0.35 \mu J cm^{-2}$ (triangles). Full (open) symbols indicate co-circular (anti-circular) excitation configurations. The theoretical traces are given for I_{exc}= 0.4 $\mu J\ cm^{-2}$ (solid traces) and I_{exc} =0.15 $\mu J\ cm^{-2}$ (dashed traces).*

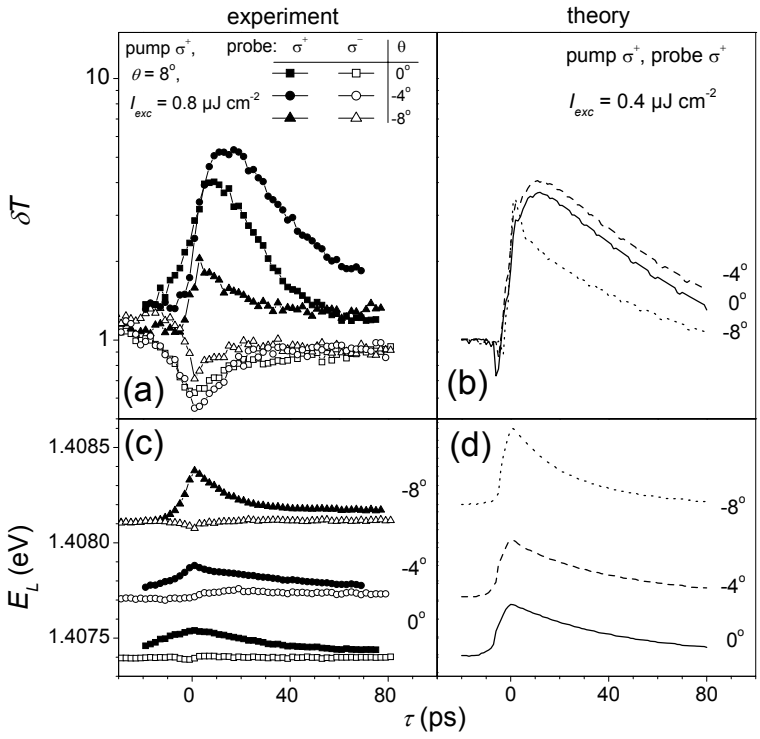

Figure 4.10: *Experimental (left panels) and calculated (right panels) dependencies of the differential transmission δT (a, b) and E_L (c, d) on the time delay for $\theta_{probe} = 0$ (squares, solid line), $\theta_{probe} = -4°$ (circles, dashed line) and $\theta_{probe} = -8°$ (triangles, dotted line). Full (open) symbols indicate co-circular (anti-circular) excitation configurations. Theory is given for co-circular excitation only.*

At moderate excitation densities the line shift is accompanied by (i) a reduced rather than an enhanced transmission and (ii) a strong broadening rather than a narrowing of the LPB line. These effects are caused by free carriers excited in the QW for above band gap excitation. The blue shift of E_L is connected to the reduction of the exciton oscillator strength by phase-space filling and screening by the carriers, whereas the decrease of the line intensity and its broadening are caused by additional absorption due to enhanced exciton scattering with carriers. Intensity enhancement and spectral narrowing appear only at very high excitation densities close to the transition from strong- to weak-coupling where the cavity approaches the lasing regime.

In contrast, in our experiments the excitation below E_X generates mainly excitons instead of free carriers. Therefore, the concentration of unbound carriers is too small to produce significant effects on the susceptibility. In turn, exciton-exciton interaction and filling of localized exciton states can become important in causing changes in the polariton properties. Indeed, unlike unbound carriers, filling of localized states leads to a reduced, rather than enhanced, absorption and therefore to an enhanced transmission and a reduced γ. The differences in the nonlinear optical response between co- and anti-circular pump-and-probe configurations can also be explained by this approach. The σ polarized pump light fills potential fluctuations with excitons of a given spin. Subsequent transitions of excitons with the same spin into the localized exciton states are forbidden by the Pauli exclusion principle. However, the Pauli exclusion principle does not forbid transitions into states of opposite circular polarization. Consequently, the excitation with σ^+ light leads to different changes in the susceptibility for σ^+ and σ^- polarized probe pulses, which is observed in the present experiment. Within this

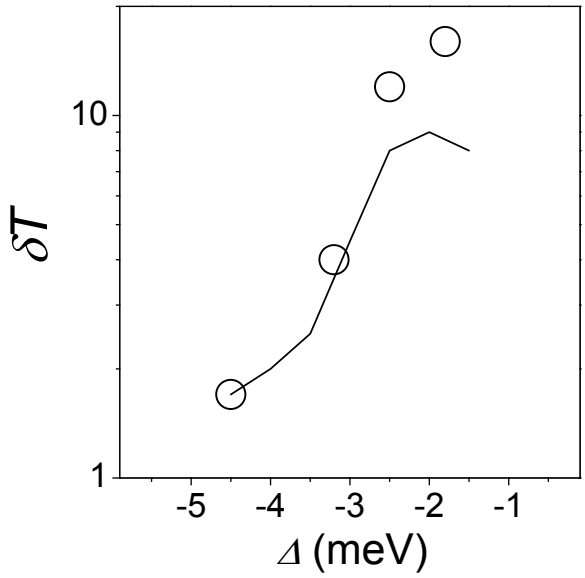

Figure 4.11: *Dependence of δT on the cavity detuning at fixed excitation intensity. Circles mark experimental data while the solid trace shows calculated values.*

approach, a strong dependence of δT on the cavity detuning is predicted, since the density of localized states D decreases quickly with increasing separation from the exciton level. This is investigated in Fig. 4.11. Indeed, we find that the maximum in δT decreases from 15 to 1.8 when Δ changes from -1.5 to -5 meV and the LPB becomes photon dominated. The strict polarization selection rules indicate, that the localized exciton states are indeed circularly polarized. The localization sites, however, are not expected to be perfectly circular in shape. Hence, one would expect elliptically polarized exciton eigenstates.

A theoretical model to describe the impact of exciton localization on the nonlinear optical response of a MC has been developed in cooperation with N. A. Gippius, V. D. Kulakovskii, and S. G. Tikhodeev. We can assume that δT is independent of I_{probe}. This means that the nonlinear effect solely arises from the temporal modulation of the exciton susceptibility by the pump pulse, while the weak, probe induced modulation does not cause nonlinear effects. This assumption is justified, as the probe pulse is more than one order of magnitude weaker than the pump pulse. First, we reconstruct the susceptibility χ of the unexcited QW in the spectral vicinity of E_X. This is done by measuring the linear absorption near E_X. It is determined by fluctuations in the QW potential which can be described within an approach for the optical interband density that considers the localization of the excitonic center of mass motion, as described by Schnabel *et al.* [146]. In this approximation, the QW susceptibility is given by

$$\chi(E) = \frac{\hbar^2 J_0^2}{E^2} \int \frac{dE_X \; D(E_X)}{E_X - E - \mathrm{i}\Gamma_X}, \tag{4.8}$$

with an interband density of states

$$D(E) = \frac{1}{\sqrt{\pi}\sigma\Lambda} \int_0^\infty dE_K e^{-(E_X^* + E_K - E)^2/\sigma^2} \cdot e^{-E_K/\Lambda}. \tag{4.9}$$

$J_0 = e v_{cv} \Phi_X(0) \int dz \psi_e(z_e) \psi_h(z_h)$ is the exciton current with v_{cv} the electron velocity. χ contains three energy parameters characterizing the exciton: σ is a measure of the

inhomogeneous broadening of the exciton, Λ characterizes the disorder induced exciton states with in-plane wave numbers larger than the light momentum, and Γ_X is the homogeneous exciton linewidth.

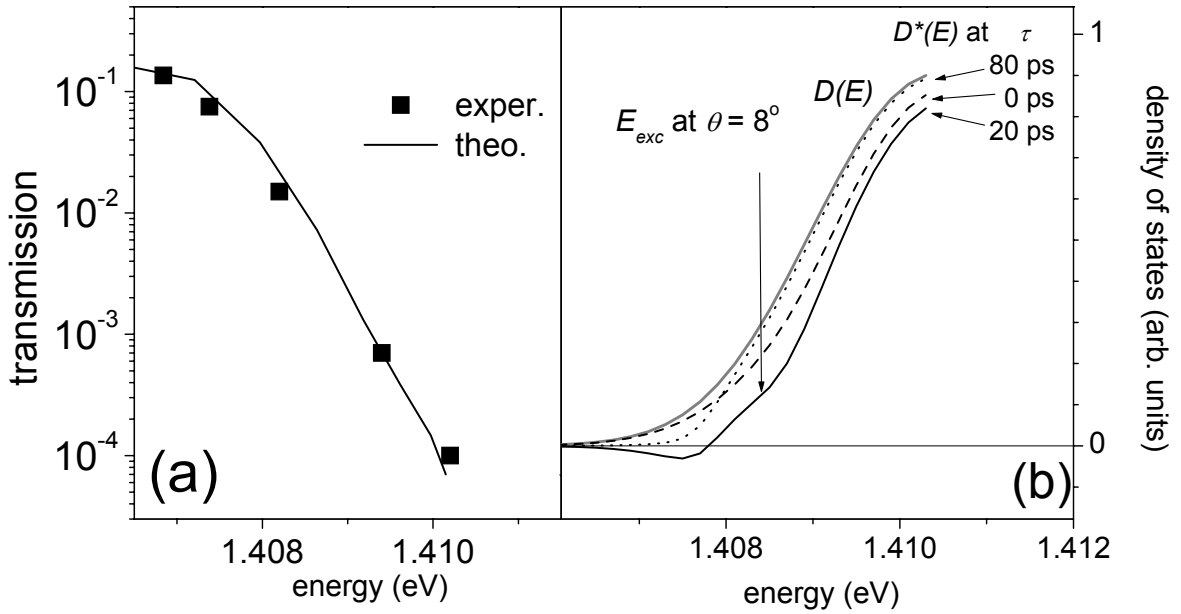

Figure 4.12: *(a) LPB transmission as a function of E_L for the unexcited QW. (b) Calculated effective density of states D^* for $\tau = 0$ (dashed trace), $\tau = 20$ ps (solid trace), and $\tau = 80$ ps (dotted trace) as a function of energy. The grey trace gives the density of states D without excitation.*

Fig. 4.12 (a) shows the MC transmission of the LPB mode versus energy. The symbols give the experimental data obtained from angle resolved transmission studies in the range $\theta_{probe} = 0 - 25°$. The data can be well described (solid line) using the parameters $\sigma = 1.5$ meV, $\Lambda = 3$ meV, and $\Gamma_X = 0.08$ meV, which are similar to those used by Schnabel *et al.* [146]. Pauli blocking results in a strict limitation of the number of excitons N_X^{sat} with the same spin that can be localized in a fluctuation with localization area A_{loc}. N_X^{sat} can be estimated by simply dividing the localization area by the area occupied by a single exciton: $N_X^{sat} = A_{loc}\pi^{-1}a_X^{-2}$. The mean number N_X of localized excitons found in the fluctuation is also proportional to A_{loc} due to the increase of the exciton-photon interaction with increasing exciton delocalization. In consequence, the fluctuation occupation N_X/N_X^{sat} is independent of A_{loc} and a function of the localized exciton energy and the excitation parameters, only.

Since excitons trapped in a localization site behave similarly to carriers confined in a quantum dot, we can treat them as a set of two level systems. The dynamics of an inhomogeneously broadened exciton ensemble embedded in a MC can thus be described by a density matrix formalism. We assume that all direct interactions between the localized states can be treated in the relaxation approximation, i.e. the trapped carriers interact only with the photon field at the QW. The Hamiltonian of the i-th localized

state is given by

$$H^i = \begin{pmatrix} 0 & (V^i)^* \\ V^i & E_X^i \end{pmatrix}, \tag{4.10}$$

where $V^i = \mathtt{i}\frac{ev_{cv}\Phi_X(0)}{\omega_{cv}}\sqrt{A_{loc}^i}\mathcal{E}(\mathbf{r}_{X,i},t)$, ω_{cv} is the exciton transition frequency, E_X^i is the energy of the state with coordinate $\mathbf{r}_{X,i}$. $\mathcal{E}(\mathbf{r},t) = \mathcal{E}_\mathbf{k}(t)e^{\mathtt{i}(\mathbf{kr}-\omega_0 t)}$ is the electric field in rotating wave approximation [144].

The dynamics of the system is determined by the following set of equations:

$$-\mathtt{i}\hbar\,\dot{\tilde{\rho}}^i = [\tilde{\rho}^i, H^i], \tag{4.11}$$

$$(\mathtt{i}\hbar\partial_t - E_{P,\mathbf{k}})\mathcal{E}_\mathbf{k}(t) = \alpha_\mathbf{k}J_\mathbf{k}(t) + \beta_\mathbf{k}\mathcal{E}_\mathbf{k}^{exc}(t), \tag{4.12}$$

$$J_\mathbf{k}(t) = \sum_{E_X} ev_{cv}\Phi_X(0)\sqrt{A_{loc}}\;\tilde{\rho}_{2,1}^{E_X}(t)\tilde{N}(E_X). \tag{4.13}$$

In Eq. 4.11 $\tilde{\rho}^i$ is the density matrix of the localized exciton state. Eq. 4.12 gives the evolution of the electric field in the cavity at energy $E_{P,\mathbf{k}}$. $J_\mathbf{k}(t)$ is the exciton interband current and $\mathcal{E}_\mathbf{k}^{exc}(t)$ is the field of the incident light pulse. The coefficients $\alpha_\mathbf{k}$ and $\beta_\mathbf{k}$ were calculated using the transfer matrix formalism. Eq. 4.13 finally connects the exciton current $J_k(t)$ to the density matrices $\tilde{\rho}^{E_X}$ and the localized exciton distribution $\tilde{N}(E_X)$.

The calculations for our MC with Δ = -2.7 meV are shown in Fig. 4.8 (b) for the $\sigma^+\sigma^+$ configuration. Two adjustable parameters have been used in the calculations, the exciton radiative lifetime τ_X^D =40 ps and a density dependent relaxation time τ_r^D of the excitons. At low excitation intensity we find $\tau_r^D(I_{exc} = 0.05\ \mu\ \mathrm{J\ cm^{-2}})$ = 20 ps, it decreases to $\tau_r(I_{exc} = 0.5\ \mu\ \mathrm{J\ cm^{-2}})$ = 2 ps due to enhanced exciton-exciton scattering. Spin relaxation is neglected as the signal observed in anti-circular polarization is negligible. For the high excitation regime we are dealing with a density of photoexcited excitons in the order of $\approx 2\cdot 10^{10}$ cm^{-2}. The comparison of the calculated spectra with the experimental ones in Fig. 4.8 shows that they exhibit qualitatively the same behavior, namely the transmission increases, its blue shift, and its narrowing.

The right panels in Figs. 4.9 and 4.10 show the results of calculations at various I_{exc} and θ_{probe}, respectively. In particular, the two main results of the experiments are well reproduced: (i) At high excitation, maximum transmission occurs at delays of about 10 ps. (ii) At long delays, δT decays with a time constant of $\sim$ 60 ps. ΔE_L is relatively small and does not exceed 0.3 meV as compared to a Rabi splitting of 3.8 meV, which means that the cavity remains in the strong coupling regime. The line shift is determined by the changes in the refractive index that result from the difference in the localized exciton occupations above and below the observation energy. The strong (more than exponential) decrease of the density of states of localized excitons with decreasing energy prevents a strong change of this occupation. This explains that the maximum line shift occurs at $\tau \approx 0$. The reduction of ΔE_L with τ results mainly from changes in the refractive index due to recombination of localized excitons.

The changes in δT are very sensitive to filling of localized states at the probe energy and hence are strongly influenced by energy relaxation of excitons. In particular, relaxation explains the strong increase of δT at small $\tau > 0$ for $\theta = 0$ and $-4°$, for which the probe energy is smaller than E_{exc}. For θ_{probe} = -8 ° the probed state is as high in energy as the pumped stated ($E_{L,exc} = E_{L,probe}$). Therefore the probe state is not accessible in a simple relaxation process. This explains why δT drops for higher θ_{probe}.

The calculations show that the large amplification coefficients observed at $\theta = 0$ and $-4°$ are only possible for an inversion of the localized exciton population ($\frac{N_X}{N_X^{sat}} > \frac{1}{2}$) [147]. This is shown in Fig. 4.12 (b) illustrating the saturation effects on the density of vacant states $D^*(E) = D(E)(1-2\frac{N_X}{N_X^{sat}})$ due to Pauli blocking. The grey solid line gives $D^*(E)(= D(E))$ for the unexcited cavity. For short delays and high excitation density, $D^*(E)$ decreases strongly around the excitation energy E_{exc} and even becomes negative indicating that the filling of localized states due to energy relaxation of photoexcited excitons exceeds $\frac{1}{2}$. Here the system demonstrates a negative absorption coefficient, i.e. light amplification, and approaches the lasing threshold. This leads to the strong narrowing of γ and the increase of δT. For long delays, exciton recombination results in a recovery of the density of states of the unexcited QW $D^*(E) \approx D(E)$. As expected, the maximum δT calculated at fixed excitation intensity decreases strongly (about 5 times) with changing Δ from -2 to -5 meV (solid trace in Fig. 4.11). This decrease is connected to a lower density of localized states and is in qualitative agreement with the data. The amplification of the transmission signal is limited by two factors:

- the energy relaxation rate of excitons,
- the enhanced exciton broadening at high exciton densities resulting in enhanced losses in the low energy tail of the exciton line.

This explains the observed saturation of δT at high I_{exc} (Fig. 4.9). When the exciton source is exhausted, the differential transmission decreases quickly to the level characteristic for a site occupation of $\frac{1}{2}$. Then it decays on a time scale of $\approx$ 60 ps, which is comparable to the localized exciton lifetime.

Hence, bleaching of the exciton absorption due to occupation of localized exciton states can explain the slowly decaying nonlinearity observed earlier [141]. This process is simply caused by a decrease in the QW absorption. This has to be distinguished from optical gain. In such a process, like for example in parametric polariton scattering into the $k_{||} = 0$ state, the population of this state is increased. This leads to a rise in the emission from this state, which should be observable in the differential transmission [141], as well as in the differential reflection [125]. In contrast, the spectral hole burning as described above gives rise to a positive signal in the differential transmission, while causing a negative signal in the differential reflection.

The separation of both processes becomes feasible, when comparing the transmission signal to the reflection signal, as will be demonstrated in the following. For these

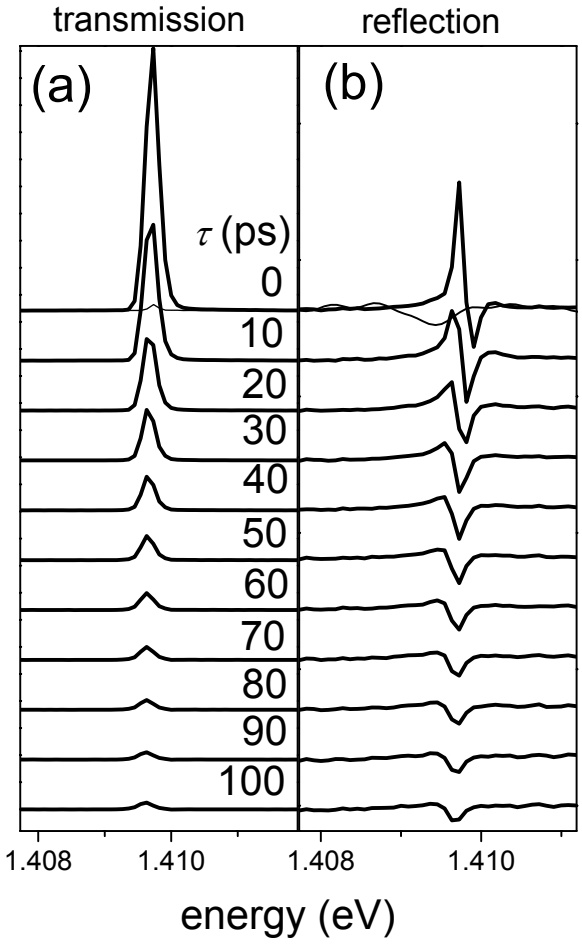

Figure 4.13: *(a) Spectrally resolved differential transmission at $\Delta = 0$ for the indicated τ's ($\theta_{exc} = 8°$, co-circular excitation). Panel (b) shows the same for the differential reflection. The thin curves at $\tau = 0$ give the linear transmission (reflection) of the LPB.*

experiments a detuning close to zero was chosen. Under these conditions the 'magic angle' for parametric polariton scattering agrees with the excitation angle used in the present experiment ($\theta_{exc} = 8°$). In two consecutive measurements under identical excitation conditions first the transmitted signal and then the reflected signal have been recorded as a function of τ. The left panel of Fig. 4.13 shows the time evolution of the transmission starting from $\tau = 0$ in steps of 10 ps to $\tau = 100$ ps. The $\tau = 0$ trace gives the transmission signal under pump excitation and when the pump is switched off (thin trace). We find that the signal increases by a factor of 60 under influence of the pump excitation. As compared to the situation where θ_{exc} is detuned from the 'magic angle', the nonlinear signal increases by about one order of magnitude. This is attributed to additional parametric polariton scattering, which is no longer suppressed. As expected this signal decays quickly, while the signal at long delays is dominated by the spectral hole burning described above. The right hand side shows the corresponding signal recorded in reflection geometry.

Looking at the data, we find the superposition of both phenomena: At zero delay we observe a strong positive signal on the low energy side and a pronounced dip on the high energy side. Comparing the magnitude of the nonlinear signal to that of the linear signal shows that the positive signal exceeds the linear signal by a factor of 15,

while the dip is about 6 times deeper than observed in the linear regime. At zero delay gain and bleaching partly compensate each other. While the positive signal arising from parametric scattering decays rather quickly, the dip in the differential reflection remains observable in the entire delay range recorded, here. At $\tau = 100$ ps the relative magnitude of the signals in reflection and transmission geometry are comparable. The comparison of both signals and their time evolution shows that we are dealing with a superposition of two processes. One of them takes place only in the short delay regime. It shows positive signals in both geometries, which means that we are facing a gain process where the polariton population at $k_{||} = 0$ is increased. This process is identified as parametric polariton scattering. In addition, a second process is resolved where we find positive signal in transmission and negative signal in reflection. This observation gives further evidence of the interpretation of the slow process in terms of filling of localized excitonic states, giving rise to a reduced absorption.

4.3 Exchange interaction in strained cavities

In the previous section we demonstrated that describing excitons and polaritons only by their energy and momentum is insufficient. It is essential to also include the spin of the particle to obtain a reasonable description of the system. The spin properties of carriers in semiconductors attract considerable attention, in particular because of their long decoherence times [148, 149, 150] as compared to the charge degrees of freedom. Exciton spins are coupled by exchange interaction. This interaction acts on the angular momenta electron and hole and leads to an energy splitting between the different spin configurations (see section 3.4). The resulting fine structure multiplet has been studied intensively during the past years [151, 152, 85], mainly in quantum dots [153, 154, 155]. Very little attention has been paid to the fine structure of cavity polaritons. Only recently, efforts have been undertaken to understand the spin of cavity polaritons [156, 157, 158]. The spin shows a rich phenomenology and its understanding is far from complete. The rewarding perspective of a highly spin polarized quantum system, where exchange couples the spins demands further investigation. In contrast to section 3.4, here we will concentrate on conventional wavevector independent exchange. As wavevector dependent contributions are expected to be on the order of few μeV, they are not resolvable in the present experiment.

For this study, we apply uniaxial strain in the cavity plane (x, y-plane), to lower the symmetry of the QW. In turn the exciton eigenstates are no longer circularly polarized. This gives rise to an exchange splitting of the exciton spin configurations, as we will see below. To apply uniaxial strain, two approaches have been followed:

- A planar MC was placed in a brass holder. Due to the difference in the coefficients of thermal expansion, stress is applied to the cavity when the temperature is lowered from room temperature to 2 K. The design of the holder is such that the cavity is free to expand in one lateral direction, while the force is applied normal

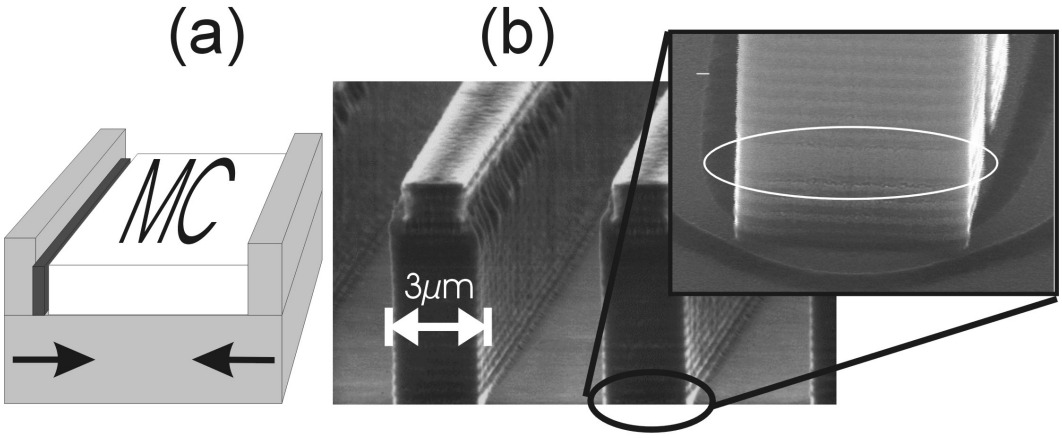

Figure 4.14: (a) *Schematic picture of a planar microcavity in a brass holder. Cooling causes uniaxial strain, as indicated by the arrows. (b) SEM-micrograph of wire shaped cavities. The arrow marks the width of the wire. The inset shows the resonator layer with the neighboring layers of the Bragg mirror. The resonator and the top mirror are etched, while the bottom mirror remains mostly unpatterned.*

to this direction. Between the edge of the cavity sample and the brass holder a thin layer of indium protects the sample from damage (Fig. 4.14 (a)) [159].

- From planar cavities, wire structures with a lateral width of $L_y = 3$ μm have been fabricated by lithography and etching. Fig. 4.14 (b) shows a SEM-micrograph of the structure. The sample is etched through the top mirror and the cavity itself whereas the bottom mirror remains mostly unpatterned (see magnified section of Fig. 4.14 (b)) [160].

Because of the lateral photon confinement in the wire structure, the cavity mode fans out into a series of subbranches. The subbranches correspond to optical modes that are discretized normal to the wire direction and are characterized by an index $i_y = 0, 1, 2 \ldots$, which gives the number of nodes in the electric field distribution across the wire [161]. In the strong coupling regime each of these photon modes i forms polaritons with the QW exciton. For the coupled modes the usual polaritonic dispersion is observed along the wire (see Fig. 4.29) [162]. The details of this modification of the mode spectrum will be treated in section 4.4. In the following we will only focus on the lowest polariton mode that is formed by the photonic $i_y = 0$ mode and the heavy hole exciton. The same Rabi splitting is observed for those resonators ($\hbar\Omega_R = 3.8$ meV) as in a planar cavity.

Again, pump-and-probe experiments with the setup as described in section 4.2 were performed in transmission geometry. To achieve a spectral resolution of ≈ 30 μeV we used a monochromator with a focal length of 0.6 m. For both sample types a detuning of $\Delta =$ -3.5 meV was chosen. For clarity the spectral positions of the various resonances are sketched in Fig. 4.15 (a). The shaded Gaussian curve gives the spectral shape of the pump pulse, while the solid line indicates a section of the spectrally broad probe

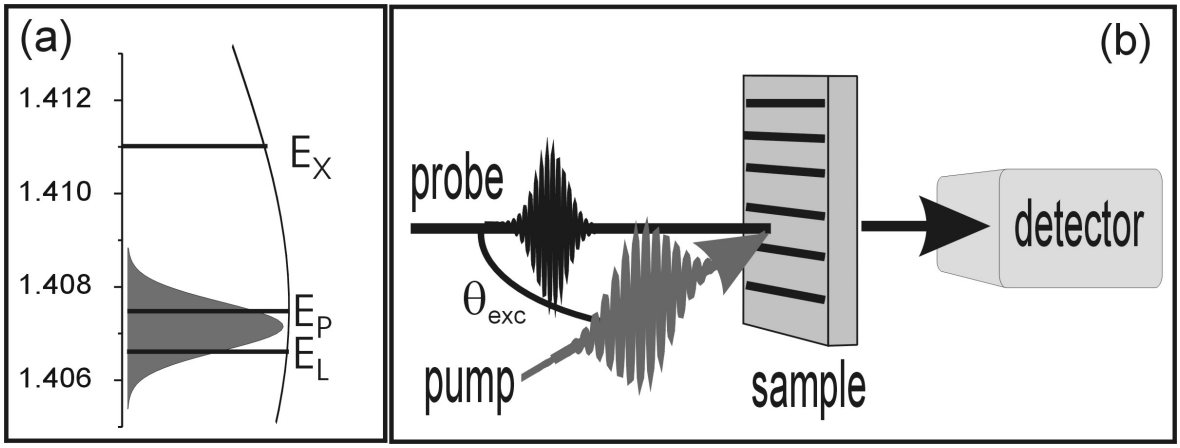

Figure 4.15: *(a) Energy level scheme: E_L marks the spectral position of the bottom of the lowest polariton mode. In addition, the uncoupled resonances of the heavy hole exciton (E_X) and the $i_y = 0$ cavity mode (E_P) are shown. The spectral shape of the pump pulse is given by the shaded Gaussian. The solid curve shows a spectral section of the probe pulse. (b) Schematics of pump-and-probe configuration. The dark lines give the orientation of the wires. The probe beam is directed normal to the sample surface. The pump beam is tilted by $\theta_{exc} = 8°$ in the plane defined by the sample normal and the wires.*

pulse. Both beams were focused onto the same spot of the sample, having a diameter of ≈ 100 μm. While the probe beam was directed normal to the surface (probing the polariton population at $k_{||} = 0$), the pump beam hits the sample under an angle of 8°.[2] The pump pulse was centered at an energy slightly above the bottom of the LPB, to be resonant with the polariton mode at the chosen θ_{exc} ($E_{exc} = E_L(\theta_{exc})$).

First, we present the experimental data, before we develop an explanation for the observed phenomena. Fig. 4.16 (a) gives the transmission of the planar cavity. In the linear transmission spectrum of the probe beam (no pump excitation) we observe the LPB in the shown energy range (solid grey trace). The dashed (dotted) line gives the pump-and-probe transmission signal at $\tau = 3$ ps for excitation with co-circularly (anti-circularly) polarized pulse trains at a pump power of $P_{exc} = 10$ mW. In the co-circular configuration we find a pronounced rise of δT caused by Pauli blocking. Since Pauli blocking does not occur for pulses of opposite circular polarizations, thus leaving the transmission unchanged (dotted trace) [163]. At very short delays there are also contributions from residual parametric wave mixing, which is restricted to co-circular excitation as well (see the spikes at $\tau = 0$ in Fig. 4.17) [125, 126, 129, 141].

This selectivity with respect to the relative pulse polarizations vanishes when corresponding experiments are performed on stressed resonators (Fig. 4.16 (b) and (c)). For the planar cavity stressed in the brass holder an increase of the probe transmis-

[2]We note that for the present exciton-photon detuning the magic angle for parametric polariton scattering [125] would be 11°. Therefore this scattering process is strongly suppressed (see the previous chapter).

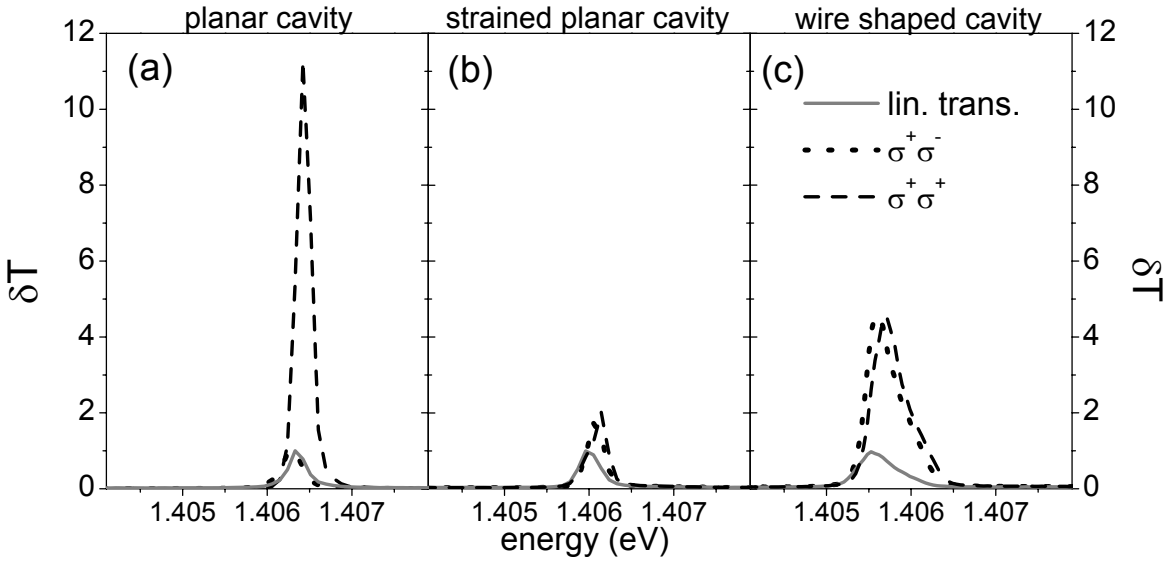

Figure 4.16: *MC transmission spectra for various pump-and-probe polarizations. The grey solid traces mark the linear transmission (no pump). The dotted (dashed) lines correspond to the anti-circular (co-circular) pump-and-probe signal. Panel (a) shows the data for the unstrained planar MC, (b) that for the strained planar resonators, and (c) that for wire shaped cavities with a width of 3μm.*

sion still occurs for co-circular excitation, but now it is also observed for anti-circular excitation. The magnitude of the amplification stays well below the values observed in the unperturbed cavity. However, finding comparable intensities for co- as well as anti-circular excitation demonstrates that the cavity modes are no longer circularly polarized. The same applies for the wire shaped resonators. Here the sum of both signals reaches the value observed in the 2D-cavity. Obviously, the lateral patterning also has destroyed the in-plane symmetry, breaking the polarization selection rules. As the principle behavior is the same for strain applied via external force or via patterning of the cavity structure, we will concentrate on results obtained on the patterned sample, where it is experimentally easier to keep the stress at a constant level.

Next we investigate the time evolution of δT. The left panel of Fig. 4.17 shows the spectrally integrated pump-and-probe signal obtained for the wire shaped microcavities for different P_{exc}. At low $P_{exc} = 5$ mW, after its rise the time evolution of the signal can be described by an exponential decay for both polarizations. When increasing P_{exc} we find pronounced oscillations superimposed on the signal which are in anti-phase for the two configurations: The $\sigma^+\sigma^-$ signal reaches a maximum when the $\sigma^+\sigma^+$ signal is at its minimum and vice versa.

The oscillations are observed also in the spectral domain and become even more evident there. Fig. 4.17 (b) shows the spectral position of the pump-and-probe signal at $P_{exc} = 15$ mW. At $\tau = 0$ the signal is blue-shifted with respect to the initial energy of the LPB. With increasing τ the peak position relaxes back. However, the shift is

not monotonous but it shows oscillations which are phase-shifted by π for the $\sigma^+\sigma^+$ and $\sigma^+\sigma^-$ configuration. The beat period is identical to that observed in the intensity domain. The solid line in Fig. 4.17 (b) is calculated by averaging the line positions for both polarizations. No oscillation can be found in this case, but the line shifts back smoothly, as is the case for a planar cavity [163].

We have performed a detailed polarization analysis of the pump-and-probe signal, for which we placed a linear polarizer between the sample and the detector and excited in $\sigma^+\sigma^+$-configuration (Fig. 4.18). We find an energy splitting between the polarization states along and perpendicular to the wire axis and even more convincing is the fact that no beating occurs. The line polarized perpendicular to the wire axis is lowered in energy with respect to that polarized along the wires. When rotating the polarization plane to be tilted by 45° with respect to the wire axis we observe beatings again. This demonstrates that the oscillation results from a coherent superposition of polariton spin states, which are polarized along and perpendicular to the wire. The emission of the two linearly polarized states is slightly different in energy. We excite a coherent superposition of these states, either with linear polarization, where the polarization axis is not along one of the eigenpolarizations or with circular polarization. The superposition of the emission from both states can now interfere, where the interference

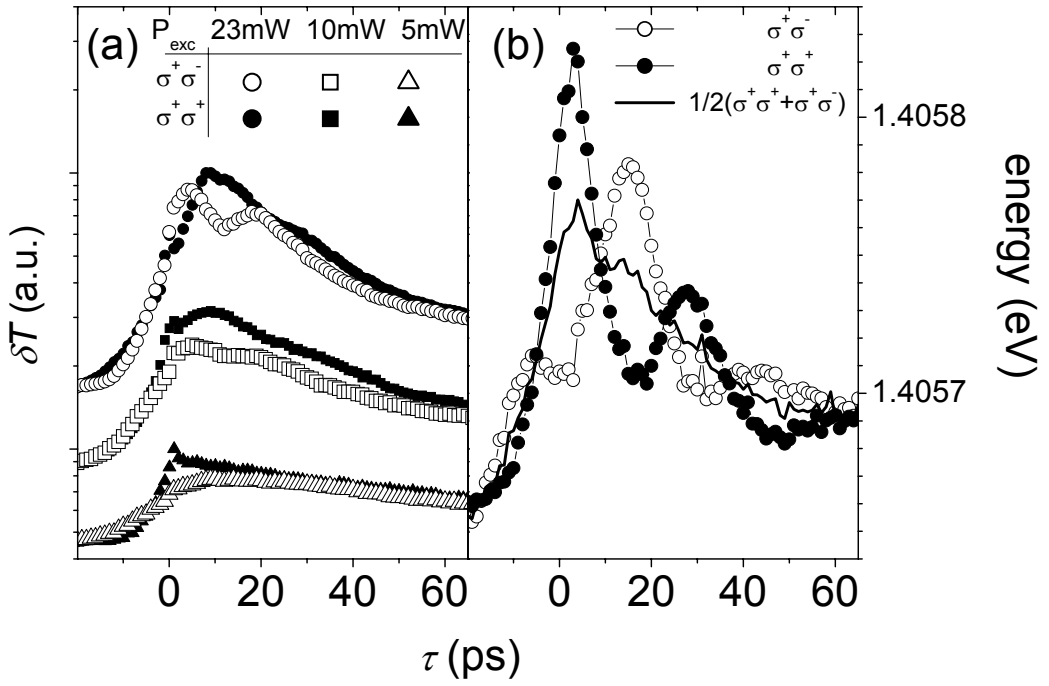

Figure 4.17: *(a) Spectrally integrated pump-and-probe signal (logarithmic scale) as a function of delay for three different pump powers (for clarity the corresponding spectra are shifted vertically). (b) Spectral position of δT as a function of τ for P_{exc} = 15 mW. Open (solid) symbols mark anti-circular (co-circular) excitation conditions. The solid line was calculated by averaging the line positions for the two polarization configurations.*

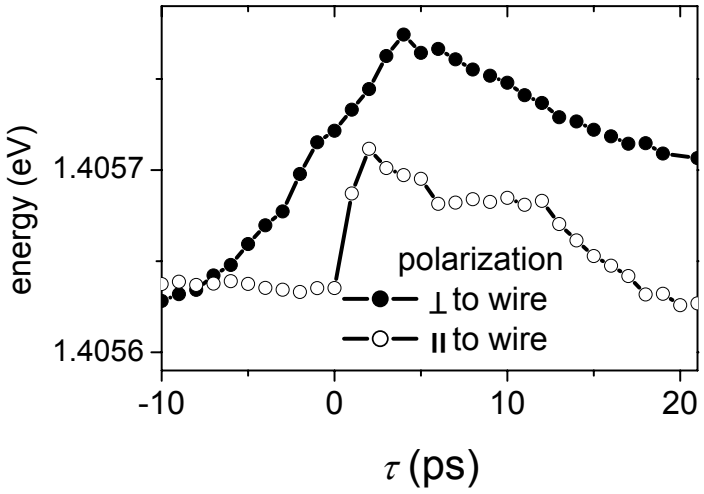

Figure 4.18: *Spectral position of δT as a function of τ for P_{exc} = 15 mW. A linear polarizer is placed between sample and detector. For open (solid) symbols the linear polarization is parallel (perpendicular) to the wire axis.*

period T_{osci} directly gives the energy difference

$$\frac{h}{T_{osci}} = \Delta E = E_{\perp} - E_{||}. \tag{4.14}$$

As this is a coherent phenomenon, the damping of the beat amplitude gives the decoherence time of the spin system [164, 144]. We have demonstrated that the linearly polarized eigenstates replace the circularly polarized ones of the conventional planar cavity. In principle, this might originate from either the photonic or the excitonic contribution, a question to be discussed below.

Fig. 4.19 shows the energies of the transmission resonance after subtracting the averaged line shift (compare solid trace in Fig. 4.17 (b)) for increasing P_{exc}. At low P_{exc} the polarization splitting can be described by an exponential decay. No oscillation is observed, here. With increasing P_{exc} oscillations become observable and more pronounced. Looking at the first half period we find $T_{osci} \approx 29$ ps.

After having presented the experimental data we now turn to the discussion of the results. The oscillations in δT and E_L at high pump densities and their polarization selection rules suggest that the beats originate from a spin precession of the polariton population at $k_{||} \approx 0$. As derived from the beat period, we expect a splitting ΔE = 130 μeV = $\frac{h}{T_{osci}}$. Taking into account the large linewidth, the latter is in reasonable agreement with the splitting of 100 μeV found in the spectral domain.

Let us first clarify the origin of the polariton splitting: At first sight, one might consider the optical mode splitting observed earlier in wire shaped resonators. Each mode i_y splits into two components which are polarized either along (TE) or normal (TM) to the wires. Calculations show that in 3 μm wide wires the TE mode is the one of lower energy, lying about 50 μeV below the TM mode [161]. However, this splitting can be excluded, since the order in energy observed in the experiment for the two linearly polarized states is opposite to that expected for the TE and TM modes: The state with polarization parallel to the wire is located at higher energies in our studies. The same applies to the TE-TM splitting in a planar cavity where a splitting

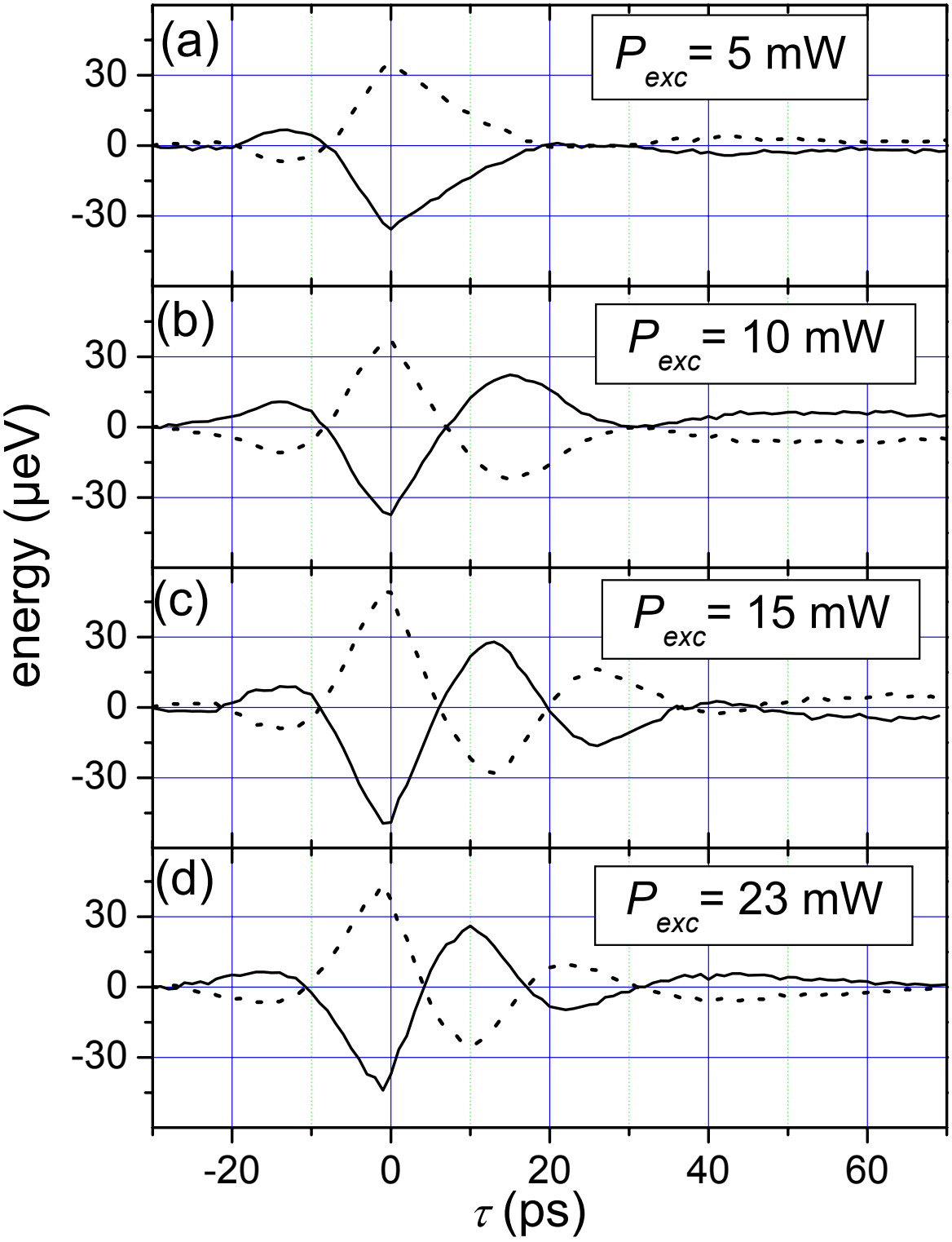

Figure 4.19: *Evolution of the line shift as a function of τ, where the averaged line position has been subtracted from the data. The dotted (solid) line marks co-circular (anti-circular) excitation conditions. From top to bottom P_{exc} has been increased from 5 mW to 23 mW.*

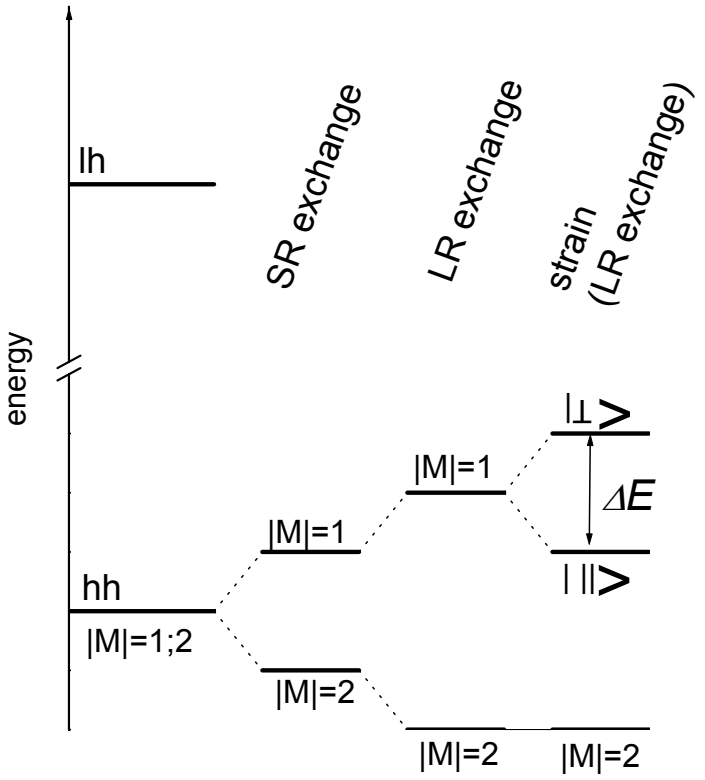

Figure 4.20: *Schematic of the exciton energy levels. Here we assume pure heavy hole and light hole character. SR and LR exchange split the bright from the dark excitons. Leaving the bright doublet degenerate. When reducing the symmetry of the QW, LR exchange splits the bright exciton doublet into two linearly polarized states.*

of the TE and TM modes occurs, due to the different boundary conditions at the Bragg mirror interface. Here the spectral position of the TE mode is also lower than that of the TM mode. Furthermore, this splitting is negligible for the small angles used in the present studies [165]. Finally, it should also be observable in an unstrained cavity and not only in a cavity under strain. Thus we conclude that the observed splitting does not originate from the photon contribution, but rather arises from a splitting of the exciton fraction of the polariton.

Since the splitting is not observed in an unstrained planar MC it has to be caused by uniaxial strain either arising from patterning or the externally applied force. Because of the lattice mismatch between GaAs and $In_{0.14}Ga_{0.86}As$ the QW is strained. The stress however is uniform in the quantum well plane. In the wire structures the translational invariance is broken by the patterning. The strain can relax perpendicular to the wire axis. This uniaxial strain release leads to a reduction of the QW symmetry. The energy of the two bright, quasi-two-dimensional heavy hole excitons can be described as [152, 166]

$$E_1 = \frac{c_z}{2} - \frac{1}{2}(c_x + c_y) \qquad E_2 = \frac{c_z}{2} + \frac{1}{2}(c_x + c_y), \tag{4.15}$$

where c_x, c_y and c_z are the electron-hole exchange parameters. The unstrained ideal QW has symmetry D_{2d} and a fourfold rotation-reflection axis. In this symmetry we find $c_x = -c_y$, which leaves the excitons degenerate. When uniaxial strain is applied to the quantum well we lower the symmetry to $C_{2,v}$ with $c_x \neq -c_y$ lifting the degeneracy of the excitons due to exchange [151, 85, 166].

In quantum structures, particularly in those under strain, heavy hole-light hole mixing often is considered to be negligible due to the large energy splitting between those states (see chapter 4). Pure heavy hole character is attributed to the ground state exciton. The states in this exciton manifold are characterized by the angular momentum projection $M = J_{h,z} + J_{e,z}$ along the heterostructure growth direction z. The long range exchange contributes to a splitting between the bright excitons with $|M| = 1$ and dark excitons with $|M| = 2$ (see Fig. 4.20). In addition, when the symmetry of the system is reduced, it leads to a further splitting of the bright exciton into the states $|\perp\rangle$ and $|||\rangle$, whereas it does not affect the dark states. The short-ranged part, on the other hand, contributes as well to the splitting of bright and dark excitons. It does not affect the bright exciton doublet, except for effects of higher order which typically are small. This is summarized in Fig. 4.20. If, however, mixing with the light hole is not negligible, the short range interaction will contribute to the bright exciton splitting when the symmetry of the system is reduced [85].

Summarizing the effects of electron-hole exchange interaction, it will cause a hybridization of the excitons with angular momentum $|M| = 1$ in low symmetry systems. The resulting states $|\perp, ||\rangle = \frac{1}{\sqrt{2}}(|+1\rangle \pm |-1\rangle)$ are split by an energy ΔE. They can be excited independently by light with linear polarization either along or normal to the direction of uniaxial strain with the state polarized perpendicular to the wire being higher in energy [152], in agreement with the present experiments. For spectrally broad excitation with circular polarization (or linear polarization that does not point along or perpendicular to the wire) coherent superpositions of these linear combinations are excited. These superpositions are described by $|\perp\rangle \pm \mathrm{i}|||\rangle$ in the cases of $\sigma^{\pm}$ excitation and $|\perp\rangle \pm |||\rangle$ for excitation with light linearly polarized at $\pm 45°$ with respect to the strain (wire) axis. The splitting ΔE leads to a spin precession. Changing the circular polarization gives rise to a π phase shift, which explains why the signals for co- and anti-circular excitation are exactly out of phase.

The long decay time of the beats supports their assignment to different spin configurations, for which the dephasing time is significantly longer than for charge excitations [148, 149, 150]. Previous studies have shown that carrier dephasing due to polariton-polariton scattering is almost an order of magnitude faster than the decay of the beats observed here [167, 120]. Moreover, increasing P_{exc} leads to strongly accelerated dephasing in the polariton system, just opposite to the effect described above.

After having discussed the origin of the splitting, we turn our attention to the power dependence of the beating behavior as seen in Fig. 4.19. The probe beam tests the population in (i) the $k_{||} = 0$ state of the LPB and (ii) in the exciton localization sites. Let us first discuss the behavior at low pump densities. Here δT rises is due to Pauli blocking [163]. The localized electron-hole pairs are either created directly by the pump pulse or originate from polaritons, which are scattered into such long living states. This process becomes relevant for pump generated polaritons, since direct relaxation into the polariton ground state ($k_{||}$=0) is strongly suppressed [121]. Scattering into localized excitonic states conserves spin coherence. Carriers that are transferred from the localization sites into $k_{||} = 0$ states are quickly emitted from the cavity on a time

scale of few ps, which is given by the finesse of the resonator. Therefore the polariton density at the bottom of the LPB is negligible in the low power regime and does not influence the optical response of the system.

The strain is well oriented but changes strongly from the wire edge to the center, causing a variation of the state splitting ΔE_i among the localization sites i. In each site the spin precesses with the period $T_{osci,i} = \frac{h}{\Delta E_i}$. In the experiment the superposition of the signal from many localization sites is detected. Due to the differences in $T_{osci,i}$ no uniform beatings can be observed [168]. The long lifetime of the localized states gives rise to a homogeneous linewidth of ≈ 10 μeV. As the homogeneous linewidth is smaller than the exchange splitting it would allow for the observation of the spin precession in studies resolving single localization sites.

Let us now discuss the origin of the quantum beats observed at increased P_{exc}. When the site population saturates, elastic scattering of polaritons into these sites is prevented. Because of this complete 'bleaching' of the localization sites the transmission is not affected any further by Pauli-blocking from them. Still, in the experiment δT increases further which is traced to a strong increase of the polariton population in the $k_{||} \approx 0$ states, where a macro filling of the polariton states can be reached [134]. Such a population could arise from two processes:

- Relaxation of polaritons by polariton-polariton scattering, which is effective among particles of the same spin orientation in the high density regime [120]. Due to the short cavity lifetime, it will contribute to the generation of a high polariton density mainly at short delays.

- Feeding of the macroscopic population at $k_{||} \approx 0$ by a seeded transfer from exciton states. These exciton states can be either localized excitons or free excitons with large wave numbers, which are only weakly coupled to the light field. The free exciton population is generated in the high P_{exc} regime since the absorption of the polariton line is bleached. Furthermore, these excitons are generated by the high energy tail of the pump pulse. They have wavenumbers significantly larger than that of the light ($k_{light} \approx 1 \cdot 10^7 \mathrm{m}^{-1}$).

The macro filled state at $k_{||} \approx 0$ reaches a spatial extension on the order of a few μm. This coherent state averages over the fluctuations in the exchange splittings ΔE_i. The coherent spins of this macro population oscillate in phase between the states with an effective splitting $\Delta E = \frac{\sum_i \Delta E_i}{i}$, which allows the observation of the oscillations. The long spin coherence time observed here excludes a generation of the $k_{||} \approx 0$ population exclusively by polariton-polariton scattering, since such scattering has been shown to result in a fast loss of exciton spin coherence [167]. Furthermore, the loss of spin coherence would become faster with increasing carrier density, in contrast to the present findings. Hence, the experimental data support a seeded feeding from the exciton reservoir.

The population in the exciton reservoir undergoes a rather fast dephasing. Therefore, the spin coherent population at the bottom of the LPB has to be fed by a stimu-

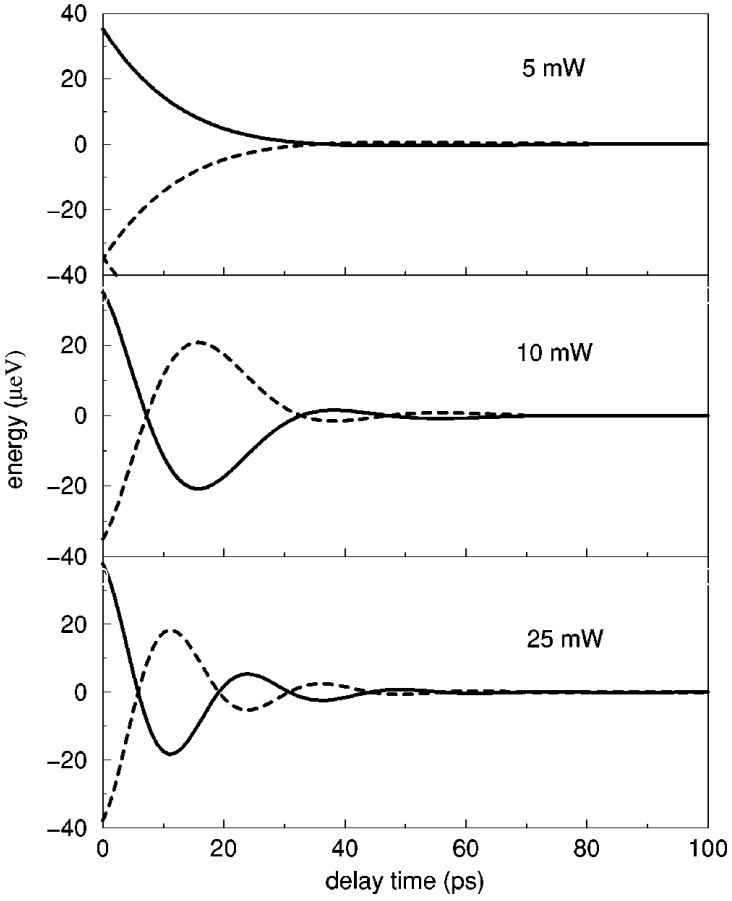

Figure 4.21: *Line position ($E_L(k_{||}) = 0$) as a function of delay, for both circular polarization configurations. From top to bottom the excitation power has been increased. Taken from L.M. Woods and T.L. Reinecke Phys. Rev. B* ***67****, 115336 (2003).*

lated transfer from the reservoir. In contrast to conventional relaxation, such a stimulation will take place only for excitons with a spin phase identical to the phase of the macro-population. In this way a high degree of spin coherence of the $k_{||} = 0$ states will be maintained and the quantum beats can be observed in a large delay range. From the envelope of the oscillations a spin coherence time of ≈ 30 ps is obtained, which is in first approximation independent of P_{exc}. The beatings are to be understood as a spin precession of the collective polariton phase between the linearly polarized and exchange split states.

Finally, in Figs. 4.17 and 4.19 we find one half period of an oscillation at negative delays. It is observed even at the lowest P_{exc}, where no oscillations appear at positive delays. The absorption of the probe pulse in the QW and the substrate is weak. Therefore a significant fraction of the pulse hits the sample back surface and gets reflected there. The reflected probe pulse generates polaritons which now can interfere with polaritons generated by the pump pulse. This interpretation is supported by the fact that any signal at negative delays disappears with increasing temperature, which leads to enhanced absorption in the QW. The interference will depend on the relative spin phase of the two polariton populations, which is given by the spin precession. The period of the oscillation (24 ps) is determined by the substrate thickness.

Recently, this phenomenon was investigated theoretically by L.M. Woods and T.L. Reinecke [166]. Their treatment is based on a polariton Hamiltonian, initially derived to describe parametric wave mixing of polaritons in planar microcavities [129]. This Hamiltonian has been extended by an exchange term [169] treating the exchange splitting of the bright exciton doublet in the low symmetry quantum well. Applying the pump and probe fields and assuming a macroscopic population in the pump and probe states the nonlinear optical response of the cavity is derived analytically. As $k_{||,exc}$ is clearly off the wave mixing resonance, no macroscopically populated idler is expected. Hence, the assumption of only two macro populated states is well justified. For co- and anti-circular pump-and-probe configurations the energy of the LPB was calculated as a function of delay time. The results are shown in Fig. 4.21. As in the experiment (compare Fig. 4.19) beats between the exchange split states appear only at increased excitation densities. In the theoretical modelling, the appearance of oscillations at higher P_{exc} is attributed to the higher number of free excitons, that become available.

Even more exciting, the calculations indicate that T_{osci} decreases with increasing P_{exc}. The calculations show that this effect is due to phase space filling and nonlinear exciton-exciton interaction [166]. It is not attributed to an increase in the exchange interaction. As a consequence the line shifts at $\tau = 0$ remain constant for all excitation powers. Looking closely at Fig. 4.19 a similar, even though much less pronounced effect can be seen. Seemingly the oscillation period deceases with increasing P_{exc} as well. Intuitively, this effect was interpreted as an increase of the exchange interaction. Indeed, also a slight increase in the splitting at τ =0 is seen in Fig. 4.19. A first explanation of this effect was given by considering an increase of the coherence size of the exciton by the cavity light field [159]. This in turn should give rise to an increase in the LR exchange. The calculations show that this is not the case but a consequence of the nonlinearities gaining importance at high excitation densities.

In summary, in this section we have observed broken polarization selection rules for optical nonlinearities in wire shaped semiconductor microcavities, which are explained by the reduced symmetry of the QW. This goes in line with an exchange splitting of the bright exciton doublet caused by uniaxial strain relaxation. At high excitation powers the polariton ground state becomes macro occupied. This spin coherent population gives rise to quantum beats due to the strain induced splitting of polariton states with $|M| = 1$ into $|\perp, ||\rangle = \frac{1}{\sqrt{2}}(|+1\rangle \pm |-1\rangle)$ states. The macro occupation allows for spin coherent transfer of excitons into the polariton ground state, maintaining a spin coherent polariton phase way beyond the cavity lifetime.

4.4 Tailoring parametric polariton scattering channels

While carriers are confined by potential barriers, photons can be confined by dielectric discontinuities. In a MC the mirror boundaries keep photons inside the resonator. So far we have been dealing with photons confined along the growth direction z of the

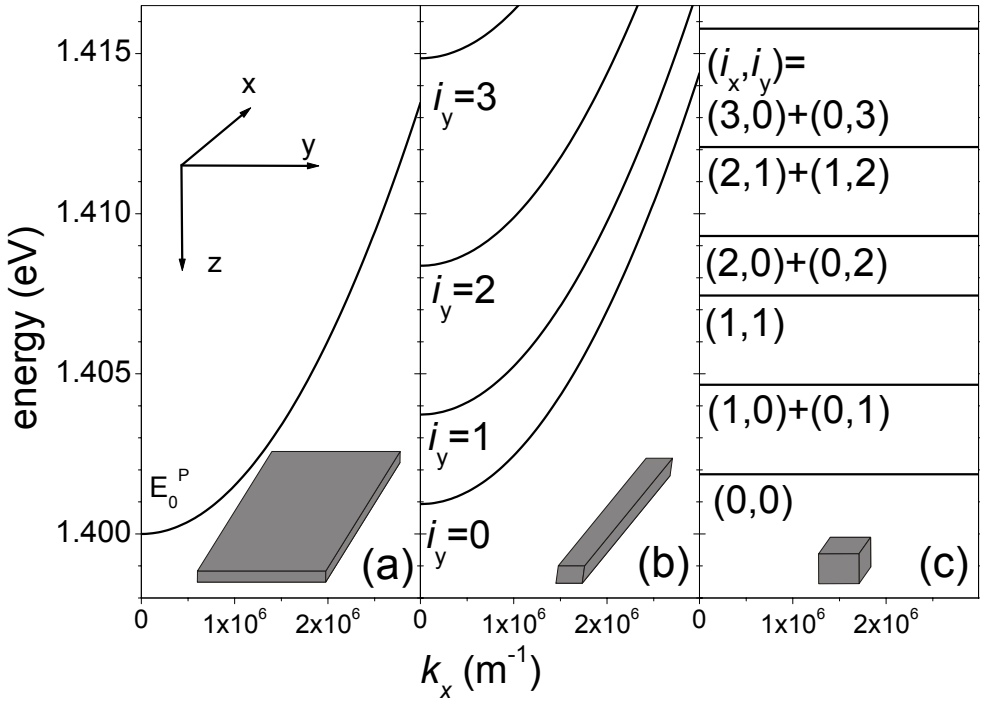

Figure 4.22: *Calculated mode spectrum of a planar resonator (a), a photonic wire (L_y = 4 μm) (b) and a photonic dot (L_y = L_x = 4 μm) (c) versus k_x. The cavity geometries are sketched in each panel, the orientations are defined by the coordinate system sketched in panel (a). The modes are labelled as described in the text. E_P^0 was set to 1.40 eV.*

heterostructure. We will now turn to additional photon confinement in the resonator plane. Recent developments in nanofabrication techniques allow for producing high quality resonators with lateral dimensions comparable to the photon wavelength in the optical range [170]. Lateral photon confinement modifies the optical mode spectrum of a planar MC. In growth direction cavity photons are confined by the Bragg mirrors, while they are free to propagate within the resonator plane (x-y-plane). From Eq. 4.4 the photon dispersion can be written as:

$$E_P^2(k) = \left(\frac{\hbar c_0}{n}\right)^2 \left(\left(\frac{2\pi}{L_R}\right)^2 + k_y^2 + k_x^2\right) = (E_P^0)^2 + \left(\frac{\hbar c_0}{n}\right)^2 k_{||}^2 \,. \tag{4.16}$$

Here E_P^0 is the energy of the fundamental cavity mode that is determined by the resonator thickness. Typically, $E_P^0 \approx E_P$, so that the dispersion is well approximated by a parabola (see Fig. 4.22 (a)).

In the next step an uniaxial discontinuity of the refractive index in the resonator plane is introduced by preparing wire-shaped structures from the planar structure (see Fig. 4.14). The wire width L_y is typically on the order of few μm. In these systems the light is still free to propagate along the wire axis (x), while perpendicular to the wire (y) the electric field is confined at the discontinuity of the refractive index which

jumps from $n \sim 3$ to unity at the resonator edges. Equation 4.17 gives the energy of the photon modes in such a quasi-one-dimensional cavity [161]:

$$E_P^2(k_x, i_y) = (E_P^0)^2 + \left(\frac{\hbar c_0}{n}\frac{\pi}{L_y}(i_y+1)\right)^2 + \left(\frac{\hbar c_0}{n}\right)^2 k_x^2, \qquad (4.17)$$

where the index $i_y = 0, 1, ...$ gives the number of nodes in the electric field distribution across the wire. The unidirectional confinement gives rise to a splitting of the fundamental mode of the planar cavity into a multiplet of branches. Along the y-direction the photon modes show no dispersion ($E_P(k_y) = \text{const.}$). On the other hand, when $E_P(k_x)$ is mapped, each mode (i_y) of the multiplet shows quadratic dispersion, as found in planar resonators (compare Fig. 4.22 (b)). Due to the analogy with other quasi-one-dimensional systems we will refer to these structures as photonic wires in the following.

From the one-dimensional case we proceed to the treatment of quasi-zero-dimensional resonators, which means also shrinking the cavity extensions along the x-direction to be comparable to the photon wavelength. Technically, this is realized by etching micropillars from a planar cavity [171, 172]. In case of resonators with a rectangular cross section the cavity modes are described by [172, 173]:

$$E_P^2(i_x, i_y) = (E_P^0)^2 + \left(\frac{\hbar c_0}{n}\frac{\pi}{L_y}(i_y+1)\right)^2 + \left(\frac{\hbar c_0}{n}\frac{\pi}{L_x}(i_x+1)\right)^2. \qquad (4.18)$$

Here E_P is the sum of three quantized energies; no momentum dependent term occurs. The energy levels of 4x4 μm wide cavities are shown in Fig. 4.22 (c). The modes are labelled as (i_x, i_y), where the $i_{x,y}$ again gives the number of nodes in the field distribution along x, y. In comparison to photonic wires, the bands arising from propagation along the wire now split further into a series of discrete modes. This gives direct evidence of the three dimensional field trapping [173]. These characteristics justify the term 'photonic dots' for such micropillars.

Photonic wires and dots can be looked at as the prototype model systems for low dimensional cavities. Starting from here a rich variety of geometries can be thought of. In varying the geometry we are in effect manipulating the photon mode spectrum. We can think of modelling a crystal-like mode spectrum by building chains of coupled photonic dots [153]. We can also mimic molecule-like modes by simply coupling two photonic dots [174]. Several review articles give an overview on this fascinating field [175, 176, 177].

For demonstrative purposes we will stick with the most simple cases of quasi-zero-dimensional and quasi-one-dimensional systems. Whereas the linear optical properties of these resonators have been investigated in quite some detail [178, 173, 174, 153, 161, 179, 180, 181], the study of the optical nonlinearities [182, 183], particularly in the strong coupling regime [184, 160, 185], is still at the very beginning. After having obtained a far reaching control of the photonic mode spectrum by lateral cavity confinement, we want to discuss to which extent this can be exploited to manipulate

polariton properties. For this purpose we have to go back into the strong coupling regime. Now we not only couple a single photon mode $E_P(k_{||})$ to the exciton, but we couple the entire mode spectrum defined by the cavity geometry to the QW exciton. This can easily be described in the framework of the coupled oscillator model, where now the 2×2 matrix is extended to the number of photon modes plus the exciton mode. Eq. 4.19 gives an example for four photon modes coupled to the exciton:

$$H = \begin{pmatrix} E_P(k_x,0) & 0 & 0 & 0 & \frac{\hbar\Omega_{R,0}}{2} \\ 0 & E_P(k_x,1) & 0 & 0 & \frac{\hbar\Omega_{R,1}}{2} \\ 0 & 0 & E_P(k_x,2) & 0 & \frac{\hbar\Omega_{R,2}}{2} \\ 0 & 0 & 0 & E_P(k_x,3) & \frac{\hbar\Omega_{R,3}}{2} \\ \frac{\hbar\Omega_{R,0}}{2} & \frac{\hbar\Omega_{R,1}}{2} & \frac{\hbar\Omega_{R,2}}{2} & \frac{\hbar\Omega_{R,3}}{2} & E_X(k_x) \end{pmatrix}. \tag{4.19}$$

After having introduced parametric scattering in a standard planar cavity (see introduction of chapter 4), we now move forward towards parametric scattering in low dimensional cavities. Our goal will be to modify scattering channels at will, as the limited polaritonic phase space in planar cavities restricts the number and properties of potential pair scattering channels. We will explore how we can tailor parametric polariton scattering among the polariton modes in low dimensional resonators.

Tailoring scattering processes means obtaining some control of the kinetics of carriers in semiconductors. Depending on the goal to be achieved, an enhancement or a suppression of scattering is desirable. For applications in quantum information processing, for example, scattering has to be avoided as it destroys the phase coherence of the carriers. On the other hand, to facilitate carrier transfer and relaxation it is preferable to optimize the efficiency of certain scattering channels. In the past decade tailoring of scattering has been aimed at by proper design of heterostructures. One of the most sophisticated examples for such engineering is the quantum cascade laser. Its operation crucially relies on adjusting carrier energy levels and wave functions [186]. Typically, in semiconductor heterostructures the carrier phase space is tailored. In our approach we design the photon spectrum and use the strong exciton-photon coupling to create polaritons. Polaritons can scatter like conventional carriers, but now we want to control the scattering channels by choosing the appropriate cavity geometry.

For this purpose the following setup has been developed. As the polariton modes are typically separated by $\lesssim 1$ meV excitation with pulses of few ps inevitably excites more than one polariton state. To obtain a well defined resonant excitation of a single polariton state a Ti:Sapphire laser operating in cw-mode was used. The studies of Stevenson *et al.* [131] and Ciuti *et al.* [133] demonstrate that parametric stimulated scattering is not restricted to excitation with ps pulses, but also occurs for cw-excitation. The laser energy E_{exc} can be tuned continuously, at least on the energy scales of relevance here, by a birefringent crystal. This is controlled by a computer. The laser beam was focused onto the sample with a focal spot of about 50 μm in diameter. The sample is mounted on the cold finger of a micro-photoluminescence cryostat, which allows a variation of the temperature. The experiments were performed at a temperature of ≈ 5 K. As the sample surface is only a few mm's from the cryostat window this mount-

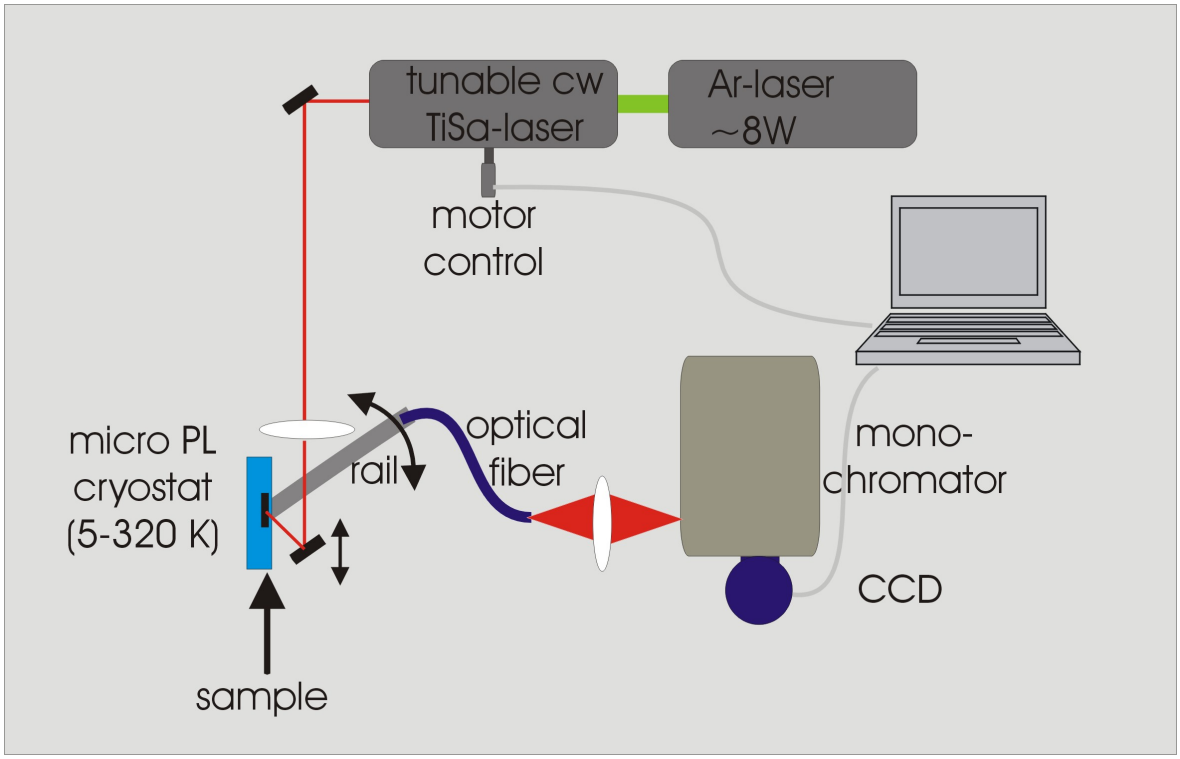

Figure 4.23: *Setup for angle resolved studies on parametric scattering.*

ing permits angle resolved studies in a range of $\approx \pm 80°$. The emitted photons pass through an aperture providing an angle resolution of $\lesssim 0.5°$. The light is then coupled into an optical fiber. A linear polarizer placed between sample and aperture blocks reflected and scattered light from the exciting laser. This arrangement is mounted on a rail. The rail is fixed exactly below the sample and is free to rotate around this point by the angle θ. Hence, rotating the rail permits scanning the polariton momentum without further alignment. The light exiting the fiber is focused onto the entrance slit of a monochromator, where the emission was spectrally analyzed and finally detected by a CCD-camera. This combination gives a spectral resolution of ≈ 0.1 meV. For characterization of the sample, an Ar^+-laser ($\lambda = 514$ nm), which normally pumps the Ti:Sapphire laser, was used for above band gap excitation. The photoluminescence was then detected in the standard way. While this setup marks the final and most convenient configuration, much of the data shown in the following were obtained using a conventional bath cryostat in transmission geometry. Due to the limited aperture of the cryostat windows only an angle range of $\pm 8°$ was accessible. Higher angles could only be realized by tilting the sample, which naturally also affects the pump angle and requires realignment.

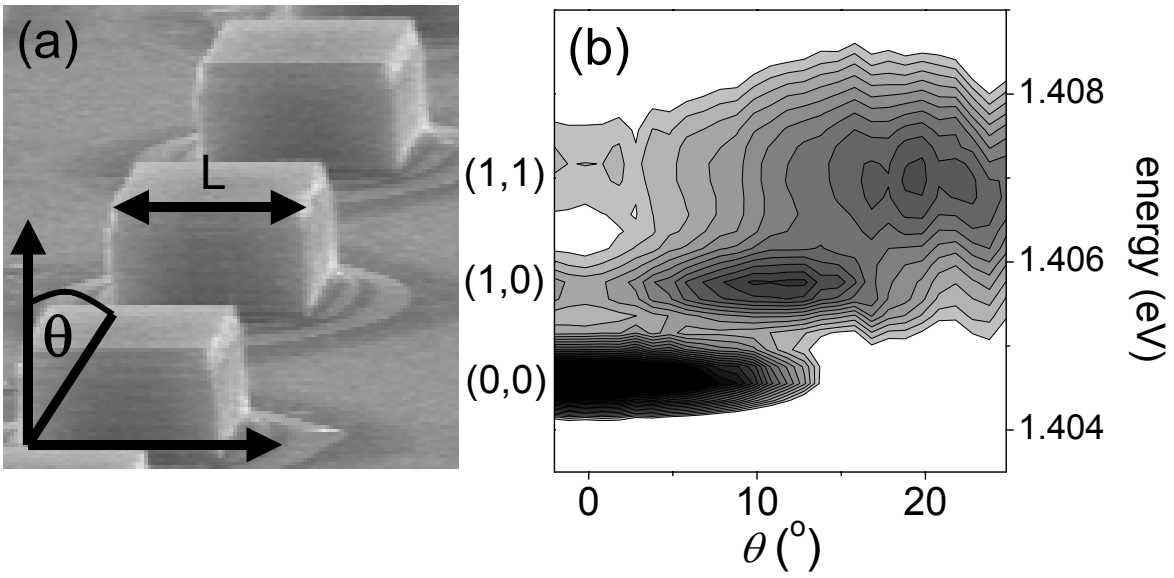

Figure 4.24: *(a) Scanning electron micrograph of an ensemble of photonic dots. The arrow marks the width of the structure ($L_x = L_y = 4$ μm). In the experiment the direction of detection is tilted with respect to the cavity normal by the angle θ (see coordinate system). (b) Energy of the three lowest modes of the photonic dot as a function of θ. The intensity is plotted on a logarithmic grey scale.*

4.4.1 Parametric polariton scattering in photonic dots

As a starting point investigate optical nonlinearities in quasi-zero-dimensional cavities. The investigated sample is based on a planar λ-cavity as described earlier. A scanning electron micrograph of a section of an array of photonic dots is shown in Fig. 4.24 (a).[3]

Fig. 4.24 (b) shows the spectrally resolved emission of the three lowest modes of photonic dots plotted on a logarithmic grey scale versus the detection angle. Non-resonant, above band gap, excitation with an Ar^+-laser was used. The photoluminescence recorded normal to the sample plane ($\theta = 0$) is dominated by emission from thermalized carriers in the ground mode. In addition, weak emission from the excited modes is seen. For increasing θ the higher excited modes become dominant in the spectrum. The first excited mode reaches maximum intensity for $\theta \approx 10°$ and the second excited mode reaches its maximum for a detection angle of 20°. The intensity in the far field is the Fourier transform of the near field distribution of the electromagnetic field. As the near field is strongly localized, the modes are delocalized in k-space. This means they extend over a wide range of angles. All modes show no dispersion, that is their energies do not vary with θ, demonstrating the 3D-confinement of the electromagnetic field. Since $E_P^0 \approx E_P$ the energy spacing between the ground (0,0) and the

[3]We note that the first excited mode is two-fold degenerate (neglecting the polarization of the electromagnetic field). Its field distribution has a nodal plane which can be either along the x-direction (1, 0) or along the y-direction (0, 1). For simplicity we will use here only the notation (1, 0) for the first excited mode.

first excited mode (1,0) is equal to the spacing between the first excited (1,0) and the second excited mode (1, 1) (see Eq. 4.18) with a splitting of ≈ 1.5 meV. Because of the considerable energy separation from the exciton mode ($E_X = 1.411$ eV), as compared to the Rabi splitting, this equidistance is hardly changed by the excitonic admixture. In principle, an increased excitonic admixture would increase the parametric scattering efficiency, as it is mediated by exciton-exciton interaction. However, as it destroys the equidistance between the modes, it would make this scattering channel inaccessible.

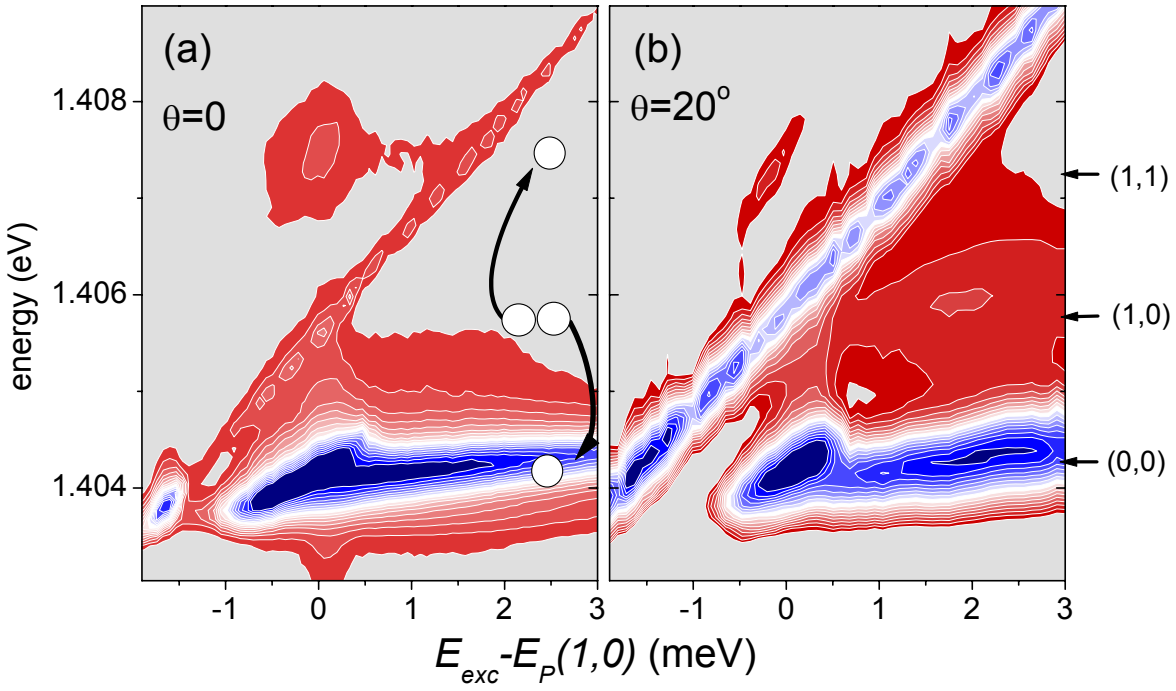

Figure 4.25: *Logarithmic contour plot of the spectrally resolved emission as a function of $E_{exc} - E_P(1,0)$. The excitation angle was fixed at 10°, while the detection angle was 0° (panel (a)) and 20° (panel (b)). The dots in the left panel represent polaritons, which undergo parametric scattering as sketched by the arrows.*

In the second stage of the experimental investigations we focus on the behavior under resonant excitation. Fig. 4.25 shows the spectrally resolved emission of the resonators versus the detuning of the laser energy from the first excited mode in a logarithmic grey scale for two different detection angles. The left panel shows the emission normal to the resonator, the right panel was recorded for $\theta = 20$ °. In both cases the laser beam hits the sample under an angle of 10°, where the emission from the first excited mode has maximum intensity (compare Fig. 4.24 (b)). The ordinate shows the mode energies, while the abscissae are calculated from the energy separation of E_{exc} and the $E_P(1, 0)$ resonance. The laser energy is therefore represented by the line running from the upper right to the bottom left of the graphs: E_{exc} is scanned from above the (1, 1) mode to below the ground mode.

At $\theta = 0$, for excitation above the $E_P(1, 1)$ mode only luminescence from the ground mode is visible. Decreasing E_{exc} down to the (1, 1) mode causes a slight

enhancement of the emission from this mode. Lowering E_{exc} further the (1, 1) emission drops again. However, when E_{exc} becomes resonant with the first excited mode (1, 0) ($E_{exc} = E_P(1,0)$) pronounced emission from the energetically higher (1, 1) mode appears. This goes in line with a strong increase of the signal from the (0,0) mode. When E_{exc} is decreased further below $E_P(1,0)$ the emission from the ground mode and the second excited mode decrease towards zero. When E_{exc} finally resonantly excites the (0,0) mode a strong signal from this mode is detected. However, for this situation, no (1, 1) or (1, 0) emission is observed. These findings also hold qualitatively for the large detection angle in panel (b) where the mode intensities are considerably smaller, as compared to the laser intensity. We find emission from the high energy mode as soon as the middle mode is resonantly pumped. In line with the rise of this emission feature the ground mode emission increases. The drop in intensity goes in parallel in both modes, just as much as the rise does. This documents that the emission features are correlated.

In addition, as expected from Fig. 4.24 (b), at such high angles emission from the (1, 0) resonance is observed. This feature appears only as long as E_{exc} is larger than $E_P(1,0)$. In particular, it does not show up for $E_{exc} = E_P(0,0)$. This indicates that thermal excitation effects can be excluded when explaining the (1, 1) emission for $E_{exc} = E_P(1,0)$. To double check this, the sample temperature has been increased from 2 K to 10 K while resonantly pumping the (1, 0) mode. This should lead to a significant increase of the thermal population in the (1, 1) mode, considering splittings in the 1 meV range. However, we observed no increase of the (1, 1) emission; the effect even decreases for increasing temperature. Hence, the polaritons are not lifted into the (1, 1) mode via phonon interaction or other thermal activation processes. The data clearly suggest a parametric polariton conversion process as an explanation for the observed emission features. This process is sketched in Fig. 4.25 (a): The laser resonantly generates polaritons in the (1, 0) mode. Due to carrier-carrier scattering one polariton is down-converted into the ground state and a second one is up-converted into the second excited mode. The total energy has to be conserved in such a two polariton scattering mechanism, which is satisfied here due to the harmonic mode spacing. The ground mode gives the signal state, while the idler is found in the (1, 1) mode. As soon as the laser energy becomes off-resonant with the (1, 0) mode the initial state of the pair scattering processes loses its macroscopic population and the scattering process is truncated.

We noted already that the scattering induced emission from the (0,0) mode and the (1, 1) mode are closely correlated, as expected for signal and idler states. We further see that, as the laser energy is tuned through the (1, 0) mode, the emissions from the (0,0) and (1, 1) modes both shift, which is surprising at first sight. These line shifts are analyzed in detail in Fig. 4.26. In panel (a) the energies of the emission lines of signal (open dots) and idler (full dots) are plotted against E_{exc}. As E_{exc} is increased both modes are blue shifted, with the second excited mode stronger than the ground state one. While the lines shift, the energy spacing between E_{exc} (diamonds) and the ground mode and the spacing between the second excited mode and the laser energy increase. However $E_P(1,1) - E_{exc}$ equals $E_{exc} - E_P(0,0)$ for all E_{exc}. This is

direct evidence of the energy conservation. However, the microscopic reason for the line shift remains to be identified. Let us first consider the origin of the linewidth of the modes observed in the PL-spectra. From studies of single resonators we know that the finesse is about 8000 for structure sizes of $L_x = L_y = 4$ μm, corresponding to a linewidth of less than 0.2 meV.[4] Hence, the homogenous linewidth is considerably smaller than the linewidth of 0.5 meV that we observe in the experiments. Therefore, the emission is inhomogeneously broadened. In the experiment a focus spot of 50 μm excites an ensemble of about 100 photonic dots with slight size fluctuations (see inset in Fig. 4.26 (b)). With shrinking lateral resonator size the confinement energy increases, resulting in larger mode splittings. The broadening observed here corresponds to size fluctuations in the range of $\approx \pm 0.4$ μm.

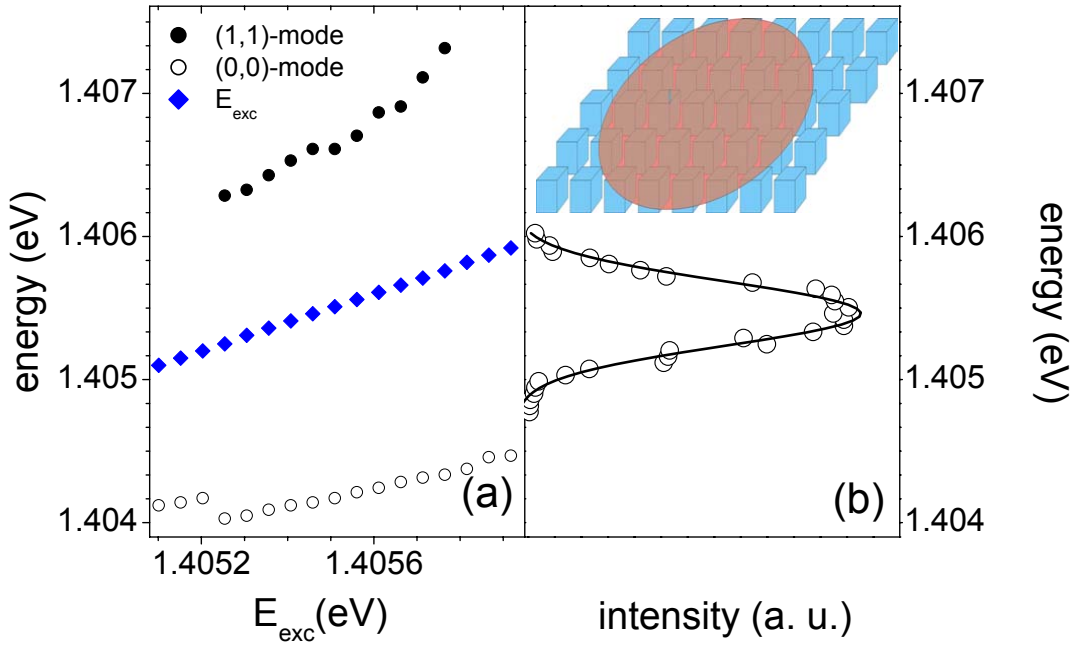

Figure 4.26: *(a) Spectral position of the (1, 1) mode (solid dots) and the (0,0) mode (open dots) as a function of E_{exc}. The diamonds mark the position of the exciting laser. (b) Peak intensity of the (0,0) mode, as a function of E_{exc}. The solid line shows a Gaussian fit to the data which serves as a guide to the eye. The data were obtained for $\theta = 20°$. The inset illustrates the illumination of the dot ensemble by the focused laser beam.*

Now let us consider the consequences of this inhomogenous broadening for the parametric polariton scattering process: As the E_{exc} approaches the low energy tail of the inhomogeneously broadened (1, 0) mode the energy conservation condition is satisfied only for the largest dots in the ensemble, with the smallest mode splittings. Tuning the laser to higher energies makes this scattering channel accessible for smaller

[4] At such large negative detuning the weak exciton admixture has no significant impact on the linewidth.

dots while excluding the larger cavities from the scattering process. Consequently, the emissions from the (0,0) mode and the (1, 1) mode shift as E_{exc} is scanned through the first excited mode. Fig. 4.26 (b) shows how the corresponding amplitude of the parametric scattering evolves, as a function of the excitation energy. Shown is the peak intensity of the (0,0) mode (circles) as a function of E_{exc}. We see how the parametric scattering gains intensity as the laser energy reaches $E_P(1,0)$. This is followed by a decay symmetric to the rise. In principle, this amplitude should reflect the number of dots having the size corresponding to the required energy spacing. Hence, it should directly give the size distribution of the dot ensemble. The data can be approximated by a Gaussian (solid line) with a full width of $\approx$ 0.5 meV which agrees with the linewidth of the (1, 0) mode in Fig. 4.24 (b).

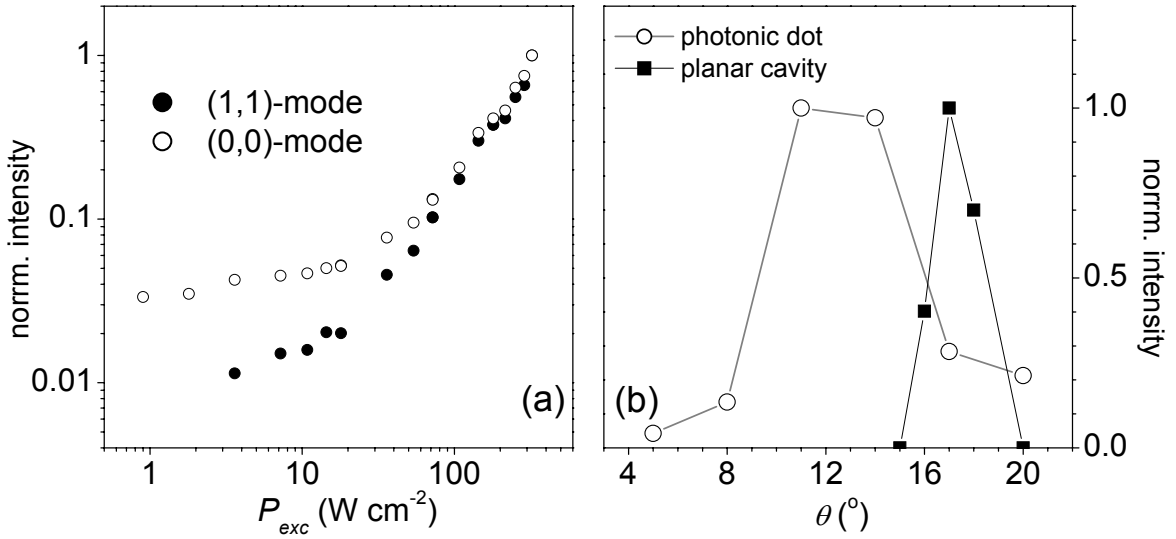

Figure 4.27: *(a) Normalized intensity of the (1, 1) mode (solid dots) and the (0,0) mode (open dots) as a function of the excitation power plotted on a log-log scale. (b) Angle dependence of the parametric scattering for photonic dots (open symbols) and a planar cavity (solid symbols), as a function of the detection angle.*

To obtain further insight into the proposed scattering processes, in particular to map out similarities as well as differences to parametric scattering in planar cavities, the excitation power P_{exc} has been varied. The spectrally integrated, normalized intensity of the (1, 1) mode ((0,0) mode) under resonant excitation of the (1, 0) resonance is illustrated by the solid (open) symbols in Fig. 4.27 (a) on a log-log scale. In the low P_{exc} regime the signal from the ground mode remains almost constant, which indicates a reduced relaxation by acoustic phonons between the discrete polariton modes. The emission from the (1, 1) mode is negligible. In the high excitation regime a strong correlation between the increase of the emission from the (0,0) mode and the (1, 1) mode is evident. Here the intensities of both modes increase superlinear $\sim P_{exc}^2$, as one would expect from a population that is created by exciton-exciton scattering. At even higher powers, a strong exponential increase of the emission would be expected. However, this range was not accessible in the present experiment.

In Fig. 4.27 (b) the angle dependence of the conversion process is analyzed. The open dots mark the intensity of the (1, 1) mode as a function of θ. For the photonic dots idler emission is resolved in a wide angular range of $\approx 12°$. For comparison, data for a planar cavity is shown (dark symbols) [141]. The symbols mark the intensity of the idler emission. For the planar cavity case, a sharp angle resonance is observed, permitting the parametric scattering only in a range of $\pm 2°$. In both cases energy conservation is the crucial parameter which has to be satisfied. In the two-dimensional case additionally momentum conservation is of equal importance. This results in an observability of the idler emission and hence parametric scattering in a narrow angle range only. For the zero dimensional system conservation of $k_{||}$ is not required. Because of the broken translational invariance and the photon confinement no in-plane momentum can be attributed to the polariton states. Hence, $k_{||}$ is no longer a good quantum number and the momentum conservation constraint does no longer apply. As a consequence the idler emission intensity follows the field amplitude of the (1, 1) mode observed under above band gap excitation (see Fig. 4.24 (b)). The (1, 1) mode idler emission can be observed as well, when the angle of excitation is tuned over a similarly wide range and only drops as the field amplitude of the (1, 0) mode vanishes.

Let us take a look at the symmetry of the states involved in the scattering process. All states can be classified by the parity of the electromagnetic field distribution along the x- and y-direction. While the ground mode has even parity in x- as well as y-direction, the (1, 0) mode has odd parity in x-direction and even parity in y-direction (see Fig. 4.28). We have to keep in mind, that the (1, 0) mode is degenerate with the (0, 1) mode, which has even parity in x-direction and odd parity in y-direction. The (1, 1) mode has odd parity in both directions. Looking at the potential scattering events of Fig. 4.28, we find that the process on the left does not conserve the total parity in y- direction. The process on the right, where the initial states are in the (1, 0) state and the (0, 1) state, would conserve the total parity in the pair scattering event. If parity conservation is relevant for parametric scattering in photonic dots, could be investigated by adjusting the polarization of the exciting laser beam. This question remains to be clarified.

Finally, the detuning dependence of the process has to be discussed. All data presented above were obtained for rather large negative detunings. In the experiment the parametric scattering is observed for even larger negative detunings. When the photon lines are shifted further up towards the exciton, a clear identification of parametric scattering becomes difficult: With increasing excitonic admixture, the modes become broader, complicating the spectral resolution of the parametric scattering. Intuitively, we expect an increase of the scattering efficiency as the excitonic fraction of the modes is increased. However, the level repulsion will lead to a violation of the equidistance of the modes and truncation of the process.

It can, however, be thought of parametric processes in higher polariton modes, which have no equidistant photon modes. The mode spacing can then be tuned by adjusting the cavity detuning. As the higher lying modes feel the polaritonic level repulsion much more strongly they can be pushed towards the lower lying modes to

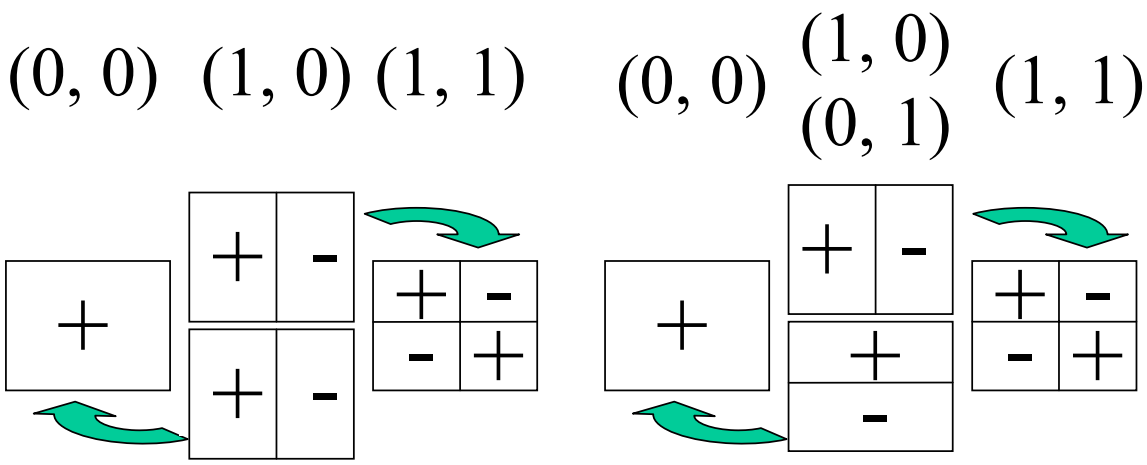

Figure 4.28: *Electric field distribution of the three lowest optical modes in photonic dots. The arrows mark potential scattering channels. Left: process violating parity conservation. Right: parity conserving process.*

achieve equidistance. So far we have not discussed the impact of the dot size. Here we have chosen $L_x = L_y = 4$ μm. The dot size has no impact on the relative mode spacing, but it determines the absolute energy differences. This tool at hand, we can tune the energy transfer of the parametric scattering by simply adjusting the size of the cavity. Naturally, there are limits to this, as for $L_{x,y} < 1$ μm the photon confinement becomes less perfect. Increasing the size further, line broadening and mode spacing become comparable. We still have one degree of freedom left. Reducing the symmetry of the resonator $L_x \neq L_y$ lifts the degeneracy of the modes into doublets. Proper design of the cavity geometry again allows for equidistant states and possibly parametric scattering. In general, we can even think of process among non neighboring modes. We now, however, turn our attention to a case which is fundamentally different from the quasi-zero-dimensional case: Parametric scattering in wire shaped resonators.

4.4.2 Parametric polariton scattering in photonic wires

A rich polariton mode spectrum is obtained by unidirectional lateral optical confinement in quasi one dimensional wire shaped cavity structures. From the planar cavity wire structures with a width of $L_y = 3$ μm were fabricated by lateral patterning. The confinement leads to a splitting of the polariton modes known from planar cavities into a fan of subbranches (see Fig. 4.22 (b)) [161], labelled $i_y = 0, 1, 2....$ As i_y gives the number of nodes in the field distribution, it indicates the parity of the field. Even (odd) i_y corresponds to a symmetric (antisymmetric) electro-magnetic field distribution across the wire.

Fig. 4.29 (right half) shows the dispersion of the mode multiplet in the strong coupling regime at an exciton-photon detuning $\Delta = -7.5$ meV.[5] The data were obtained by angle-resolved photoluminescence spectroscopy under non-resonant excitation. Four optical modes are resolved below E_X. Each of these modes couples strongly to the exciton. In the dispersion this leads to pronounced anti-crossings as θ is scanned. In addition, faint traces of the upper polariton multiplet are found. The data are well described by a coupled oscillator model of Eq. 4.19 (see solid traces in Fig. 4.29) [162]. From the fits to the data we obtain $\hbar\Omega_R = 3.8$ meV for each anti-crossing, which equals the Rabi splitting in the planar resonator.

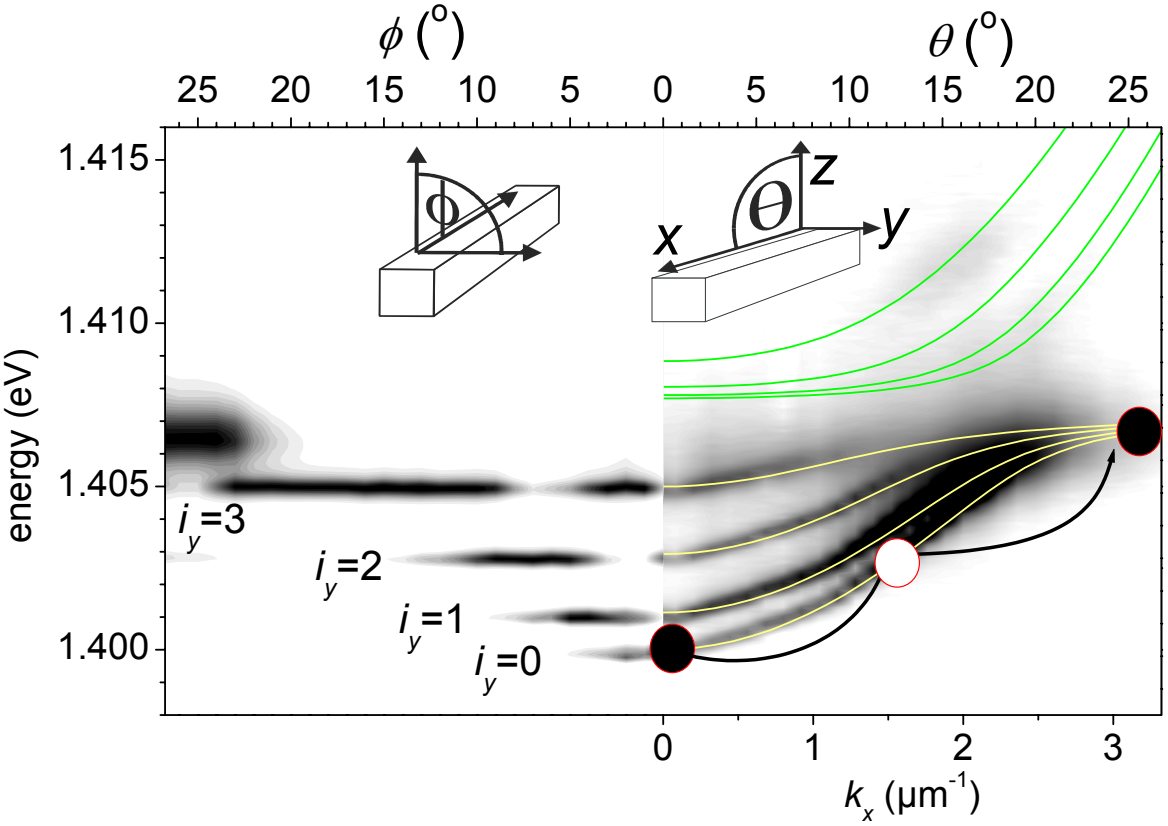

Figure 4.29: *Angle resolved photoluminescence of wire shaped cavities with $L_y = 3$ μm. In the left half the detection angle ϕ was scanned perpendicular to the wire axis while in the right half θ (k_x) was scanned along the wire axis (logarithmic grey scale). The solid traces give the calculated mode dispersions. Dots mark the signal and idler states (full) plus the pump state (open).*

In the LPB multiplet all subbranches have a point of inflection. Therefore within each subbranch elastic pair scattering should occur when the laser energy is tuned to its point of inflection. Figs. 4.30 (a) and (b) show the corresponding photoluminescence spectra for the $i_y = 0$ polariton resonance ($k_{exc,x} = 1.7\mu\text{m}^{-1}$ corresponding to $\theta_{exc} =$

[5] Δ is determined from the energy spacing between the exciton and the photon energy E_P^0, as defined in a planar cavity.

13°). θ_{det} was tuned to $\theta_{signal} = 0$ (Fig. 4.30 (a)) and $\theta_{idler} = 2\theta_{exc} = 26°$ (Fig. 4.30 (b)). Above a cw-excitation power level of $P_{exc}^{T} > 200$ mW emission from the idler state with $k_x = 2k_{exc,x}$ is observed (Fig. 4.30 (a)), which is accompanied by strong emission from the $(k_x = 0, i_y = 0)$ signal state (Fig. 4.30 (b)). The power density dependence of the emission from the signal state gives further evidence for resonant pair scattering, as it shows a threshold-like dependence (see Fig. 4.30 (c)). In the low P_{exc} regime a linear increase of the intensity is observed, which emerges into a strongly superlinear increase above the threshold P_{exc}^{T} for elastic pair scattering.

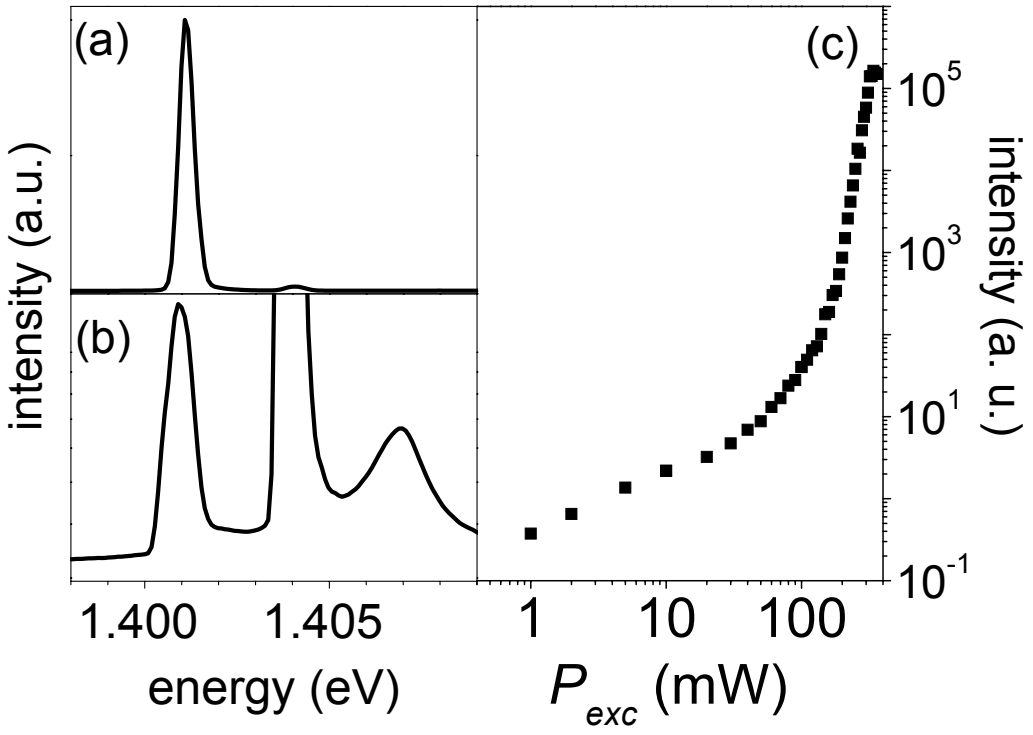

Figure 4.30: *(a) and (b) Spectrally resolved emission for $\theta_{det} = 0$ (a) and $\theta_{det} = 26°$ (b) for $E_{exc} = E_0(\theta_{exc} = 13°)$ above the excitation power threshold. (c) Emission from the signal state as a function of P_{exc} on a log-log scale.*

The process occurs on a time scale of a few ps's [125]. Due to the cw-character of the experiment we are not sensitive to dynamics. Thus the spectra show contributions from parametric luminescence superimposed on signals from polariton populations that build up after the coherence is destroyed. Below P_{exc}^{T} the emission is determined by the decay of such populations that have relaxed into the ground mode via phonon emission. This gives rise to a linear power dependence for low P_{exc}. At $P_{exc} > P_{exc}^{T}$ this emission is superimposed with signal arising from polaritons that are transferred into the signal state by coherent pair scattering. This signal dominates at high excitation powers.

All branches of the lower multiplet converge towards the exciton level at higher k_x. Therefore they are very closely spaced in energy at $k_x = 2k_{exc,x}$ and it is not clear from the spectra to which branch i_y the idler emission has to be attributed. Insight into this question can be derived from a symmetry consideration. The parity of the product

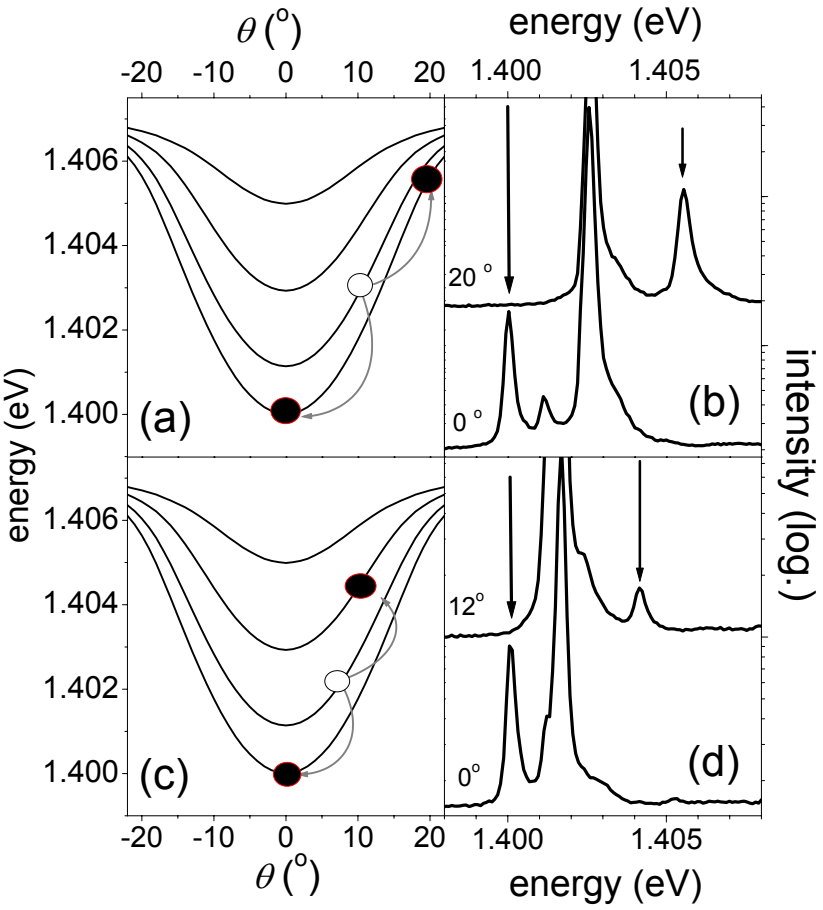

Figure 4.31: *(a) and (c) Schematics of the scattering processes where the solid traces give the mode dispersion. (b) and (d) Spectrally resolved emission obtained for the angles indicated. Arrows mark emission features corresponding to final states of the scattering process. In panel (b) the excitation is resonant with the i_y=1 mode at $\theta_{exc} = 10°$. In panel (d) the i_y=1 mode is excited under $\theta_{exc} = 6°$.*

state of the two initial polaritons is always even, independent of the parity of the branch i_y into which they are excited optically. For the specific process under study, the signal state has even parity ($i_y = 0$). To conserve the total parity in conversion process the idler state has to have even parity as well. This represents an additional constraint besides energy and momentum conservation. For the scattering process described in Fig. 4.30 parity conservation requires that the idler state can only be located in the $i_y = 0$ or in the $i_y = 2$ branch, but not in the $i_y = 1$ or $i_y = 3$ branch. It is expected that scattering into higher lying modes is less efficient and the idler emission originates from the $i_y = 0$ mode. The process described here is most similar to the conventional pair scattering in a planar resonator: From the point of inflection polaritons scatter into the polaritonic ground state, while polaritons scattered into the excitonic section of the LPB compensate energy and momentum transfer. Besides the parity argument there is no qualitative difference to the planar cavity case. However, taking a closer look at the LPB multiplet, several additional pair scattering channels can be postulated. For example, within each subbranch energy and momentum conservation can be satisfied for excitation close to the specific point of inflection.

More interestingly, scattering events within the LPB multiplet that do involve more than one subbranch can be proposed. For example, pair scattering from the ($i_y = 1, k_x = 1.2\ \mu\text{m}^{-1}$) pump state into the signal state at ($i_y = 0, k_x = 0$) with the

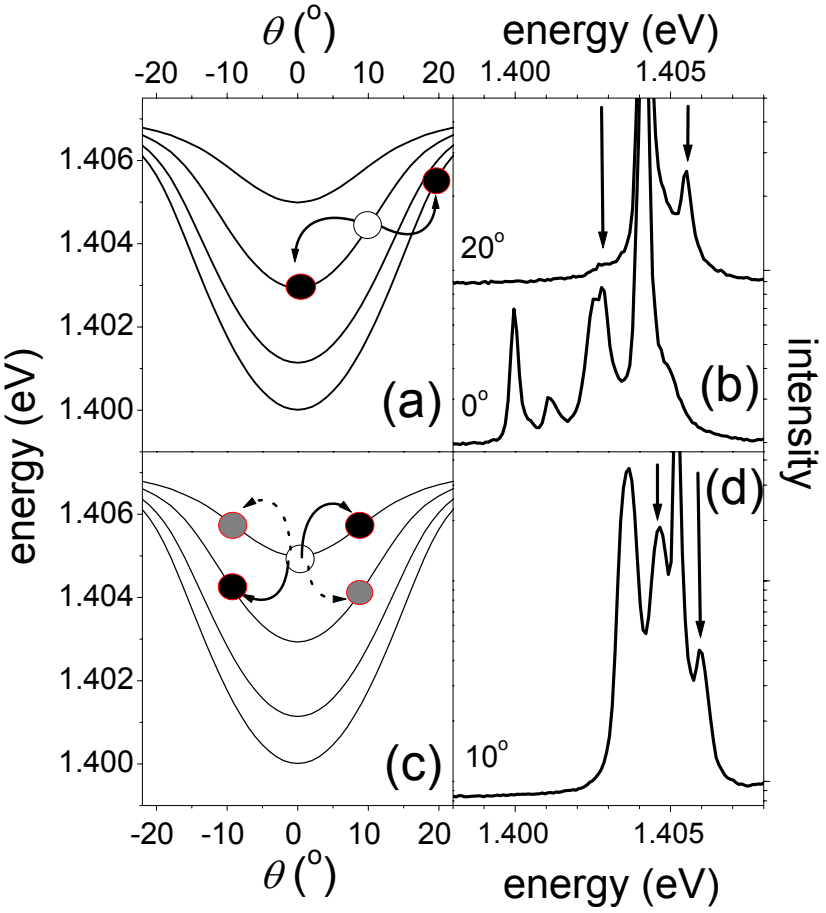

Figure 4.32: *(a) and (c) Schematic pictures of pair scattering process (compare Fig. 4.31 (a) and (c) and see text for details). (b) Emission spectra for* $\theta_{exc} = 10°$ *(*$E_{exc} = E(i_y = 2; \theta = 10°)$*). (d) Spectrum for* $\theta_{exc} = 0$ *(*$E_{exc} = E_(i_y = 2; \theta = 0)$*) at* $\theta = 10°$*. The arrows mark the emission features corresponding to the final states of the scattering process.*

idler at ($i_y = 0, k_x = 2.4\ \mu\text{m}^{-1}$) (Fig. 4.31 (a)) should be observable. Photoluminescence spectra, where the excitation conditions match this resonance for parametric luminescence, are shown in Fig. 4.31 (b) for $P_{exc} > P^T_{exc}$. At $\theta = 20°$ (0) we find strong emission from the idler state (signal state) in the $i_y = 0$ branch, giving evidence of inter-subbranch scattering between $i_y = 0$ and $i_y = 1$ states. The linewidth observed for the idler mode (< 0.5 meV) is significantly smaller than the linewidth observed for photoluminescence under above band-gap excitation (≈ 1 meV). Spectral narrowing is characteristic for coherent parametric scattering [125, 129]. Going one step further, a scattering channel where all three states are found in different modes opens up when reducing E_{exc} and θ_{exc} slightly, following the dispersion of the $i_y = 1$ branch (see Fig. 4.31 (c)). Doing so, we switch off the channel described in Figs. 4.31 (a) and (b) but we obtain access to a process for which the idler state is lifted into the $i_y = 2$ mode. This resonance is obtained for $\theta_{exc} = 6°$. In these experiments (see Fig. 4.31 (d)) emission from the idler is observed at $\theta = 12°$. Again, all conservation laws are obeyed by down-conversion of a second polariton into the ($i_y = 0$, $k_x = 0$) signal state. Comparing both processes we find that the idler was shifted from one even parity branch to the next higher even parity branch, as required by the parity conservation constraint.

So far the signal state was the polariton ground state as in a planar cavity. The mode fan gives us the freedom to study scattering events that do not involve this state

e.g. when the laser excites the $i_y = 2$ branch at $k_{exc,x} = 1.2\ \mu\text{m}^{-1}, \theta_{exc} = 10°$ (see Fig. 4.32 (a)). For this process the signal state is located at ($i_y = 2$, $k_x = 0$), while the idler state is found at ($i_y = 0$, $k_{exc,x} = 2.4\ \mu\text{m}^{-1}$). In the experiment the idler is nicely seen in the photoluminescence recorded at $\theta = 20°$ (Fig. 4.32 (b)). The spectrum at $\theta = 0$ shows emission from all ($i_y \leq 2$, $k_x = 0$) states. Below threshold the intensity of the ($i_y = 0$, $k_x = 0$) state dominates followed by the ($i_y = 1$, $k_x = 0$) state and the ($i_y = 2$, $k_x = 0$) state intensities, in decreasing order. Above threshold the emission from the $i_y = 2$ mode, which is the signal state of the parametric conversion process, is strongly enhanced. In the spectrum at $\theta = 0$ we find a line doublet in the $i_y = 2$ mode. Due to size fluctuations in the wire ensemble, the polariton modes are broadened. Energy conservation is only satisfied for the smallest wires in the ensemble for this excitation condition. Therefore, the pair scattering signal appears in the high energy tail of the $i_y = 2$ mode. Its spectral distance to E_{exc} exactly equals the spacing between E_{exc} and E_{idler} (see previous section) [184]. We note that for all pair scattering processes about the same P_{exc}^T is observed.

In the following we want to test the validity of the parity conservation in more detail. For this purpose we consider a specific scattering channel, where signal and idler are located on opposite sides of $k_x = 0$. When the laser energy is tuned to the ($i_y = 3$, $k_x = 0$) state, energy and momentum conservation permit a process in which the signal state is located in the $i_y = 2$ branch at $k_x = +1.2\ \mu\text{m}^{-1}$ while the idler is found at $k_x = -1.2\ \mu\text{m}^{-1}$ in the $i_y = 3$ branch (grey dots in Fig. 4.32 (c)). Due to the inversion symmetry of the polariton dispersion ($E(-k_x) = E(+k_x)$), the wavenumbers can be reversed in this process, the signal may also be located at ($i_y = 2$, $k_x = -1.2\ \mu\text{m}^{-1}$) with the idler at ($i_y = 3$, $k_x = +1.2\ \mu\text{m}^{-1}$), as indicated by the black dots in Fig. 4.32 (c). However, as the signal state has even parity while the idler state has odd parity (grey dots) or vice versa (black dots), this process should be forbidden due to parity conservation. Fig. 4.32 (d) shows the corresponding spectrum which has been recorded at very high $P_{exc} \gg P_{exc}^T$. Symmetrically to the laser line, two modes appear which have to be attributed to signal and idler emission, indicating a breaking of the parity selection rule. However, the intensities of the corresponding emissions are rather weak when compared to the emission from the $i_y = 1$ and the $i_y = 0$ branches, which cannot be resolved separately due to their small energy separation. This thermal emission clearly dominates, although it purely originates from phonon relaxation and thus should be weak for the used P_{exc}. Therefore parity conservation is only weakly broken. The violation of this constraint must be due to symmetry breaking in the system, the origin of which is not completely clear. Possible candidates are the wedge shape of the cavity or imperfections of the lateral sidewalls.

After having demonstrated intra- as well as inter-subbranch polariton-polariton scattering within the LPB multiplet we move on to parametric processes involving the upper polariton modes, which are prohibited in a planar cavity. For these studies, the detuning was reduced to $\Delta = -6$ meV to increase the exciton admixture to the UPB modes and thus the efficiency of the scattering process (see Fig. 4.33 (a)). A scattering channel can be proposed (see arrows Fig. 4.33 (a)), where polaritons, generated in the lower ($i_y = 2$, $k_{exc,x} = 1.4\ \mu\text{m}^{-1}$) state, are transferred into the ($i_y = 0$, $k_x = 0$)

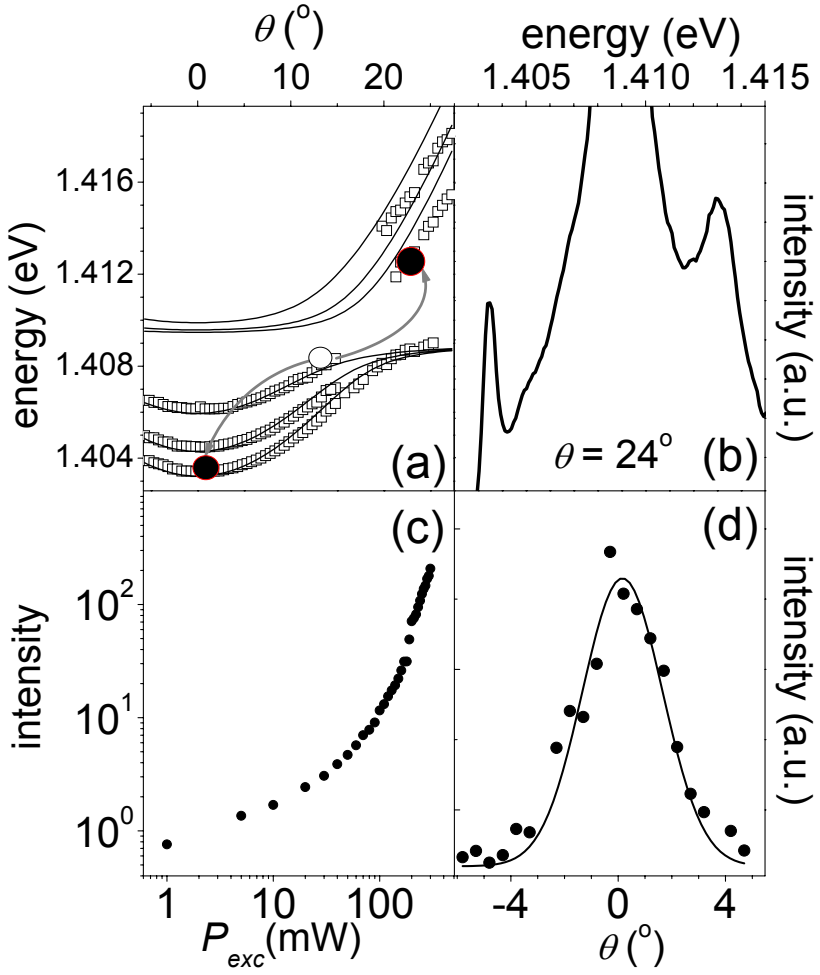

Figure 4.33: *(a) Mode energies (squares) as a function of θ. The solid traces give a fit to the data. (b) Spectrally resolved emission for $\theta = 24°$ ($\theta_{exc} = 12°$, $E_{exc} = E(i_y = 2; 12°)$). (c) Signal state emission as a function of P_{exc} on a log-log scale.(d) Signal state emission as a function of θ. The solid trace gives a Gaussian fit to the data.*

state of the LPB's and into the ($i_y = 0$, $k_x = 2.8\ \mu\text{m}^{-1}$) state of the upper polariton manifold. The corresponding experiments are shown in Fig. 4.33 (b): When θ matches $k_{idler,x}$, intense emission from the upper $i_y = 0$ resonance is detected for $P_{exc} > P_{exc}^T$. In line with the idler emission goes a considerable rise of the intensity from the signal state. Fig. 4.33 (c) shows the power density dependence of the signal emission, which is similar to the findings of Fig. 4.30 (c). We observe a linear increase at low P_{exc} followed by a strongly superlinear behavior above threshold. The signal arising from parametric down conversion around $k_x = 0$ is monitored as a function of θ in Fig. 4.33 (d). Due to momentum conservation, the emission shows a sharp angular resonance, which can be described by a Gaussian (solid trace) with a full width at half maximum of $\lesssim 3°$. In addition, sharp dependencies on E_{exc} and θ_{exc} are found (not shown).

Involving the UPB's allows for investigation of another scattering channel for which the parity conservation can be tested. For this purpose we return to $\Delta = -7.5$ meV with the dispersion relation given in Fig. 4.29. If the laser beam is directed under an angle of $\sim 9°$ ($k_{exc,x} = 1.1\ \mu\text{m}^{-1}$) onto the sample to be resonant with the lower $i_y = 3$ polariton branch, a scattering channel with the signal state in the lower ($i_y = 0$, $k_x = 0$) state and the idler at ($i_y = 3$, $k_x = 2.2\ \mu\text{m}^{-1}$) in the upper polariton resonances satisfies energy and momentum conservation. However, it violates parity conservation.

We have tested this channel intensively, but no indication of parametric scattering could be found whatever level of excitation power we applied. Further potential scattering channels obeying energy and momentum conservation, but breaking the parity selection rule, have been searched for at various detunings. However, no experimental evidence for such parametric scattering could be obtained.

As can be seen in Fig. 4.29 wire shaped cavities have a twofold nature, while polaritons posses a momentum along the wire axis, they are perfectly confined perpendicular to the wire. We will now focus on polariton conversion processes which do not require a momentum transfer. In analogy to photonic dots we find a discrete set of levels when scanning ϕ. However, here the mode spacings are different as we are facing quantization only along one direction. In wire shaped cavities the three lowest cavity modes are not equidistant and $E(i_y)$ grows as $\sim (i_y + 1)^2$. As proposed in the previous section, the polaritonic level repulsion can be utilized to adjust the mode spacings. Looking at the left panel of Fig. 4.29 we find that the $i_y = 1$, $i_y = 2$ and $i_y = 3$ modes show almost harmonic mode spacing. By adjusting the detuning we can achieve equidistance between those modes for $\Delta = -5.5$ meV.

The harmonic mode spacing is evident in the upper panel of Fig. 4.34. The laser energy is tuned slightly above E_X. We can resolve the first four resonances. The lower part shows the mode emission on a logarithmic grey scale. The laser energy was continuously tuned from above E_X (upper edge of panel (b)) to below the $i_y = 2$ mode (lower edge of panel (b)). In the contour plot the laser energy is represented by the line running from the upper right corner towards lower energies. The energy scale on the ordinate gives the detuning between E_{exc} and the second excited mode. As long as the excitation energy is equal or higher than the energy of the $i_y = 3$ mode, emission from all four modes is observed. For $E_{exc} < E(i_y = 3)$ the emission from the $i_y = 3$ mode drops to zero. Only when E_{exc} becomes resonant with the $i_y = 2$ mode, is emission from the third excited mode again resolved. This emission disappears as soon as E_{exc} is tuned below the $i_y = 2$ mode. The emission above the excitation energy and the sharp energy resonance show that polaritons generated in the second excited mode undergo parametric conversion into the neighboring modes in a pair scattering event. The behavior observed here is very much comparable to that observed for photonic dots. Again, the high energy line shifts as the E_{exc} is tuned through the ($i_y = 2$)-resonance, giving proof of the relevance of energy conservation [184]. As in photonic dots the constraint of momentum conservation does not apply.

The parametric scattering in planar cavities shows a blue shift of the nonlinear emission. This blue shift was found to be comparable to the linewidth of the polariton mode [125, 133, 184]. Here only a slight shift is observed. For example, in Fig. 4.32 (b) the nonlinear signal shows a slight shift towards higher energy with respect to $i_y = 3$ mode. However, the shift is smaller than the linewidth. To understand this, we again have to take into account that the lines are broadened due to size fluctuations in the wire ensemble. This inhomogeneous broadening does not influence the line shift. Furthermore, because of the large negative detuning the exciton fraction is rather small. From these considerations the blue shift is expected to be < 0.2 meV and it is

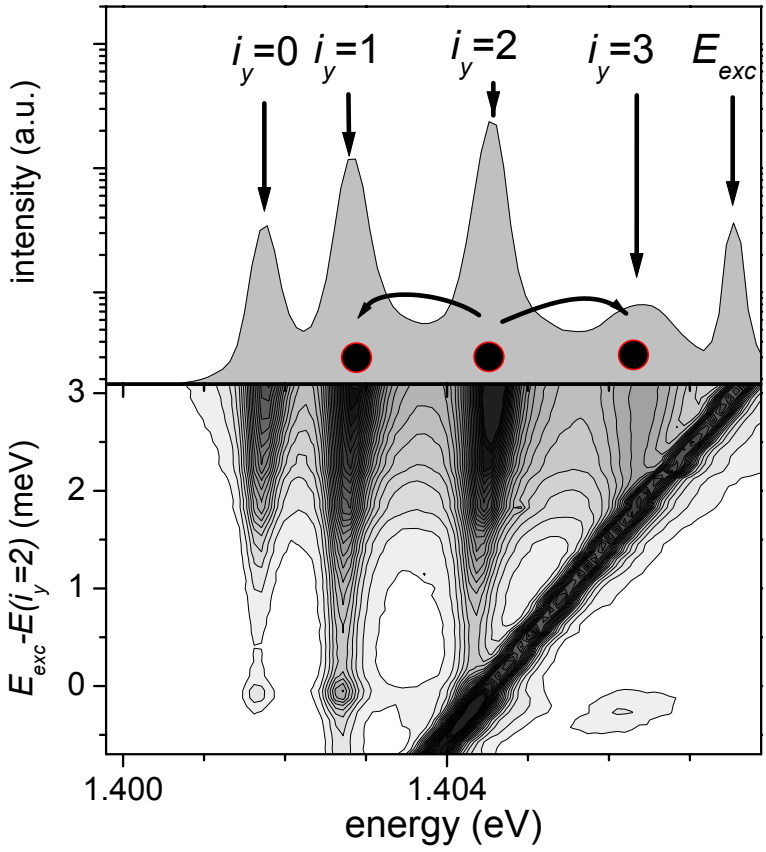

Figure 4.34: *(a) Mode spectrum of photonic wires ($L_y = 3\ \mu m$) at $k_x = 0$. $E(i_y = 1), E(i_y = 2)$ and $E(i_y = 3)$ show harmonic mode spacings. (b) Spectrally resolved emission while E_{exc} is scanned. Intensities are given on a logarithmic grey scale.*

not surprising that it is masked by the inhomogeneous broadening of the lines.

Unfortunately, the present experiment is not sensitive to the dynamics of the polariton conversion processes. Also, an estimate of the efficiency of the scattering channels is difficult. This analysis would become possible in a pump-and-probe experiment, as described in sections 4.2 and 4.3. The drawback of such an experiment is the spectral width of the ultra short laser pulse, which inevitably excites states neighboring the pump state. A recent theoretical study by L.M. Woods and T.L. Reinecke [166] provides valuable insight to these questions. They focused on a scattering process involving the UPB. Their analysis shows that scattering in photonic wires is indeed very similar to its analogue in planar cavities. It takes place on timescales of a few picoseconds, where the process slows down with increasing cavity finesse. The higher the losses, the quicker the wave mixing signal decays. This can be understood when looking at the density dependence of the process. In agreement with the experiment the theory shows a threshold in the excitation power dependence. In a lossy cavity this threshold density is maintained in a much shorter delay range, giving rise to dynamics on a sub picosecond timescale for a cavity linewidth of 1 meV. This goes in line with an increased power threshold and reduced optical gain. To verify this theoretical finding experimentally reducing the wire width seems to be a feasible concept. This increases the mode spacing and using spectrally broad pulses is less critical. However this reduces the cavity finesse significantly for a wire width below $\approx 1\ \mu$m. Theory tells us that this broadening is extremely critical for the parametric polariton conversion and

using spectrally sharper pulses again blurs the dynamics of the system. Hence, it is questionable wether a time resolved experiment can answer these questions.

In summary, parametric polariton scattering has been demonstrated in quasi-one-dimensional resonators. Various such scattering processes have been demonstrated, in contrast to the findings in planar cavities, where the mode spectrum strongly limits the number of elastic pair scattering channels to one. Furthermore, these scattering channels can be tailored by adjusting the exciton-photon detuning or the resonator geometry. Besides the conservation laws of energy and momentum, the cavity symmetry gives rise to the constraint of parity conservation.

Chapter 5

Summary

The presented studies add to the understanding of the optical properties of polaritons. Bulk quadrupole polaritons were studied with extremely high spectral resolution. This gave new fundamental insights into the electron-hole exchange fine structure. It could be demonstrated that exchange interaction in solids is not limited to wavevector independent contributions, but, as theory predicts, exchange in solids indeed shows a dependence on the exciton wavevector. This dependence could be identified for the first time using a novel approach to high resolution solid state spectroscopy. Beyond the elaborate treatment of exchange the potential of this spectroscopic technique is demonstrated. The most remarkable outcome of these studies is the observation of an absorption phenomenon in the high density regime, which shows a linewidth of ≈ 15 neV. This is orders of magnitude below all previous reports.

The investigation of cavity polaritons focused on the optical properties beyond the linear regime. It was demonstrated that exciton localization can give rise to hole burning in the cavity absorption. Furthermore, using quantum beat spectroscopy a coherent precession of the polariton spin was demonstrated. The spins precess between fine structure split exciton states, where the splitting arises from exchange interaction in QW's of lowered symmetry.

Finally it was pointed out how polariton band structure engineering gives access to a controlled manipulation of polariton pair scattering channels. For this purpose micro structured cavities were designed to create the desired polariton mode spectrum. Resonantly driving one selected polariton state the proposed scattering processes with well defined final states could be triggered. It was also shown that the selection rules for such processes depend on the resonator geometry. The constraint of momentum conservation can be lifted along a direction of confinement. Furthermore, parametric scattering has to conserve the total parity. This was demonstrated for inter-subbranch scattering in wire shaped cavities.

Chapter 6

Outlook

Using frequency stabilized lasers for the spectroscopy of semiconductors opens doors in the field of high resolution spectroscopy and the studies presented here mark a starting point and can be understood as a successful proof of principle. Some future aspects have already been pointed out in the corresponding chapters. In this outlook we want to explore the potential of this technique in a broader context. Concerning the studies on Cu_2O the most appealing aspect is the investigation of BEC of excitons. The phenomena described in section 3.5 are a promising starting point. Currently there are many experiments and proposals to the realization of such collective exciton coherence. For all of them, resonant single mode pumping would present a significant improvement and an absorption experiment demonstrating quasi zero broadening of the exciton resonance would be one of the most characteristic signatures of condensation. Conversely the experiment described here can be improved significantly by taking into account the results of previous studies on BEC in Cu_2O. Potential improvements can be done by:

- Trapping excitons in a harmonic strain trap [42, 98]. As in atomic physics [187], it is desirable to trap the carriers as it is much easier to provide well defined experimental conditions in such a trap. Furthermore, the trap prevents the carriers from drifting apart. Using a single mode laser even the discretized levels in the trap could be resolved. The interaction with the environment can also be reduced by carrier confinement. Our approach excites excitons with a finite $\mathbf{k}$, which implies a propagating condensate. This brings along further difficulties.

- Instead of attempting BEC of the orthoexciton one could investigate the paraexciton. Using strain or magnetic fields the paraexciton can be excited optically. As this is the true ground state of the exciton system no further relaxation is possible. The coupling to light can also be adjusted for the paraexciton by adjusting e.g. the strength of the magnetic field. First studies have proven the feasibility of this approach. Even a pulsed magnetic field can be used to populate the state optically during the pulse, while trapping the carriers in the optically forbidden state after the pulse.

- One advantage of exciton BEC, compared to BEC of ions, is the comparably high critical temperature. Our experiments were carried out at about 2 K. This is still a high temperature for condensation phenomena. By using conventional He_3/He_4 cryogenic equipment the mK regime becomes accessible, which will decrease the critical density significantly.

Besides studies on the 1S excitons of Cu_2O single mode spectroscopy is appealing whereever systems with long lifetime and little dephasing are investigated. The first candidates for such studies would be quantum dots, which show dephasing on a ns timescale. So far, all studies on quantum dots in the spectral domain using a monochromator are resolution limited. This could be overcome using single mode excitation. Besides the spectral resolution, single mode spectroscopy provides an alternative access to single dot spectroscopy: The emission energy of a quantum dot ensemble is inhomogeneously broadened by size fluctuations in the ensemble. Exciting with a single mode laser would provide a spectral selection tool to pick a single dot out of this ensemble. This approach might prove superior to current approaches, where etched mesa structures or shadow masks are used to spatially isolate single dots. These approaches are critical, as both techniques represent a modulation in the dielectric environment of the dot. A second side effect of conventional spectroscopy can also be avoided: If the excitation energy does not match the energy of the exciton state additional carriers are excited in the environment of the dot. These carriers again interact with the carriers in the dot, which gives rise to a spectral wandering of the quantum dot emission [188, 189]. For such studies we can take advantage of the large spectral range covered by a dye laser, as compared to single mode diode lasers. The flexibility permits the investigation of several material systems such as CdTe. If these studies are successful it might be desirable to extend them to GaAs/InGaAs quantum dot systems, which would require replacing the dye by a Ti:Sapphire oscillator as active medium.

The study of parametric scattering in low dimensional cavities showed encouraging results, while not exploring the full potential of this approach. Studies in the weak coupling regime demonstrate that designing the cavity geometry is a powerful tool for engineering the photonic band structure [177]. The full flexibility of this approach not nearly fully exploited. Based on the results shown here, we expect that a broad range of scattering channels could be designed at will.

Currently, extensive activities are undertaken to achieve polariton condensates and polariton lasers. Increasing the critical temperature for polariton condensates is the main focus in this active field of research. So far, this issue has been tackled by investigating various material systems [134, 139, 140]. Calculations, however, predict a rise of the critical temperature with shrinking cavity size [190]. This makes photonic dots a promising system for potential high temperature applications of these phenomena.

Appendix

In this appendix we will explicitly calculate the matrixes for the SR exchange of order k^2 (Eqs. 3.39, 3.41, and 3.44). First, we will extract the spin operators in H_1, H_3, and H_5. Using these operators we will develop a spin algebra, that is then applied to the orthoexciton states $\mid O_{yz}\rangle$, $\mid O_{zx}\rangle$ and $\mid O_{xy}\rangle$. Finally, we will calculate the individual matrix elements.

H_1 is given by

$$H_1 \sim (\mathbf{J_e} \cdot \mathbf{J_h})(\mathbf{k} \cdot \mathbf{k}). \tag{6.1}$$

and contains the spin operator

$$\begin{aligned} \mathbf{J_e} \cdot \mathbf{J_h} &= J_{e,z}J_{h,z} + J_{e,x}J_{h,x} + J_{e,y}J_{h,y} \\ &= J_{e,z}J_{h,z} + J_{e,+}J_{h,+} + J_{e,-}J_{h,-} \\ &\stackrel{!}{=} \widehat{O}. \end{aligned} \tag{6.2}$$

Here we have used the momentum ladder operators, to replace the x and y components of the momenta, as follows:

$$\begin{aligned} J_{e,x} &= \tfrac{1}{2}(J_{e,+} + J_{e,-}), \\ J_{e,y} &= \tfrac{1}{2}(J_{e,+} - J_{e,-}), \\ J_{h,x} &= \tfrac{1}{2}(J_{h,+} + J_{h,-}), \\ J_{e,y} &= \tfrac{1}{2}(J_{h,+} - J_{h,-}). \end{aligned} \tag{6.3}$$

Thus we can rewrite Eq. 6.1 as

$$H_1 \sim \widehat{O} \cdot (\mathbf{k} \cdot \mathbf{k}). \tag{6.4}$$

As shown in section 3.4 the SR exchange of Γ_3^+ symmetry is given by

$$H_3 \sim \tfrac{1}{6}(\mathbf{J_e} \cdot \mathbf{J_h} - 3J_{e,z}J_{h,z})(\mathbf{k} \cdot \mathbf{k} - 3k_z^2) + \tfrac{1}{2}(J_{e,x}J_{h,x} - J_{e,y}J_{h,y})(k_x^2 - k_y^2), \tag{6.5}$$

In Eq. 6.5 we find in addition to $\widehat{O}$ the spin operators

$$J_{e,z}J_{h,z} \stackrel{!}{=} \overline{O}, \tag{6.6}$$

$$\begin{aligned} J_{e,x}J_{h,x} - J_{e,y}J_{h,y} &= \tfrac{1}{2} \quad (J_{e,+}J_{h,+} + J_{e,-}J_{h,-}) \\ &\stackrel{!}{=} \widetilde{O}. \end{aligned} \tag{6.7}$$

Thus we can rewrite Eq. 3.40 as

$$\begin{aligned} H_3 \sim & \ \tfrac{1}{6} \ (\mathbf{J_h}\cdot\mathbf{J_h} - 3J_{e,z}J_{h,z})\cdot(\mathbf{k}\cdot\mathbf{k} - 3k_z^2) + \tfrac{1}{2}(J_{e,x}J_{h,x} - J_{e,y}J_{h,y})\cdot(k_x^2 - k_y^2) \\ = & \ \tfrac{1}{6} \ (\widehat{O} - 3\overline{O})\cdot(\mathbf{k}\cdot\mathbf{k} - 3k_z^2) + \tfrac{1}{2}\,\widetilde{O}\cdot(k_x^2 - k_y^2). \end{aligned} \tag{6.8}$$

The exchange of Γ_5^+ is given by

$$\begin{aligned} H_5 \sim \quad & (J_{e,y}J_{h,z} \quad + J_{e,z}J_{h,y})\cdot(k_y k_z) \\ & + (J_{e,z}J_{h,x} \quad + J_{e,x}J_{h,z})\cdot(k_z k_x) \\ & + (J_{e,x}J_{h,y} \quad + J_{e,y}J_{h,x})\cdot(k_x k_y) \end{aligned}$$

and remains to be rewritten. It contains the spin operators

$$\begin{aligned} J_{e,y}J_{h,z} + J_{e,z}J_{h,y} = & \ -\tfrac{\mathrm{i}}{2} \ [(J_{e,+} - J_{e,-})J_{h,z} + J_{e,z}(J_{h,+} - J_{h,-})] \\ \stackrel{!}{=} & \ O_1 \quad , \end{aligned} \tag{6.9}$$

$$\begin{aligned} J_{e,z}J_{h,x} + J_{e,x}J_{h,z} = & \ \tfrac{1}{2} \ [J_{e,z}(J_{h,+} + J_{h,-}) + (J_{e,+} + J_{e,-})J_{h,z}] \\ \stackrel{!}{=} & \ O_2 \quad , \end{aligned} \tag{6.10}$$

$$\begin{aligned} J_{e,x}J_{h,y} + J_{e,y}J_{h,x} = & \ -\tfrac{\mathrm{i}}{2} \ [J_{e,+}J_{h,+} - J_{e,-}J_{h,-}] \\ \stackrel{!}{=} & \ O_3 \quad . \end{aligned} \tag{6.11}$$

and can expressed as

$$H_5 \sim \ O_1\cdot(k_y k_z) \ + \ O_2\cdot(k_z k_x) + O_3\cdot(k_x k_y). \tag{6.12}$$

To calculate the impact of the spin operators on the orthoexciton states, we start with the fundamental relations for single spins:

$$\begin{aligned} J_{e/h,+}\,|{\uparrow_{e/h}}\rangle &= 0 & J_{e/h,+}\,|{\downarrow_{e/h}}\rangle &= |{\uparrow_{e/h}}\rangle \\ J_{e/h,-}\,|{\downarrow_{e/h}}\rangle &= 0 & J_{e/h,-}\,|{\uparrow_{e/h}}\rangle &= |{\downarrow_{e/h}}\rangle \\ J_{e/h,z}\,|{\uparrow_{e/h}}\rangle &= \tfrac{1}{2}\,|{\uparrow_{e/h}}\rangle & J_{e/h,z}\,|{\downarrow_{e/h}}\rangle &= -\tfrac{1}{2}\,|{\downarrow_{e/h}}\rangle. \end{aligned}$$

Now we apply the spin operators to the electron-hole spin states. For $\widehat{O}$ we obtain:

$$\begin{aligned} \widehat{O}\,|{\uparrow_e,\uparrow_h}\rangle &= \ \ |{\uparrow_e,\uparrow_h}\rangle, \\ \widehat{O}\,|{\downarrow_e,\downarrow_h}\rangle &= \ \ |{\downarrow_e,\downarrow_h}\rangle, \\ \widehat{O}\,|{\uparrow_e,\downarrow_h}\rangle &= -|{\uparrow_e,\downarrow_h}\rangle + 2\,|{\downarrow_e,\uparrow_h}\rangle, \\ \widehat{O}\,|{\downarrow_e,\uparrow_h}\rangle &= -|{\downarrow_e,\uparrow_h}\rangle + 2\,|{\uparrow_e,\downarrow_h}\rangle. \end{aligned} \tag{6.13}$$

In the same fashion we find for $\overline{O}$ and $\widetilde{O}$:

$$\begin{aligned} \overline{O}\,|{\uparrow_e,\uparrow_h}\rangle &= \ \ \tfrac{1}{4}\,|{\uparrow_e,\uparrow_h}\rangle, \\ \overline{O}\,|{\downarrow_e,\downarrow_h}\rangle &= \ \ \tfrac{1}{4}\,|{\downarrow_e,\downarrow_h}\rangle, \\ \overline{O}\,|{\uparrow_e,\downarrow_h}\rangle &= -\tfrac{1}{4}\,|{\uparrow_e,\downarrow_h}\rangle, \\ \overline{O}\,|{\downarrow_e,\uparrow_h}\rangle &= -\tfrac{1}{4}\,|{\downarrow_e,\uparrow_h}\rangle, \end{aligned} \tag{6.14}$$

$$
\begin{aligned}
\widetilde{O}\,|{\uparrow_e},{\uparrow_h}\rangle &= \tfrac{1}{2}\,|{\downarrow_e},{\downarrow_h}\rangle,\\
\widetilde{O}\,|{\downarrow_e},{\downarrow_h}\rangle &= \tfrac{1}{2}\,|{\uparrow_e},{\uparrow_h}\rangle,\\
\widetilde{O}\,|{\uparrow_e},{\downarrow_h}\rangle &= \;0,\\
\widetilde{O}\,|{\downarrow_e},{\uparrow_h}\rangle &= \;0.
\end{aligned}
\tag{6.15}
$$

The results for O_1, O_2, and O_3 are given by:

$$
\begin{aligned}
O_1\,|{\uparrow_e},{\uparrow_h}\rangle &= \;\;\tfrac{\mathtt{i}}{4}(|{\downarrow_e},{\uparrow_h}\rangle + |{\uparrow_e},{\downarrow_h}\rangle),\\
O_1\,|{\downarrow_e},{\downarrow_h}\rangle &= \;\;\tfrac{\mathtt{i}}{4}(|{\uparrow_e},{\downarrow_h}\rangle + |{\downarrow_e},{\uparrow_h}\rangle),\\
O_1\,|{\uparrow_e},{\downarrow_h}\rangle &= -\tfrac{\mathtt{i}}{4}(|{\downarrow_e},{\downarrow_h}\rangle + |{\uparrow_e},{\uparrow_h}\rangle),\\
O_1\,|{\downarrow_e},{\uparrow_h}\rangle &= -\tfrac{\mathtt{i}}{4}(|{\uparrow_e},{\uparrow_h}\rangle + |{\downarrow_e},{\downarrow_h}\rangle),\\
\\
O_2\,|{\uparrow_e},{\uparrow_h}\rangle &= \;\;\tfrac{1}{4}(|{\uparrow_e},{\downarrow_h}\rangle + |{\downarrow_e},{\uparrow_h}\rangle),\\
O_2\,|{\downarrow_e},{\downarrow_h}\rangle &= -\tfrac{1}{4}(|{\downarrow_e},{\uparrow_h}\rangle + |{\uparrow_e},{\downarrow_h}\rangle),\\
O_2\,|{\uparrow_e},{\downarrow_h}\rangle &= \;\;\tfrac{1}{4}(|{\uparrow_e},{\uparrow_h}\rangle + |{\downarrow_e},{\downarrow_h}\rangle),\\
O_2\,|{\downarrow_e},{\uparrow_h}\rangle &= -\tfrac{1}{4}(|{\downarrow_e},{\downarrow_h}\rangle + |{\uparrow_e},{\uparrow_h}\rangle),\\
\\
O_3\,|{\uparrow_e},{\uparrow_h}\rangle &= \;\;\tfrac{\mathtt{i}}{2}\,|{\downarrow_e},{\downarrow_h}\rangle,\\
O_3\,|{\downarrow_e},{\downarrow_h}\rangle &= -\tfrac{\mathtt{i}}{2}\,|{\uparrow_e},{\uparrow_h}\rangle,\\
O_3\,|{\uparrow_e},{\downarrow_h}\rangle &= \;\;0,\\
O_3\,|{\downarrow_e},{\uparrow_h}\rangle &= \;\;0.
\end{aligned}
\tag{6.16}
$$

Using the equations above, we can evaluate the impact of the spin operators on the orthoexciton states $|\,O_{yz}\rangle, |\,O_{zx}\rangle, |\,O_{xy}\rangle$, which we write as:

$$
\begin{aligned}
&|\,O_{yz}\rangle =\\
&\tfrac{1}{\sqrt{6}}\phi_{c,s}\left[\phi_{v,yz}(|{\uparrow_e},{\downarrow_h}\rangle - |{\downarrow_e},{\uparrow_h}\rangle) + \mathtt{i}\phi_{v,zx}(|{\uparrow_e},{\downarrow_h}\rangle + |{\downarrow_e},{\uparrow_h}\rangle) + \phi_{v,xy}(|{\uparrow_e},{\uparrow_h}\rangle + |{\downarrow_e},{\downarrow_h}\rangle)\right],\\
&|\,O_{zx}\rangle =\\
&-\tfrac{\mathtt{i}}{\sqrt{6}}\phi_{c,s}\left[\phi_{v,yz}(|{\uparrow_e},{\downarrow_h}\rangle + |{\downarrow_e},{\uparrow_h}\rangle) + \mathtt{i}\phi_{v,zx}(|{\uparrow_e},{\downarrow_h}\rangle - |{\downarrow_e},{\uparrow_h}\rangle) + \phi_{v,xy}(|{\uparrow_e},{\uparrow_h}\rangle - |{\downarrow_e},{\downarrow_h}\rangle)\right],\\
&|\,O_{xy}\rangle =\\
&-\tfrac{1}{\sqrt{6}}\phi_{c,s}\left[\phi_{v,yz}(|{\downarrow_e},{\downarrow_h}\rangle + |{\uparrow_e},{\uparrow_h}\rangle) - \mathtt{i}\phi_{v,zx}(|{\uparrow_e},{\uparrow_h}\rangle - |{\downarrow_e},{\downarrow_h}\rangle) + \phi_{v,xy}(|{\downarrow_e},{\uparrow_h}\rangle - |{\uparrow_e},{\downarrow_h}\rangle)\right].
\end{aligned}
$$

Using Eq. 6.13 we find for $\widehat{O}$:

$$\begin{aligned}
\widehat{O} \mid O_{yz}\rangle = \; & \tfrac{1}{\sqrt{6}}\phi_{c,s}\Big[(\phi_{v,yz}+\mathtt{i}\phi_{v,zx})(|{\downarrow_e},{\uparrow_h}\rangle - \tfrac{1}{2}\,|{\uparrow_e},{\downarrow_h}\rangle) \\
& -(\phi_{v,yz}-\mathtt{i}\phi_{v,zx})(|{\uparrow_e},{\downarrow_h}\rangle - \tfrac{1}{2}\,|{\downarrow_e},{\uparrow_h}\rangle) + \phi_{v,xy}\tfrac{1}{2}(|{\uparrow_e},{\uparrow_h}\rangle + |{\downarrow_e},{\downarrow_h}\rangle)\Big], \\
\widehat{O} \mid O_{zx}\rangle = & -\tfrac{\mathtt{i}}{\sqrt{6}}\phi_{c,s}\Big[(\phi_{v,yz}+\mathtt{i}\phi_{v,zx})(|{\downarrow_e},{\uparrow_h}\rangle - \tfrac{1}{2}\,|{\uparrow_e},{\downarrow_h}\rangle) \\
& +(\phi_{v,yz}-\mathtt{i}\phi_{v,zx})(|{\uparrow_e},{\downarrow_h}\rangle - \tfrac{1}{2}\,|{\downarrow_e},{\uparrow_h}\rangle) + \tfrac{1}{2}\phi_{v,xy}(|{\uparrow_e},{\uparrow_h}\rangle - |{\downarrow_e},{\downarrow_h}\rangle)\Big], \\
\widehat{O} \mid O_{xy}\rangle = & -\tfrac{1}{2\sqrt{6}}\phi_{c,s}\Big[(\phi_{v,yz}+\mathtt{i}\phi_{v,zx})\,|{\downarrow_e},{\downarrow_h}\rangle \\
& +(\phi_{v,yz}-\mathtt{i}\phi_{v,zx})\,|{\uparrow_e},{\uparrow_h}\rangle + \phi_{v,xy}3(|{\uparrow_e},{\downarrow_h}\rangle - |{\downarrow_e},{\uparrow_h}\rangle)\Big].
\end{aligned} \tag{6.17}$$

For $\overline{O}$ we find with Eq. 6.14:

$$\begin{aligned}
\overline{O} \mid O_{yz}\rangle = \; & \tfrac{1}{4\sqrt{6}}\phi_{c,s}\Big[\phi_{v,yz}(-|{\uparrow_e},{\downarrow_h}\rangle + |{\downarrow_e},{\uparrow_h}\rangle) \\
& -\mathtt{i}\phi_{v,zx}(|{\uparrow_e},{\downarrow_h}\rangle + |{\downarrow_e},{\uparrow_h}\rangle) + \phi_{v,xy}(|{\uparrow_e},{\uparrow_h}\rangle + |{\downarrow_e},{\downarrow_h}\rangle)\Big], \\
\overline{O} \mid O_{zx}\rangle = & -\tfrac{\mathtt{i}}{4\sqrt{6}}\phi_{c,s}\Big[-\phi_{v,yz}(|{\uparrow_e},{\downarrow_h}\rangle + |{\downarrow_e},{\uparrow_h}\rangle) \\
& +\mathtt{i}\phi_{v,zx}(-|{\uparrow_e},{\downarrow_h}\rangle + |{\downarrow_e},{\uparrow_h}\rangle) + \phi_{v,xy}(|{\uparrow_e},{\uparrow_h}\rangle - |{\downarrow_e},{\downarrow_h}\rangle)\Big], \\
\overline{O} \mid O_{xy}\rangle = & -\tfrac{1}{4\sqrt{6}}\phi_{c,s}\Big[\phi_{v,yz}(|{\downarrow_e},{\downarrow_h}\rangle + |{\uparrow_e},{\uparrow_h}\rangle) \\
& -\mathtt{i}\phi_{v,zx}(|{\uparrow_e},{\uparrow_h}\rangle - |{\downarrow_e},{\downarrow_h}\rangle) + \phi_{v,xy}(-|{\downarrow_e},{\uparrow_h}\rangle + |{\uparrow_e},{\downarrow_h}\rangle)\Big].
\end{aligned} \tag{6.18}$$

The operator $\widetilde{O}$ transforms the spins as:

$$\begin{aligned}
\widetilde{O} \mid O_{yz}\rangle = \; & \tfrac{1}{2\sqrt{6}}\phi_{c,s}\Big[\phi_{v,xy}(|{\uparrow_e},{\uparrow_h}\rangle + |{\downarrow_e},{\downarrow_h}\rangle)\Big], \\
\widetilde{O} \mid O_{zx}\rangle = \; & \tfrac{\mathtt{i}}{2\sqrt{6}}\phi_{c,s}\Big[\phi_{v,xy}(|{\uparrow_e},{\uparrow_h}\rangle - |{\downarrow_e},{\downarrow_h}\rangle)\Big], \\
\widetilde{O} \mid O_{xy}\rangle = & -\tfrac{1}{2\sqrt{6}}\phi_{c,s}\Big[(\phi_{v,yz}+\mathtt{i}\phi_{v,zx})\,|{\uparrow_e},{\uparrow_h}\rangle + (\phi_{v,yz}-\mathtt{i}\phi_{v,zx})\,|{\downarrow_e},{\downarrow_h}\rangle)\Big].
\end{aligned} \tag{6.19}$$

Finally, for O_1, O_2, and O_3 we find:

$$
\begin{aligned}
O_1 \mid O_{yz}\rangle = \;& \tfrac{1}{2\sqrt{6}}\phi_{c,s}\Big[-\mathtt{i}2(\phi_{v,yz}+\mathtt{i}\phi_{v,zx})(|{\downarrow_e},{\downarrow_h}\rangle+|{\uparrow_e},{\uparrow_h}\rangle)\\
&+\tfrac{\mathtt{i}}{2}(\phi_{v,yz}-\mathtt{i}\phi_{v,zx})(|{\uparrow_e},{\uparrow_h}\rangle+|{\downarrow_e},{\downarrow_h}\rangle)+\mathtt{i}\phi_{v,xy}(|{\downarrow_e},{\uparrow_h}\rangle+|{\uparrow_e},{\downarrow_h}\rangle)\Big],\\
O_1 \mid O_{zx}\rangle = & -\tfrac{1}{4\sqrt{6}}\phi_{c,s}\Big[(\phi_{v,yz}+\mathtt{i}\phi_{v,zx})(|{\downarrow_e},{\downarrow_h}\rangle+|{\uparrow_e},{\uparrow_h}\rangle)\\
&+(\phi_{v,yz}-\mathtt{i}\phi_{v,zx})(|{\uparrow_e},{\uparrow_h}\rangle+|{\downarrow_e},{\downarrow_h}\rangle)\Big],\\
O_1 \mid O_{xy}\rangle = & -\tfrac{\mathtt{i}}{4\sqrt{6}}\phi_{c,s}\Big[(\phi_{v,yz}+\mathtt{i}\phi_{v,zx})(|{\uparrow_e},{\downarrow_h}\rangle+|{\downarrow_e},{\uparrow_h}\rangle)\\
&+(\phi_{v,yz}-\mathtt{i}\phi_{v,zx})(|{\downarrow_e},{\uparrow_h}\rangle+|{\uparrow_e},{\downarrow_h}\rangle)\Big],
\end{aligned}
$$

$$
\begin{aligned}
O_2 \mid O_{yz}\rangle = \;& \tfrac{1}{2\sqrt{6}}\phi_{c,s}\Big[\tfrac{1}{2}(\phi_{v,yz}+\mathtt{i}\phi_{v,zx})(|{\uparrow_e},{\uparrow_h}\rangle-|{\downarrow_e},{\downarrow_h}\rangle)\\
&+\tfrac{1}{2}(\phi_{v,yz}-\mathtt{i}\phi_{v,zx})(|{\downarrow_e},{\downarrow_h}\rangle-|{\uparrow_e},{\uparrow_h}\rangle)+\phi_{v,xy}(|{\uparrow_e},{\downarrow_h}\rangle+|{\downarrow_e},{\uparrow_h}\rangle)\Big],\\
O_2 \mid O_{zx}\rangle = & -\tfrac{\mathtt{i}}{2\sqrt{6}}\phi_{c,s}\Big[\tfrac{1}{2}(\phi_{v,yz}+\mathtt{i}\phi_{v,zx})(|{\uparrow_e},{\uparrow_h}\rangle-|{\downarrow_e},{\downarrow_h}\rangle)\\
&-\tfrac{1}{2}(\phi_{v,yz}-\mathtt{i}\phi_{v,zx})(|{\downarrow_e},{\downarrow_h}\rangle-|{\uparrow_e},{\uparrow_h}\rangle)+\phi_{v,xy}(|{\uparrow_e},{\downarrow_h}\rangle+|{\downarrow_e},{\uparrow_h}\rangle)\Big],\\
O_2 \mid O_{xy}\rangle = & -\tfrac{1}{4\sqrt{6}}\phi_{c,s}\Big[-(\phi_{v,yz}+\mathtt{i}\phi_{v,zx})(|{\downarrow_e},{\uparrow_h}\rangle+|{\uparrow_e},{\downarrow_h}\rangle)\\
&+(\phi_{v,yz}-\mathtt{i}\phi_{v,zx})(|{\uparrow_e},{\downarrow_h}\rangle+|{\downarrow_e},{\uparrow_h}\rangle)\Big],
\end{aligned}
\tag{6.20}
$$

$$
\begin{aligned}
O_3 \mid O_{yz}\rangle = & -\tfrac{\mathtt{i}}{2\sqrt{6}}\phi_{c,s}\Big[\phi_{v,xy}(|{\uparrow_e},{\uparrow_h}\rangle+|{\downarrow_e},{\downarrow_h}\rangle)],\\
O_3 \mid O_{zx}\rangle = & -\tfrac{1}{2\sqrt{6}}\phi_{c,s}[\phi_{v,xy}(|{\downarrow_e},{\downarrow_h}\rangle-|{\uparrow_e},{\uparrow_h}\rangle)\Big],\\
O_3 \mid O_{xy}\rangle = \;& \tfrac{\mathtt{i}}{2\sqrt{6}}\phi_{c,s}\Big[(\phi_{v,yz}+\mathtt{i}\phi_{v,zx})\,|{\uparrow_e},{\uparrow_h}\rangle-(\phi_{v,yz}-\mathtt{i}\phi_{v,zx})\,|{\downarrow_e},{\downarrow_h}\rangle\Big].
\end{aligned}
$$

Now we can evaluate the explicit matrix elements of the exchange matrices. Starting with H_1 we calculate:

$$
\begin{aligned}
\langle O_{ij} \mid H_1 \mid O_{i'j'}\rangle &\sim \langle O_{ij} \mid (\mathbf{k}\cdot\mathbf{k})\cdot\widehat{O} \mid O_{i'j'}\rangle\\
&= (k_x^2+k_y^2+k_z^2)\langle O_{ij} \mid \widehat{O} \mid O_{i'j'}\rangle.
\end{aligned}
\tag{6.21}
$$

The Wannier functions are orthonormal ($\phi_{v,ij} \cdot \phi_{v,i'j'} = \delta_{ij,i'j'}$). For $ij = i'j' = yz$ we find

$$\begin{aligned}
&(k_x^2 + k_y^2 + k_z^2)\langle O_{yz} \mid \widehat{O} \mid O_{yz}\rangle \\
=&\tfrac{1}{6}(k_x^2 + k_y^2 + k_z^2)\Big[\tfrac{3}{2}(\langle\uparrow_e,\downarrow_h| -\langle\downarrow_e,\uparrow_h|)(|\downarrow_e,\uparrow_h\rangle - |\uparrow_e,\downarrow_h\rangle) \\
&+ \tfrac{1}{2}(\langle\uparrow_e,\downarrow_h| +\langle\downarrow_e,\uparrow_h|)(|\downarrow_e,\uparrow_h\rangle + |\uparrow_e,\downarrow_h\rangle) \\
&+ \tfrac{1}{2}(\langle\uparrow_e,\uparrow_h| +\langle\downarrow_e,\downarrow_h|)(|\uparrow_e,\uparrow_h\rangle + |\downarrow_e,\downarrow_h\rangle)\Big] \\
=&\ \ \tfrac{1}{6}(k_x^2 + k_y^2 + k_z^2)\Big[\tfrac{3}{2}(0-1-1-0) + \tfrac{1}{2}(0+1+1+0) + \tfrac{1}{2}(1+0+0+1)\Big] \\
=&-\tfrac{1}{6}(k_x^2 + k_y^2 + k_z^2).
\end{aligned} \tag{6.22}$$

This holds for all diagonal elements. For $ij \neq i'j$ we find:

$$(k_x^2 + k_y^2 + k_z^2)\langle O_{ij} \mid \widehat{O} \mid O_{i'j'}\rangle = 0. \tag{6.23}$$

Consequently the matrix representation of the SR exchange of Γ_1^+ symmetry.

$$J_1 = \Delta_1 \cdot \begin{pmatrix} k_x^2 + k_y^2 + k_z^2 & 0 & 0 \\ 0 & k_x^2 + k_y^2 + k_z^2 & 0 \\ 0 & 0 & k_x^2 + k_y^2 + k_z^2 \end{pmatrix} = \Delta_1 k^2 \cdot \mathbf{1}. \tag{6.24}$$

Using the relations 6.14 and 6.15 we derive the matrix form of H_3. In addition to $\langle O_{ij} \mid \widehat{O} \mid O_{i'j'}\rangle$ we have to evaluate $\langle O_{ij} \mid \overline{O} \mid O_{i'j'}\rangle$ and $\langle O_{ij} \mid \widetilde{O} \mid O_{i'j'}\rangle$

$$\begin{aligned}
\langle O_{yz} \mid \overline{O} \mid O_{yz}\rangle &= -\tfrac{2}{18}, && (6.25)\\
\langle O_{zx} \mid \overline{O} \mid O_{zx}\rangle &= -\tfrac{2}{18}, && (6.26)\\
\langle O_{xy} \mid \overline{O} \mid O_{xy}\rangle &= \ \ \tfrac{1}{18}, && (6.27)\\
\langle O_{ij} \mid \overline{O} \mid O_{i'j'}\rangle &= \ \ 0 \qquad ij \neq i'j', && (6.28)
\end{aligned}$$

$$\begin{aligned}
\langle O_{yz} \mid \widetilde{O} \mid O_{yz}\rangle &= \ \ \tfrac{1}{6}, && (6.29)\\
\langle O_{zx} \mid \widetilde{O} \mid O_{zx}\rangle &= -\tfrac{1}{6}, && (6.30)\\
\langle O_{xy} \mid \widetilde{O} \mid O_{xy}\rangle &= \ \ 0, && (6.31)\\
\langle O_{ij} \mid \widetilde{O} \mid O_{i'j'}\rangle &= \ \ 0 \qquad ij \neq i'j'. && (6.32)
\end{aligned}$$

Using Eq. 6.8 this gives us for the diagonal elements of the exchange matrix

$$\begin{aligned}
&\langle O_{yz} \mid H_3 \mid O_{yz}\rangle \\
&\sim \tfrac{1}{6}(-\tfrac{1}{6} - 3\tfrac{-2}{18})(k_x^2 + k_y^2 - 2k_z^2) + \tfrac{1}{2}\cdot\tfrac{1}{6}(k_x^2 - k_y^2) \\
&= \tfrac{1}{18}(2k_x^2 - k_y^2 - k_z^2), \\
&\\
&\langle O_{zx} \mid H_3 \mid O_{zx}\rangle \\
&\sim \tfrac{1}{6}(-\tfrac{1}{6} - 3\tfrac{-2}{18})(k_x^2 + k_y^2 - 2k_z^2) + \tfrac{1}{2}\cdot\tfrac{-1}{6}(k_x^2 - k_y^2) \\
&= \tfrac{1}{18}(-k_x^2 + 2k_y^2 - k_z^2), \\
&\\
&\langle O_{xy} \mid H_3 \mid O_{xy}\rangle \\
&\sim \tfrac{1}{6}(-\tfrac{1}{6} - 3\tfrac{1}{18})(k_x^2 + k_y^2 - 2k_z^2) \\
&= \tfrac{1}{18}(-k_x^2 - k_y^2 + 2k_z^2).
\end{aligned} \tag{6.33}$$

The off-diagonal elements are zero and we end up with the matrix form of H_3:

$$J_3 = \Delta_3 \cdot \begin{pmatrix} 2k_x^2 - k_y^2 - k_z^2 & 0 & 0 \\ 0 & 2k_y^2 - k_x^2 - k_z^2 & 0 \\ 0 & 0 & 2k_z^2 - k_x^2 - k_y^2 \end{pmatrix}. \tag{6.34}$$

This brings us to term of Γ_5^+ symmetry. Using the relations in Eq. 6.16 we evaluate $\langle O_{ij} \mid O_1 + O_2 + O_3 \mid O_{i'j'}\rangle$ and obtain

$$\langle O_{ij} \mid O_1 + O_2 + O_3 \mid O_{i'j'}\rangle = 0 \qquad ij = i'j'. \tag{6.35}$$

For the off-diagonal terms we explicitly treat one example.[1]

$$\begin{aligned}
&\langle O_{xy} \mid O_1 \cdot k_y k_z + O_2 \cdot k_z k_x + O_3 \cdot k_x k_y \mid O_{yz}\rangle \\
&\sim -\Big[\tfrac{-\mathtt{i}}{4}(\phi_{v,yz} + \mathtt{i}\phi_{v,zx})^*(\phi_{v,yz} + \mathtt{i}\phi_{v,zx})k_y k_z - \tfrac{1}{4}(\phi_{v,yz} + \mathtt{i}\phi_{v,zx})^*(\phi_{v,yz} + \mathtt{i}\phi_{v,zx})k_z k_x \\
&+ \tfrac{\mathtt{i}}{4}(\phi_{v,yz} - \mathtt{i}\phi_{v,zx})^*(\phi_{v,yz} - \mathtt{i}\phi_{v,zx})k_y k_z - \tfrac{1}{4}(\phi_{v,yz} - \mathtt{i}\phi_{v,zx})^*(\phi_{v,yz} - \mathtt{i}\phi_{v,zx})k_y k_z\Big] \\
&= k_z k_x.
\end{aligned}$$

All other off-diagonal terms are evaluated in the same fashion. Finally, this gives us the exchange matrix of Γ_5^+ symmetry:

$$J_5 = \Delta_5 \cdot \begin{pmatrix} 0 & k_x k_y & k_x k_z \\ k_x k_y & 0 & k_y k_z \\ k_x k_z & k_y k_z & 0 \end{pmatrix}. \tag{6.36}$$

[1] In principle, the other elements can also be derived from symmetry considerations and cyclic permutations

Bibliography

[1] C. H. Bennet, Physics Today **24**, 30 (1995).

[2] D. P. DiVincenzo, Science **27**, 255 (1995).

[3] D. Bouwmeester, A. Ekert, & A. Zeilinger, *The Physics of Quantum Information* (Springer, Berlin, 2000).

[4] C. Kittel, *Introduction to Solid State Physics* (John Wiley & Sons, 1995).

[5] J. J. Hopfield, Phys. Rev. **112**, 1555 (1958).

[6] C. F. Klingshirn, *Semiconductor Optics* (Spinger-Verlag, Berlin Heidelberg, 1995).

[7] M. S. Skolnick, T. A. Fisher, & D. M. Whittaker, Semicond. Sci. Technol. **13**, 645 (1998).

[8] L. C. Andreani, *Optical Transitions, Excitons, and Polaritons in Bulk and Low-Dimensional Semiconductor Structures*, 57– 112 (Kluwer Academic / Plenum Publishers, 1995).

[9] I. I. Rabi, Phys. Rev. **49**, 324 (1936).

[10] J. R. Jensen, P. Borri, W. Langbein, & J. M. Hvam, Appl. Phys. Lett. **76**, 3262 (2000).

[11] T. Baars, G. Dasbach, M. Bayer, & A. Forchel, Phys. Rev. B **63**, 165311 (2001).

[12] W. C. Tait, Phys. Rev. B **6**, 648 (1972).

[13] D. Fröhlich, A. Kulik, B. Uebbing, A. Mysyrowicz, V. Langer, H. Stolz, & W. von der Osten, Phys. Rev. Lett. **67**, 2343 (1991).

[14] A. P. Kotsyumakha, Y. N. Kuchner, & A. V. Pereligin, Rost Kristallov **VI** (1965).

[15] P. Markworth, R. Chang, Y. Sun, G. Wong, & J. Ketterson, J. Mat. Res. **6**, 914 (2001).

[16] K. Kawaguchi, R. Kita, M. Nishiyama, & T. Morishita, J. Cryst. Growth **143**, 221 (1994).

[17] Y. Sun, K. Rivkin, J. Chen, , J. B. Ketterson, P. Markworth, & R. P. Chang, Phys. Rev. B **66**, 245315 (2002).

[18] M. Hayashi & K. Katusuki, J. Phys. Soc. Jpn. **5**, 381 (1950).

[19] E. F. Gross & A. Karryev, Dokl. Akad. Nauk SSSR **84**, 471 (1952).

[20] M. Hayashi & K. Katsuki, J. Phys. Soc. Jpn. **7**, 599 (1952).

[21] J. Frenkel, Phys. Rev. **37**, 1276 (1931).

[22] G. H. Wannier, Phys. Rev. **52**, 191 (1937).

[23] R. J. Elliott, Phys. Rev. **108**, 1384 (1957).

[24] P. W. Baumeister, Phys. Rev. **121**, 359 (1961).

[25] V. T. Agekyan, phys. stat. sol. (a) **43**, 11 (1977).

[26] S. Nikitine, *Optical Properties of Solids*, chap. 9, 197 (Plenum, New York, 1969).

[27] R. J. Elliott, Phys. Rev. **124**, 340 (1961).

[28] E. F. Gross, B. P. Zakharchenya, & L. M. Kanskaya, Fiz. tverd. Tela **3**, 972 (1961).

[29] R. G. Waters, F. H. Pollak, R. H. Bruce, & H. Z. Cummins, Phys. Rev. B **21**, 1665 (1980).

[30] H. R. Trebin, H. Z. Cummins, & J. L. Birman, Phys. Rev. B **23**, 597 (1981).

[31] L. V. Keldysh & A. N. Kozlov, Sov. Phys. JETP **521**, 521 (1968).

[32] S. A. Moskalenko & D. W. Snoke, *Bose-Einstein Condensation of Excitons and Biexcitons* (Cambridge University Press, Cambridge, 2000).

[33] D. Snoke, J. P. Wolfe, & A. Mysyrowicz, Phys. Rev. Lett. **59**, 827 (1987).

[34] D. W. Snoke, J. P. Wolfe, & A. Mysyrowicz, Phys. Rev. Lett. **64**, 2543 (1990).

[35] D. W. Snoke, J. P. Wolfe, & A. Mysyrowicz, Phys. Rev. B **41**, 11171 (1990).

[36] J. L. Lin & J. P. Wolfe, Phys. Rev. Lett. **71**, 1222 (1993).

[37] K. E. O'Hara, L. Ó. Sólleabháin, & J. P. Wolfe, Phys. Rev. B **60**, 10565 (1999).

[38] L. V. Butov, A. L. Ivanov, A. Imamoglu, P. B. Littlewood, A. A. Shashkin, V. T. Dolgopolov, K. L. Campman, & A. C. Gossard, Phys. Rev. Lett. **86**, 5608 (2001).

[39] J. J. Baumberg, P. G. Savvidis, R. M. Stevenson, A. I. Tartakovskii, M. S. Skolnick, D. M. Whittaker, & J. S. Roberts, Phys. Rev. B **62**, R16247 (2000).

[40] D. Porras, C. Ciuti, J. J. Baumberg, & C. Tejedor, Phys. Rev. B **66**, 085304 (2002).

[41] N. Naka & N. Nagasawa, phys. stat. sol. B **238**, 397 (2003).

[42] D. P. Trauernicht, J. P. Wolfe, & A. Mysyrowicz, Phys. Rev. B **34**, 2561 (1986).

[43] W. Ketterle, Physics Today 30 (December 1999).

[44] J. Dahl & A. Switendick, J. Phys. Chem. Solids **27**, 931 (1965).

[45] L. Kleinman & K. Mednick, Phys. Rev. B **21**, 1549 (1980).

[46] G. F. Koster, J. O. Dimmock, R. G. Wheeler, & H. Statz, *Properties of the Thirty-Two Point Groups* (M.I.T- Press, Cambridge, Massachusetts, 1963).

[47] A. Goltztené & C. Schwab, *Landolt-Börnstein*, vol. 17e, chap. Physics of Non-Tetrahedrally Bonded Elements and Binary Compounds I, 144 (Springer, Berlin, 1983).

[48] G. Kuwabara, M. Tanaka, & H. Fukutani, Solid State Commun. **21**, 599 (1977).

[49] P. D. Bloch & C. Schwab, Phys. Rev. Lett. **41**, 514 (1978).

[50] C. Uihlein, D. Fröhlich, & R. Kenklies, Phys. Rev. B **23**, 2731 (1981).

[51] D. Fröhlich, R. Kenklies, C. Uihlein, & C. Schwab, Phys. Rev. Lett. **43**, 1260 (1979).

[52] J. W. Hodby, T. Jenkins, C. Schwab, H. Tamura, & D. Trivich, J. Phys. C **9**, 1429 (1976).

[53] G. M. Kavoulakis, Y.-C. Chang, & G. Baym, Phys. Rev. B **55**, 7593 (1997).

[54] P. Y. Yu & Y. R. Shen, Phys. Rev. B **12**, 1377 (1975).

[55] D. W. Snoke, D. Braun, & M. Cardona, Phys. Rev. B **44**, 2991 (1991).

[56] L. Hanke, D. Fröhlich, A. L. Ivanov, P. B. Littlewood, & H. Stolz, Phys. Rev. Lett. **83**, 4365 (1999).

[57] M. Bayer & A. Forchel, Phys. Rev. B **65**, 041308 (2002).

[58] P. Borri, W. Langbein, S. Schneider, U. Woggon, R. Sellin, D. Ouyang, & D. Bimberg, Phys. Rev. Lett. **87**, 157401 (2001).

[59] L. Hanke, *Transformation Von Licht in Wärme in Kristallen*, Ph.D. thesis, Universität Dortmund (1999).

[60] C. F. Klingshirn, *Semiconductor Optics* (Springer Verlag, Heidelberg, New York, 1995).

[61] H. Stolz, Phys. Stat. Sol. B **173**, 99 (1992).

[62] V. Langer, H. Stolz, & W. von der Osten, Phys. Rev. B **51**, 2103 (1995).

[63] A. Mysyrowicz, D. Hulin, & F. A. Antonetti, Phys. Rev. Lett. **43**, 1123 (1979).

[64] K. Reimann & K. Syassen, Phys. Rev. B **39**, 11113 (1989).

[65] N. W. Ashcroft & N. D. Mermin, *Solid State Physics* (Holt, Rinehart and Winston, New York, 1976).

[66] A. Mysyrowicz, D. P. Trauernicht, J. P. Wolfe, & H. R. Trebin, Phys. Rev. B **27**, 2562 (1983).

[67] M. D. Lukin & A. Imamoglu, Phys. Rev. Lett. **84**, 1419 (2000).

[68] A. Imamoglu, Phys. Rev. Lett. **89**, 163602 (2002).

[69] A. B. Matsko, Y. V. Rostovtsev, H. Z. Cummins, & M. O. Scully, Phys. Rev. Lett. **84**, 5752 (2000).

[70] K.-J. Boller, A. Imamolu, & S. E. Harris, Phys. Rev. Lett. **66**, 2593 (1991).

[71] A. Kasapi, M. Jain, G. Y. Yin, & S. E. Harris, Phys. Rev. Lett. **74**, 2447 (1995).

[72] M. M. Kash, V. A. Sautenkov, A. S. Zibrov, L. Hollberg, G. R. Welch, M. D. Lukin, Y. Rostovtsev, E. S. Fry, & M. O. Scully, Phys. Rev. Lett. **82**, 5229 (1999).

[73] L. Hau, S. Harris, Z. Dutton, & C. Behroozi, Nature **397**, 594 (1999).

[74] C. Liu, Z. Dutton, C. Behroozi, & L. Hau, Nature **409**, 490 (2001).

[75] M. Fleischhauer & M. D. Lukin, Phys. Rev. Lett. **84**, 5094 (2000).

[76] D. F. Phillips, A. Fleischhauer, A. Mair, R. L. Walsworth, & M. D. Lukin, Phys. Rev. Lett. **86**, 783 (2001).

[77] A. V. Turukhin, V. S. Sudarshanam, M. S. Shahriar, J. A. Musser, B. S. Ham, & P. R. Hemmer, Phys. Rev. Lett. **88**, 023602 (2002).

[78] M. J. Frankel & J. L. Birman, Phys. Rev. A **15**, 2000 (1977).

[79] D. L. Johnson, Phys. Rev. Lett. **41**, 417 (1978).

[80] R. G. Ulbrich & G. W. Fehrenbach, Phsy. Rev. Lett. **43**, 963 (1979).

[81] D. Awschalom, D. Loss, & N. Samarth, *Semiconductor Spintronics and Quantum Computation* (Springer, Berlin, 2002).

[82] G. Dasbach, D. Fröhlich, H. Stolz, R. Klieber, D. Suter, & M. Bayer, Phys. Rev. Lett. **91**, 107401 (2003).

[83] K. Cho, Phys. Rev. B **14**, 4463 (1976).

[84] G. L. Bir & G. E. Pikus, *Symmetry and Strain-Induced Effects in Semiconductors* (John Wiley and Sons, New York, 1974).

[85] E. L. Ivchenko & G. E. Pikus, *Superlattices and Other Heterostructures* (Springer-Verlag, Berlin, 1995).

[86] M. Bayer, G. Ortner, O. Stern, A. Kuther, A. A. Gorbunov, A. Forchel, P. Hawrylak, S. Fafard, K. Hinzer, T. L. Reinecke, S. N. Walck, J. P. Reithmaier, F. Klopf, & F. Schäfer, Phys. Rev. B **65**, 195315 (2002).

[87] U. Rössler & H. R. Trebin, Phys. Rev. B **23**, 1961 (1981).

[88] I. Bronstein & K. Semendjajew, *Taschenbuch der Mathematik* (Nauka, Moskau, 1991).

[89] J. S. Schwinger, L. L. Deraad Jr., K. A. Milton, W.-Y. Tsai, & J. Schwinger, *Classical Electrodynamics* (Perseus Books, Reading, Massachusetts, 1998).

[90] S. A. Moskalenko, A. I. Bobyrysheva, & E. S. Kiselyova, phys. stat. sol. (b) **213**, 377 (1999).

[91] J. M. Luttinger, Phys. Rev. **102**, 1030 (1956).

[92] G. Dasbach, D. Fröhlich, H. Stolz, R. Klieber, D. Suter, & M. Bayer, phys. stat. sol. B **238**, 541 (2003).

[93] F. Bassani & M. Rovere, Solid State Commun. **19**, 887 (1976).

[94] D. Hulin, A. Mysyrowicz, & C. Benoît à la Guillame, Phys. Rev. Lett. **45**, 1970 (1980).

[95] A. Griffin, D. Snoke, & S. Stringari, *Bose-Einstein Condensation* (Cambridge University Press, Cambridge, 1995).

[96] T. Goto, M. Y. Shen, S. Koyama, & T. Yokouchi, Phys. Rev. B **55**, 7609 (1997).

[97] M. Y. Shen, T. Yokouchi, S. Koyama, & T. Goto, Phys. Rev. B **56**, 13066 (1997).

[98] N. Naka & N. Nagasawa, Phys. Rev. B **65**, 245203 (2002).

[99] G. Khitrova, H. M. Gibbs, F. Jahnke, M. Kira, & S. W. Koch, Review of Modern Physics **71**, 1591 (1999).

[100] V. Savona, L. C. Andreani, P. Schwendimann, & A. Quattropani, Solid State Comm. **93**, 733 (1995).

[101] V. Savona, C. Piermarocchi, A. Quattropani, P. Schwendimann, & F. Tassone, Phase Transitions **68**, 169 (1999).

[102] C. Weisbuch, M. Nishioka, A. Ishikawa, & Y. Arakawa, Phys. Rev. Lett. **69**, 3314 (1992).

[103] Le Si Dang, D. Heger, R. Andrè, F. Boef, & R. Romestain, Phys. Rev. Lett. **81**, 3920 (1998).

[104] D. G. Lidzey, D. D. C. Bradley, T. Virgili, A. Armitage, M. S. Skolnick, & S. Walker, Phys. Rev. Lett. **82**, 3316 (1999).

[105] D. G. Lidzey, D. Bradley, M. Skolnick, T. Virgili, S. Walker, & D. Whittaker, Nature **395**, 53 (1998).

[106] R. Houdré, C. Weisbuch, R. P. Stanley, U. Oesterle, P. Pellandini, & M. Ilegems, Phys. Rev. Lett. **73**, 2043 (1994).

[107] J. J. Hopfield & D. G. Thomas, Phys. Rev. **132**, 563 (1963).

[108] B. Hönerlage, A. Bivas, & V. Phach, Phys. Rev. Lett. **41**, 49 (1978).

[109] D. Fröhlich, E. Mohler, & P. Wiesner, Phys. Rev. Lett. **26**, 554 (1971).

[110] P. G. Savvidis, *Polariton Dynamics in Semiconductor Microcavities*, Ph.D. thesis, University of Southampton (2001).

[111] J. J. Baumberg, *Spin Condensates in Semiconductor Microcavities*, chap. 6, 195–219 (Springer, 2002).

[112] S. Pau, G. Björk, J. Jacobson, H. Cao, & Y. Yamamoto, Phys. Rev. B **51**, 7090 (1995).

[113] A. Imamoglu, R. J. Ram, S. Pau, & Y. Yamamoto, Phys. Rev. A **53**, 4250 (1996).

[114] S. Pau, H. Cao, J. Jacobson, G. Björk, Y. Yamamoto, & A. Imamoglu, Phys. Rev. A **54**, 1789 (1996).

[115] M. Kira, F. Jahnke, S. W. Koch, J. D. Berger, D. V. Wick, T. R. Nelson Jr., G. Khitrova, & H. M. Gibbs, Phys. Rev. Lett. **79**, 5170 (1997).

[116] H. Cao, S. Pau, J. M. Jacobson, G. Björk, Y. Yamamoto, & A. Imamoglu, Phys. Rev. A **55**, 4632 (1997).

[117] P. Senellart & J. Bloch, Phys. Rev. Lett. **82**, 1233 (1999).

[118] F. Tassone, C. Piermarocchi, V. Savona, A. Quattropani, & P. Schwendimann, Phys. Rev. B **56**, 7554 (1997).

[119] M. Müller, J. Bleuse, & R. André, Phys. Rev. B **62**, 16886 (2000).

[120] T. Baars, M. Bayer, A. Forchel, F. Schäfer, & J. P. Reithmaier, Phys. Rev. B **61**, R2409 (2000).

[121] A. I. Tartakovskii, M. Emam-Ismail, R. M. Stevenson, M. S. Skolnick, V. N. Astratov, D. M. Whittaker, J. J. Baumberg, & J. S. Roberts, Phys. Rev. B **62**, 2283 (2000).

[122] P. Borri, J. R. Jensen, W. Langbein, & J. M. Hvam, Phys. Rev. B **61**, 13377 (2000).

[123] G. Cassabois, A. L. Triques, F. Bogani, C. Delalande, P. Roussignol, & C. Piermarocchi, Phys. Rev. B **61**, 1696 (2000).

[124] J. J. Baumberg, A. Armitage, M. S. Skolnick, & J. S. Roberts, Phys. Rev. Lett. **81**, 661 (1998).

[125] P. G. Savvidis, J. J. Baumberg, R. M. Stevenson, M. S. Skolnick, D. M. Whittaker, & J. S. Roberts, Phys. Rev. Lett. **84**, 1547 (2000).

[126] P. G. Savvidis, J. J. Baumberg, R. M. Stevenson, M. S. Skolnick, D. M. Whittaker, & J. S. Roberts, Phys. Rev. B **62**, 13278 (2000).

[127] R. Houdré, C. Weisbuch, R. P. Stanley, U. Oesterle, & M. Ilegems, Phys. Rev. Lett. **85**, 2793 (2000).

[128] A. Huynh, J. Tignon, O. Larsson, P. Roussignol, C. Delalande, R. André, R. Romestain, & L. S. Dang, Phys. Rev. Lett. **90**, 10640 (2003).

[129] C. Ciuti, P. Schwendimann, B. Deveaud, & A. Quattropani, Phys. Rev. B **62**, 4825 (2000).

[130] D. M. Whittaker, Phys. Rev. B **63**, 193305 (2001).

[131] R. M. Stevenson, V. N. Astratov, M. S. Skolnick, D. M. Whittaker, M. Emam-Ismail, A. I. Tartakovskii, P. G. Savvidis, J. J. Baumberg, & J. S. Roberts, Phys. Rev. Lett. **85**, 3680 (2000).

[132] A. I. Tartakovskii, D. N. Krizhanovskii, D. A. Kurysh, V. D. Kulakovskii, M. S. Skolnick, & J. S. Roberts, Phys. Rev. B **65**, 081308 (2002).

[133] C. Ciuti, P. Schwendimann, & A. Quattropani, Phys. Rev. B **63**, 041303 (2001).

[134] M. Saba, C. Ciuti, J. Bloch, V. Thierry-Mieg, R. André, L. S. Dang, S. Kundermann, A. Mura, G. Bongiovanni, J. Staehli, & B. Deveaud, Nature **414**, 731 (2001).

[135] J. Erland, V. Mizeikis, W. Langbein, J. R. Jensen, & J. M. Hvam, Phys. Rev. Lett. **86**, 5791 (2001).

[136] H. Deng, G. Weihs, C. Santori, J. Bloch, & Y. Yamamoto, Science **298**, 199 (2002).

[137] P. R. Eastham & P. B. Littlewood, Phys. Rev. B **64**, 235101 (2001).

[138] G. Malpuech, A. Kavokin, A. D. Carlo, & J. J. Baumberg, Phys. Rev. B **65**, 153310 (2002).

[139] G. Malpuech, A. Kavokin, J. J. Baumberg, M. Zamfirescu, & F. P. Lugli, Appl. Phys. Lett. **81**, 412 (2002).

[140] M. Zamfirescu, A. Kavokin, B. Gil, G. Malpuech, & M. Kaliteevski, Phys. Rev. B **65**, 161205 (2002).

[141] G. Dasbach, T. Baars, M. Bayer, A. Larionov, & A. Forchel, Phys. Rev. B **62**, 13076 (2000).

[142] R. Huang, F. Tassone, & Y. Yamamoto, Phys. Rev. B **61**, 7854 (2000).

[143] G. Dasbach, *Ultrakurzzeitspektroskopie an Halbleiter-Mikroresonatoren*, Master's thesis, Universität Würzburg (2000).

[144] J. Shah, *Ultrafast Spectroscopy of Semiconductors and Semiconductor Nanostructures* (Springer, Berlin, 1996).

[145] F. Jahnke, M. Kira, S. W. Koch, G. Khitrova, E. K. Lindmark, T. R. Nelson Jr., D. V. Wick, J. D. Berger, O. Lyngnes, H. M. Gibbs, & K. Tai, Phys. Rev. Lett. **77**, 5257 (1996).

[146] R. F. Schnabel, R. Zimmermann, D. Bimberg, H. Nickel, R. Lösch, & W. Schlapp, Phys. Rev. B **46**, 9873 (1992).

[147] X. Fan, H. Wang, H. Q. Hou, & B. E. Hammons, Phys. Rev. B **56**, 15256 (1997).

[148] J. Kikkawa, I. Smorchkova, N. Samarth, & D. Awschalom, Science **277**, 1284 (1997).

[149] J. A. Gupta, D. D. Awschalom, X. Peng, & A. P. Alivisatos, Phys. Rev. B **59**, 10421 (1999).

[150] M. Paillard, X. Marie, R. Renucci, T. Amand, A. Jbeli, & J. M. Gérard, Phys. Rev. Lett. **86**, 1634 (2001).

[151] H. W. van Kesteren, E. C. Cosman, W. A. J. A. van der Poel, & C. T. Foxon, Phys. Rev. B **41**, 5283 (1990).

[152] E. Blackwood, M. J. Snelling, R. T. Harley, S. R. Andrews, & C. T. B. Foxon, Phys. Rev. B **50**, 14246 (1994).

[153] M. Bayer, T. Gutbrod, A. Forchel, T. L. Reinecke, P. A. Knipp, R. Werner, & J. P. Reithmaier, Phys. Rev. Lett. **83**, 5374 (1999).

[154] J. Puls, M. Rabe, H.-J. Wünsche, & F. Henneberger, Phys. Rev. B **60**, 16303 (1999).

[155] L. Besombes, K. Kheng, & D. Martrou, Phys. Rev. Lett. **85**, 425 (2000).

[156] M. D. Martín, G. Aichmayr, L. Viña, & R. André, Phys. Rev. Lett. **89**, 077402 (2002).

[157] M. Martin, L. Vina, J. Son, & E. Mendez, Solid State Commun. **117**, 267 (2001).

[158] P. G. Lagoudakis, P. G. Savvidis, J. J. Baumberg, D. M. Whittaker, P. R. Eastham, M. S. Skolnick, & J. S. Roberts, Phys. Rev. B **65**, 161310 (2002).

[159] G. Dasbach, A. A. Dremin, M. Bayer, N. Gippius, V. Kulakovskii, & A. Forchel, Physica E **13**, 394 (2002).

[160] G. Dasbach, A. A. Dremin, M. Bayer, V. D. Kulakovskii, N. A. Gippius, & A. Forchel, Phys. Rev. B **65**, 245316 (2002).

[161] A. Kuther, M. Bayer, T. Gutbrod, A. Forchel, P. A. Knipp, T. L. Reinecke, & R. Werner, Phys. Rev. B **58**, 15744 (1998).

[162] A. I. Tartakovskii, V. D. Kulakovskii, A. Forchel, & J. P. Reithmaier, Phys. Rev. B **57**, 6807 (1998).

[163] D. Krizhanovskii, G. Dasbach, A. Dremin, V. Kulakovskii, N. Gippius, M. Bayer, & A. Forchel, Solid State Commun. **119**, 435 (2001).

[164] Y. R. Shen, *The Principles of Nonlinear Optics* (Wiley-Interscience, New York, 1984).

[165] G. Panzarini, L. Andreani, A. Armitage, D. Baxter, M. Skolnick, V. Astratov, J. Roberts, A. Kavokin, M. Vladimirova, & M. Kaliteevski, Phys. Solid State **41**, 1223 (1999).

[166] L. M. Woods & T. L. Reinecke, Phys. Rev. B **67**, 115335 (2003).

[167] C. Ciuti, V. Savona, C. Piermarocchi, A. Quattropani, & P. Schwendimann, Phys. Rev. B **58**, R10123 (1998).

[168] H. Nickolaus, H.-J. Wünsche, & F. Henneberger, Phys. Rev. Lett. **81**, 2586 (1998).

[169] M. Z. Maialle, E. A. de Andrada e Silva, & L. J. Sham, Phys. Rev. B **47**, 15776 (1993).

[170] in *Lecture Notes in Physics 531*H. Benisty, J. Gérard, R. Houdré, J. Rarity, & C. Weisbuch, eds., (Springer, New York, 1999).

[171] J. M. Gérard, D. Barrier, J. Y. Marzin, R. Kuszelewicz, L. Manin, E. Costard, V. Thierry-Mieg, & T. Rivera, Appl. Phys. Lett. **69**, 449 (1996).

[172] J. P. Reithmaier, M. Röhner, H. Zull, F. Schäfer, A. Forchel, P. A. Knipp, & T. L. Reinecke, Phys. Rev. Lett. **78**, 378 (1997).

[173] T. Gutbrod, M. Bayer, A. Forchel, P. A. Knipp, T. L. Reinecke, A. Tartakovskii, V. D. Kulakovskii, N. A. Gippius, & S. G. Tikhodeev, Phys. Rev. B **59**, 2223 (1999).

[174] M. Bayer, T. Gutbrod, J. P. Reithmaier, A. F. T. L. Reinecke, P. A. Knipp, A. A. Dremin, & V. D. Kulakovskii, Phys. Rev. Lett. **81**, 2582 (1998).

[175] M. Bayer, A. Forchel, T. Reinecke, P. Knipp, & S. Rudin, Phys. Stat. Sol. A **191**, 3 (2002).

[176] M. Bayer & A. Forchel, Adv. in Solid State Phys. **41**, 15 (2001).

[177] G. Dasbach, M. Bayer, M. Schwab, & A. Forchel, Semicond. Sci. Technol. **18**, 339 (2003).

[178] T. Gutbrod, M. Bayer, A. Forchel, J. P. Reithmaier, T. L. Reinecke, S. Rudin, & P. A. Knipp, Phys. Rev. B **57**, 9950 (1998).

[179] G. Guttroff, M. Bayer, J. P. Reithmaier, A. Forchel, P. A. Knipp, & T. L. Reinecke, Phys. Rev. B **64**, 155313 (2001).

[180] G. Guttroff, M. Bayer, A. Forchel, P. A. Knipp, & T. L. Reinecke, Phys. Rev. E **63**, 036611 (2001).

[181] V. Zhuk, D. Regelman, D. Gershoni, M. Bayer, J. Reithmaier, A. Forchel, P. Knipp, & T. Reinecke, Phys. Rev. B **66**, 115302 (2002).

[182] J. Gérard, B. Sermage, B. Gayral, B. Legrand, E. Costard, & V. Thierry-Mieg, Phys. Rev. Lett. **81**, 1110 (1998).

[183] M. Bayer, T. L. Reinecke, F. Weidner, A. Larionov, A. McDonald, & A. Forchel, Phys. Rev. Lett. **86**, 3168 (2001).

[184] G. Dasbach, M. Schwab, M. Bayer, & A. Forchel, Phys. Rev. B **64**, 201309(R) (2001).

[185] G. Dasbach, M. Schwab, D. N. Krizhanovskii, M. Bayer, & A. Forchel, Phys. Rev. B **66**, 210210 (2002).

[186] J. Faist, F. Capasso, D. L. Silvco, C. Sirtori, A. L. Hutchinson, & A. Cho., Science **264**, 553 (1994).

[187] M. Inguscio, S. Stringari, & C. E. Wieman, *Bose-Einstein Condensation in Atomic Gases* (Italian Physical Society, 1998).

[188] V. Türck, S. Rodt, O. Stier, R. Heitz, R. Engelhardt, U. W. Pohl, D. Bimberg, & R. Steingrüber, Phys. Rev. B **61**, 9944 (2000).

[189] J. Seufert, R. Weigand, G. Bacher, T. Kümmell, A. Forchel, K. Leonardi, & D. Hommel, Appl. Phys. Lett. **76**, 1872 (2000).

[190] A. Kavokin, G. Malpuech, A. Di Carlo, J. Baumberg, & M. Zamfirescu, Proceedings of ICPS 2002 .

Index

Symbols and abbreviations

symbol	**meaning**
$\|\downarrow_H\rangle$, $\|\downarrow_e\rangle$	hole state, electron state
$\| 0\rangle$	vacuum level
$a^\dagger, (a)$	creation (annihilation) operator of photon
α	absorption coefficient
A_{loc}	localization area
a_X	exciton Bohr radius
$b^\dagger, (b)$	creation (annihilation) operator of exciton
BEC	Bose-Einstein condensation
c_0	speed of light in vacuum (299 792 458 m s^{-1})
CCD	charged coupled devices camera
cw	continuous wave
c_x, c_y, c_z	electron-hole exchange parameters
D	density of states
D^*	density of vacant states
δ_i	strain parameter
Δ_Q	long range exchange parameter
Δ_i	exchange parameters of the short range exchange
$\Delta_{\mathbf{k}} = E_{P,\mathbf{k}} - E_{X,\mathbf{k}}$	detuning
δT	normalized differential transmission
ΔT	differential transmission
$\mathcal{E}$	electric field
e	unit charge ($1.602176 \cdot 10^{-19}$ C)
$\mathbf{e}$	polarization vector
ϵ_0	static dielectric constant
ϵ_∞	dielectric constant in the high frequency limit
E_b	binding energy
E_g	gap energy
E_P, E_X	photon energy, exciton energy
E_P^0	energy of fundamental cavity mode

E_{Ry}	Rydberg energy (13.60569 eV)
eV	electron volt ($1.602176 \cdot 10^{-19}$ J)
f	oscillator strength (unit less)
fs	femtosecond
FWHM	full width at half maximum
g	spin degeneracy
Γ	damping constant
γ	homogenous linewidth
H	Hamilton operator
$\hbar$	$h/2\pi = 1.054571 \cdot 10^{-34}$ J s$= 6.582118 \cdot 10^{-16}$ eV s
I	intensity
$\mathtt{i}$	complex unity
i	integer index $i = 0, 1, 2 \ldots$
J_{ex}	exchange interaction
J_{ex}^{Q}	long range quadrupole exchange
$J_{e(h)}$	momentum of electron (hole)
$J_{e(h),z}$	z-component of the momentum of electron (hole)
J_i	matrix representation of the short range exchange
j_l	Bessel function
$J_{\mathbf{k}}(t)$	exciton interband current
$\mathbf{k}$	momentum vector
$k_{\|\|}$	in-plane momentum
k_x, k_y	x, (y) component of the in-plane momentum $k_{\|\|}$
k_B	Boltzmann constant $1.38062 \cdot 10^{-23} JK^{-1}$
κ	imaginary part of the refractive index (extinction coefficient)
$\mathbf{K_i}$	reciprocal lattice vector
λ	wavelength
L_{eff}	effective cavity length
LR	long range exchange
L_R	resonator thickness
$\mathcal{M}$	Fourier transform of charge distribution
M	exciton angular momentum
MC	microcavity
m_0	electron mass ($9.109381 \cdot 10^{-31}$ kg)
m_e	effective electron mass
m_h	effective hole mass
m_r	reduced mass

m_P	effective photon mass
m_X	effective exciton mass
μ	chemical potential
$\tilde{N}(E_X)$	exciton distribution
$\widetilde{n}$	complex refractive index
n	real part of the refractive index
neV	nano electron volt
ns	nanosecond
N_X	number of excitons
$\mid O_{yz}\rangle, \mid O_{zx}\rangle, \mid O_{xy}\rangle$	orthoexciton basis states
$\mid P\rangle$	paraexciton state
P_{exc}	excitation power
P_{exc}^T	excitation power threshold
$P_{\mathbf{k}}$,$X_{\mathbf{k}}$	Hopfield coefficients
ϕ_v, ϕ_c	Wannier functions of valence and conduction band
ψ	angle of the polarization vector $\mathbf{e}$ (ψ=0 horizontal $\mathbf{e}$)
ps	picosecond
QA	quadrupole amplitude
q_m	quadrupole moment
QW	quantum well
r	reflectivity
$\mathbf{R}$	lattice vector
$\mathbf{r}$	position vector
$\tilde{\rho}$	density matrix
ρ	charge distribution
$\mid S\rangle$	singlet state
S_i	strain matrix
SR	short range exchange
T	temperature
$\mid T\rangle$	triplet state
T_0	linear transmission
T_1	population lifetime
T_2	dephasing time
T_2'	pure dephasing time
τ	delay time
τ_X	exciton radiative lifetime
τ_r	exciton relaxation time
θ_{probe}, θ_{exc}	probe and pump angle

T_{osci}	oscillation period
$\mid U\rangle$, $\mid L\rangle$	upper and lower polariton state
UPB, LPB	upper and lower polariton branch
v_P	phase velocity
v_g	group velocity
Ω_R	Rabi frequency
$\mid X\rangle$, $\mid P\rangle$	exciton state, photon state
χ	susceptibility
$Y_{l,m}$	spherical harmonics
ζ	energy distribution function

Acknowledgements

This work would not have been possible without the support of numerous collaborators, friends, sponsors et cetera. First of all, I thank Manfred Bayer (Prof. Dr. meanwhile) for his continued scientific guidance and help. I would not have tried without his support. I'm grateful to Prof. Dr. M. Tolan for refereeing this thesis. Prof. Dr. D. Fröhlich offered me deepest insights into the Cu_2O-universe. I profited from his extensive experience, thank you. A special thanks to Brian Patton for correcting the linguistic errors of this work.

Scientific support came from many sides and I'm not going to try to list everyone in person. *Spasiba* to *the Russians*. I thank Robert Klieber for his help in the early days of the Cu_2O project. No spectroscopy without good samples. I thank Prof. Dr. A. Forchel (mother nature) and M. Emmerling (N. Lenser) for the cavity (Cu_2O) samples. Frank Plückebaum and Michaela Wäscher made many things possible on short notice, thank you. Furthermore, I would like to express my gratitude to all members of the groups in Würzburg (Technische Physik) and Dortmund (E2) for the good time we had. I acknowledge Matthias Schwab and Gerhard Ortner for joining me to my (west)westfalian homeland.

Finally, I thank Pia Dawidowski for not questioning the sense of spending three years on something strange.